SERS biosensors based on special optical fibers for clinical diagnosis

Flavien Beffara

Ph.D. Thesis

Université de Limoges

University of Limoges

ED610 - Sciences et Ingénierie des Systèmes, Mathématiques, Informatique (SISMI)

XLIM CNRS UMR-7252 Fiber photonics and coherent sources
Laboratory of Bio Optical Imaging, Singapore BioImaging Consortium, A*STAR

A thesis submitted to University of Limoges
in partial fulfillment of the requirements of the degree of

Doctor of Philosophy

High Frequency Electronics, Photonics and Systems

Presented and defensed by

Flavien BEFFARA

On January 11th, 2021

SERS biosensors based on special optical fibers for clinical diagnosis

Thesis supervisors:

XLIM Research Institute:
Dr. Georges Humbert
Dr. Sylvain Vedraine
Dr. Jean-Louis Auguste

Singapore BioImaging Consortium:
Dr. Dinish U.S
Prof. Malini Olivo

JURY:

President of jury
Philippe Roy, CNRS Research director, XLIM Research Institute, Limoges, France.

Reporters
Marc Lamy de la Chapelle, Professor, Le Mans University, France.
Géraud Bouwmans, Professor, Lille University, France.

Examiners
Stefan Andersson-Engels, Professor, Tyndall National Institute, Cork, Ireland.

Guests
Fabrice Lalloué, Professor, Limoges University, France.

I dedicate this manuscript to my loved ones
A. F. F. T.

Acknowledgments

First, I would like to acknowledge the Labex Sigma-Lim for funding half of my PhD. I would also like to acknowledge A*STAR Graduate Academy for funding the second half of my PhD. I thank Biomedical Research Council (BMRC), Agency for Science Technology and Research (A*STAR), Singapore and, the International Research Program "FiberMed" from CNRS, France for their contribution.

Second, I would like to thank the members of the jury who accepted to review this manuscript and attended the defense despite the difficult sanitary conditions due to Covid-19.

I would like to express my deepest gratitude to my two direct supervisors, Dr. Georges Humbert, in France, and Dr. Dinish U.S., in Singapore, for their guidance and support during these three years. The work presented here is the result of the very good synergy between XLIM and SBIC and more specifically between Georges and Dinish. I would like to thank both of them for allowing me to be a part of this project and for their countless advice during my PhD.

In France, I would like to extend my sincere thanks to Jean-Louis Auguste for his expertise and help during the fiber fabrication and the tapering sessions. A special thanks to Sylvain Vedraine for his help and the rich discussions we had on SERS and plasmon theory. Thanks should also go to Sébastien Rougier for the time he spent taking the SEM pictures presented in the following. I also wish to thank Maggy Colas and Julie Cornette for allowing me to use the Renishaw spectrometer at IRCER before I went to Singapore. Finally, I would like to thank the team and all the people who helped in a way or another during my stay at XLIM, this list is, of course, non-exhaustive: Philippe, Raphaël, Geoffroy, Baptiste, Romain, Marie Alicia, and all those I will inevitably fail to mention...

In Singapore, my deepest thanks go to Prof. Malini Olivo and Prof. Patrick Cozzone for welcoming me in SBIC and for their help and support to facilitate my return to France during the pandemic. *'Merci beaucoup'* to Douglas for his artistic advice, our discussions and most of all for making my stay in SBIC so enjoyable. Special thanks to Jayakumar, Stephanie, Riazul, Amelia and Stanley for their numerous advice regarding the sample preparations and the handling of the spectrometer. Finally, I would also like to thank the entire LBOI group, Lunch Kakis and Beer group for welcoming me with open arms into their midst. I hope we will meet again soon.

On a more personal note, I must mention all my friends, from the start of my college years to those I met during my PhD. Citing all of them would be too long. Anyway, I wish to thank *'les Ixeo'*, *'les Matériaux'*, *'les Bios'*, *'les Profs'*, ... for all the moments we shared during these eight years together. These acknowledgments would not be complete if I did not mention the other PhD students: Étienne, Max, Lova, Gabin and Thomas for the daily jokes and laughs. This adventure would definitely not have been the same without them. Very special thoughts for Hugo and Matthieu who have been there for the past eight years, despite the distance. I am sure that we will keep saving kittens in the years to come.

I am also extremely grateful to Nathalie, Ilona and Patrice for hosting me on my return from Singapore and for allowing me to work on my manuscript during the move. I cannot begin to express my thanks to my parents, Fabienne and Thierry, and my sister Astrid, for their unconditional love and support. They always believed in me and pushed me further even if they often did not understand what I was doing. The success of my PhD is undoubtedly thanks to them. Finally, I would also like to extend my deepest gratitude and love to Fiona, who followed me across the world and supported me daily, especially during the hardest moments. I could not have done all of this without her.

Rights

Table of Contents

List of Figures

List of Tables

Abbreviations

2-NT	2-naphthalenethiol
4-MBA	4-mercaptobenzoic acid
4-MBT	4-methylbenzenthiol
A1AT	Alpha-1-antitrypsin
AB	Antibody
AFP	Alpha-fetoprotein
Ag NPs	Silver nanoparticles
AgFON	Bare silver film-over-nanosphere
ALD	Atomic layer deposition
APTES	(3-Aminopropyl)triethoxysilane
APTMS	(3-Aminopropyl)trimethoxysilane
ATP	4-aminothiophenol
Au NPs	Gold nanoparticles
BSA	Bovine serum albumin
CCD	Charge coupled device
CD	Coverage density
CH	Cumene hydroperoxide
CM	Chemical mechanism
Cy5	Cyanine5
DBA	4-(dihydroxyborophenyl) acetylene
EBL	Electron beam lithography
EDC	1-éthyl-3-(3-diméthylaminopropyl)carbodiimide
EF	Enhancement factor
EGFR	Epidermal growth factor receptor
ELISA	Enzyme-linked immunosorbent assay
EM	Electromagnetic mechanism
FEM	Finite element method
HC-PCF	Hollow-core PCF
Hp	Haptoglobin
LAA	Linoleamide alkyne
LC-PCF	Liquid core PCF
LOD	Limit of detection
LSPR	Localized surface plasmon resonance
MBN	4-mercaptobenzonitrile
MFON	Metallic film over nanosphere
MGITC	Malachite green isothiocyanate
MMF	Multimode fiber
MPTMS	(3-Mercaptopropyl)trimethoxysilane
MS	Molecular sentinel
NANF	Nested anti-resonant nodeless fiber
NHS	N-hydroxysuccinimide
NIL	Nanoimprint lithography
NIR	Near infrared
NP	Nanoparticle
NSL	Nanosphere lithography
OCF	Ovarian cyst fluid
PBG	Photonic band gap
PBS	Phosphate buffer saline
PCF	Photonic crystal fiber
PCR	Polymerase chain reaction
PET	Polyethylene terephthalate
PMMA	Poly-(methyl methacrylate)

PNBA	P-nitrobenzoic acid
R6G	Rhodamine 6G
RCF	Ring core fiber
RhB	Rhodamine B
RSD	Relative standard deviation
SC-PCF	Solid-core PCF
SD	Standard deviation
SEM	Scanning electron microscopy
SERS	Surface enhanced Raman spectroscopy
SHIN	Shell isolated nanoparticles
SHINERS	Shell isolated nanoparticle enhanced Raman spectroscopy
SiC-PCF	Side-channel PCF
SMF	Single mode fiber
SuC-PCF	Suspended core PCF
TEM	Transmission electron microscopy
TERS	Tip enhanced Raman spectroscopy
TIR	Total internal reflection
VOCs	Volatile organic compounds

Introduction

Introduction

Biochemical sensing in general is an important research domain that has tremendous applications in various disciplines such as environmental monitoring, food industry, homeland security and healthcare. In this manuscript, we focus on the latter and more precisely on the detection of severe diseases. To this day, countless patients are still dying from cancer, neurodegenerative disorders, and so on. Therefore, new sensors are still in need to facilitate early diagnosis to start the treatment as soon as possible and improve the survival rate of the patients. In this context, traditional tissue biopsy still represents the gold standard in many diagnoses. It consists of taking a portion of tissue to determine the stage of a disease. Unfortunately, diseases like cancer are constantly evolving and tissue biopsy only gives an insight on the disease stage at the time of the sampling. Since this technique is invasive, it cannot be repeatedly performed. Thus, monitoring periodically the evolution of the disease and the effect of the treatment becomes arduous. Recently, another form of biopsy, called liquid biopsy, has emerged. This technique aims to detect a disease by identifying biomarkers in body fluids, such as blood, saliva, urine, ascites and cerebrospinal fluid. The target biomarkers take many forms. For instance, in the detection of cancer, the biomarkers can be circulating tumor cells, DNAs and non-coding micro-RNAs, extracellular vesicles or proteins. Circulating tumor cells are cells that have entered the circulatory system after having been separated from the tumor tissue. Circulating tumor DNAs and non-coding micro-RNAs are genetic content of the cancerous cells that can enter the circulatory system after a cell apoptosis (death) for example. Similar to healthy cells, tumor cells also secrete extracellular vesicles, such as exosomes, to communicate with their surroundings. These vesicles can contain protein, lipids or genomic material that reveal the state of the original cell. All these biomarkers are present in body fluids, and their concentration may be linked to the disease stage. They can also be used to monitor the efficiency of treatment. This technique is much less invasive compared to biopsy tissue and can thus be used more regularly in order to evaluate the evolution of the disease or the efficiency of the treatment. Unfortunately, body fluids are very complex mixtures and detecting trace amount of a target biomarker can be extremely challenging.

Among the techniques that could allow detecting the biomarkers, Raman spectroscopy presents several advantages. It allows characterizing the chemical nature, chemical structure as well as the orientation of many analytes. In addition, the sharp signature peaks of Raman scattering allow multiplex detection, which can be useful for studying complex fluids. This technique is based on the interaction of an excitation light with an analyte, and for a long time, it has been neglected due to the extremely low intensity of the Raman signal. However, the discovery of surface enhanced Raman spectroscopy (SERS) and the development of nanoscience helped in democratizing this sensing technique. It was demonstrated that nanoparticles (NPs) made of noble metal were able to enhance locally both the excitation light and the Raman signal, resulting in enhancement factor ranging from 10^6 to 10^{11}. This allowed overcoming the main limitation of Raman spectroscopy while preserving the fingerprint spectra of the molecules. Even though single molecule sensing was reported under constrained conditions, current substrates still lack sensitivity and reliability for real-life applications. Nanopatterning helped in improving the sensitivity and reliability of state-of-the-art SERS substrates. Nevertheless, there is still a great demand for improved sensitivity and reliability, especially for the detection of biomarkers in clinical bio fluids.

A solution could be to use optical fibers as substrates. Indeed, they are known for their compactness, and their flexibility. In addition, they allow for a low-loss guiding of the light in their core. A special class of fibers, i.e. photonic crystal fibers (PCFs), possess holes that run along their entire length. These holes allow for the incorporation of liquid or gas inside the fiber. Therefore, PCFs represent an ideal candidate for SERS sensing since they exhibit the advantages of optical fibers while allowing for a

potential larger surface of interaction between the light and the analyte. Indeed, since the analyte is inside the sensing medium, the light can interact with it for relatively long lengths. This increased interaction surface area results in an increased sensitivity. In addition, since the light can interact with a much larger number of NPs along the fiber length, PCFs should also improve the reliability of planar substrates, which is currently limited by the precision of nanofabrication techniques. In summary, SERS-based PCFs feature the remarkable advantages of optical fibers while preserving the great identification properties of SERS. In this context, they should simultaneously improve the sensitivity and the reliability of SERS sensors while being compatible with the development of optofluidic platforms with one-step collection/readout processes. All these interests could help in overcoming the remaining limitations that currently forbid SERS for advancing as the gold standard in many biosensing procedures.

The Laboratory of bio-optical imaging (LBOI) from Singapore BioImaging Consortium (SBIC), A*STAR, is specialized in bio-imaging and optical sensing. They develop photoacoustic imaging devices [1] and innovative Raman spectroscopy techniques [2,3]. A few years ago, they started studying the interest of optical fibers for SERS biosensing. Using commercial PCFs, they achieved multiplex detection of cancer biomarkers [4,5]. However, this type of fiber was not specifically designed for SERS sensing and a fiber specifically fabricated for this application could have helped in improving the results further. On the other hand, the team Fiber photonics in XLIM research institute, a joint research unit between CNRS and the University of Limoges (France), is specialized in the fabrication of optical fibers. They develop specialized optical fibers for various applications, such as high-power lasers [6,7], ultra-short pulsed lasers [8,9] and sensing [10]. Thus, a collaboration between SBIC and XLIM to fabricate specifically designed SERS-based fiber sensors appears logic and meaningful. In this context, they developed a novel design of PCF that improved by three orders of magnitude the detection of Rhodamine 6G (R6G) [11]. They also demonstrated the potential of this fiber for biosensing by detecting 2.5 fmol of sialic acid at the surface of a single cell while previous reported techniques required 10^5 cells [12]. Based on these very promising results, they obtained a joint grant for a PhD student to further improve their SERS-active fiber probes. I began my PhD in XLIM to fabricate new optical fibers, which parameters have been specifically designed to improve SERS sensing and I spent the other half of my PhD at SBIC, in Singapore, to realize biosensing experiments with the fabricated fibers. With this scheme, I benefitted from a strong expertise in fiber fabrication while I was in France and in the SERS and biosensing domain from Singapore.

The ultimate goal of my PhD was to design and fabricate SERS-based fiber probes that could be used routinely in a clinical environment in the future. In other words, to be clinically viable, these sensors need to be practical and present an improvement compared to the gold standards, such as enzyme-linked immunosorbent assay (ELISA), polymerase chain reaction (PCR), immunofluorescence or Western-Blot. The ideal sensor should be more sensitive, more reliable, easy to handle, faster and cheaper than the current techniques. To develop a sensor that could overcome most, if not all, of the limitations of existing methods, we listed out several important requirements. The first one was to improve the sensitivity of actual SERS-based fiber sensors. In this way, diseases could be detected at early stages, when the concentration of biomarkers is still low in the body. It also means that biomarkers could be detected in small volume. This is important to create probes that are less invasive as possible. The second requirement was to improve the reliability of the sensors. Indeed, unreliable sensors could lead to false positive and lead to wrong diagnosis. Another requirement was to improve the practicability of the sensor, since at the end, it should be used by clinicians who are not necessarily familiar with the optical fibers. Finally, we also aim to prepare a probe that could eventually replace the current biopsy needle-based two-step sample collection and readout process by realizing it with a one-step sample collection of body fluids and sensing to achieve a faster disease diagnosis.

As we saw previously, SERS is a powerful technique of detection. In the first chapter of this manuscript, we will demonstrate its interest for biosensing. The description of the physical phenomenon will allow revealing the great features of SERS from the origin of the sharp peaks that allow for multiplex detection to the giant increase in the electromagnetic field that allows for detection of trace amount of analyte. In a second time, the review of SERS substrates will point out the limitations that need to be addressed so that SERS sensors can be used more routinely in a clinical environment. Finally, we will review promising biosensing studies realized with both label-free and labeled SERS to demonstrate the versatility of this detection technique and to illustrate the possibility to detect relevant biomarkers for liquid biopsy.

Since PCFs possess holes that allow for the incorporation of fluids inside them, they raised the interest of many researchers for sensing in general and more particularly for SERS. In the second chapter, studying the different fiber topologies available will demonstrate why fibers, and more specifically PCFs, represent a good alternative to standard planar SERS substrates. In particular, it will detail how PCFs can overcome the limitations presented in chapter I. More than just a simple state-of-the-art, the review of reported work will highlight the relevance of optical fibers for biosensing. In addition, it will show that PCFs allow detecting, in a clinical range, biomarkers for various diseases. Finally, we will discuss the different options available that would allow improving the current SERS-based fiber probe to benefit from the best sensitivity and reliability.

Based on the observations made in the state-of-the-art in chapter II, we decided to focus our work on an already reported fiber topology, i.e. suspended core PCF (SuC-PCF), since it presented several advantages over the other fiber designs. Unfortunately, so far the reported studies are contradictory and do not allow selecting the fiber parameters that would give the best sensitivity and reliability sensor. In chapter III, we propose to optimize different aspects of the fiber in order to create the most sensitive, reliable and practical fiber probe possible. The effect of the core size, the size of the cladding holes, the technique used to make the fiber SERS-active and other aspects will be discussed in full detail through simulations and experiments. In a second time, as a proof of concept, we will present the exciting results of a clinical study to show that our fiber sensors could be used for liquid biopsy in order to detect severe diseases at an early stage.

Although we achieved remarkable results with the optimized SuC-PCF, we noted during our investigations and based on the reported work that the sensitivity of SERS-based fiber probes was limited by the topology of the fiber. To further improve it, we will present in chapter IV an innovative fiber design specially conceived to increase the interaction surface between the excitation light and the analyte. The logic behind the conception will be detailed and simulation will illustrate how the fiber topology can increase the sensitivity of the sensor. Unfortunately, the novel design is not compatible with standard excitation techniques, such as focusing the laser directly into the core. Therefore, several envisioned techniques that can be used to properly excite the core will be discussed. Finally, to experimentally demonstrate the interest of the new topology, we will compare its sensitivity to that of our best SuC-PCFs.

Chapter I. Introduction to Raman scattering and surface enhanced Raman spectroscopy

Chapter I. Introduction to Raman scattering and surface enhanced Raman spectroscopy

I.1. Introduction

In this chapter, we present the Raman scattering from its origin to its application as a detection technique. We develop the general theoretical background required to understand the tests conducted in chapters 3 and 4. We also present the inherent limitations of Raman scattering that forbade it to become more widely used.

Subsequently, we present how surface enhanced Raman scattering (SERS) overcame these limitations and allowed for Raman scattering to be more and more used since the late 1970s. We describe the physical phenomenon by detailing both electromagnetic and chemical mechanisms. We also present the different requirements needed to achieve the most effective configuration.

Finally, we present a state-of-the-art of the different types of SERS substrates ranging from colloidal solutions to nanopatterned surfaces. We present both under research and already commercialized SERS substrates to situate precisely our work in the current context of SERS sensing.

I.2. Raman scattering

I.2.1. Discovery

In the early twentieth century, many scientists were working on light scattering. In 1910, Rayleigh published Colours of the Sea and Sky [13], in which he laid the foundations for the elastic scattering. In 1923, Adolf Smekal predicted that a monochromatic light could be scattered in shorter and longer wavelengths, in addition to the original wavelength [14]. He stated that these shifts corresponded to the energy difference between two states of a molecule, thus paving the way for the discovery of inelastic scattering.

In 1928, Chandrasekara Venkata Raman and Kariamanikkam Srinivasa Krishnan published a paper entitled “A New Type of Secondary Radiation” in which they confirmed Smekal’s theory [15]. They used a blue-violet filter to select a small range of wavelengths from a beam of sunlight and focused it on a purified liquid or its vapor. After positioning a yellow-green filter between the scattering material and the observer’s eye, a feeble light was visible, proving that the excitation light was scattered at longer wavelengths when encountering the material. If only Rayleigh scattering was happening, the scattered photons would possess the same wavelength as the excitation ones and would be stopped by the second filter. Though Grigory Landsberg and Leonid Mandelstam independently demonstrated the same effect in crystalline quartz also in 1928, Raman’s experiment was the first report to validate Smekal’s hypothesis and to this day this type of scattering bears his name.

I.2.2. Principle and application to Raman spectroscopy

When a monochromatic beam at λ_0 is focused on a molecule, the incident photons are either transmitted, reflected or absorbed. In addition, as introduced above, a small portion will be scattered at the same wavelength λ_0 (Rayleigh scattering) and an even smaller portion will be scattered with a wavelength shift (Raman scattering), as illustrated in Figure 1.

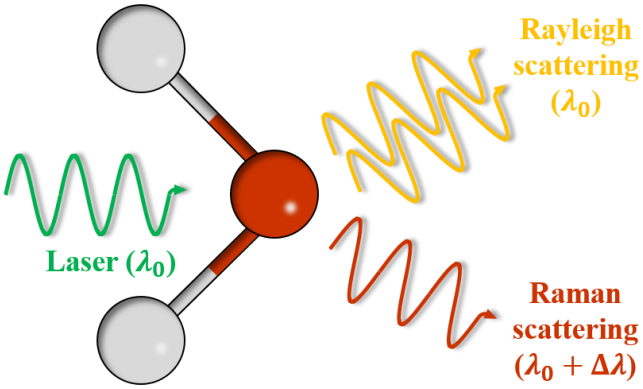

Figure 1 Schematic illustrating the two scattering phenomena occurring when a molecule is submitted to an electromagnetic field.

Raman scattering corresponds to the interaction of the incident light wave with the polarizability of the molecule. When submitted to an electromagnetic field E, the cloud of electrons of the molecule is distorted due to Lorentz force, which, in turn, results in the creation of a radiating dipole. The resulting polarization P can be defined as:

$$P = [\alpha]E \tag{1}$$

With: $[\alpha]$ the polarizability tensor, i.e. the capacity of the electronic cloud to be distorted when exposed to E. In the case of Raman scattering (inelastic scattering), the radiating dipole oscillates with a frequency different from the frequency of the incident light, this results in the emission of a photon with a different energy than the incident one. Indeed, the energy of an incident photon is given by Planck-Einstein relation:

$$E_0 = h.\nu_0 = h\frac{c}{\lambda_0} \tag{2}$$

With: E_0: energy of a photon (J), h = 6.62.10^{-34}: Planck constant (J.s), ν_0: frequency of the incident electromagnetic field (Hz), c: speed of light (m.s^{-1}), λ_0: wavelength of the incident electromagnetic field (m).

As explained above, the incident photon will excite the molecule by giving its energy. When the molecule vibrates and emits a photon, three emission types are possible. The first one is the emission of a photon with the same wavelength as the incident light and corresponds to Rayleigh scattering. The remaining two are emissions with wavelength shift. If the molecule dissipates more energy by emitting an optical phonon for instance, it will emit a photon that possesses a smaller energy than the incident one. Because the energy of the emitted photon is smaller, the wavelength is bigger and thus the emitted light is shifted towards red wavelengths. This is the Stokes Raman scattering. On the contrary, if the molecule absorbs a phonon, it will be able to emit a photon with a bigger energy than the incident one. According to Planck-Einstein relation, the wavelength of this photon will be blue-shifted compared to the incident light. This is anti-Stokes Raman scattering. Figure 2 summarizes the three types of scattering possible. However, anti-Stokes scattering is less intense than Stokes scattering; thus, many Raman spectroscopy techniques are based on Stokes scattering. This will be the case in the following of this manuscript.

When the molecule is excited by the incident light, several variations in the molecule structure can occur, such as stretching, bending, twisting or rotation. Each of these structural variations corresponds to a well-known Raman peak. Because every molecule possesses a unique three-dimensional structure, they

also possess a unique combination of Raman peaks, i.e. Raman spectrum. This spectrum is a true fingerprint of the molecule. Therefore, since the molecules can be uniquely identifiable, it resulted in a new method of detection: Raman spectroscopy. The position of the Raman peaks in the spectrum is independent from the excitation wavelength and excitation power. For instance, a molecule excited with 532 nm or 785 nm laser exhibits similar spectra. Thus, to have the same abscissa scale between the spectra whatever the excitation wavelength it is customary to quantify the wavelength shift by using the Raman shift. It is defined by:

$$Raman\ shift = \frac{1}{\lambda_{incident}} - \frac{1}{\lambda_{scattered}} \quad (3)$$

With: $Raman\ shift$ (in cm^{-1}) and $\lambda_{incident}, \lambda_{scattered}$ the incident and scattered wavelengths (in cm).

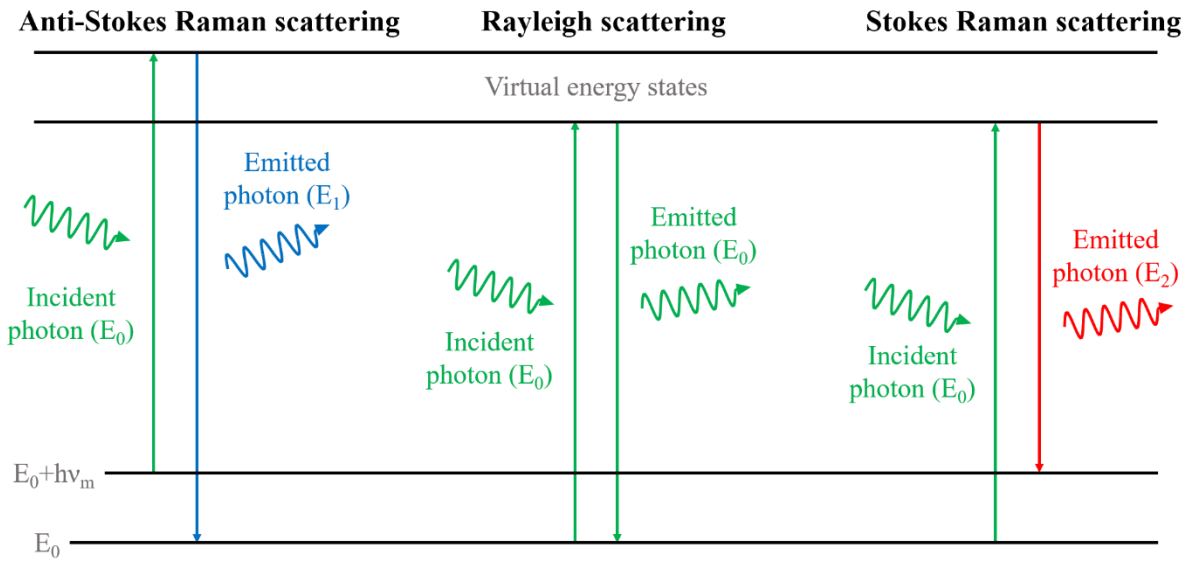

Figure 2 Simplified energy diagram illustrating Rayleigh, Stokes and anti-Stokes scatterings.

Raman spectroscopy presents many advantages. For instance, the analyte can be directly tested under all its forms, i.e. solid, liquid or gaseous, with minimal preparation. Furthermore, the peaks of the Raman spectrum are extremely narrow compared to fluorescence peaks, making it highly selective. This high selectivity is demonstrated by the possibility to achieve multiplex detection [16,17]. Finally, the intensity of a peak can be correlated to the concentration of a chemical present in the tested sample. All these advantages make Raman spectroscopy an ideal candidate for biosensing, however, it also possesses several limitations.

I.2.3. Limitations

The main limitation of Raman scattering is its extremely weak cross-section. Here, the Raman cross-section refers to the probability that a molecule absorbs a photon and emits a Raman photon. As mentioned previously, not all the photons are scattered when they encounter a molecule. Some of them are transmitted, reflected or absorbed. The scattered photons only represent a small portion of the total photons. In addition, most of the scattered photons follow Rayleigh scattering (one out of ten thousand). It is generally admitted that only one photon out of one hundred million is Raman scattered. Thus, the resulting signal is extremely weak. It has been shown that Raman scattering cross-section is 10^6 to 10^{10} times weaker than fluorescence or infrared spectroscopy [18,19]. An ideal solution to overcome this limitation would be to increase the useful signal for improving the sensitivity while maintaining the same excellent selectivity.

The first immediate solution to overcome this drawback is to increase the concentration of the analyte. Indeed, the incident photons will encounter more molecules and the probability to emit a Raman scattered photon will thus be more important than before. However, this solution does not really have a sense because the point of developing a sensor is that it must be as sensitive as possible to detect the lowest concentrations possible.

The second solution is to increase the power of the incident light and the time of measurement in order to increase the number of photons and statistically increase the number of scattered Raman photons. This is what C. V. Raman did in 1928 when he focused the sun light in order to be able to see the scattered light at the end of his setup. However, increasing the power of the incident light might result in overheating the tested sample and might denature it. The development of lasers in the 1960s and the development of CCD detectors have significantly increased in the use of Raman spectroscopy. However, this remained insufficient to increase significantly the interest of Raman spectroscopy.

I.3. Surface enhanced Raman scattering (SERS)

I.3.1. Principle

Even with the improvements made in Raman spectroscopy setups, the useful signals remained weak and hard to detect at low concentrations. Therefore, a solution had to be found to detect small concentrations of analyte with relatively low laser power. Surface enhanced Raman scattering (SERS), which appears when a molecule is adsorbed onto nano-roughened noble metal surfaces or their colloidal nanoparticles (NPs), drastically increases the signals while preserving the sharp Raman peaks and the possibility of multiplex detection [20–25].

It was first observed in 1974, when pyridine was adsorbed onto a silver electrode [26]. The intensity of the Raman signature peaks of pyridine was significantly increased when the molecules were adsorbed on the electrode surface. Three years later, Albrecht and Creighton estimated that this enhancement can rich factor 10^5 [27]. The same year, Jeanmaire and Van Duyne also established the importance of the excitation wavelength in the enhancement phenomenon and they hypothesized that this enhancement was due to the formation of active sites as well as an increase in surface area due to the etching of the silver surface [28]. This theory was confirmed by Moskovits and Billman few years later when they demonstrated the importance of surface roughness in the enhancement mechanism [29,30].

Since these first discoveries, it has been shown that SERS is based on two mechanisms. The first one is called electromagnetic mechanism (EM) and is independent of the tested analyte. The second one, less important, is named chemical mechanism (CM) and strongly depends on the nature of the analyte.

I.3.1.1. Electromagnetic mechanism

This mechanism is based on the enhancement of the electric field thanks to localized surface plasmon resonance (LSPR). In a metal, the conduction electrons can move randomly inside the material. However, when they are submitted to an electromagnetic field, these electrons orient themselves according to this field because of Lorentz force resulting in a small delocalization (about 10^{-13} m) as illustrated in Figure 3. Though this delocalization is extremely small, it is important enough to create a shift in the position of the electrical charges barycenter. Indeed, the atom nucleus, which is heavier than the cloud of electrons, can be considered motionless. The positive and negative charges are then separated and will attract each other until the electrons are back in their original position. The cloud of electrons may be delocalized again if the mechanical energy did not wear off leading to oscillations of the electrons plasma. The quantification of these plasma oscillations is called “plasmon” [31]. These oscillations enhance the electromagnetic field near the surface between the metal and the dielectric. The

field is maximum at the interface and decreases exponentially. The frequency at which the plasma oscillates can be expressed as:

$$f_p = \sqrt{\frac{ne^2}{\pi m_e}} \tag{4}$$

With: n the number of electrons, e the elementary charge of an electron and m_e the mass of an electron [32]. We can distinguish two kinds of surface plasmons. The first one is delocalized and occurs in planar surfaces and the second one is localized in small structures of a few nanometers, i.e. LSPR.

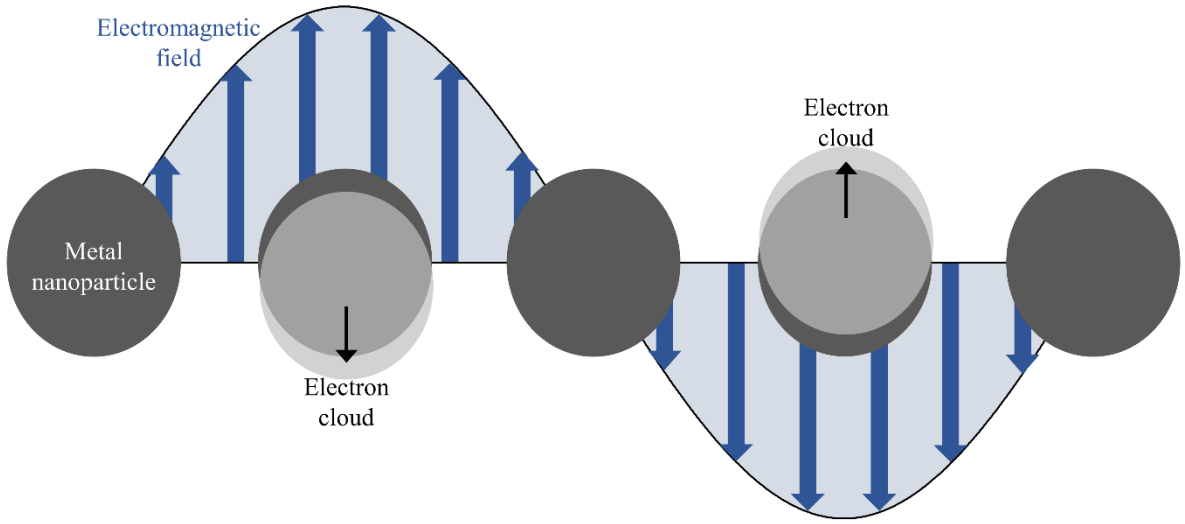

Figure 3 Illustration of the electron cloud delocalization undergone by a metallic nanoparticle when submitted to an electromagnetic field.

Several factors can modify the plasmon resonance such as the material, the shape and the size of the particles, but also the wavelength and the polarization of the excitation light and the angle with which it encounters the particles. In the following, we will focus on the plasmon resonance theory of nanospheres.

Using Drude model, we can express the permittivity of the metal as:

$$\varepsilon_{metal} = 1 - \frac{\omega_p^2}{\omega^2 + i\gamma\omega} = 1 - \frac{\omega_p^2}{\omega^2 + \gamma^2} + i\frac{\omega_p^2\,\gamma}{\omega(\omega^2 + \gamma^2)} \tag{5}$$

With γ a constant specific to the metal and ω_p, the plasma pulsation defined as:

$$\omega_p = \sqrt{\frac{n\,e^2}{\varepsilon_0 m}} \tag{6}$$

As we can see in equation 5, the permittivity of the metal depends non-linearly on the pulsation of the incident light. According to the value of ω, the metal will not react in the same way with the incident light:

- if $\omega > \omega_p$ → $0 < \varepsilon_{metal} < 1$ → the incident wave will be transmitted
- if $\omega_p = \omega$ → $\varepsilon_{metal} = 0$ → the plasma can resonate
- if $\omega < \omega_p$ → $\varepsilon_{metal} < 0$ → the incident wave will be reflected

Here, in order to simplify the explanations, we only consider the conduction electrons. In noble metals, the core electrons are also important in the definition of the permittivity. This matter is addressed further in [33].

Considering a metal sphere, one can express its polarizability α according to the metal permittivity (ε_m), the permittivity of the surrounding media (ε_{sur}) and the radius of the NP (r) [33]:

$$\alpha = 4\pi r^3 \frac{\varepsilon_m - \varepsilon_{sur}}{\varepsilon_m + 2\varepsilon_{sur}} = 4\pi r^3 g \quad (7)$$

As explained above, the polarizability represents the ability of a particle to form instantaneous dipoles. If g tends towards infinity, the polarizability also tends towards infinity. This means that dipoles are continuously forming. In other words, the electron cloud is always distorted, i.e. it oscillates around the nucleus (plasmon). Therefore, equation 7 gives the condition of resonance for which the plasmon exists:

$$\varepsilon_m = -2\,\varepsilon_{sur} \quad (8)$$

This relation shows that the position of the resonance depends on the metal used and on the surrounding media. Once the plasma is oscillating, it will hugely magnify the electromagnetic field at the surface of the NP. In Raman spectroscopy, the scattered intensity is linear with the incident field intensity E_0^2 [34]. Thus, the Raman intensity is linked to the absolute square of E_{out} at the surface of the NP and can be expressed as:

$$|E_{out}|^2 = E_0^2\,[|1 - g|^2 + 3cos^2\theta(2Re(g) + |g|^2)] \quad (9)$$

With θ, the angle between the incident field vector and the vector to the position of the molecule on the surface.

The maximum enhancement happens when the molecule is on the axis of propagation, i.e. when $\theta = 0°$ or $\theta = 180°$, and the minimum enhancement occurs when $\theta = 90°$. In addition, as mentioned previously, g needs to tend towards infinity for the plasma oscillation to occur. Thus, we can simplify expression 9 into:

$$|E_{out}|^2{}_{max} = 4E_0^2|g|^2 \text{ and } |E_{out}|^2{}_{min} = E_0^2|g|^2 \quad (10)$$

The ratio between the maximum and minimum enhancement being four, we can define the average enhancement as:

$$|E_{out}|^2{}_{max} = 2E_0^2|g|^2 \quad (11)$$

As highlighted previously, when the incident light encounters a molecule, it creates an oscillating dipole around the molecule. The vibrational frequency of the molecule can shift the frequency of a small portion of the incident light and it results in the emission of Stokes or anti-Stokes shifted photons.

If the molecule is in the vicinity of a metallic NP, the scattered electromagnetic field can also be enhanced. Although, the treatment of this enhancement is more complex than for the enhancement of

incident light [35,36], it can be simply understood with a first-order approximation, resulting in an equation similar to equation 9 at the scattered wavelength:

$$|E'_{out}|^2 = E_0^2\ [|1 - g'|^2 + 3cos^2\theta(2Re(g') + |g'|^2)] \quad (12)$$

With g', defined by the metal permittivity (ε'_m) and the permittivity of the surrounding media (ε'_{sur}) at the scattered wavelength.

The theoretical electromagnetic enhancement factor (EF) can then be defined by:

$$EF_{th} = \frac{|E_{out}|^2|E'_{out}|^2}{|E_0|^4} = 4|g|^2|g'|^2 \quad (13)$$

If the Raman shift is small, the incident and scattered wavelengths are close to one another, thus g and g' can be considered equal, and the EF varies according to g^4. This is commonly known as the fourth power enhancement of the electromagnetic field. Depending on the value of g, EF_{th} can reach values up to 10^8-10^{10}.

I.3.1.2. Chemical mechanism

The CM enhancement, also known as electronic enhancement, is considered to be responsible for a much smaller enhancement and despite all the studies made so far it is less understood than the EM enhancement. It seems to be limited to the first layer of molecules directly adsorbed on the surface of the NP responsible for the enhancement [37,38]. The theory behind CM relies on two components: (i) the non-resonant and (ii) the resonant transfer of an electron (or hole) to the adsorbed molecule [37].

The non-resonant transfer of an electron to the adsorbed molecule is an extremely short phenomenon, the electron returning to the metal after less than a femtosecond in the molecule. This transfer, also called "impulse mechanism", happens when the electron energy does not match the resonance condition and seems to be responsible for the excitation of a vast majority of modes resulting in an enhancement in the range of 30-40 folds in addition to the EM enhancement. It is supposed that all the adsorbed molecules contribute to this phenomenon [37].

On the other hand, the resonant transfer of an electron to an adsorbed molecule seems to be rarer and happens only in certain sites (SERS-active sites). It seems to be responsible for the excitation, and thus the enhancement of only certain modes, such as C—C stretch mode in C_2H_4 for instance [37]. Although this phenomenon is rarer and concerns only certain modes, it leads to a more important enhancement than the impulse mechanism and it could enhance the favorable modes up to 10^3 fold.

Because it is difficult to differentiate the CM and EM enhancements, EM enhancement will usually be considered more important in most of the cases [39], even though, the total SERS enhancement is a combination of the two mechanisms.

I.3.1.3. Wavelength dependence

As explained previously, the SERS response of a substrate varies with the incident wavelength. Several studies were conducted to determine the effect of the excitation wavelength on a given SERS substrate [40–44]. This would allow determining the best excitation wavelength for a given SERS substrate or it would allow optimizing the parameters of the SERS substrates for a given excitation wavelength in order to achieve the strongest enhancement possible. The experimental setups required at least a tunable laser source, a set of adapted filters and several detectors. In the case of isolated NP, or arrays of weakly interacting objects, McFarland *et al.* demonstrated that the maximum EFs did not occur when the

excitation laser is tuned to the peak of the plasmon resonance [41]. Using benzenethiol adsorbed on Ag NPs arrays, they showed that the maximum EFs occur when the laser wavelength is slightly blue shifted compared to the LSPR peak. Indeed, in this configuration, both the laser and the Raman scattered signals are strongly enhanced, which leads to the highest SERS EF. They also illustrated the fact that adsorbing the analyte molecules on the surface of the NP arrays tends to shift the LSPR peak towards longer wavelengths. Zhang *et al.* confirmed that the strongest EF occurs when the LSPR peak is situated between the excitation wavelength and the wavelength of the vibration mode [42].

In addition, it is important to remember that the final goal of this thesis is to create SERS sensors that might be used in clinical environment. Therefore, an extra care should be taken in the selection of the excitation wavelength [45,46]. Indeed, body tissues, such as skin or fatty tissues, and body fluids, such as oxygenated or deoxygenated blood, possess several transparency windows in the near-infrared region (NIR) where the scattering and absorption of the light are the lowest: the first one is between 650 nm and 950 nm (NIR-I); the second one is between 1000 nm and 1350 nm (NIR-II) and the last one is between 1500 nm and 1800 nm (NIR-III) [46–48]. Moreover, the LSPR of coinage metals, such as silver and gold, are situated in the visible range. Therefore, exciting the analyte with a wavelength in the first region (NIR-I) is ideal to benefit from the best SERS enhancement possible with coinage metal and low absorption. In the following, we will use wavelengths that fall into this range.

I.3.1.4. Distance dependence

The final aspect of SERS that needs to be taken into consideration is the distance dependence of this phenomenon. Indeed, from a practical point of view, the distance plays an important role, especially in biodetection. For some studies [49–54], the analyte needs to be immobilized near the metal surface thanks to a capture layer, such as a layer of antibodies. This inevitably results in greater distance between the metal surface and the targeted molecule. In addition, some SERS platforms monitor the variations in Raman intensity for different distances between the Raman tag and the metallic surface to detect the presence of an analyte [55–57].

As stated previously, the CM enhancement is extremely localized and occurs only where the molecules are directly adsorbed onto the metal surface. However, theoretical considerations predict that the EM enhancement occurs even though the analyte molecule is not directly adsorbed onto the metal surface. It has been shown [58] that the SERS intensity varies with:

$$I_{SERS} = \left(\frac{a + r}{a}\right)^{-10} \tag{14}$$

With: a the radius of curvature of the roughness feature on the metal surface. In the case of an NP, a is the radius of the NP. r represents the distance between the metal surface and the analyte. In addition to showing that SERS enhancement is theoretically possible when a molecule is not directly adsorbed on a metal surface, equation 14 also demonstrates that SERS enhancement decreases extremely rapidly with the distance from the metal surface.

So far, numerous studies have been conducted to estimate the range of the SERS enhancement. In the early stage of SERS, Murray *et al.* used poly(methylmethacrylate) (PMMA) as a spacer layer between a rough silver film and p-nitrobenzoic acid (PNBA) to determine the effect of the distance on the SERS signal [59]. They deposited PMMA layers of few Å and measured the PNBA SERS signal after each deposition. They observed a fall-off of the enhancement by a factor 10 for every 35-50 Å deposited layers in the range 0-12 nm. In 2006, Dieringer *et al.* used atomic layer deposition (ALD) to coat layers of aluminum oxide (Al_2O_3) with four different thicknesses onto Ag film over nanosphere (AgFON) [60]. Then, they adsorbed pyridine onto the different Al_2O_3 films and measured the resulting SERS signal.

The four spectra are available in Figure 4(a). After fitting the experimental data (Figure 4(b)), they were able to determine that, for this particular configuration, the intensity of the signal was ten times lesser after only 2.8 nm.

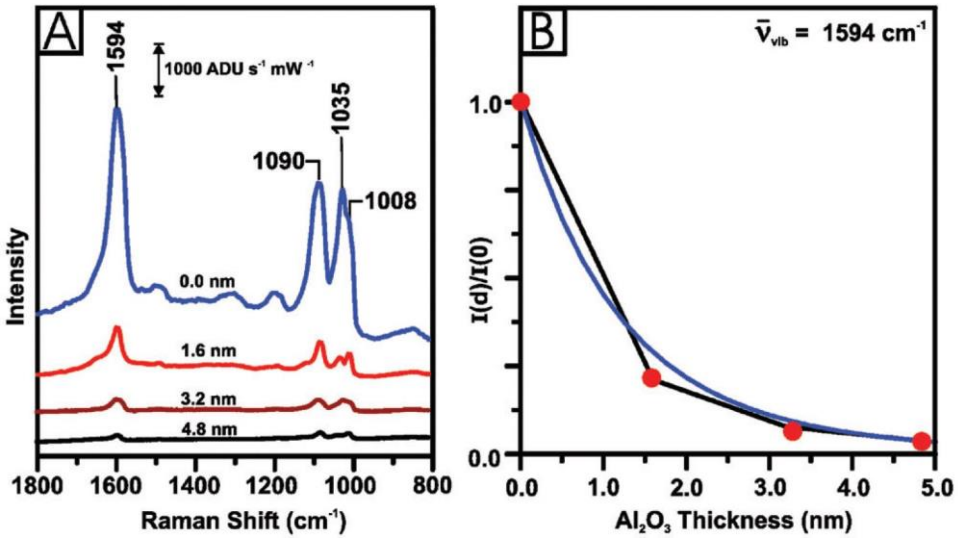

Figure 4 (a) SERS spectra measured when the molecules of pyridine are adsorbed on different thicknesses of alumina, coated on AgFON. (b) Variations of the normalized SERS intensity of 1594 cm^{-1} peak of pyridine for the different alumina thicknesses. Reproduced from [60].

More recently Masango *et al.* demonstrated that, in some cases, equation 14 failed to fit the experimental data [61]. They deposited monolayers of Al_2O_3 on bare AgFONs and AgFONs functionalized with self-assembled monolayers of toluenethiol. Subsequently, they monitored the intensity of the 2892 cm^{-1} peak of trimethylaluminum with increasing distance from the AgFONs. The experimental results are available in Figure 5. Then, they tried to fit the experimental data with equation 15 for different curvature radii. They noted that a section of the experimental data could be fitted by the equation with a small curvature radius (2 nm) and the second section of the curve by the equation with a larger curvature radius (8.5 nm). This means that small NPs were responsible for the SERS intensity close to the NPs, whereas larger NPs were responsible for the SERS intensity further away from the NPs. In order to represent this phenomenon, they proposed the following equation:

$$I_{SERS} = C_1\left(1+\frac{r}{a_1}\right)^{-10} + C_2\left(1+\frac{r}{a_2}\right)^{-10} \quad (15)$$

With a_1 and a_2, the radii of curvature of AgFON features that are responsible for the long-range and short-range effect. C_1, C_2 are constants that account for the relative contributions of the two terms. This equation allowed fitting much closer to the experimental data. This study demonstrates further the importance of the geometry of the SERS substrate. If the SERS substrate presents NPs with relatively large variations in geometry, the distance dependence of the SERS response is more complex. In summary, SERS enhancement depends on the topology of the metallic SERS substrate and it remains an extremely localized phenomenon that occurs mainly in the first 10-15 nanometers near the metal surface [62,63].

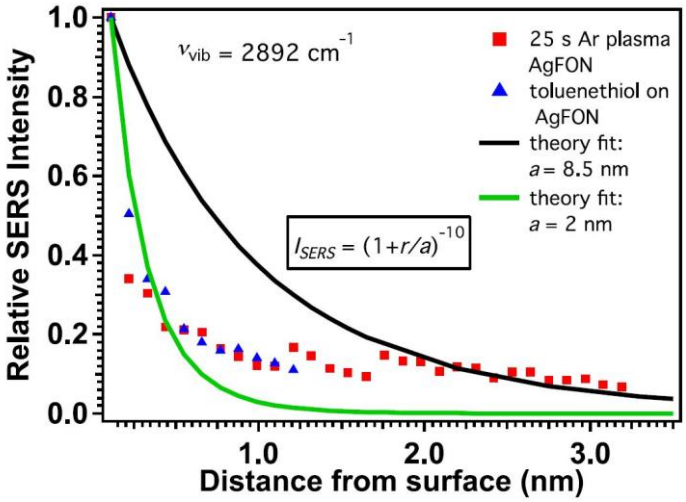

Figure 5 Variations of the relative SERS intensity of the 2892 cm^{-1} peak of trimethylaluminum with distance from a bare AgFON surface and AgFON functionalized with toluenethiol self-assembled monolayers. Reproduced from [61].

In addition, it has been shown that SERS intensity can be further enhanced in small specific locations called hotspots. These locations can be sharp tips, nanogaps between NPs or nanogaps between an NP and a metallic surface [64–68]. For instance, Moskovits explained the mechanism behind this phenomenon using a dimer of metallic NPs as illustrated in Figure 6 [69]. In the two panels of Figure 6, the little dots in the center of the dimer represent the analyte molecule. The electronic field polarizes the NPs, creating an excess of positive charges on one side of the NPs and an excess of negative charges on the other side. The difference between the two panels is the polarization of the light represented on the right of the figure. In the top panel, the polarization is perpendicular to the main axis of the dimer, whereas it is parallel in the bottom panel. From there, it results that the excesses of charge are not localized in the same locations in the NPs. When the excitation field is polarized along the main axis of the dimer, decreasing the distance d between the two NPs allows reducing the proximity of the charges between the two NPs. This results in an increased electric field between the two NPs where the analyte is situated. In addition, since the excess of charge in an NP is located towards the other NP, each NP has an impact on the polarizability of the other, yielding an increase in the electromagnetic field. In

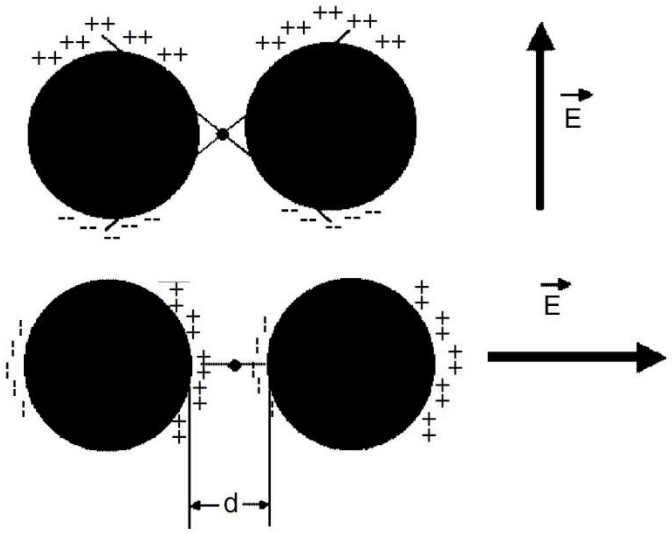

Figure 6 Illustration of the mechanism that creates a giant increase of the EF in a hotspot. Reproduced from [69].

summary, for a polarization along the main axis of the dimer, the NPs polarization results from the excitation field and the induced dipole created in the other NP. This yield tremendous EF. However, bringing the NPs closer when the light is polarized perpendicularly to the main axis does not allow the same interaction between the two NPs resulting in a smaller electric field and thus a smaller EF.

Moreover, it has been shown that closing the gap between the NPs results in giant EFs. Le Ru *et al.* showed that it was $\sim 5 \times 10^5$ for a 10 nm gap between two 25 nm Au NPs and it became $\sim 3 \times 10^9$ when the gap was only 2 nm [19]. It was reported that the EF is proportional to $\frac{1}{d^2}$ [70]. In some cases, the maximum enhancement inside a hotspot can be up to 300 times larger than the averaged enhancement over the whole surface [19]. Since the EF in the hotspot is much greater, it was argued that the majority of the EF came from the hotspot. To illustrate this, Camargo *et al.* fabricated two types of silicon substrates. On the first one, they deposited isolated Ag nanocubes and, on the second one, they deposited nanocubes dimers with narrow gaps. Then, they functionalized the two types of substrates with 4-methylbenzenthiol (4-MBT). All the substrates exhibited the SERS signal. Subsequently, they treated the two substrates with plasma. This removed the molecules of 4-MBT everywhere on the substrates except inside the nanogap. The cleaned substrate with isolated Ag nanocubes no longer exhibited the SERS signal of 4-MBT. However, the substrate with the dimers exhibited a signal similar to the one measured prior to the plasma treatment. This means that the majority of the measured SERS signal on the substrates with the dimers was due to the 4-MBT molecules present in the nanogap, thereby demonstrating that the EF of hotpots contributes to a large portion of the measured SERS signal.

I.3.1.5. Total enhancement

As described before, the total theoretical SERS enhancement factor is the combination of the two mechanisms. It can be described by:

$$EF_{th} = EM * CM \tag{16}$$

The combination of EM and CM results in extremely high enhancements [71–73]. In certain configurations, SERS EF even allows for single molecule detection [74–81]. This represents the main advantage of SERS: it enhances tremendously useful signal while also maintaining the extremely good selectivity of Raman scattering. Since the signal is drastically increased, the required power of the excitation light can be decreased significantly, which helps to preserve the analyte and avoid any deterioration.

As explained previously, it is difficult to isolate one enhancement mechanism from the other and the total EF can be obtained experimentally [41]. The technique takes into account the EM enhancement of both the incident and scattered signals and the CM enhancement. To calculate it, one needs to measure the SERS intensity (I_{SERS}) when the analyte is in the vicinity of the metal surface and the normal Raman intensity (I_{NR}) of the analyte alone. One also needs to estimate the number of molecules bound to metallic particles surface (N_{surf}) and the number of molecules in the excitation volume (N_{vol}). Experimental EF is defined as follows:

$$EF_{exp} = \frac{I_{SERS}/N_{surf}}{I_{NR}/N_{vol}} \tag{17}$$

In summary, in order to create a SERS sensor that exhibits the best EF, one should keep in mind to create a sensor that possesses a short distance between the analyte and the metallic surface, an excitation

wavelength adapted to both the LSPR and the Raman scattered signal and if possible create hotspots in order to further increase the signal.

I.3.2. Fabrication of SERS substrates

I.3.2.1. Principal parameters of a SERS substrate

In this section, we introduce the parameters that will be used in the following of this manuscript to estimate and compare the sensitivity and reliability of a SERS sensor. These two features are of key importance in the creation process of a SERS probe. Brown *et al.* refer to the interplay between sensitivity and reliability as the "SERS uncertainty principle"[82]. They suggest that the SERS substrates exhibiting the highest enhancement are the less reproducible and vice versa. They base their reasoning on the fact that SERS substrates using unstructured NPs often exhibits the highest SERS enhancement and that increasing the uniformity of the enhancement across the substrate tends to decrease the maximum enhancement. A schematic illustrating this is available in Figure 7.

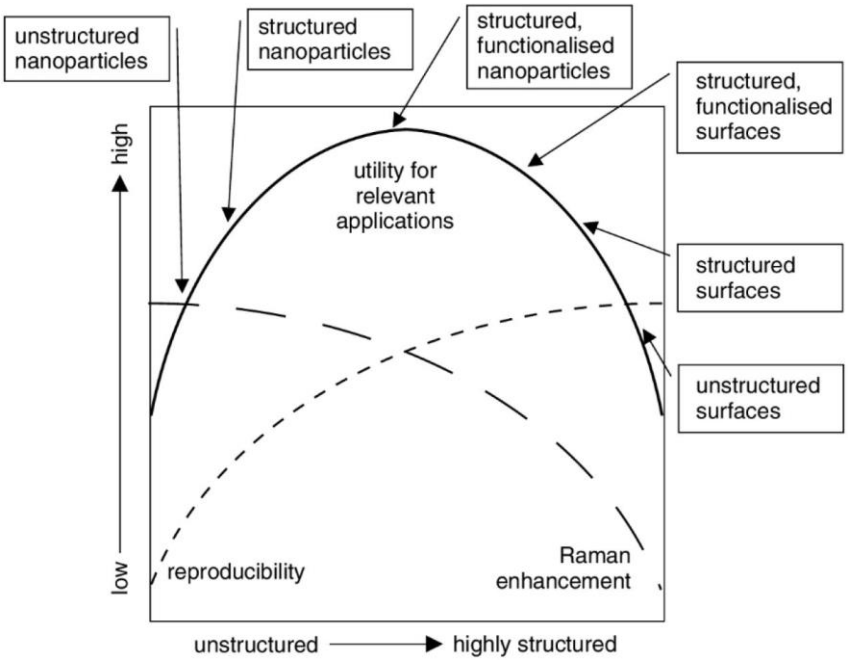

Figure 7 Diagram showing the changing characteristics of SERS structures between the unstructured and highly structured variety. Reproduced from [82].

Similarly, in order to have sensors with clinical relevance, a compromise between sensitivity and reliability has to be found. A sensor exhibiting good reliability but poor sensitivity might fail in the detection of trace amount of analyte, whereas a sensor with extremely high sensitivity but with poor reliability might result in the detection of false positive. In addition, a good clinical sensor needs to be sensitive enough to detect low concentrations of analyte in small volumes to detect diseases at an early stage. Selectivity and specificity are also important for biosensing since the analyte can be present in small amount inside a complex matrix, such as blood, that may exhibit parasitic Raman signals. Therefore, sensors that allow targeting specifically the analyte represent a giant advantage.

To determine the sensitivity of a SERS sensor, several criteria are often used. The first one is the limit of detection (LOD). It consists of the lowest concentration of analyte the sensor can detect. Intuitively, between several sensors, the most sensitive will be the one able to detect the lowest concentration. Another criterion used to compare the sensitivity of several sensors is the Raman intensity obtained in similar conditions. For example, common Raman reporters are molecules with strong Raman signature

peaks. The intensity of one of these signature peaks can be monitored using different sensors. The sensitivity is directly linked to the Raman intensity of this peak, i.e. the most sensitive sensor gives the highest intensity.

The reliability corresponds to the ability of a sensor to give uniform SERS signals. Ideally, when measuring several times the Raman signal emitted by an analyte, a SERS sensor should exhibit the exact same spectrum every time, both in terms of Raman shift and intensity, i.e. all the signature peaks of the analyte should be present and each peak should have the same intensity. Reliability is often defined by two parameters: reproducibility and reliability. Reproducibility represents the ability of a unique sensor to give uniform signals over the entire active surface, as illustrated in Figure 8. It is generally agreed that SERS sensors exhibiting relative standard deviation (RSD) below 5% are considered extremely reproducible [83–86]. Repeatability represents the ability of several sensors prepared in the same condition to give uniform signals (Figure 8). It is of tremendous importance as it demonstrates the ability to fabricate sensors that will respond similarly under the same conditions. Despite its importance for the commercialization of SERS sensors and for them to be used in a clinical environment, repeatability is often not presented in research papers. However, Nathan stated that a batch of SERS sensors with variations lower than 20% could be considered acceptable [87].

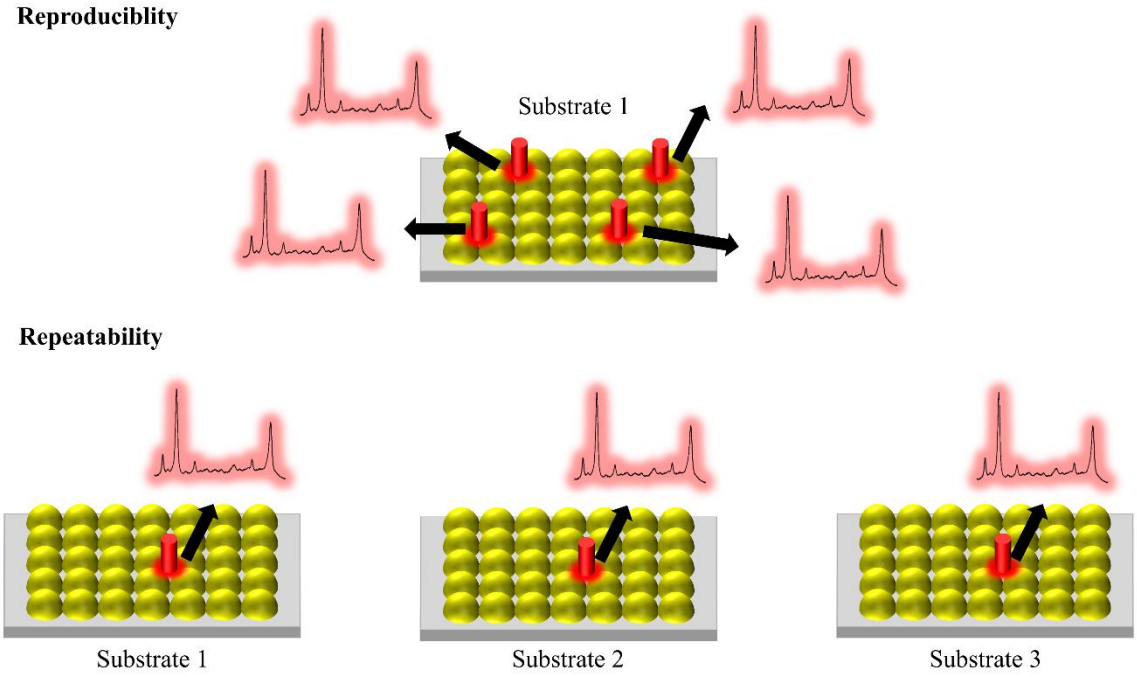

Figure 8 Schematics presenting the notions of reproducibility and repeatability. A single substrate should exhibit uniform SERS signals under the same conditions, i.e. reproducibility. A batch of substrates prepared in the same conditions should exhibit identical SERS response, i.e. repeatability.

Since its discovery on roughened silver electrodes, numerous substrates have been developed as SERS sensors, which can be classed in three main sorts: colloidal solutions, NPs deposited on planar substrates and nanopatterning. In the following, we present a non-exhaustive list of techniques used to prepare SERS substrates in these three configurations. The idea is not to present all the existing SERS substrates, but rather to present an overview of the major techniques used to prepare them.

I.3.2.2. Colloidal solutions of metallic NPs

Colloidal solutions are two-phase solutions where particles are suspended in a continuous phase. Such solutions are usually prepared through chemical reduction. A representation of the main steps is available in Figure 9 [88]. To do so, precursor salts, such as sodium borohydride or sodium citrate, are used to initiate the nucleation process, which consists of a combination of metallic atoms into small groups called nuclei. The following step consists of increasing the size of the nuclei to form the final NPs. The choice of the reducing agent is extremely important as it affects the final size of the NPs. Strong reducing agents, such as sodium borohydride, produce relatively small NPs whereas weaker precursors like sodium citrate give larger NPs [89]. In addition to reducing agents, chemical synthesis of NPs requires the use of capping agents, which act as electrostatic stabilizers and keep the NPs from agglomerating [90]. The main advantage of chemical synthesis lies in the possibility to produce a wide variety of NPs such as nanorods, nanospheres, nanotriangles or even nanostars [89,91–94]. The different shapes are obtained by adding surfactants during the synthesis process.

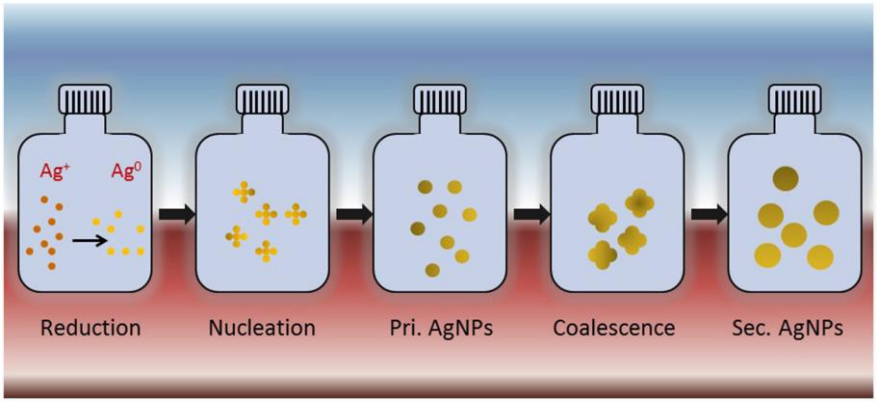

Figure 9 Representation of the chemical reduction process to synthesize colloidal Ag NPs. Silver ions (Ag^+) form silver atoms (Ag) when they are submitted to chemical reduction. These atoms undergo nucleation to form primary Ag NPs that further coalesce with each other to form final Ag NPs. Reproduced from [88].

In order to limit the chemical species involved and improve the purity of the solutions, physical techniques have also been developed. One of these techniques consists of ablating a silver or gold target with pulsed lasers directly into the liquid [95–97]. The focused laser results in the creation of plasma near the metallic target that will allow tearing the material from the surface. Once torn from the target, the material will be able to interact with the liquid (water or organic solvent), which will result in the nucleation and growth of the nuclei [98]. Unlike chemical reduction, this technique is mainly used for the fabrication of nanospheres.

For SERS applications, the size of the particles in suspension are usually below the 100 nm range and they are principally made of silver or gold as these two metals possess absorption peaks in the visible range [72]. The maximum absorption wavelength of the solution, i.e. the LSPR, depends on the size of the NPs in solution [89,99]. In addition, the choice of the selected material also plays a role in the LSPR maximum wavelength [100]. Depending on the excitation wavelength and the resonance of the analyte one should consider using preferably Ag or Au NPs. For a given size, Ag NPs will have its absorption peak blue shifted compared to Au NPs. In addition, Ag is considered a more effective plasmonic material, whereas Au is considered more chemically stable [101]. That is why bimetallic NPs are also investigated. Several studies demonstrated that bimetallic Ag/Au NPs present stronger SERS activity than pure Ag or Au NPs [102–104]. However, as expected, they are more complicated to fabricate than pure NPs.

Another important aspect of SERS sensing with NP colloids is the shape of the NPs. Indeed, it has been demonstrated that NPs with a large number of sharp tips, i.e. nanostars exhibited significantly larger SERS intensities [92]. Indeed, these tips act as hotspots where the SERS intensity is further enhanced as explained in the section I.3.1.4, thus because there are more hotspots in nanostars colloids than in any other colloids, the resulting SERS intensity is stronger.

SERS measurements with colloidal solutions are usually done by mixing the analyte directly with the colloidal solution. In this configuration, the analyte molecules are in the vicinity of the NPs into the entire solution and one only needs to focus the excitation laser into the solution and collect the resulting SERS signal. However, after the analyte is incorporated into the colloidal solution, the NPs tend to aggregate. This aggregation reduces the diffusion of the analyte molecules between the NPs, thus limiting the creation of hotspots. This can also affect the LSPR peak as bigger NPs exhibit redshifted absorption compared to smaller ones [105]. The two aspects result in a decrease of the enhancement, which in turn leads to poorer sensitivity. In order to avoid the NPs agglomeration, a technique called SHINERS (Shell Isolated Nanoparticle Enhanced Raman Spectroscopy) has been developed in 2010 [106]. It consists of capping the metallic NPs with a shell electronically and chemically inert, such as SiO_2 or Al_2O_3. The resulted SHINs (Shell Isolated Nanoparticles) exhibit a better stability compared to usual NPs. However even if the shell is extremely thin, it will necessarily lead to a smaller enhancement as direct contact between NPs and analyte molecules are forbidden in this configuration [106].

Because both the analyte molecules and the NPs can move freely inside the sensing volume, measurements with colloidal solutions do not usually exhibit excellent reliability. As highlighted previously, reproducibility and repeatability are two important criteria when it comes to SERS sensing. Thus, even though colloidal sensing is already promising, other techniques are developed to improve the overall reliability of the sensor, such as the immobilization of NPs on a planar substrate.

I.3.2.3. Nanoparticles immobilized on planar substrates

The deposition of NPs on planar substrates benefits from two main advantages. The first one is the improvement of the sensor reliability. Indeed, the fact that the NPs are immobilized limits the impact of the Brownian motion of the NPs in solution. This advantage is based on the condition that the deposited NPs are extremely well arranged on the substrate, if not, the reproducibility and repeatability may decrease rapidly according to the quality of the deposition. The second advantage is the possibility to fix NPs close to one another to benefit from the important enhancements of hotspots describe previously. This interest is also limited to the quality of the deposition.

The first way to immobilize NPs on a planar substrate is by chemical anchoring. To do this, the planar substrate needs to be functionalized by silanization. We quickly describe this technique in the case of a silica substrate but it is worth noting that it can also be applied to a wider range of substrates such as quartz, plasma-treated Teflon and platinum for example [107]. Briefly, silica substrates possess hydroxyl groups (R--OH) at their surface. Putting a silane in contact with the hydroxyl groups displace the alkoxy groups (R—O—R') of the silane in order to form a covalent bond between the silane and the silica [108], as shown in Figure 10 [109]. Usually, the selected silane possesses another chemical group that will be able to bond to the metallic NPs. Once the silica substrate is functionalized, it can be dipped in a colloidal solution containing the NPs, which will chemically bind to the additional group of the silane. Often used silanes are (3-Aminopropyl)trimethoxysilane (APTMS) or (3-Mercaptopropyl)trimethoxysilane (MPTMS). For APTMS, NPs will be able to bind with the amine group (--NH_2), whereas for MPTMS they will bind with the thiol group (--SH) [110]. The SERS signal from the silane is usually very weak and does not interfere with the signal from the analyte. In addition, this technique is quite flexible since a wide variety of NPs (in size, shape and material) can be

immobilized on the substrate and relatively large surfaces, in the range of few cm^2, exhibiting good enhancement and reproducibility can be prepared [107,111,112].

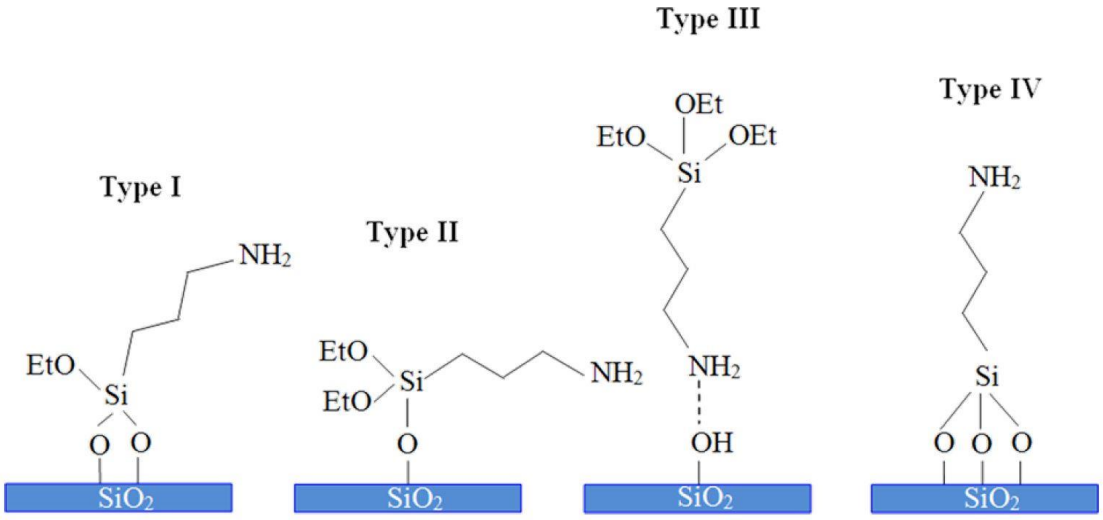

Figure 10 Four possible orientations of APTES molecules on -OH terminated glass substrates. Reproduced from [109].

Another solution consists of embedding the NPs in a dielectric medium instead of immobilizing them onto the substrate [113]. Several techniques allow fabricating such substrates, such as laser or ionic implantation [114,115], thermal treatment of thin metallic layers [116] and electric field-assisted diffusion [117]. Representative TEM micrographs of Ag NPs impregnated in a polycarbonate substrate are available in Figure 11. Embedding the NPs into a matrix limits the uncontrolled aggregation of the NPs, which result in improved sensitivity and reliability. In addition, the host material acts as a protective layer, which maintains the SERS ability of the substrate over time. Hasell *et al.* obtained an enhancement factor of 10^7 with the substrates prepared in Figure 11 and they were still able to obtain a SERS response with substrates prepared over a year ago and stored in air [118]. This technique is applicable with different types of materials, such as polymers and glasses.

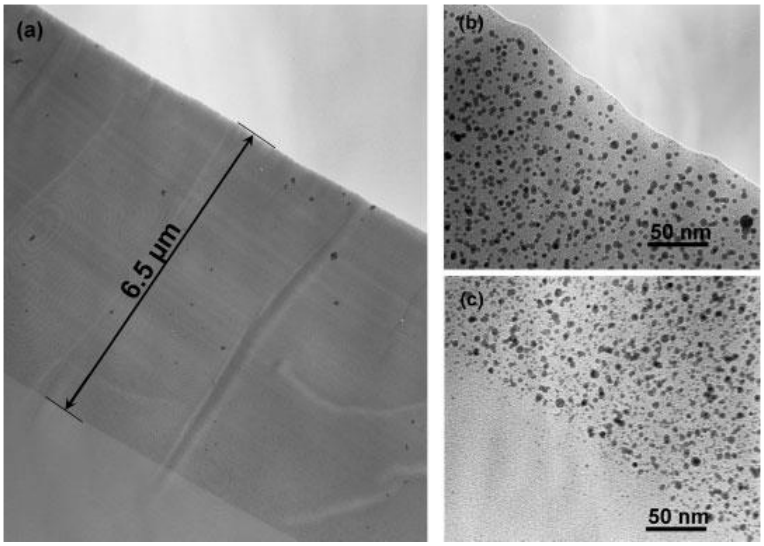

Figure 11 TEM micrographs of (a) The surface located band of silver nanoparticles in a cross section of the polycarbonate substrate. (b) A magnified section showing nanoparticles on the outside edge of the polymer. (c) A magnified section showing nanoparticles at the limit of furthest impregnation of the nanoparticles. Reproduced from [118].

NPs can also be deposited or grown directly onto semiconductor or dielectric substrates using physical vapor deposition (PVD). The substrate could have been previously nanopatterned to serve as a guide for the NPs growth [119,120]. For instance, Gkogkou *et al.* patterned nanoripples at the surface of a silicon substrate using ion beam irradiation [121]. Then, they used thermal evaporation to deposit Ag NPs in the nanoripples. The resulting substrate is visible in Figure 12(a). The NPs were well aligned along the nanoripples. Subsequently, they measured the optical resonances along the axis perpendicular and parallel to the ripples. They showed that the plasmon resonance peak occurred at 514 nm in the perpendicular direction and 745 nm in the parallel direction. Finally, they studied the impact of the light polarization on the SERS response of 4-mercaptobenzonitrile (MBN) using two polarized lasers that were close to the maximum resonance (514 nm and 647 nm) (Figure 12(b)). For that, they rotated the substrate according to the polarization angle θ and acquired SERS signals. They showed that the measured SERS intensity of the 1079 cm^{-1} band of MBN alternated between maxima and minima when the substrate rotated (Figure 12(c)). Using 514 nm excitation a $\cos^2\theta$-dependence was found while using 647 nm excitation a $\sin^2\theta$-dependency was found. This corresponded well with the resonance plasmon peaks measured on the perpendicular and parallel axis, respectively. In summary, this fabrication technique allows controlling more precisely the NPs parameters and helps in creating homogeneous and stable SERS substrates with large active areas. Nevertheless, the NPs here are not protected in contrast to when they are embedded in the substrate. Thus, the substrates are not reusable after washing and their lifetime is much shorter.

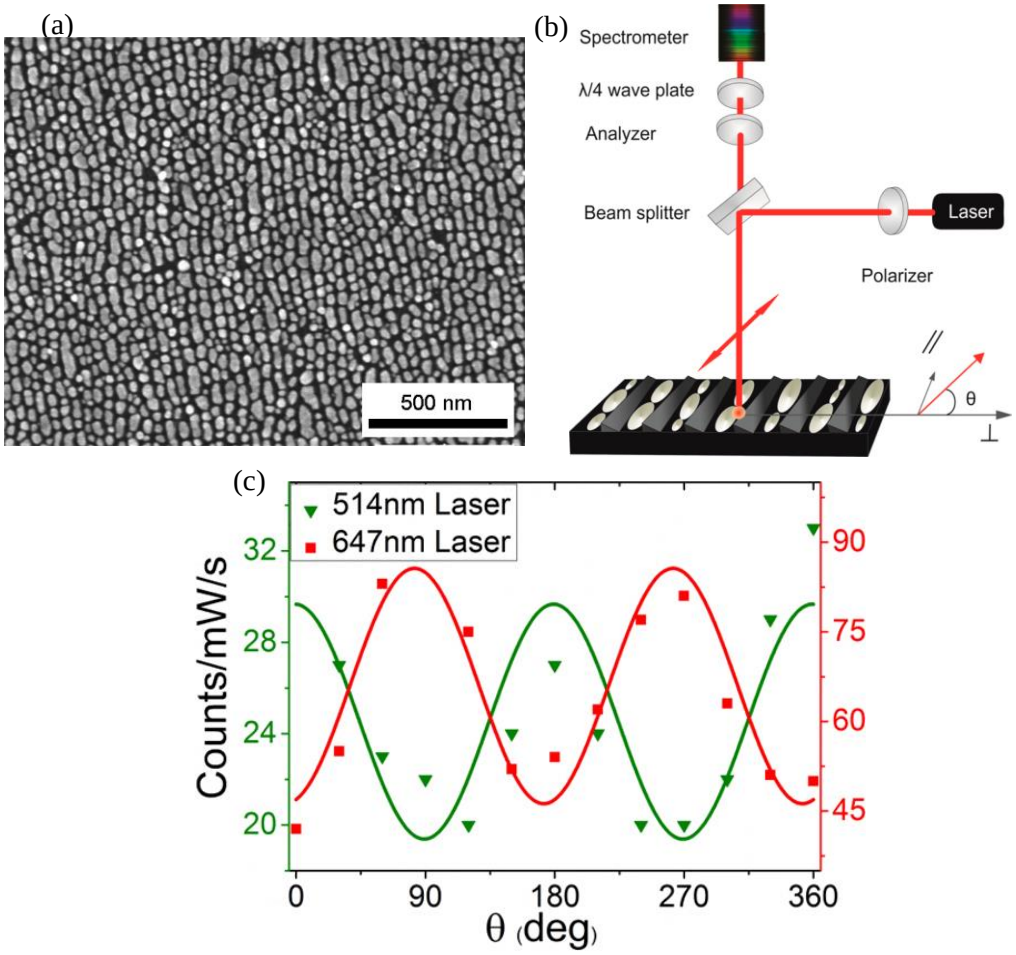

Figure 12 (a) SEM picture showing silver nanoparticles aligned along nanoripples on silicon. (b) Raman setup for polarized measurements. (c) Normalized intensity of the 1079 cm^{-1} band of MBN as a function of θ obtained with 514 nm (green triangles) and the 647 nm (red squares) excitation. The respective solid lines correspond to fits of $\cos^2(\theta)$ (green) and $\sin^2(\theta)$ (red) function to the data. Reproduced from [121].

Until now, we presented deposition techniques on solid planar substrates. However, several techniques can be used to deposit NPs on flexible substrates like paper. Among these techniques, we can cite ink-jet [122], screen printing [123], drop casting [124] or dip coating [125] for example. Paper SERS substrates present many advantages in addition to being more flexible than hard planar substrates. They are quite simple to fabricate, with the ink-jet technique, for example. This facilitates the storage of the SERS substrates, since one can make them on demand thus avoiding long term storing. They are also low cost and can be used in different ways, such as drop casting, dipstick or swab. The latter is very interesting for detecting the presence of an analyte at the surface of an item, though it does not allow for very precise quantitative analysis. White *et al.* used chromatography paper as SERS substrate by depositing Ag NPs using an ink-jet printer [122]. They chose chromatography paper since it exhibited a low Raman signal. However, they needed to make the active region hydrophobic so that the ink would not spread too deep inside the paper. Later, they fabricated the Ag NPs and prepared the ink by re-dispersing the centrifuged NPs in a water/glycerol solution. After filling reusable cartridges, they finally printed the ink several times on the same spot on the paper to increase the density of the NPs. They also reported a cheap and easy way to concentrate the analyte on the SERS active region of the paper. They simply dipped the paper in the solution to test and by capillarity, the analyte moved to the active region. With this technique, they were able to detect R6G concentration as low as 10 femtomoles in 1 µL. Screen printing is the same procedure. The only difference lies in the printing process. Instead of using a printer, a screen plate with a desired pattern is fabricated [126]. Then, the ink is placed on the screen and a squeegee is used to apply the ink in the apertures of the pattern as shown in Figure 13 with PET substrates. The advantage of this technique is that predefined arrays of NPs can be fabricated, to create SERS hotspots for instance.

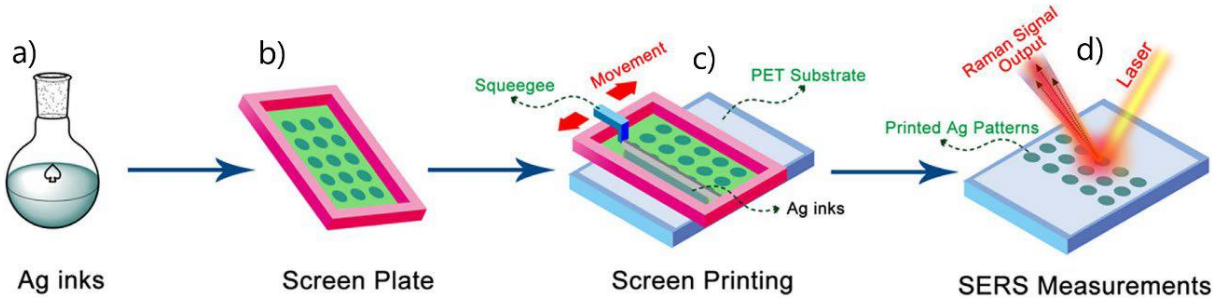

Figure 13 Schematic illustrating the screen printing process. Reproduced from [126].

I.3.2.4. Nanopatterning

Previously, we saw that nanopatterning could be used to guide the deposition of NPs. It can also be used to create relevant shapes on which a metal can be deposited or directly create the nanopattern on the metal in order to create a SERS-active substrate. Several techniques can be used to create the pattern. The first one we present is called laser ablation. It consists of ablating unwanted sections of a substrate to obtain the desired shape using a laser. Once the pattern is created, thin layers of metal can be deposited on the substrate surface. For example, Yang *et al.* created microsquares by scanning horizontally and vertically a nanosecond laser on Si surfaces as shown in Figure 14 [127]. This also contributed to forming silica NPs of various shapes and size in the center of the microsquares. Then, they deposited a 40 nm Ag film over the entire structure. The Ag coated silica NPs created hotspots, which lead to increasing the SERS enhancement. Using such substrates, they were able to measure enhancement factors superior to 10^6 and standard deviations of 6% across eight microsquares. In certain conditions, the nanostructuration and the deposing of NPs can be done at the same time. For instance, Lin *et al.* placed silicon wafers in aqueous solution of silver nitrate [128]. Subsequently, they wrote grating-like patterns on the wafers using a femtosecond laser. Simultaneously, the laser induced the photoreduction

of silver, which resulted in the formation of NPs on the wafer surface following the pattern. They measured EF up to 10^9 using such substrates. In summary, laser ablation allows fabricating reliable and sensitive SERS sensors. However, the time required to prepare large substrates is quite long.

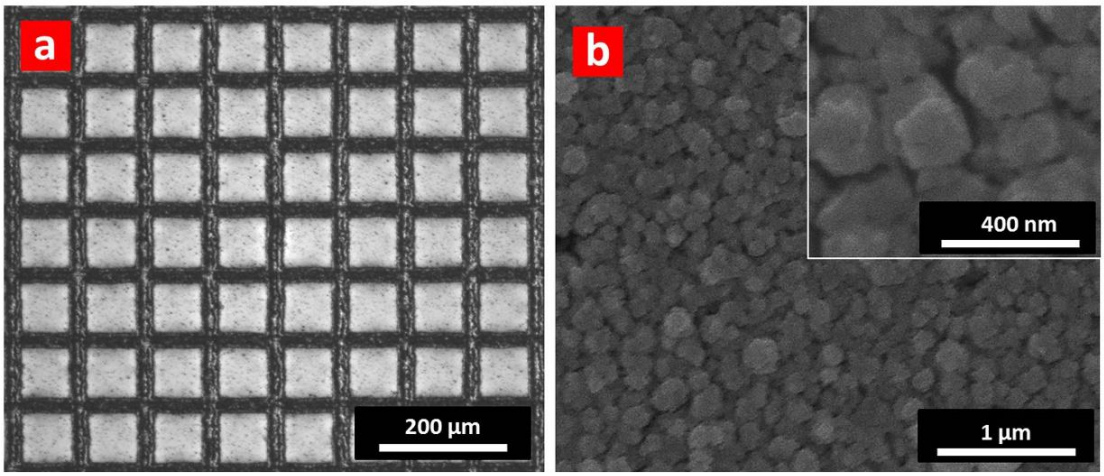

Figure 14 (a) Microscope picture showing the array of silica microsquares obtained by scanning horizontally and vertically a nanosecond laser on a silica substrate. (b) SEM pictures of the surface of a microsquare showing the silica NPs that resulted from the interaction with the laser. Reproduced from [127].

Electron beam lithography (EBL) represent another technique to create a pattern on the surface of a substrate [129]. First, a polymer is deposited on the substrate. This polymer, called resist, is sensitive to electrons. When an electron beam is focused onto it, its solubility changes: it can become soluble (positive resist) or insoluble (negative resist). Therefore, by scanning precisely the focused electron beam, one can create a pattern inside the resist. Subsequently, the substrate is plunged in a solution to remove the soluble resist. Once the pattern is generated, the resist serves as a sacrificial mask to deposit a metallic layer, yielding the creation of metallic NPs with well-defined geometries. Because the electron beam is not submitted to the diffraction of light, EBL allows fabricating patterns as small as 10 nm. Hence, EBL is well adapted to fabricate sensors whose designs have been engineered to optimize the SERS enhancement. In addition, the fabricated sensors generally exhibit good reproducibility thanks to the precision of the fabrication process. Another advantage of EBL is that it allows studying the influence of the structure on the SERS response. For instance, Billot *et al.* fabricated gold nanowires

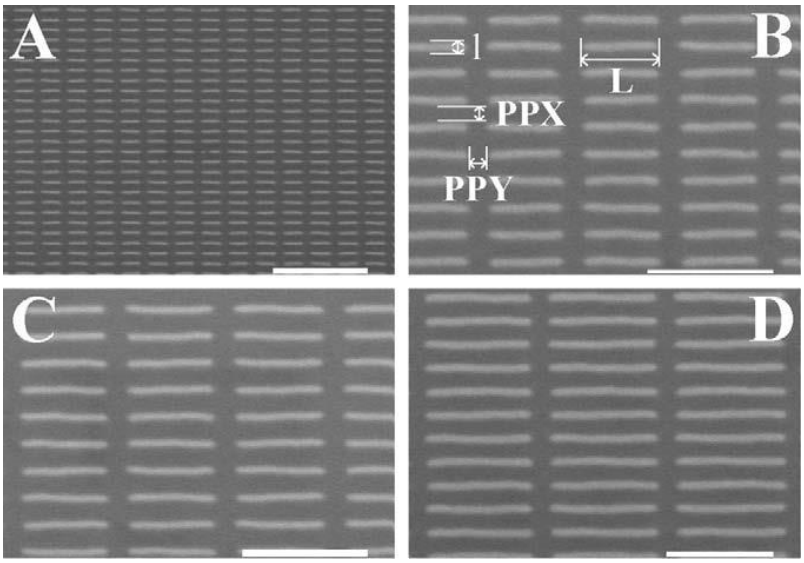

Figure 15 SEM images of the nanowires arrays fabricated by Billot *et al.* Reproduced from [130].

arrays using EBL and lift-off as shown in Figure 15 [130]. They showed that the length of the nanowires had an impact on the SERS intensity of trans-1,2-bis(4-pyridyl)ethylene. Similarly to laser ablation, for large substrates the fabrication time and the cost remain important.

In order to fabricate periodic arrays of NPs, nanosphere lithography (NSL) represent another interesting alternative. The most basic NSL consists of depositing a monolayer of close-packed nanospheres on a substrate. Typically, this can be achieved through Langmuir-Blodgett, which is a deposition technique that create well-arranged monolayers of NPs. The deposited layer of nanospheres will then serve as a mask for deposition or etching. For instance, the deposition of a metallic layer on the substrate and nanospheres produces a metallic film over nanosphere (MFON). Subsequently, the nanospheres can be removed by sonication and only an array of nanotriangles remains as shown in Figure 16. It is obvious that the size of the nanospheres has a direct impact on the dimensions of the final NPs array. This array of NPs can be used for SERS sensing. For example, McFarland *et al.* used a similar array to study the optimal position of the LSPR in regard to the excitation laser to benefit from the strongest SERS enhancement [41]. NSL is not limited to forming nanotriangle arrays. Haynes and Van Duyne demonstrated that a vast variety of motifs could be fabricated such as nanorings [131]. This is achievable by changing the thickness of the metallic layer or the angle of the deposition, by moving the substrate during the metal deposition, or by increasing the number of nanosphere layers forming the mask.

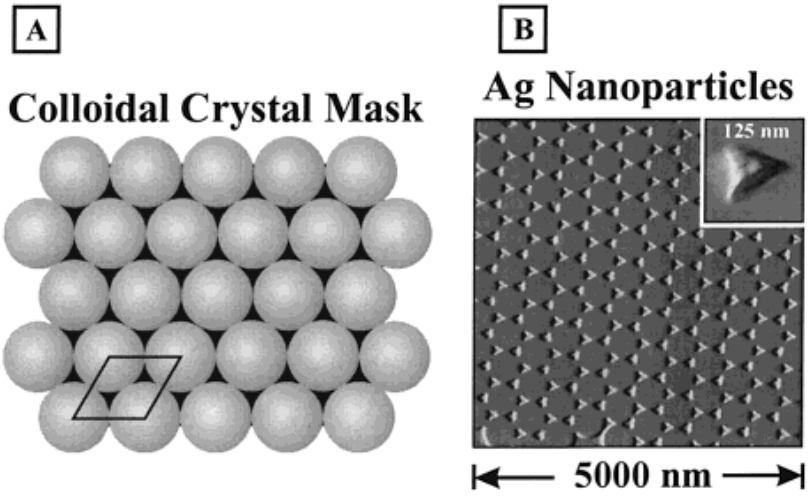

Figure 16 (a) Illustration of the single layer NSL. (b) Pattern of nanotriangles obtained with single layer NSL. Reproduced from [131].

Another technique that allows for nanopatterning is soft lithography. Here, an already nanopatterned substrate is used as a mold or stamp to fabricate the desired substrate [132]. For instance, Ou *et al.* fabricated a silicon array of nanopillars using EBL and dry silicon etching [133]. This array served as a mold using UV-curable nanoimprint lithography (NIL) to form the daughter mold, which was used to create the nanofingers. After that, they deposited gold on the tip of the nanofingers. Subsequently they immersed the substrate in solvent and dried them. Because of the capillary forces, the nanofingers were attracted to one another. A schematic illustrating the different steps is available in Figure 17. Since EBL and NIL are two very precise techniques, they were able to fabricate arrays with different types of unit cell. This resulted in the formation of digon, trigon, tetragon, pentagon and hexagon. Subsequently, they studied the SERS response of each polygon and they were able to achieve an EF of ~10^{11} with the pentagon. Soft lithography is a simple and relatively cheap technique that allows fabricating large SERS substrates that exhibit strong EF.

Many other techniques are available to fabricate nanopatterns such as interference lithography or anodic alumina template. The general idea is the same as the described methods here so we do not present them more precisely.

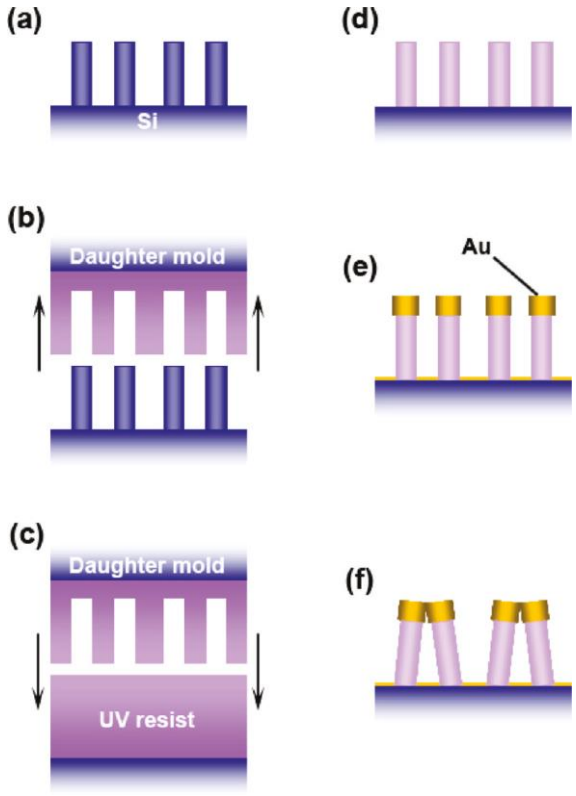

Figure 17 Different steps of NIL used by Ou *et al.* to fabricate nanofingers. Reproduced from [133].

I.3.2.5. Commercialized SERS substrates

The goal of this section is not to make a thorough review of all the existing commercial SERS substrates but rather to present their general features. They consist of either NP colloidal solutions or planar SERS substrates. For instance, Sigma-Aldrich and Nanopartz sell various types of NPs in solution [134,135]. By changing the material (gold or silver), the shape (nanospheres, nanorods, nanowires, nanoplates, ...) and the size (from 5 nm to 400 nm for the gold nanospheres), they are able to provide a wide range of absorption peaks. For instance, Sigma-Aldrich proposes gold nanorods with absorption peaks ranging from 550 nm to 1064 nm. Several companies also sell already prepared planar SERS substrates. Among them we can cite, Ocean insight, Hamamatsu, Horiba, SERSitive [136–139]. Although the fabrication process is often not presented, they generally propose Ag or Au substrates with active regions of various sizes and shapes (rectangle, square, circle, ...) placed on a standard microscope slide. Users simply need to place the analyte solution in the active region and to fix the substrate under the objective of a Raman microscope for readout.

An interesting study, conducted by Liu *et al.*, proposed to compare the reliability and the sensitivity of six commercial substrates [140]. These six substrates were not prepared with the same technique, and they did not use the same NP material. The authors analyzed the SERS response of the six substrates using three common Raman tags and 10x, 50x and 100x microscope objectives to focus the lasers. The main results of the study were that:

- the detection of trace amount of analyte could be arduous since the six substrates exhibited relatively strong backgrounds

- all the substrates exhibited similar SERS intensities and thus no substrate exhibited a major improvement in sensitivity.
- the most reproducible sensor exhibited an average RSD lower than 10% and a maximum RSD of 14% over 49 measurements.
- the less reproducible sensors exhibited in specific conditions RSD lower than 20% but they also exhibited several times RSD superior to 40%.
- for the six substrates, the lowest variations were obtained with the 10x objective lens.

They explained that the 10x objective allowed to average the SERS signal over a larger interaction surface since the size of the laser spot was larger than that of the 50x and 100x objectives. The general conclusion was that, out of the six tested substrates, only three could be applied to quantitative analysis. In addition, the cost of commercial substrates remains high. Therefore, the poor reliability coupled to the relatively high cost can explain the limited use of commercial SERS substrates.

I.3.3. Application of SERS substrates for biosensing

Here, we present briefly some biosensing applications in order to understand the great potential of SERS and its versatility. Two detection schemes are available depending on the Raman-cross-section of the target analyte. If it possesses a strong Raman cross-section, it can be detected directly, i.e. label free detection, whereas if its cross-section is weak, it needs to be indirectly detected thanks to SERS nanotags, i.e. labeled detection.

I.3.3.1. Label free detection

Since it discovery SERS has been used to detect an extremely wide range of biomarkers, such as DNA sequences, viruses, bacteria and proteins. For example, Wang *et al.* extracted RNA from urine in order to detect prostate cancer [141]. The main steps are presented in Figure 18. After the extraction, they amplified the target RNA into dsDNA sequences called amplicons. Subsequently, these amplicons were purified and incubated with positively charged Ag NPs. Finally, they measured the SERS spectra of the target amplicons. They were able to detect prostate cancer with a good specificity (93.0%), sensitivity (95.3%), and accuracy (94.2%). Colloidal NPs have also been used to differentiate the blood plasma of healthy people from the plasma of people with gastric cancer [142]. Ag NPs were directly mixed with

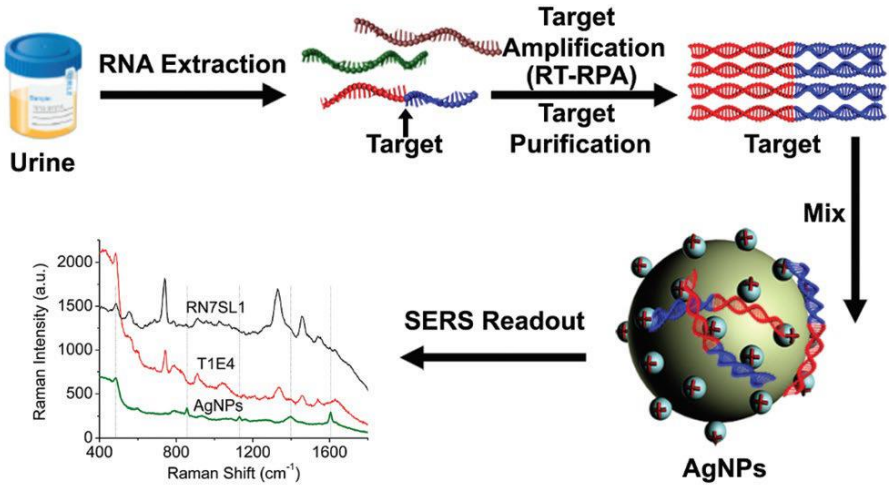

Figure 18 Process used to detect prostate cancer by extracting RNA from urine and measuring the SERS signal. Reproduced from [141].

the plasma and the mixture was excited using a polarized laser. This configuration gave particularly good results since it demonstrated a sensitivity of 100% and a specificity of 97%.

SERS was also used to analyze cellular function within the cells. For that, NPs had to be included inside the biological samples. As we already saw, Au NPs have a better biocompatibility and thus, they are preferably used for this type of sensing. The shape, the size and the functionalization of the NPs can be tuned to control which cellular barrier will be crossed by the NPs and thus, where the NPs will be located within the cells [143]. This allowed to map the distribution of phenylalanine and DNA in intestinal epithelial cells [144]. Colloidal NPs can also be used in microfluidic devices. For instance, Walter *et al.* used Ag NPs in a microfluidic chip to identify nine strains of Escherichia Coli [145].

We saw previously that NPs could also be immobilized onto a surface. This technique was used by Xu *et al.* to detect a single hemoglobin molecule [146]. They prepared a colloidal solution of Ag NPs and mixed it with a solution of hemoglobin. Then, they deposited APTMS onto a silicon wafer so that the NPs can be immobilized at the wafer surface. Subsequently, they acquired the SERS spectrum of hemoglobin and they were able to detect a single molecule when the NPs formed a cluster near the hemoglobin molecule.

Arranged arrays of metallic NPs have also been used for biosensing applications. Shanmukh *et al.* fabricated an array of oblique nanorods to identify different viruses [147]. They were able to differentiate between respiratory viruses, viruses' strains and genetically modified viruses. The tests required lower accumulation time and incident laser powers than previously reported.

SERS can also be combined with other detection techniques. For instance, Han *et al.* combined SERS with Western Blot in order to detect several proteins [148]. A mixture of myoglobin and bovine serum albumin (BSA) was separated through electrophoresis and immobilized on a nitrocellulose membrane by electroblotting. Then, the molecules were stained with a solution of Ag NPs and SERS spectrum of each molecule could be acquired. With the combination of the two techniques, they were able to detect 4 ng of myoglobin.

I.3.3.2. Labeled detection

Until now, all the presented SERS substrates were designed to detect molecules that possess a strong Raman signal. Unfortunately, all relevant biomarkers do not necessarily possess a strong Raman cross-section. To detect them, one can fabricate SERS labels or SERS nanotags. These nanotags are designed to bind specifically to a target analyte and to emit a strong and characteristic Raman signal. Since the SERS labels can only bind to the target molecule, the detection of the characteristic signal indirectly reveals the presence of the analyte in the sample. On the contrary, the absence of the nanotag signal allows ascertaining that the target analyte is not present in the sample.

The general steps for the fabrication of a nanotag are available in Figure 19 [149]. Usually, nanotags consist of a plasmonic core (typically a metallic NP), a Raman tag and a protective shell. In the following, we present the required features for these three components. The first requirement concerns biocompatibility, and it is true for the three parts of the nanotags. Since they are used for biosensing, the tags must be biocompatible to avoid any harm to the patient or for the analyte sample. This is why the core of the nanotags is generally made of gold since it has a better biocompatibility than silver [150,151]. Unfortunately, silver is considered a better plasmonic material than gold. Therefore, to benefit from sensitive and biocompatible SERS tags, the gold core of the SERS label might need to be engineered to improve the sensitivity of the nanotags. As discussed previously, changing the size and or the shape of the NP can help in matching the plasmon resonance to the excitation wavelength and to the signal of the Raman reporter, resulting in stronger enhancement and better sensitivity.

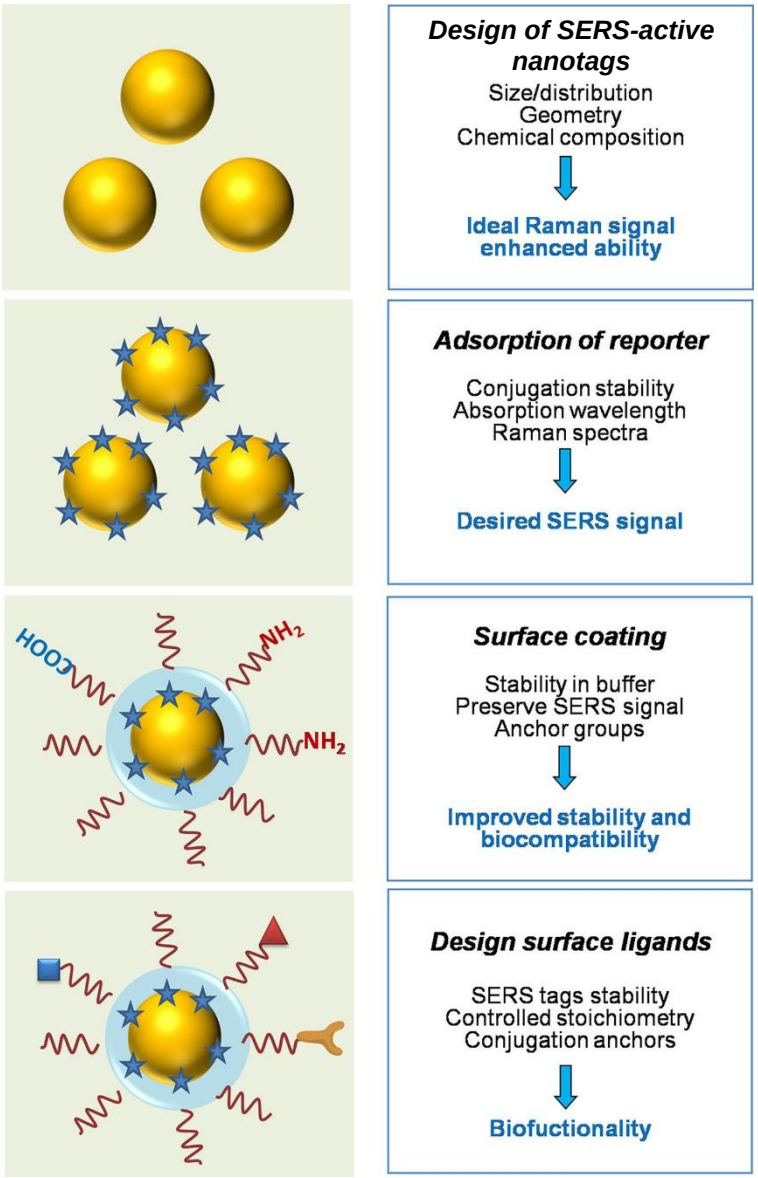

Figure 19 General steps needed to fabricate SERS nanotags. Reproduced and adapted from [149].

Regarding the Raman reporter, it has to possess a good Raman cross-section with strong peaks clear from the Raman signal of other analytes or of the matrix containing the nanotags. This is made to ensure that the measured signal is only due to the presence of the nanotags. Often used Raman reporters are crystal violet, rhodamines, and malachite green [152]. Other organic molecules with good cross-sections and the ability to bind to the NP represent a good alternative. Among them, we can cite benzenethiol or 4-aminothiophenol for instance.

Finally, the shell of the nanotags is very important. Obviously, it has to be biocompatible, since it is the major part of the nanotags that will be in contact with the external environment. They are often made in silica or polyethylene glycol (PEG) [153,154]. It also has to be as thin as possible to minimize the decay of the SERS enhancement with the distance. The first interest of the shell is to maintain the Raman reporter close to the NPs. Indeed, the Raman reporters are only adsorbed at the NP surface. Thus, the protective shell that encircles both the NP and the Raman reporters prevent them from being separated. It also prevents the Raman reporters from being denatured after the exposition of undesired molecules. Another important aspect is that the shell prevents the aggregation of the NPs that might occur when the tags are placed in the measuring environment. In addition, the shell also prevents the adsorption of

unwanted molecules on the surface of the nanotags. If the shell did not prevent such adsorption, the measured signal could be overshadowed by the spectra of unwanted molecules. Finally, in the opposite vein, the shell can be functionalized with ligands, such as antibodies, aptamers or peptides. This bio functionalization allows targeting specific biomarkers. For instance, Wang *et al.* monitored the variations of intracellular pH using Ag NPs functionalized with 4-MBA and encapsulated in 30 nm layer of silica [155]. 4-MBA is a pH-sensitive Raman reporter, i.e. the intensity of its signature peaks varies with the pH of the solution. Thus, monitoring the intensity of the signature peaks allows detecting the pH variations. In addition, the silica layer improved the colloidal stability and prevented other biomolecules, such as BSA, to interact with the NPs.

Wang *et al.* used nanotags in a sandwich-like immunoassay to detect a pancreatic cancer biomarker [50], MUC4. First, they functionalized a gold substrate with MUC4 antibodies. Then, they deposited patients' serum onto the substrate. If MUC4 were present in the serum, they could bind to the anchored antibodies and thus they were immobilized on the substrate. Subsequently, they fabricated nanotags that consisted of Au NPs functionalized with a Raman reporter and again MUC4 antibody. Adding the nanotags on top of the substrate allowed them to bind to the anchored MUC4. Finally, the SERS signal of the Raman reporter could be measured. With this technique, they were able to differentiate healthy patients from patients with pancreatic cancer. Using sandwich-like immunoassays, Song *et al.* detected a biomarker for lung cancer in extremely low concentrations (0.01 fg/mL) [156]. They also detected immunoglobulin G with concentration as low as 2.5 fg/mL [52].

SERS nanotags can take many forms and labeled detection is not limited to the detection of proteins. For example, DNA sequences can be specifically detected by a method called molecular sentinel (MS). It consists of DNA hairpin functionalized with a Raman reporter on one end and a molecule possessing a thiol group at the other end. This thiol group allows binding to a thin film of gold deposited on close-packed nanospheres as shown in Figure 20. The hairpin DNA has been specifically designed to be the complementary sequence of the target DNA. At the initial state, the hairpin is closed on itself, bringing the Raman reporter near the gold film. Upon laser excitation, a strong SERS signal is detected. Then, the target DNA sequence is put in the vicinity of the hairpin loop. Since the hairpin DNA is the

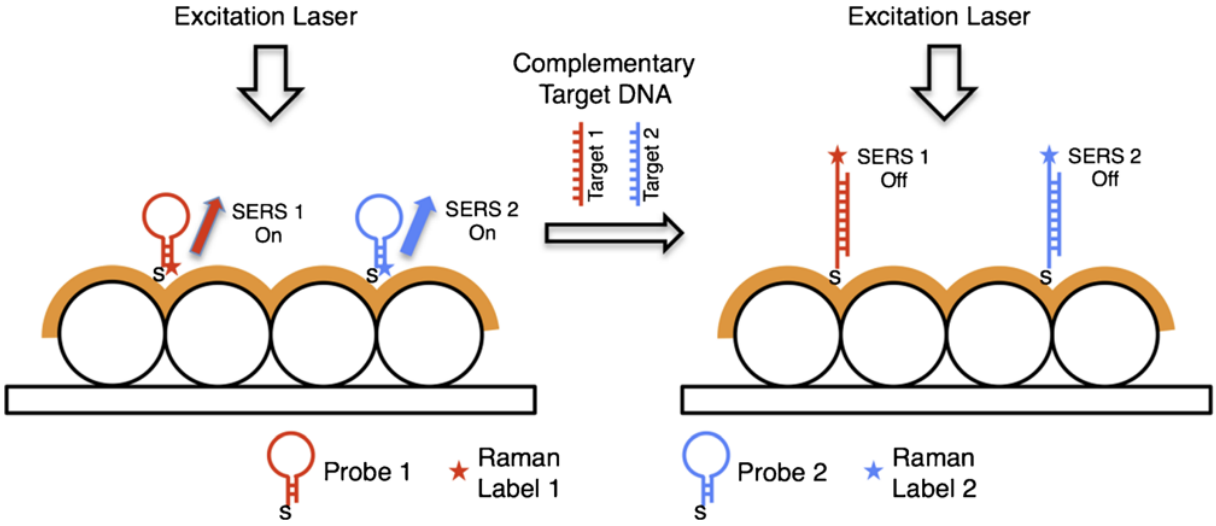

Figure 20 Illustration of multiplex sensing using the MS technique. Reproduced from [20].

complementary sequence, the two DNA strands hybridize with one another, which results in the unfolding of the hairpin loop (right of Figure 20). In this situation, the Raman reporter moves away from the gold film and the SERS signal decreases strongly. The detection mechanism can be summarized as follows: if the SERS signal is detected, the target DNA sequence is absent from the analyte solution, whereas if the SERS signal decreases, the target DNA is present. This technique can be applied for

multiplex detection as illustrated in Figure 20. For that, the hairpin DNAs are functionalized with different Raman reporters that possess different signature peaks. This configuration allowed Ngo *et al.* to detect two genes that play a critical role in host immune response to viral infection [20].

I.4. Conclusion

In this chapter, we presented the theoretical basis of Raman scattering and its limitations. We also described how SERS could be used to drastically increase the Raman signal in order to improve the sensitivity of the sensors. We saw that SERS enhancement is based on two main mechanisms and that the SERS signal varies importantly with numerous parameters, such as the wavelength of the excitation laser, the geometry of the nanostructures, the distance between the analyte and the NPs. We also realized that SERS substrates did not only need to be sensitive. For them to be used in a clinical environment, they also needed to be more reliable. Finally, we presented different geometries for SERS sensing. The most immediate one consists of NPs in colloidal solutions. They only required to mix the analyte solution with the colloidal solution and to measure the SERS response. However, since the molecules can move freely, the reliability of such sensor is limited. To improve the reproducibility and repeatability of SERS sensors, a solution would be to immobilize the NPs onto a substrate. Several techniques like chemical anchoring or printing allow the fixing of the NPs onto hard surfaces (glass) or ones that are more flexible (paper). The development of nanoscience and the improvement in nanopatterning also helped in improving the sensitivity and reliability of the sensors. SERS substrates can now be designed so that the plasmon resonance fit the excitation wavelength and the SERS signal of the analyte. In addition, thanks to the precision of the fabrication processes, the reliability of the sensors is also improved. This facilitated the industrialization of the fabrication process, which resulted in the commercialization of several SERS substrates. We then showed that SERS substrates have been used in many forms to detect a wide range of bio-analytes. In the following chapter, we will focus on optical fiber and more specifically on how they can be used to improve SERS sensing.

Chapter II. SERS-based optical fiber sensors

Chapter II. SERS-based optical fiber sensors

II.1. Introduction

Since their discovery, optical fibers have been used for different purposes, such as communication or sensing. An optical fiber is composed of a core, which guides the light, and a cladding that allows the light to be guided inside the core. However, depending on their use, their structures may differ. The cross-sections of fibers intended for communication are usually entirely filled, i.e. the core and the cladding are made of solid materials (silica). When it comes to sensing, optical fibers are used to detect and monitor a wide range of physical parameters including temperature, refractive index, fluorescence, strain or bend. Here, two configurations are possible depending on the sensing method. The fibers can be entirely solid (single mode fiber (SMFs) [157], multimode fibers (MMFs) [158], D-shape fibers [159], tapers [160]) or they can feature at least one hollow region in their cross-section. It can be the core, the cladding or both. In the following of this manuscript, this type of fiber will be called photonic crystal fibers (PCFs), although, rigorously speaking, PCFs feature holes that are periodically arranged in their cross-section. If we focus on SERS sensing with optical fibers, it has been realized in different configurations. For instance, tip-enhanced Raman spectroscopy (TERS) can be achieved with all-solid optical fibers. Briefly, it consists of coating the tip of optical fibers with a metallic SERS-active layer or NPs and plunge the tip inside the analyte solution [158,161]. The excitation light is launched from one end of the fiber and sensing is realized only at the other end, which is the coated tip inside the solution. The Raman signal is coupled back to the fiber and into the spectrometer for processing. Different fibers designs have been used in this configuration, such as SMFs, MMFs, D-shape fibers and tapers [158,161–163].

SERS can also be realized using PCFs. As mentioned previously, compared to all-solid fibers, PCFs feature holes in their cross-section. These holes run along the entire length of the fiber and allow the incorporation of liquid or gas inside the fibers, which increases the interaction between the excitation light and the analyte. The light is launched from one end of the fiber and it can interact with the analyte for relatively long length, since the analyte is also inside the fiber, as illustrated in Figure 21(a). In addition, PCFs also serve as a collection platform. In fact, the core can collect the Raman scattered photons along the fiber length. Depending on the recoupling of the photons inside the core and the fiber length, the signal collected with the fiber can be superior to the signal collected by microscope objectives in the regular SERS platforms. In addition, PCFs exhibit relatively low loss propagation, depending on the fiber design and configuration used. This allows guiding efficiently both the excitation laser and the collected Raman signal over important length, thereby increasing simultaneously the interaction surface between the laser and the NPs/analyte and the number of collected photons [164–167]. From there, we can intuitively understand that PCFs increase the sensitivity compared to direct detection. In fact, several studies showed that two to three orders of magnitude improvement could be observed [168,169]. For instance, Yang *et al.* demonstrated that the Raman signal line of nitrogen was 700 times more intense when detecting gaseous nitrogen using a PCF compared to bulk detection [17].

Moreover, the increased interaction surface has another advantage. Since the light can interact with a tremendously larger number of NPs, the contribution of each NP is averaged among the contributions of all the NPs. Comparatively, in planar substrates, the excitation light can only interact with NPs/analyte at the focus point of the laser, which is only a few micrometers wide, as illustrated in Figure 21(b). The direct consequence is that, in PCFs, NPs do not have to be as precisely arranged as in planar SERS sensors in order to obtain an improved sensitivity and reliability. This is similar to the notion seen in chapter I when Liu *et al.* compared the six commercial SERS substrates and found that the 10x objective gave more reproducible signals because the excitation light was able to interact with more NPs [140].

Furthermore, PCFs, like all optical fibers, are extremely flexible. When it comes to biosensing, this is particularly interesting since it could help in reaching remote places of the body through an endoscope. PCFs are also compatible with real time monitoring since the tested analyte lies within the sensing medium. Finally, the use of PCFs is not limited to liquid analyte. They can also be used for gas detection [16,17,170]. As mentioned previously, Yang *et al.* achieved an EF of 700 by filling a PCF with gaseous nitrogen compared to bulk detection. This giant increase in sensitivity makes PCFs a real alternative to current gas sensing devices that are rather bulky and expensive.

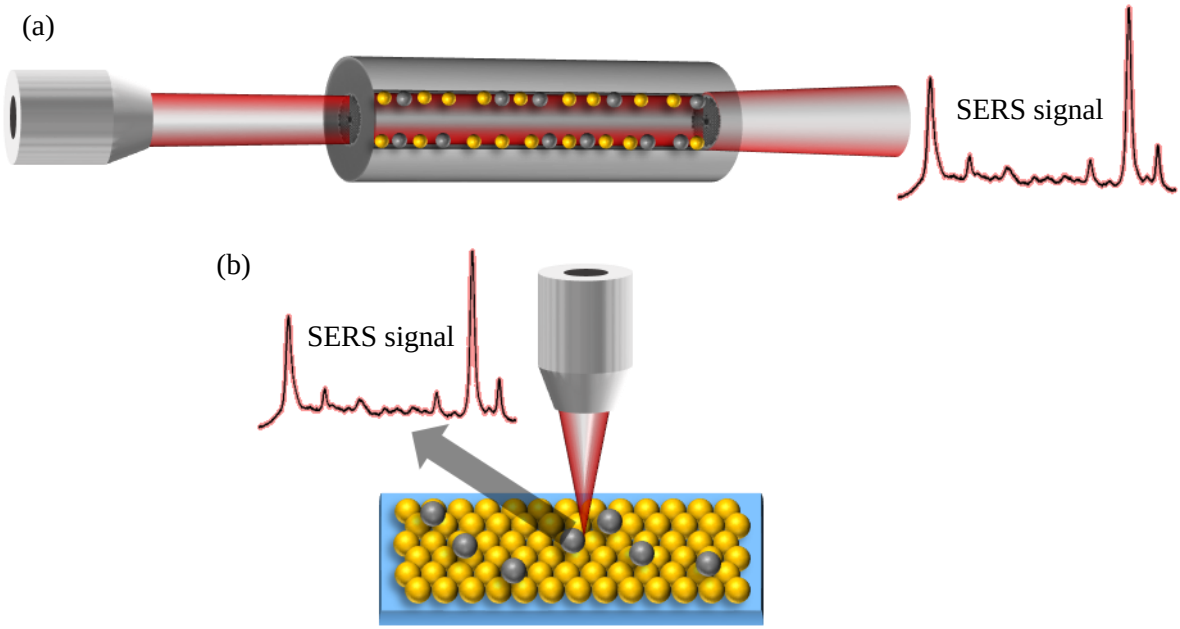

Figure 21 Schematic representation of SERS (a) in a PCF and (b) on a planar substrate. Yellow spheres: NPs, gray spheres: analyte molecules. The number of excited NPs and analyte molecules in (a) is much larger than that in the focus point of the laser in (b).

Since the analyte can be injected inside the fiber, PCFs represent an incredible optofluidic platform and several studies report PCFs implemented in microfluidic devices. For instance, Unterkofler *et al.* designed a micro-fluidic circuitry that included a hollow-core PCF (HC-PCF) [171]. This allowed them to monitor the photoaquation of cyanocobalamin to aquacobalamin when the laser could interact with a solution of cyanocobalamin inside the fiber core. In another study, PCFs have been used to fabricate all-in-fiber microcells [172]. They consisted of a HC-PCF filled with an analyte solution and closed at both ends by splicing single mode fibers (SMFs). This configuration allowed the authors to detect the Raman spectra of toluene and ethanol using laser powers six orders of magnitude lower than previously reported. Another study illustrating the great versatility of PCFs was conducted by Zhang *et al.*. They developed an in-line optofluidic Sagnac interferometer using an in-house side-channel PCF (SiC-PCF) [173]. They were able to detect in situ each step of the biological binding between cTnT proteins and antibodies on the core surface. cTnT is a cardiac regulatory protein, which is used as a biomarker for acute myocardial infarction. In this configuration, they achieve a limit of detection of 1 ng/mL.

All these aspects contribute to making PCFs particularly attractive for preclinical and clinical biosensing. In the following chapter, we will present the different PCF designs that can be used for SERS sensing. We will review some of the most promising studies that reported PCF-based SERS sensors and we will present the different configurations currently available to achieve SERS inside a PCF. Finally, we will discuss the advantages and drawbacks of the two main classes of PCF (solid or hollow core) as well as the limitations that need to be addressed for the creation of a fiber-based SERS sensor, especially when it comes to designing a clinically viable sensor.

II.2. Photonic crystal fibers for SERS sensing

All PCFs possess at least one hollow region in their cross-section. They can be separated in two classes depending on the structure of their core, i.e. solid-core PCF (SC-PCFs) and hollow-core PCFs (HC-PCFs). In the following sections, we present the different properties of each class.

II.2.1. Solid-core photonic crystal fibers

The generic cross-section of an SC-PCF is available in Figure 22(a) [174]. It consists of a solid core surrounded by a 2D-periodic pattern of holes in the cladding. In such fiber, the light is guided thanks to total internal reflection (TIR). This guiding mechanism is the same that allow the light to be guided in standard SMFs and MMFs. Briefly, the core possesses a refractive index higher than that of the cladding. As illustrated by Snell-Descartes' law, rays of light striking the surface between two materials with different refractive indices with angles large enough are totally reflected and remain in the high-index material. In other words, once inside the fiber core, rays of light that form an angle large enough with the core/cladding surface stay confined inside the core (in the first order approximation). In SC-PCF, the presence of the holes lowers the mean refractive index of the cladding yielding a difference in refractive index that allows the light to be guided inside the solid core. With SC-PCFs, the interaction between the excitation light and the analyte and NPs occurs thanks to the evanescent field, which is a small portion of light that propagates in the air cladding. This portion of light is directly linked to the size of the core. The larger the core is, the smaller the evanescent field becomes.

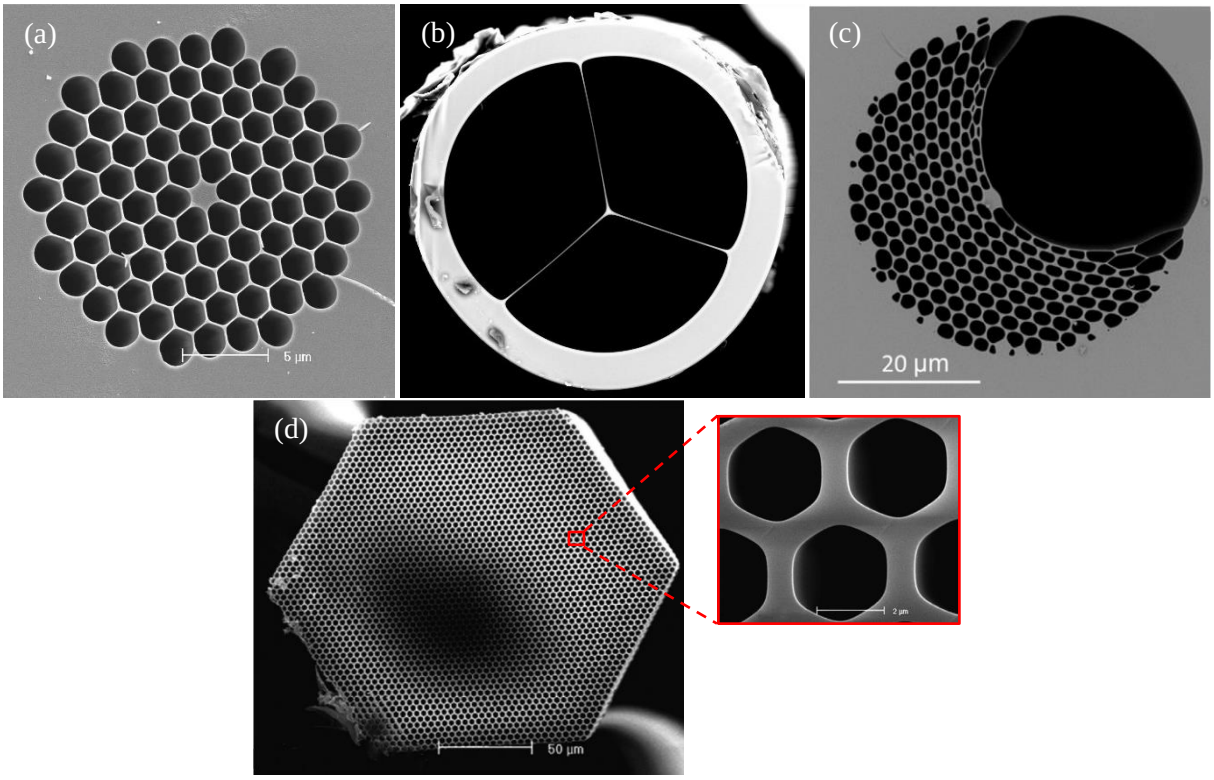

Figure 22 Cross-sections of (a) an SC-PCF, reproduced from [174], (b) a SuC-PCF, reproduced from [225], (c) a SiC-PCF, reproduced from [11], (d) a core-array PCF, reproduced from [180].

Standard SC-PCFs exhibit noticeable features such as endlessly single mode propagation [175–177], precise tailoring of group velocity dispersion curve [178] and strong evanescent field. These properties are achieved by tuning the ratio of the hole diameter on the pitch (d/Λ), the pitch being the distance between two adjacent air holes. However, their use in sensing is limited by the relative difficulty to incorporate the analyte inside the fiber. Indeed, sensing requires that a large amount of light interacts

with the analyte and this is achieved by decreasing the core size. Unfortunately, due to the ratio d/Λ, a smaller core means smaller holes in the cladding, which limits the analyte incorporation.

To facilitate the analyte incorporation inside the fiber, large holes can be implemented in the cross-section of the SC-PCF, as shown in Figure 22(b). This fiber design, called suspended core PCF (SuC-PCF), consists of a small solid core surrounded by large air channels. Depending on the number of holes, the shape of the core can vary. It could be a triangle (3 holes), a square (4 holes) or a hexagon (6 holes) and so on. Since the cladding is almost entirely made of air, the properties of this fiber are similar to those of a silica rod suspended in the air by thin silica struts. Although there is no periodicity in the cladding, the light can be guided by TIR since the index of the core is higher than that of the cladding. This remains true if liquids with a refractive index lower than the index of the core are incorporated in the cladding holes. Here, it is worth introducing the normalized frequency (V) that depends on the wavelength of the guided light, the diameter of the core (a) and the numerical aperture (NA):

$$\mathrm{V} = \frac{2\pi}{\lambda} a\, NA = \frac{2\pi}{\lambda} a \sqrt{n_{core}^2 - n_{cladding}^2} \tag{18}$$

With: n_{core} the refractive index of the fiber core and $n_{cladding}$ the refractive index of the cladding. Since the cladding is almost entirely made of liquid, except for the small silica struts, we can approximate $n_{cladding}$ with n_{liquid} the refractive index of the liquid inside the holes. A fiber is considered single mode when V is lower than 2.405. Therefore, in SuC-PCFs, for cores relatively large or depending on the liquid inside the holes, the light can be guided in multimode regime [179]. Thus, for multimode guiding, an extra-care needs to be taken to always excite the same mode in order to achieve reliable and stable SERS measurements.

Another solution to facilitate the incorporation of liquid inside the fiber consists of removing a portion of the cladding of a standard SC-PCF as shown in Figure 22(c). This fiber, called side-channel PCF (SiC-PCF), exhibits similar properties as SC-PCFs. They can be seen as a mix of standard SC-PCFs and SuC-PCFs. They are more complicated to fabricate since additional care needs to be taken to maintain the side-channel open while preserving the organized structure of the cladding. Playing on the parameters of the crystal still allows controlling precisely the guiding properties of the fiber. In addition, the large side channel allows for fast incorporation of liquids inside the fiber, which is greatly valuable for sensing. For instance, it has been used as an in-line opto-fluidic lab-in-fiber device [173].

Another subclass of SC-PCFs can be used for SERS sensing, namely core-array PCF. A representative picture is available in Figure 22(d). It consists of an array of small cores hold by silica struts. The large number of cores and their size results in large interaction surface and large fraction of evanescent field. Core-array PCFs can be fabricated by drawing down a commercial multi-hole capillary preform to a fiber [180], by fabricating a HC-PCF without removing the central capillaries of the core [181] or by exciting the silica cores of a PCF cladding with an offset coupling of the light [182,183]. However, in this configuration the light is guided in a highly multimode regime, which can limit the reliability of the measurement. In addition, three other drawbacks limit the use of such fiber. The first one is the propagation losses that are quite important (~1 dB/cm) [180,181]. The second one is the coupling losses (~28 dB) [181]. They are very important and result from the difficulty to excite several “cores” at the same time. The last one is the size of the holes that inevitably complicate the incorporation of the analyte.

II.2.2. Hollow-core photonic crystal fibers

A representative cross-section of a HC-PCF is available in Figure 23(a) [184]. In this type of fiber, the light is no longer guided by TIR. Indeed, as we saw previously, TIR requires that the refractive index of

the core is larger than that of the cladding, and in HC-PCFs, the refractive index of the core depends on the analyte inside it. If the core is filled with air for example, its refractive index will be close to 1, which is lower than the index of silica (~1.45) and thus the light should not be guided in the core. However, the periodic pattern of air holes in the cladding creates a photonic band gap (PBG). Concisely, the PBG corresponds to wavelength ranges where light cannot be guided in the silica cladding. Therefore, when a laser at a forbidden wavelength is launched inside the core of the HC-PCF, the light is reflected and cannot escape in the cladding and thus remains trapped inside the core [185,186]. In other words, the light can be guided in the air core within specific wavelength windows. Since the periodicity of the optogeometric parameters (pitch, refractive index of the material and refractive index in the holes) in the cladding is responsible for the creation of the PBG, the parameters of the pattern play a role in the position of the transmission window. Tuning the diameter of the holes and the pitch during the fiber fabrication allows one to create HC-PCFs with carefully selected operating wavelength ranges. The best HC-PCF exhibits relatively low-loss attenuation (1.2 dB/km) [187].

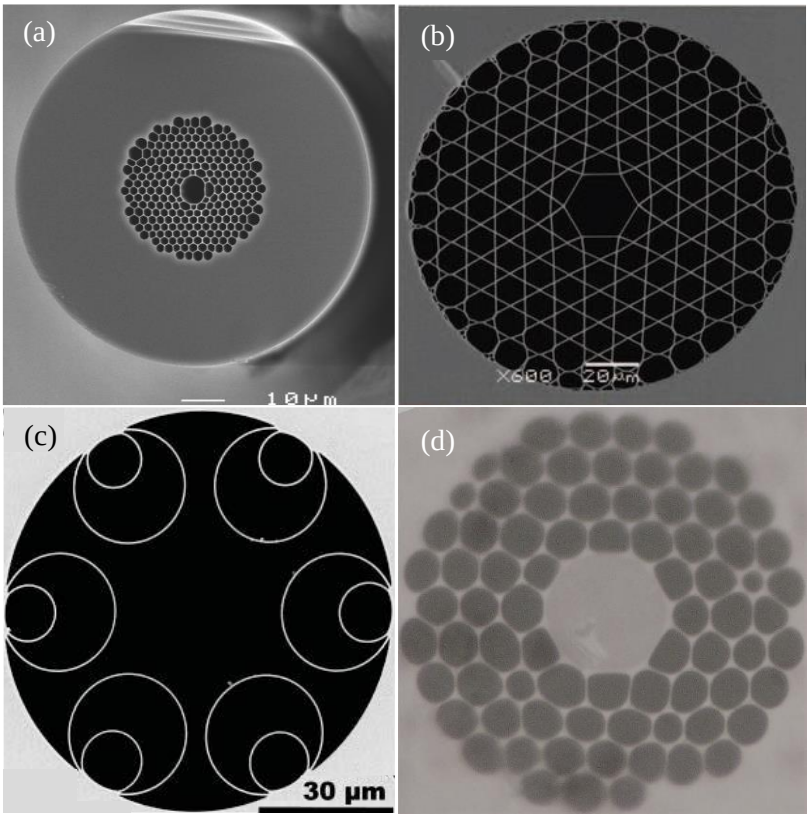

Figure 23(a) HC-PCF. Reproduced from [184]. (b) Kagome PCF. Reproduced from [195]. (c) NANF. Reproduced from [196]. (d) LC-PCF. reproduced and adapted from [198].

In HC-PCF, the excitation light is guided directly inside the analyte, thereby allowing direct interaction and avoiding parasitic signal from the fiber material. At operating wavelengths, the interaction length can be relatively long being limited only by the attenuation coefficient of the fiber and by the absorption coefficient of the analyte. However, the transmission windows of HC-PCF are rather narrow (few hundreds of nanometers). In addition, filling the HC-PCF with the analyte results in a change of the refractive index of the core and cladding holes, which in turn results in a shift of the transmission bandwidth [188]. This was experimentally demonstrated by Antonopoulos *et al.*, as shown in Figure 24 [189]. Hence, when using HC-PCF in solution, the shift of the transmission window should be anticipated so that the excitation laser and Raman signal can be guided once the fiber is filled. In addition, a special care should be taken when coupling the light inside the fiber to avoid the coupling to modes confined in the ring of glass surrounding the hollow core [190].

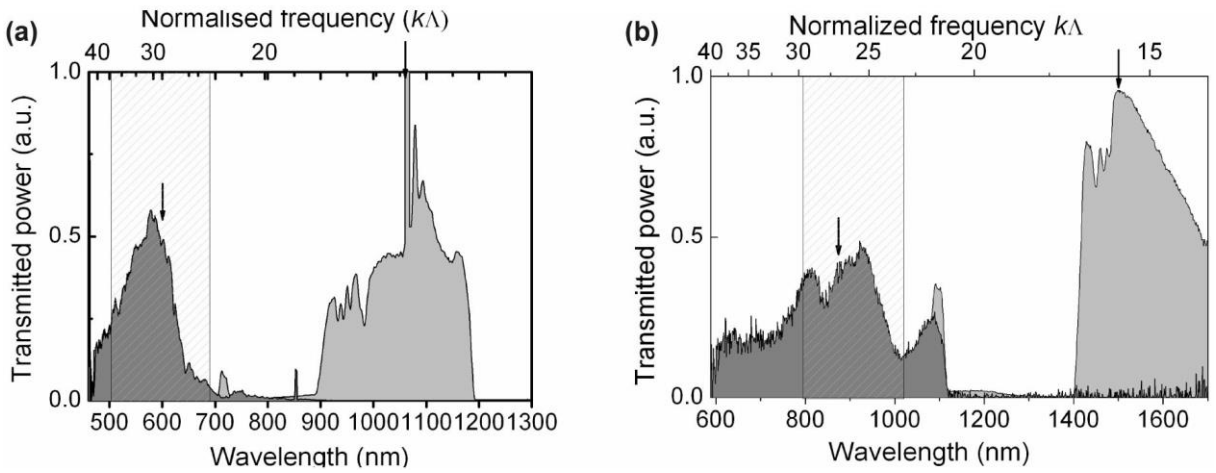

Figure 24 (a) Transmission spectra of a HC-PCF with a transmission window centered around 1060 nm when excited by a supercontinuum source and (b) of a HC-PCF with a transmission window centered around 1550 nm when excited by a tungsten lamp. The spectra were taken before (light gray) and after (dark gray) filling the holes of the HC-PCF with liquid D_2O. The transmission window shift is clearly visible for both fibers when the HC-PCF is filled. Reproduced from [189].

Another lattice, called "kagomé", can also be used to create a HC-PCF. The triangular unit cell of standard HC-PCFs is replaced by a star-of-David, as depicted in Figure 23(b). In Kagome HC-PCFs, the periodic structure in the cladding acts as a Fabry-Perot resonator [191]. At resonant wavelengths, the light can extend outside of the fiber core. However, at anti-resonant wavelengths, the light is reflected inside the hollow core and remains confined inside the core [192]. This guiding mechanism is called anti-resonant mechanism and it results in broader transmission windows, which decreases the impact of the refractive index change when the fibers are filled with the analyte. Silica based Kagome HC-PCFs have been used for generating stimulated Raman scattered light and in-fiber liquid spectroscopy [192–194]. However, despite the fact that silica-based Kagome exhibits broader transmission windows, SERS sensing has only been realized using PMMA fiber [165]. Unfortunately, Kagome HC-PCF exhibits high attenuation loss (~0.5 dB/m) [195], large bend losses and stronger decay of the field before the inner core surface compared to regular HC-PCFs (~30 dB) [193]. Therefore, both the excitation and Raman signal are strongly attenuated. This limits the length of fiber that can be used and thus it limits their interest for SERS-sensing. Recently, a novel type of anti-resonant HC-PCFs raised interest for their low-loss guiding. This fiber called nested anti-resonant nodeless fiber (NANF) exhibits a record loss of 0.65 dB/km around 1550 nm when filled with air [196], which is similar to the loss demonstrated by silica fibers. Thus, this fiber could represent a good alternative to HC-PCF since it possesses a larger transmission bandwidth and lower attenuation loss. An SEM picture of the fiber cross-section is available in Figure 23(c). Similar to HC-PCF, when they are filled with water, the transmission window of such fiber is also shifted towards shorter wavelengths due to the change of refractive index [197]. More importantly, when filled with water, these fibers exhibited much stronger attenuation loss (11-16 dB/m). Here, it is worth mentioning that the attenuation loss measured takes into account the attenuation loss of water. A solution to limit the loss could be to dry the fiber prior to the measurement. This would eliminate the loss due to the analyte solution.

Finally, HC-PCFs can be used to guide light by TIR when only the core is filled with a liquid. Figure 23(d) represents a HC-PCF whose core has been filled with ethanol [198]. This configuration is called liquid-core PCF (LC-PCF). The surrounding holes contain air and thus the difference of refractive index between the liquid core and the air in the cladding allows for TIR guidance. Thanks to TIR, the resulting transmission bandwidth is much larger than regular HC-PCF. However, here the light is guided in a

highly multimode regime, due to the large core size. In addition, to selectively fill only the fiber core, the external holes of the cladding were glued so that the liquid can only enter the core. This limits the practicability of the sensor from a clinical standpoint. A more easy-to-use LC-PCF can also be achieved using Teflon capillary and aqueous solutions [199]. Indeed, Teflon AF 2400 possesses a lower refractive index than water (1.29 and 1.33 respectively). In this configuration, the aqueous solution forms the core of the fiber and the Teflon is used as cladding. However, the high cost of this material, the relatively high attenuation loss induced by fabrication "irregularities" and the highly multimode regime limit the use of such sensor. While PCFs are very promising for SERS sensing, they are not SERS-active in nature. They need to be prepared prior to the measurements. The following section aims to provide a quick insight on the difference technique available to functionalize the PCFs.

II.3. Realizing SERS-active optical fibers

As we saw in chapter I, SERS relies on the interaction of an excitation light with the analyte and NPs. The holes in the PCF cross-section allow for the incorporation of liquid or gas analyte inside the fiber as well as the NPs responsible for the SERS enhancement. In the literature, two main configurations are used to activate the fibers. The first one (namely injected configuration) consists of pre-mixing the analyte solution with the colloidal NPs solution outside of the fiber, in a beaker, for example. Subsequently, the mixture is injected inside the PCF and the fiber can be placed under the Raman microscope for measurement. A schematic illustrating the main preparation steps is available in Figure 25(a). During the measurement, the NPs/analyte complex can move freely inside the fiber, which may lead to poorer reliability similarly to measurements in cuvette presented in chapter I. However, this method does not require many preparation steps, which makes it ideal for rapid detection and the SERS interaction are not limited to the surface of the core. This is particularly interesting for HC-PCFs where the light can interact over the entire surface of the core.

The second technique (namely anchored configuration) consists of immobilizing the NPs in the PCF holes, on their inner surface, prior to inject the analyte solution. Once inside the fiber, the analyte will be able to bind physically or chemically to the immobilized NPs. To anchor the NPs inside the fiber, one can use silanization similarly to the chemical anchoring procedures presented in the section I.3.2.3 for the immobilization of NPs on silica substrates. In planar substrates, the process often consists of dipping the planar substrate in successive solutions to functionalize it. With fibers, the solutions are injected successively inside the fiber holes, usually using a syringe pump. After drying the fiber, the analyte solution (or gas) can be injected inside the PCF. Subsequently, depending on the nature of the analyte, the molecules can bind to the anchored NPs and the fiber can be dried or the analyte can remain in solution inside the fiber. Finally, the PCF is placed under the Raman microscope for measurement. A schematic illustrating the main steps of this technique is available in Figure 25(b).

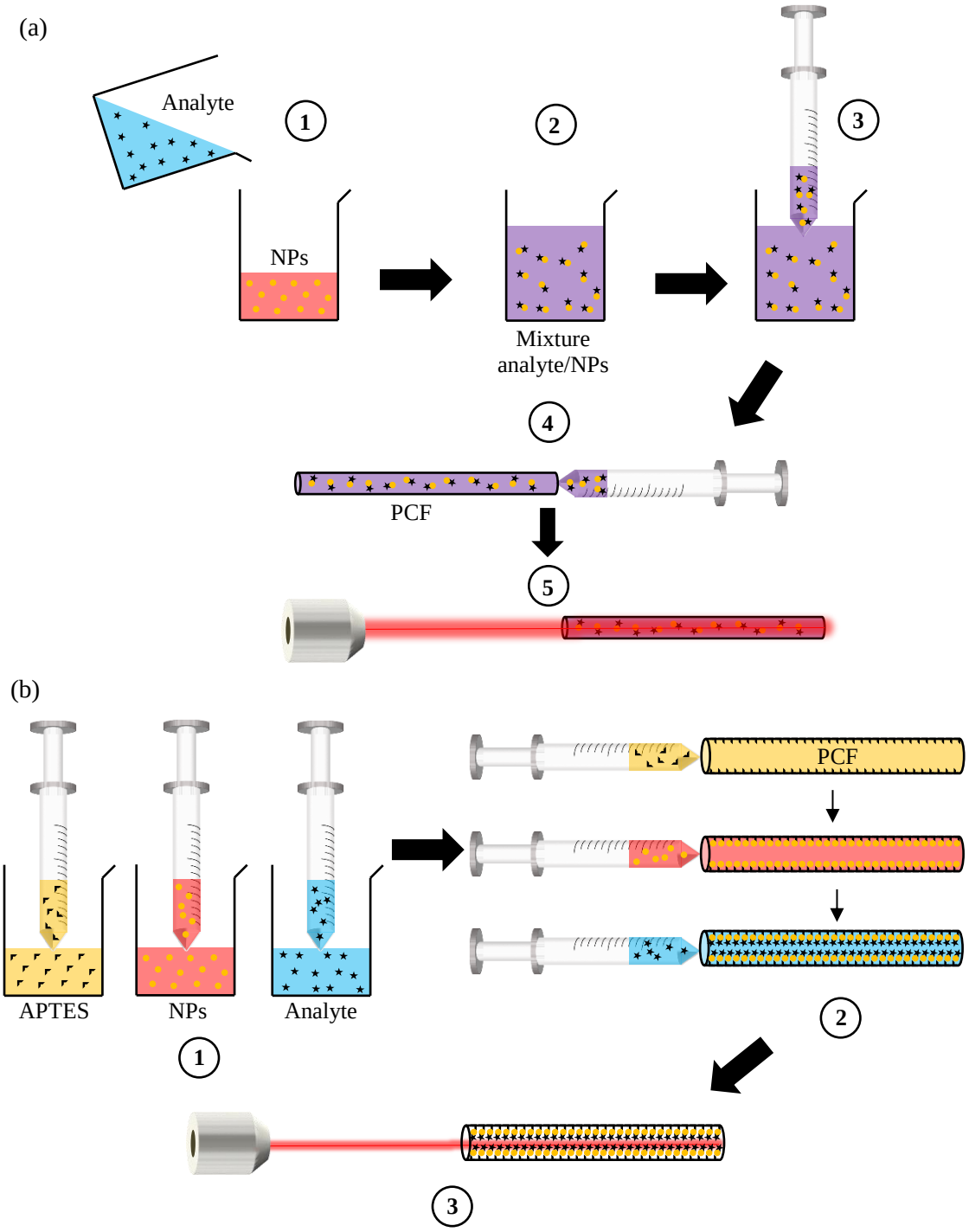

Figure 25 (a) Schematic illustrating the injected configuration. 1: Mixing of analyte and NPs solutions. 2: Resulting mixture. 3: Withdrawing of the mixture with a syringe. 4: Injection of the mixture inside the PCF. 5: SERS measurement. (b) Schematic illustrating the anchored configuration. 1: Preparation of each solution and filling of the syringes. 2: Successive injection of the solutions inside the PCF. The molecules of APTES bind to silica (top), then the NPs bind to APTES (middle) and finally, the analyte molecules bind to the NPs (bottom). 3: SERS measurement.

Now that we saw the two main techniques that are used to make PCFs SERS-active, we review the principal achievements realized with SERS-based PCFs.

II.4. State-of-the-art in PCF SERS-sensing

II.4.1. Evaluation of the performance of SERS-based PCFs using common Raman tags

In this section, we present a review of studies that have been conducted to better understand the different interplays that occur in SERS sensing with PCFs.

II.4.1.1. Illustration of the guiding mechanisms in solid and hollow-core PCFs

First, a study made by Han *et al.* allows illustrating the guiding principles of each class of PCF. They anchored Ag NPs in a standard SC-PCF and a HC-PCF. Pictures of the two fibers are available in Figure 26. Subsequently, they injected an aqueous solution of R6G inside the cladding holes of the SC-PCF and inside the core of the HC-PCF and they acquired the SERS spectra in forward propagation [166]. Here, the laser was coupled to the core at one end of the fiber and the SERS spectra were collected at the other end. Measured spectra are available in Figure 27. It is worth noting that the SERS spectra from the SC-PCF and HC-PCF exhibit some major differences. In the range 400-1200 cm^{-1} of the SC-PCF spectrum, the strong signature of silica is detected, with the maximum peak at 485 cm^{-1}. This signal is not detected by the HC-PCF. On the other hand, the strong signature peak of water, near 3381 cm^{-1}, is detected with the HC-PCF but not by the SC-PCF. These results can be explained by the guiding medium in each PCF. In the SC-PCF, the excitation light and the Raman signal travel in the silica core, resulting in the strong silica signal, whereas they travel in the analyte, which results in the strong water signal, in the HC-PCF. To further illustrate this phenomenon, they studied the distribution of the scattered signal at three Raman lines inside the two fibers using hyperspectral images. These Raman lines corresponded to signature peaks of silica, R6G and water, i.e. 485, 1351 and 3381 cm^{-1} respectively. In the SC-PCF, despite the fact that the analyte and the NPs are inside the holes, we can see on Figure 27(a) right that both the silica and R6G signals are concentrated in the solid core of the SC-PCF, while no identifiable signal from water was visible. This illustrates the fact that only the photons that are coupled back to the fiber core are transmitted and can be collected at the end of the fiber. In the HC-PCF, it can be seen on Figure 27(b) right that silica exhibits a weak signal in a dashed ring shape. This illustrates the fact that a small portion of the light is guided in the region between the core and the first few rows of the holes in the cladding. For the two images on the right, we note that the main portion of the R6G and water signals are guided inside the hollow core. This illustrates the direct excitation mentioned in the previous paragraph.

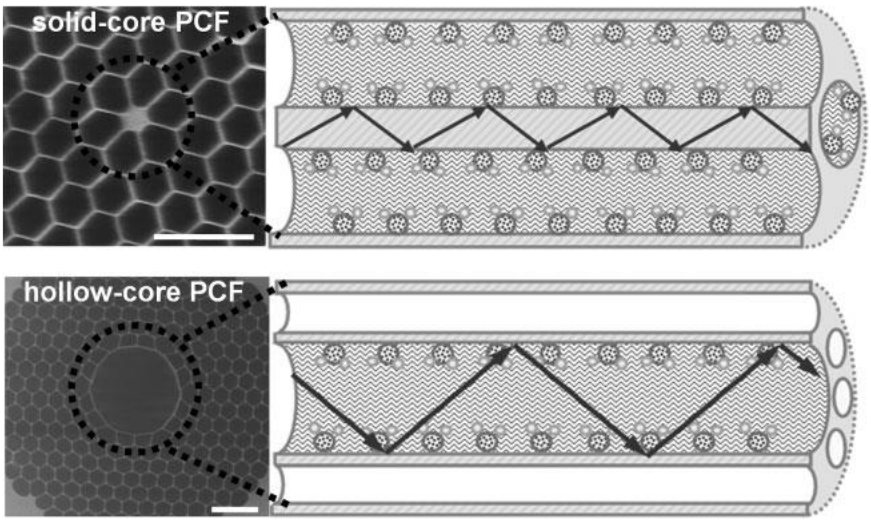

Figure 26 Left: SEM pictures of the cross-sections of the two fibers used in the study by Han *et al.*. Right: illustration of the light guiding mechanisms in the SC-PCF and LC-PCF. Reproduced from [166].

This study demonstrates one of the drawbacks of SERS sensing with PCF. Since the interaction lengths are relatively long, the guiding medium may exhibit a strong Raman signature that might overshadow the signal of the analyte, especially for trace-amount detection. Depending on the signature spectrum of the analyte, one may use an SC-PCF or a HC-PCF to avoid this overshadowing effect.

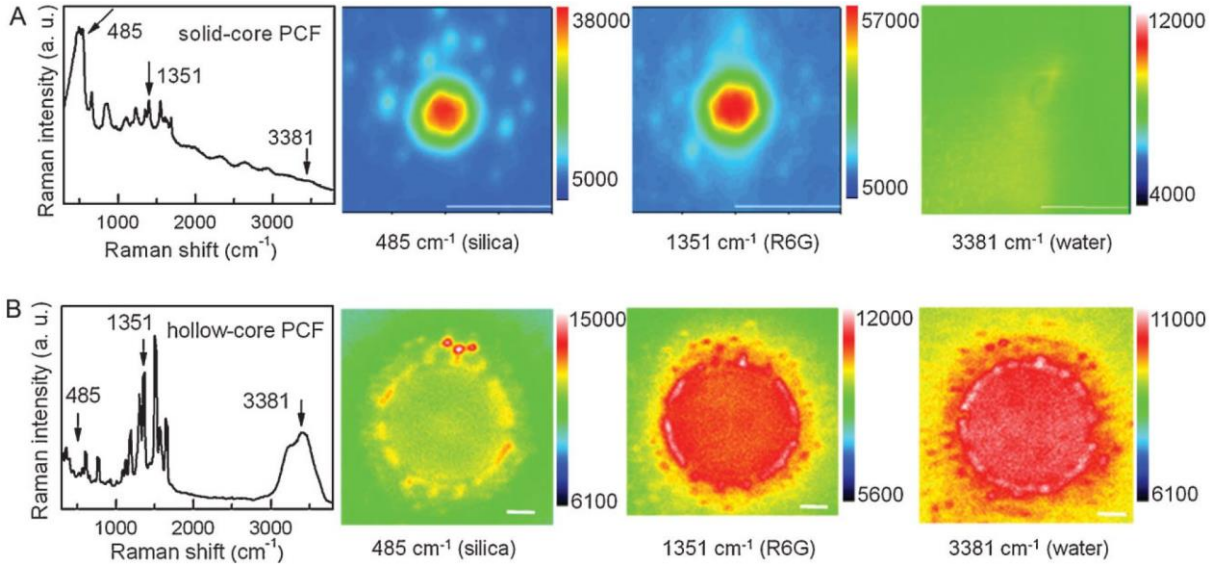

Figure 27 SERS spectrum and hyperspectral images measured at the end of (a) an SC-PCF and (b) a HC-PCF functionalized with Ag NPs and filled with an aqueous solution of R6G. Reproduced from [166].

II.4.1.2. Effect of the fiber length on the SERS intensity

We stated in the introduction section that PCFs increase the interaction surface and thus more NPs could interact with the excitation light. This should result in an increase of the SERS signal. In reality, it is not that simple. Indeed, NPs are also responsible for absorption and scattering losses. Thus, during the propagation, each NP prevents a small portion of the light to be guided further inside the fiber but at the same time, they increase, through LSPR, the EM field. This results in the creation of two separate regimes. The first one occurs when the SERS enhancement is superior to the losses. Here, increasing the density of NPs (or the fiber length) results in increasing the SERS enhancement. However, if too many NPs are anchored in the PCF, the losses become too important. This is the second regime. Here, the losses overcome the SERS signal and the light cannot be guided over the entire length of the fiber, resulting in lower SERS intensity.

This matter was studied in forward propagation by Han *et al.* [166]. They immobilized different densities of Ag NPs inside several SC-PCFs and HC-PCFs. Then, they filled the fibers with an aqueous solution of R6G. Finally, they measured the SERS response of each fiber and monitored the intensity of the 1351 cm^{-1} peak of R6G. Their results are presented in Figure 28. SC-PCFs with 0.1 and 0.5 particles/μm^2 were in the first regime mentioned above, since increasing the fiber length led to an increase in SERS intensity. However, SC-PCFs with 3 particles/μm^2 was in the second regime. For HC-PCFs, only the fibers with 0.2 particles/μm^2 were in the first regime, the other two fibers being in the second regime. For long SC and HC-PCFs, increasing the NPs coverage density led to a decrease in SERS intensity. On the other hand, high NPs density gave a strong Raman intensity for short fiber lengths. These results illustrate perfectly the interplay between the SERS signal and the losses inherent to the NPs. It is easily understandable that a compromise should be made regarding the density of NPs and the fiber length. The final use of the fiber will have an impact on the fiber length. From there, one can select the density of NPs. Short fibers can tolerate a higher coverage density while it needs to be decreased for long PCFs.

The interplay between SERS intensity and losses will be further discussed in the case of SuC-PCF in the following chapter.

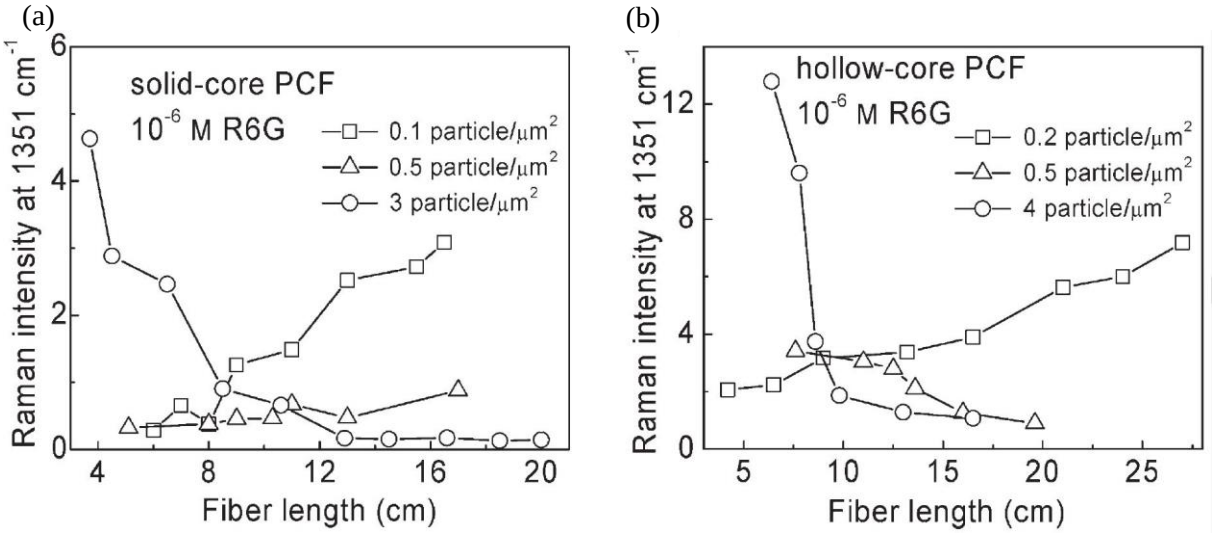

Figure 28 Variations of the Raman intensity of the 1351 cm^{-1} peak of R6G with the fiber length, for several NPs coverage density. The presented results were obtained in (a) an SC-PCF and (b) a HC-PCF. Reproduced from [166].

This matter was also studied by Tiwari *et al.* [169]. By filling HC-PCFs with a mixture of R6G and Ag NPs, they showed that increasing the fiber length from 4.7 to 6.5 cm increased proportionally the SERS intensity of R6G signal. This means that in their case the density of NPs was not too important, since longer fibers resulted in higher SERS intensity. They also estimated the enhancement factors (EFs) of the NPs and of the HC-PCF separately. For that, they pumped a solution of R6G without NPs in a HC-PCF and monitored the intensity of the 1357 cm^{-1} peak of R6G. Subsequently, they proceeded similarly after injecting a solution of R6G and Ag NPs. The comparison between the two configurations gave the EF of the NPs, ~20 times here. They also measured the signal coming from a mixture of R6G and Ag NPs in 1 cm cuvette and in 6 cm HC-PCF. This allowed them to quantify the EF due to the HC-PCF, i.e. 16 times here. The overall EF of NPs and HC-PCF combined was superior to 300 times.

Zhang *et al.* studied the impact of the fiber length on the SERS intensity using an in-house SiC-PCF [11]. They injected a mixture of Au NPs and R6G inside a fiber and they measured the SERS intensity of the 1310 cm^{-1} peak of R6G after repeatedly cutting the fiber. This study was realized in backscattering configuration. In such configuration, the excitation laser is coupled to the core at one end of the fiber and the Raman signal is collected from the same fiber end. The results showed that increasing the fiber length resulted in increasing the SERS intensity as shown in Figure 29(a). They simulated the variation of the SERS intensity with the fiber length as shown in Figure 29(b). They demonstrated that, in backscattering configuration, the SERS intensity increases with the fiber length until reaching a specific value after which increasing further the length has little effect. This optimal length corresponds to the length after which the losses inherent to the NPs become superior to the SERS enhancement. Since the losses are superior to the enhancement, increasing further the fiber length does not increase significantly the SERS intensity. In addition, it is worth mentioning that increasing the concentration of NPs in the mixture should theoretically result in decreasing the value of the optimal length, as shown in Figure 29(b).

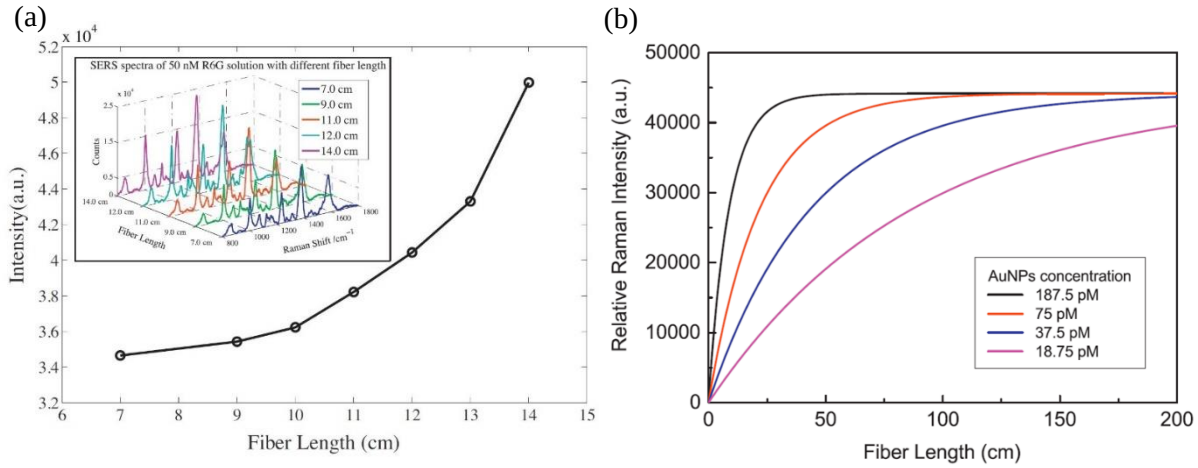

Figure 29 (a) Experimental variation of the SERS intensity with the fiber length for 50 nM of R6G. Inset: measured spectra for the different SiC-PCF lengths. (b) Simulated variations of the relative SERS intensity with fiber length for several concentrations of Au NPs in backward collection setup. Reproduced from [11].

II.4.1.3. Limitations of hollow-core PCFs for SERS sensing

We saw in section II.2.2 that the transmission bandwidths of HC-PCFs were rather narrow (less than 300 nm). This can quickly become an issue for SERS sensing. Large Raman shifts can be situated outside of the transmission window of the fiber, leading to important loss of the useful signal [200]. In addition, filling entirely fibers with a solution changes the refractive index of the cladding and the core. Since the position of the transmission window depends on the refractive indices, it is shifted once the fiber is filled. Therefore, in order to use HC-PCFs as SERS sensors, one should carefully select the HC-PCF and the excitation laser depending on the solution that will be injected inside the fiber. In this way, once the fiber is filled, the excitation and Raman signals will fall within the fiber transmission window allowing them to be guided inside the core. In their study, Tiwari *et al.* anticipated the bandwidth shift using [169]:

$$\lambda' = \lambda_0 \sqrt{\frac{1 - \left(\frac{n_{liq}}{n_{sil}}\right)^2}{1 - \left(\frac{n_{air}}{n_{sil}}\right)^2}} \tag{19}$$

With λ' the shifted wavelength and λ_0 the original wavelength at which the band gap occurred. n_{liq}, n_{sil} and n_{air} represent the refractive indices of the solvent, silica and air respectively. If no care had been taken to anticipate the bandwidth shift, the sensitivity would have been much less. For instance, Gong *et al.* measured the signal of 2-naphthalenethiol (2-NT) when mixed with 60 nm Au NPs using a SiC-PCF and a HC-PCF in the same conditions. They found that the SiC-PCF exhibited a signal six times stronger than the one measured with the HC-PCF [12]. One hypothesis to explain the poorer sensitivity exhibited by the HC-PCF lies in the light guiding mechanism of the HC-PCF. In other words, once the HC-PCF was filled with the analyte solution, the PBG shift could have decreased the sensitivity of the HC-PCF while the SiC-PCF, where the light is guided by TIR was not subjected to this shift. The poorer sensitivity observed for the HC-PCF could also be the result of higher losses or a weaker SERS enhancement.

II.4.1.4. Improvement of the sensitivity of SERS-based fiber sensors

Many studies were realized to develop the most sensitive SERS-based PCF sensor. For example, Oo *et al.* reported that increasing the evanescent field of SC-PCFs could also improve the sensitivity of SERS-based PCF probes [201]. Since the amount of evanescent field is inversely proportional to the core size, decreasing the core size increases the amount of light overlapping in the cladding. In their paper, Oo *et al.* studied the influence of the core size and the SC-PCF geometry for SERS sensing in forward propagation. They compared the sensitivity of a classic SC-PCF with a core diameter of 2.6 µm surrounded by 6 rings of air channels with two SuC-PCFs with core diameters of 3.1 µm and 1.1 µm cores surrounded by three large air holes. SEM pictures are available in Figure 30. For that, they anchored Ag NPs in each fiber and they filled the fibers with a solution of R6G. They found that the SuC-PCF with the smallest core size was the most sensitive. It could detect a concentration of 1×10^{-10} M, while the two others could only detect concentrations as low as 1×10^{-6}M. This demonstrates well that decreasing the core size of an SC-PCF can, in some cases, improve its sensitivity. However, decreasing the core size tends to decrease the effective index of the guided mode. Therefore, decreasing too much the core size can result in an effective index very close to that of the analyte solution, which can in turn compromise the guiding of the light in the core.

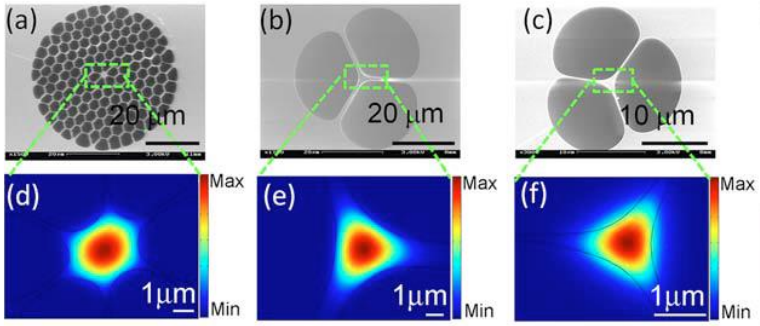

Figure 30 (a), (b), (c) SEM pictures of the three fibers used by Oo *et al.* in their study. (d), (e) and (f) simulated electric field distribution of the fundamental mode when the three fibers are filled with ethanol. Reproduced from [201].

To demonstrate that the geometry of the fiber has an influence on the final SERS sensitivity, Zhang *et al.* designed a SiC-PCF with a 2.8 µm core [11]. With it, they were able to detect a record R6G concentration of 50×10^{-15}M when injecting a mixture of Au NPs and R6G. Another approach was used by Zhang *et al.* [183]. They launched the excitation light in the cladding and not in the core of an SC-PCF. Figure 31(a) and (b) present calculated modes that propagate inside the SC-PCF with a coupling inside the solid core and with an offset respectively. Although this method is not conventional, they managed to obtain stronger signals of Rhodamine B (RhB) compared to when they excited the core directly. As described earlier, Guo *et al.* fabricated an array of silica cores that are able to guide the light similarly to the PCFs cladding [180]. They were able to detect concentrations of R6G lower than 100×10^{-15}M thanks to 10^8 EF without optimizing the fiber length, the coverage density of NPs or the excitation wavelength. However, as seen previously, such platforms exhibit high coupling loss and multimode guiding, which can result in poorer reliability. In addition, the important losses inevitably limit the length of the capillaries. For instance, in this study, the authors used ~3 mm long capillaries. Such short sensors are not easy to handle, which limits their practicability.

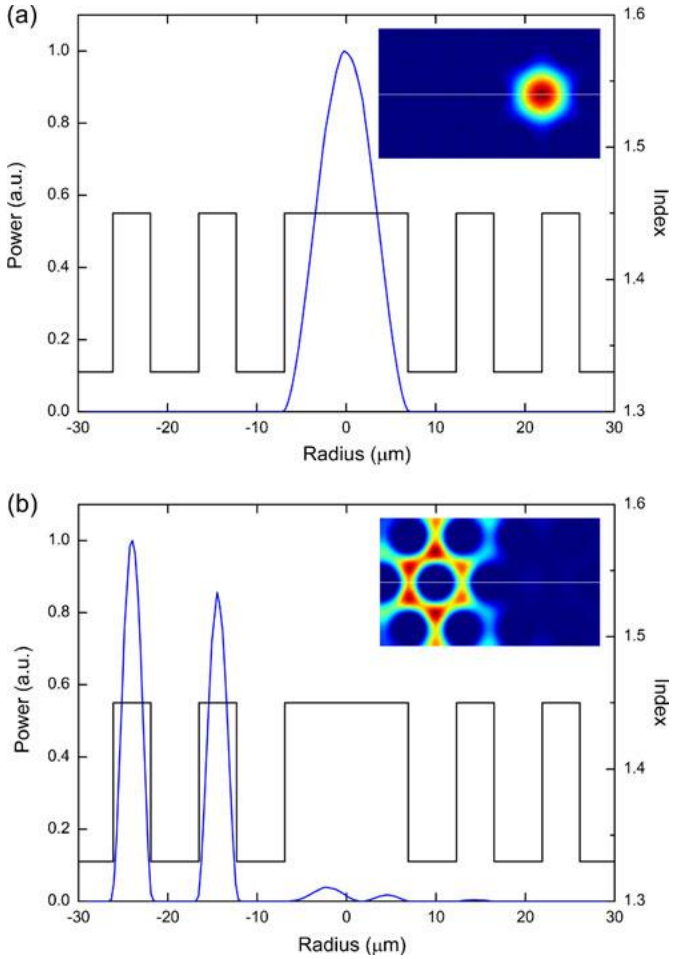

Figure 31 Calculated mode profile for a 785 nm laser coupled (a) in the solid core of an SC-PCF and (b) with an offset, in the cladding. Reproduced from [183].

II.4.2. Biosensing with SERS-based PCFs

Now that we reviewed important breakthroughs in SERS sensing with SC and HC-PCFs, we present several studies that illustrate the incredible biosensing abilities of PCFs. Similarly to planar SERS substrates, PCFs allow probing a wide variety of biomarkers. Here, we classify the studies based on the detection technique used, i.e. label-free Raman, label-free SERS and labeled SERS.

II.4.2.1. Label-free Raman detection

Biosensing with optical fibers can already be realized using direct Raman spectroscopy. Indeed, the increase of sensitivity obtained through the fiber length can suffice to detect biomolecules that possess relatively high Raman cross-sections without metallic NPs. For instance, heparin was detected by Khetani *et al*. using a commercial HC-PCF [200]. This anticoagulant is often administered during cardiac surgery and its dosage need to be precisely controlled to avoid serious bleeding during the surgery. The actual detection techniques are rather long and may lack accuracy if the measurements are not realized right away [202]. For this study, the authors filled 5 cm long HC-PCFs with heparin/serum mixture. They were able to detect heparin concentration as low as 12 USP/mL thanks to an EF of ~90. Here, USP refers to United State Pharmacopeia, which describes the strength of a drug in clinical applications. This concentration of heparin is situated in the clinical range, which means that HC-PCF sensors are sensitive enough to be clinically relevant. They also demonstrate that the intensity of the 1005 cm^{-1} peak of heparin increases linearly with the concentration of heparin in the mixture, as shown

in Figure 32. This graph is important since it allows identifying an unknown concentration of a sample thanks to the measured Raman intensity. Although these results are very promising, there is still room for improvement. Indeed, the transmission window of the commercial fiber used by Khetani *et al.* to detect heparin was 1430-1610 nm. Using equation 19, we calculated that it was shifted between 717 and 808 nm once the fiber was filled with the heparin/serum mixture. As we can see in Figure 32, the Raman spectra were measured between 900 and 1150 cm^{-1}, which corresponds to 845-863 nm. Thus, the measured Raman signal was situated outside the optimum transmission window of the fiber, yielding large attenuation losses. More adapted fibers would have exhibited stronger Raman signals and surely, they could have detected lower concentrations of heparin.

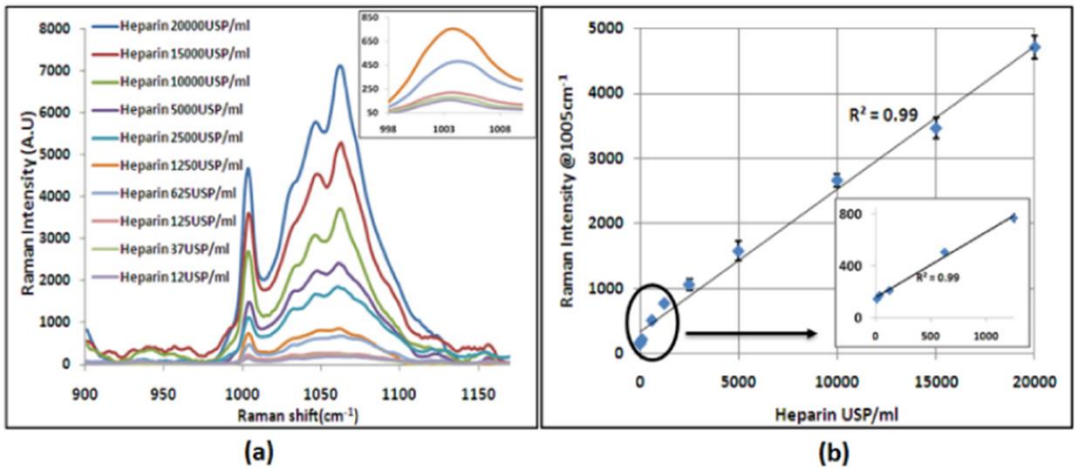

Figure 32 (a) Raman spectra obtain for different concentrations of heparin. Inset: zoom-in on the 1005 cm^{-1} peak for the lowest concentrations. (b) Intensity of 1005 cm^{-1} peak measured for each concentration. Reproduced from [200].

"Finger prick," devices allow patients with diabetes to monitor the concentration of glucose in their blood. Although it is used on a daily basis, it remains inconvenient and measures indirectly the blood glucose. Yang *et al.* also used commercial HC-PCFs to detect aqueous glucose solutions in clinically relevant concentrations [203]. They managed to detect glucose in the range 0-25 mM using lower laser power and shorter integration time than previously reported [204,205]. This is quite noticeable since glucose does not possess an extremely large Raman cross-section. More interestingly, they were able to differentiate glucose from fructose in multiplex configuration thanks to the high molecular specificity

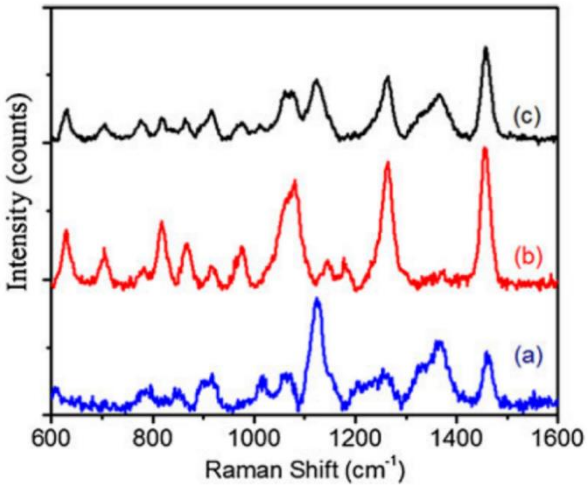

Figure 33 Raman spectra of (a) glucose, (b) fructose and (c) mixture of glucose and fructose. Reproduced from [203].

allowed by Raman spectroscopy. For that, they measured the Raman signature of glucose and fructose separately. Once mixed together, they were still able to identify the signature peaks of each molecule as shown in Figure 33.

Yan *et al.* detected moxifloxacin (antibiotic) in an aqueous solution using a commercial HC-PCF transformed in LC-PCF by selectively filling the core [206]. Figure 34 presents the transmission window of the empty HC-PCF, between 400 and 520 nm, and the transmission window of the same fiber with only the core filled with water. When the core is filled, the fiber exhibited a broadband transmission window. This can be explained by the change in guidance mechanism, i.e. PBG for the HC-PCF that became TIR for the LC-PCF, as mentioned previously. The purple dashed line represents the theoretical transmission window of a step index fiber and the general trend of the experimental data follows the calculated spectrum (outside the water absorption bands). In this configuration, they enhanced the Raman signal of moxifloxacin using several excitation wavelengths (532, 676 and 752 nm), demonstrating the benefit of a wide transmission window. Similarly to Yang *et al.* with heparin, they obtained the calibration curve of the Raman intensity with growing concentrations of moxifloxacin and they detected a limit concentration of 1.7 µM in 4 nL. This extremely small volume illustrates perfectly one of the benefits of PCF sensing, i.e. the volume required to fill the fiber is very small, which results in the possibility to create minimally invasive sensors.

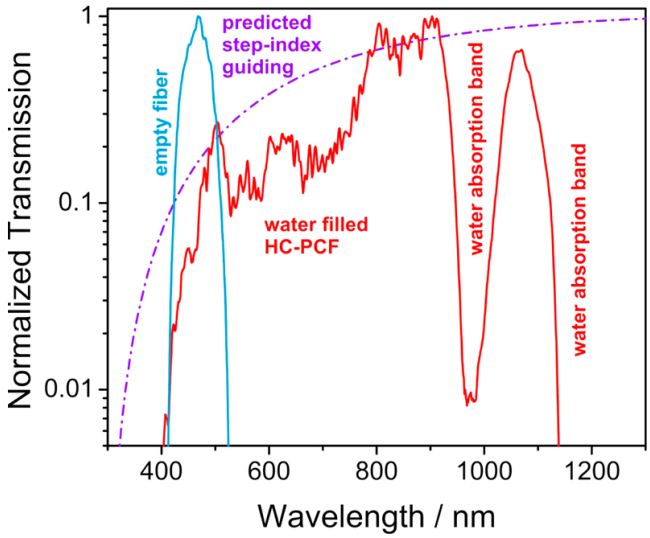

Figure 34 Transmission spectra of commercial HC-PCF when the core is empty and when it is selectively filled with water. The purple dashed line represents the ideal transmission spectrum with step index guidance. Reproduced from [206].

PCFs SERS sensors can also be used to detect gas [170,207]. They could represent a good alternative to the actual gas sensors that are expensive, bulky and unable to provide real-time data. In addition, thanks to the narrow peaks of Raman spectroscopy, they could be used for multiplex sensing in order to detect a target analyte in a complex mixture. Using a commercial HC-PCF and only Raman spectroscopy, Buric *et al.* detected N_2 [16]. They demonstrated an improvement of 130 times compared to the same measurement in free space. They also succeeded in identifying varying concentrations of methane, ethane and propane in a mixture. A similar study reported the use of 30 cm long HC-PCF to remotely detect toluene, acetone and 111-trichloroethane independently inside a sealed chamber [17]. A representation of the setup used is available in Figure 35(a). They were also able to detect each gas when mixed together in different concentrations inside the sealed chamber. A representative spectrum is available in Figure 35(b). Here, the EF was ~700 compared to conventional detection method.

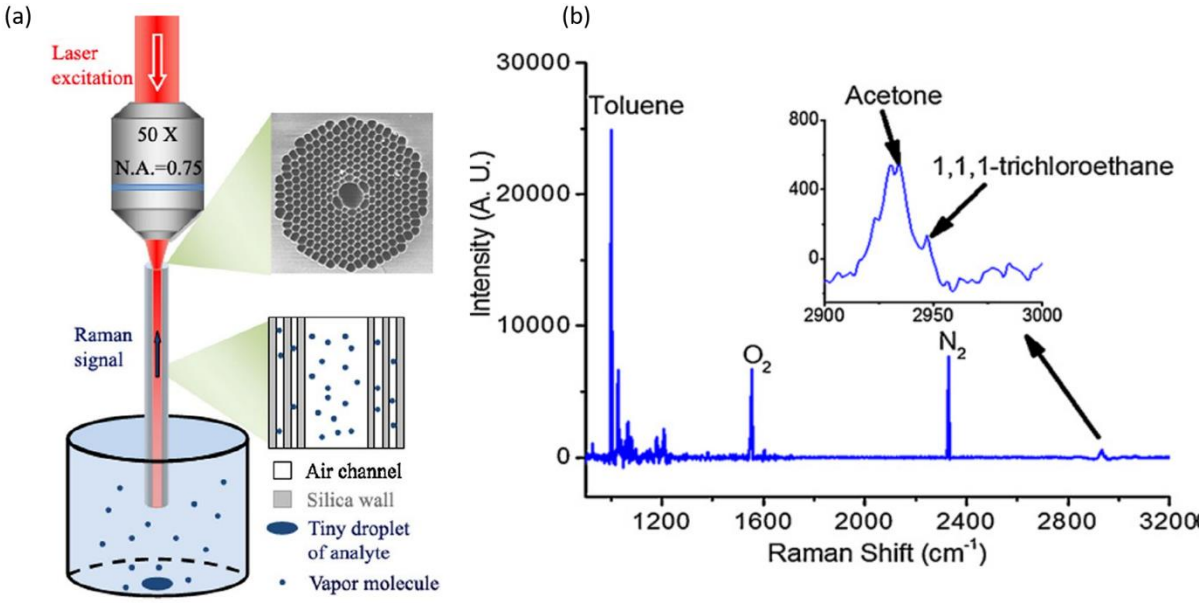

Figure 35 (a) Schematic illustrating the setup used for gas detection with SERS-based PCF probes. (b) Raman spectrum of the mixture of toluene, acetone and 111-trichloroethane obtained with a HC-PCF. Reproduced from [17].

Gas identification is also relevant in biosensing. For instance, analyzing exhaled breath and more importantly volatile organic compounds (VOCs) in the breath allowed identifying certain diseases such as lung cancer. With this in mind, Hanf *et al.* used a HC-PCF to detect H_2 and CH_4, which are marker gases for malabsorption disorders, in a mixture of the major breath components, i.e. N_2, O_2, CO_2 [208]. They were able to detect H_2 and CH_4 in the concentration range of 5-50 ppm (part per million), which is in the clinically relevant level. The same research team reported a fully automated gas filling system that allowed for alignment free and fast monitoring of multigas fluctuations [209]. This achievement is quite important since limiting the handling of the PCF fibers are a key feature to create a clinically viable sensor.

II.4.2.2. Label-free SERS detection

Here, we present important biosensing studies where the authors increased the weak Raman cross-sections of biomolecules using metallic NPs. Khetani *et al.* detected adenosine using 6 cm long commercial HC-PCF [210]. Adenosine is an important biomolecule that regulates the extracellular physiological activity. They compared the signal measured for a solution of pure adenosine in a cuvette, adenosine mixed with Ag NPs in a cuvette and the same mixture filled non-selectively in a HC-PCF. The measured spectra are available in Figure 36. It is clear that both the NPs and the fiber increased drastically the signal. Using 733 cm^{-1} peak, they estimated the overall EF to be ~2700 between the pure adenosine in cuvette (label-free Raman detection) and the mixture of NPs/adenosine in HC-PCF (in fiber label-free SERS detection).

Acute myeloid leukemia is a pediatric cancer. It represents the leading cause of disease-based morbidity in children and adolescents. Early diagnostic and monitoring of minimal residual disease are the best chance to improve the survival rate of the patients. However, current detection techniques remain costly and time-consuming. A proof of concept study was conducted with a commercial HC-PCF to detect acute promyelocytic leukemia (HL60) cells [168]. They estimated that the EF was ~2700 by dividing the signal obtained from a mixture of Ag NPs and leukemia cells injected in a HC-PCF by the signal of leukemia cells alone in a cuvette. They also obtained a linear calibration curve for increasing concentration of cells in the solution and they were able to measure a limit concentration of ~300

cells/mL. What is even more interesting is that they managed to differentiate the stage of the cells between live, necrotic and apoptotic using statistical analysis.

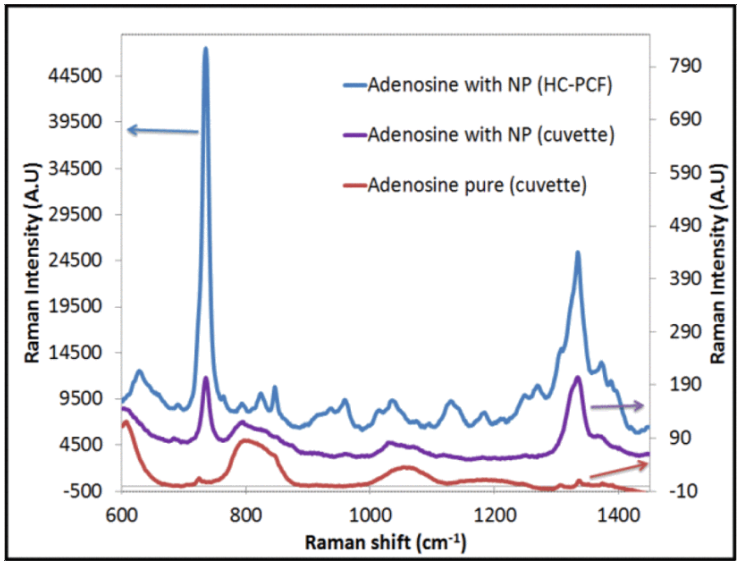

Figure 36 SERS and Raman spectra of adenosine in cuvette and in HC-PCF. Reproduced from [210].

II.4.2.3. Labeled SERS detection

For real life sensing applications, some biomolecules do not possess a clear Raman signature. Detecting trace amount in complex biological fluids can thus be arduous. A solution presented in chapter I is SERS nanotags. A ligand specific to a biomarker, such as antibodies, is used to put the bio-analyte in contact with NPs and a Raman reporter that possess a strong Raman cross-section. For instance, Dinish *et al.* detected epidermal growth factor receptors (EGFRs) using a commercial HC-PCF and SERS nanotags [4]. EGFRs are proteins commonly used as biomarkers in clinical environment as they are up regulated in many cancers. The current detection techniques, such as enzyme-linked immunosorbent assay

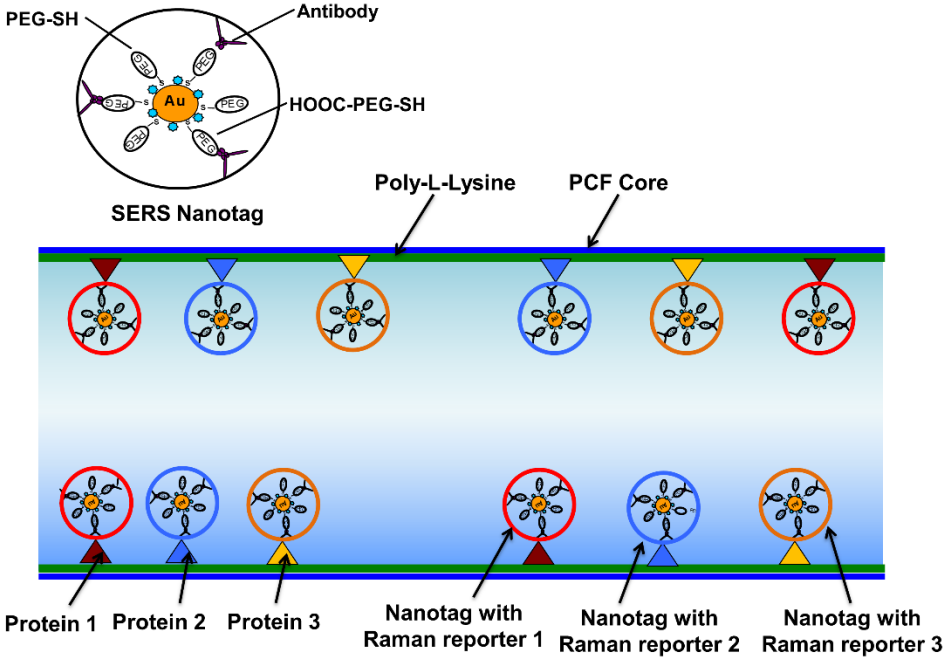

Figure 37 Top: Schematic presenting a SERS nanotag. The little blue circles represent the Raman reporter. Bottom: Representation of multiplex detection inside a HC-PCF with three nanotags. Reproduced from [5].

(ELISA) and fluorescence sensing, are tedious to perform and lack precision for trace amount sensing and multiplex detection. First, the authors functionalized 8 cm long HC-PCFs with poly-L-lysine and they injected a solution of cell lysate inside the fiber. The protein (EGFR) was able to bind to the poly-L-lysine. Subsequently, they prepared a SERS nanotag using 60 nm gold spheres, onto which they anchored malachite green isothiocyanate (MGITC), a well-known Raman reporter, and anti-EGFR antibodies. A representation of the nanotags is available at the top of Figure 37. Then, they filled the fiber with a solution containing the nanotags. The antibodies anti-EGFR at the nanotags surface were able to bind to the anchored proteins inside the fiber and the signal of MGITC could be detected. With this configuration, they achieved a limit of detection of ~100 pg/mL in a sample volume of ~10 nL. It is worth mentioning here that the fiber was dried prior to the measurement in order to ascertain that the transmission window of the HC-PCF matched the excitation laser (no shift of the transmission window). It is worth mentioning that in HC-PCF, the light is mostly guided in the center of the core and an important drop in intensity occurs near the core wall. Therefore, when the NPs are anchored on the inner side of the core, they only interact with a small portion of the excitation light, which results in a decrease in sensitivity, allowing room for improvement.

Dinish *et al.* also achieved multiplex detection of alpha-fetoprotein (AFP) and alpha-1-antitrypsin (A1AT), two biomarkers for liver cancer, using a commercial HC-PCF and two separate nanotags [5]. The process was similar to the one presented before except that this time, they prepared two SERS nanotags with different Raman reporters. They used MGITC and Cyanine5 (Cy5) because they each possess two distinct signature peaks, as shown in Figure 38. They added anti-AFP antibodies on the Cy5 nanotags and anti-A1AT antibodies on the MGITC nanotags. In this way, the detection of the Cy5 signal corresponded to the presence of AFP while the detection of MGITC signal corresponded to the presence of A1AT. After preparing the nanotags, they functionalized the HC-PCF with poly-L-lysine and injected the supernatant of Hep3b cell line. This cell is known to secrete the two target biomarkers [211,212]. Finally, they injected the mixture containing the two nanotags and they dried the fiber. They were able to detect simultaneously the signals of Cy5 and MGITC, thereby revealing the presence of AFP and A1AT in the cell supernatant. This study demonstrates that SERS-based fibers can very well be used for the simultaneous detection of several biomarkers.

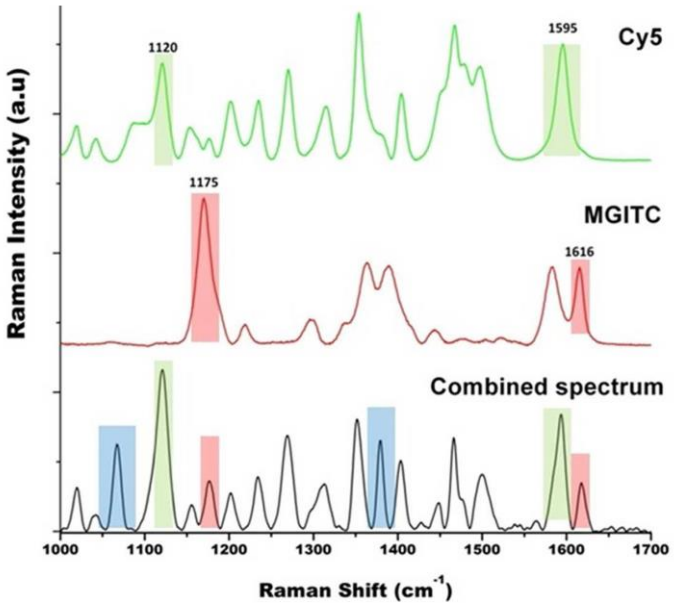

Figure 38 Raman spectra of Cy5, MGITC and mixture containing Cy5 and MGITC illustrating the possibility to obtain multiplex detection. Reproduced from [5].

Until now, we presented mainly studies realized with commercial HC-PCFs. Nevertheless, important detections of bio-analytes were reported using SC-PCFs. For instance, Gong *et al.* detected sialic acid using an in-house SiC-PCF [12] after having shown that the SiC-PCF was more sensitive than commercial HC-PCF, despite the fact that the study was realized in the injected configuration. Sialic acid modulates normal and pathological processes [213]. In many cancers, it is often overexpressed at the cell surfaces and monitoring its expression within a cell can be used to identify the tumor malignancy and metastasis. The common detection techniques include colorimetric analysis, chromatography or potentiometry. They lack sensitivity and/or suffer from photo-bleaching. To detect it, the authors used HeLa cells, which are known to overexpress sialic acid receptors [214] and 4-(dihydroxyborophenyl) acetylene (DBA) as Raman reporter. DBA was able to bind to sialic acid on the surface of HeLa cells, as shown in Figure 39, and exhibited a relatively strong peak around 2000 cm^{-1}, which is outside the complex signature spectra of the cell and silica. Therefore, this peak could be used to monitor the concentration of sialic acid at the surface of a single cell present in the side channel of the fiber. They detected a record-breaking concentration of 2.5 fmol of sialic acid at the surface of a single cell showing the extreme sensitivity that can be achieved thanks to SERS-based PCF sensors.

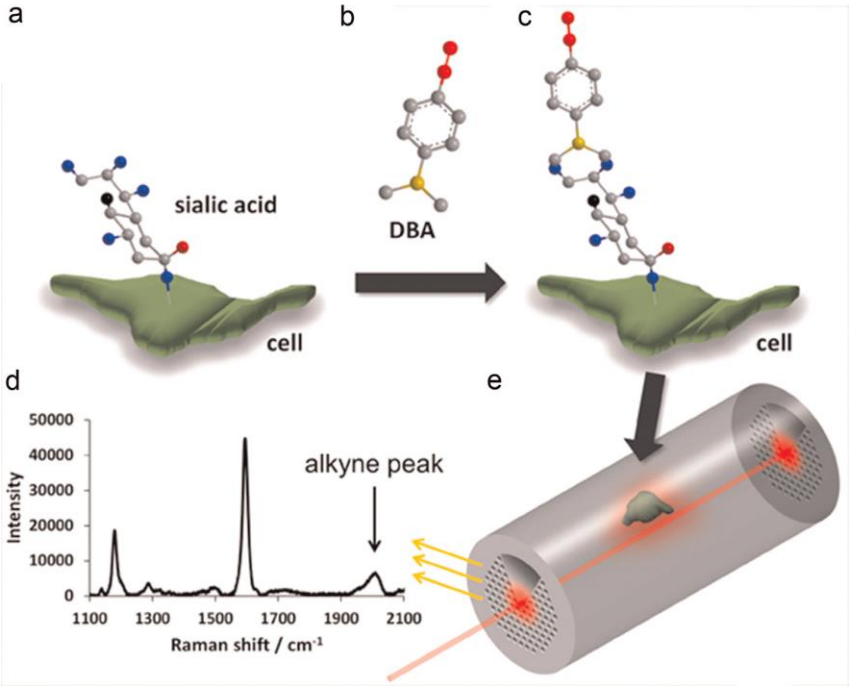

Figure 39 (a), (b) and (c) Representation of the formation of sialic acid/DBA complex. (d) Raman spectrum detected from DBA tagged cells in SiC-PCF. (e) Schematic illustrating the detection of sialic acid at the surface of HeLa cells in SiC-PCF. Reproduced from [12].

Lipid peroxidation is the oxidative degradation of polysaturated lipids. Usually, it happens in relatively small amounts in the body and the augmentation of its occurrence can be a sign of cancer or neurodegenerative disorder [215]. A proof of concept study was realized to indirectly detect lipid peroxidation using an in-house SiC-PCF [216]. They treated HepG2 liver cancer cells with linoleamide alkyne (LAA) so that LAA can incorporate into the cellular membranes. Then, they added to the mixture different concentrations of cumene hydroperoxide (CH), which is known to induce lipid peroxidation. When lipid peroxidation occurred, LAA was oxidized, which resulted in the production of alkyne-containing proteins. Finally, they filled a SiC-PCF with a mixture of 60 nm Au NPs and the different previous solutions and they monitored the intensity of the alkyne peak (presented in the previous paragraph) for cells treated with LAA alone and with increasing concentrations of CH. The cells treated with LAA alone did not exhibit any alkyne signal, while the intensity of the peak increased with the

concentration of CH, showing that lipid peroxidation was more important for higher CH concentrations. This study represents another proof that SERS-based fiber probes can be used for the detection of an extremely wide range of biomarkers. Here, it was used to detect a physiological reaction and not a biomarker directly.

II.5. Discussion and conclusion

In this chapter, we presented a class of fiber that possesses enormous advantages for SERS sensing, i.e. PCFs. The hollow regions in their cross-sections allow for liquid or gas incorporation inside them, which results in increased surface of interaction between the analyte and the laser. This improves the sensitivity and the reliability of SERS-based fiber sensors. Moreover, because the sensitivity is improved in PCFs, it allows detecting trace amount of analyte and thanks to the size of the fibers, the required filling volume is extremely small. In addition, the flexibility and versatility of PCFs allowed to implement PCFs in microfluidic devices and some interesting studies have demonstrated that SERS-based PCF sensors are not only limited to liquid biosensing. PCFs have been used to rapidly monitor the concentration of gases relevant in the detection of disease in human breath. Finally, SERS-based fiber sensors are not limited to biosensing. They can be employed in a much wider range of applications such as homeland security and industrial or environmental monitoring.

Based on the studies reported so far, we pointed out the main advantages and drawbacks of each class of PCFs. Direct interaction is possible with HC-PCFs, which avoids the collection of the parasitic signal from silica. For instance, the peaks used to detect adenosine [210] and leukemia cells [168] could not have been detected with an SC-PCF. Indeed, it might have been overshadowed by the silica signal inherent to the fiber core. However, due to the guiding mechanism, HC-PCFs suffer from rather small transmission windows. In addition, the change in refractive index results in a shift of the transmission window, which can in turn result in lower sensitivity. We illustrated this phenomenon with the study of heparin by Khetani *et al.* where they used a commercial fiber that possessed a transmission window between 717 and 808 nm to study Raman signals between 850 and 863 nm. A solution to avoid the shift of the transmission bandwidth consists of anchoring the analyte on the inner surface of the core and to dry the fiber subsequently [4,5]. However, this might require heating the fiber to evaporate the solvent, which can result in denaturing the analyte. In addition, the drop in the field distribution near the core surface forbid a proper excitation when the NPs and the analyte molecules are anchored on the core surface, which results in poorer sensitivity. Finally, it is important to note that the two studies cited here could not be realized easily in a clinical environment. Indeed, for more practicability, the nanotags should be anchored first inside the fiber and the target analyte should be injected last. In this way, the sensor would be ready to use. Clinicians would simply need to pump the solution containing the target analyte inside the PCF and measure the SERS signal for readout.

Several solutions can be used to overcome the small transmission windows inherent to HC-PCFs. The first one is to use HC-PCFs that possess wider bandwidths such as Kagome HC-PCFs. However, they exhibit higher transmission loss compared to usual HC-PCFs. Recently reported nodeless HC-PCFs represent another interesting solution [196,217,218]. In such fiber, the light is also guided thanks to the anti-resonant mechanism. They exhibit relatively low transmission attenuation (record below1 dB/km), broad transmission bandwidths (440-1200 nm), low bending-loss (0.2 dB/m) and single-mode profile. Thanks to the size of the core (superior to 30 µm), they would also allow fast analyte incorporation. Despite these promising properties, no study of SERS sensing with such design has been reported. Another solution could be to selectively fill the core of a HC-PCF to obtain a LC-PCF and TIR guidance. In their study of the impact of the NPs coverage density and fiber length on the SERS intensity (Figure 27), Han *et al.* managed to measure the signal up to 4000 cm^{-1} (Stokes wavelength ~845 nm for excitation at 633 nm) by selectively filling the core of the HC-PCF. Using a similar configuration, Zhang

et al. obtained an EF of ~100 by selectively filling a HC-PCF with a solution of Ag NPs and R6G [219]. The last option to benefit from large transmission windows is to use SC-PCFs. Gong *et al*. demonstrated that SiC-PCF can exhibit better sensitivity compared to HC-PCF [12]. This difference in sensitivity was due to a difference of guiding mechanism that resulted in a more confined light in the case of SiC-PCF.

At this point, it is worth taking a step back to observe the full picture. The ultimate goal of this thesis is to fabricate a fiber sensor that can one day be used on a daily basis in a clinical environment. This creates some additional requirements. For instance, one of the envisioned possibilities is to create a functionalized biopsy needle with a PCF immobilized inside it. In this way, the clinician would only have to collect a sample from the patient body and put the needle under the microscope for readout. It is then obvious that the length of the fiber would be limited in this configuration: it could not exceed the length of the biopsy needle, which has an impact on the NPs coverage density.

Another important requirement that arises from the necessity to create a sensor clinically viable lies in the SERS-activation technique. Indeed, from a practical standpoint, the injected configuration is not well suited to create clinically viable biosensors. If we imagine that a clinician uses a PCF sensor, he would need to mix the fluid withdrawn from the patient with the colloidal solution of NPs and inject the mixture in the fiber prior to the measurement. This is not very convenient, and clinicians would not be interested in such sensors. The ideal solution consists of an already-functionalized fiber inside a biopsy needle, the clinician would only need to withdraw the fluid from the patient and measure the SERS response immediately. Unfortunately, to this day there is no clear direction regarding which configuration (injected or anchored) gives the most sensitive and reliable sensor.

The current procedures for clinical sensing are quite tedious. Usually, they consist of sampling from the clinician, often with a biopsy needle, followed by a test under the respective method. The concept of functionalized biopsy needle would deeply accelerate the procedure, since the collection and readout of the results could be realized with the same platform. The last advantage of the anchored protocol is that it can be used to target specific biomarkers in complex body fluids in order to look for specific diseases. We can imagine anchoring antibodies of a targeted biomarker. When the body fluid passes in the fiber during the sampling, the target molecules can bind to the anchored antibodies so that they are immobilized onto the fiber walls. Although this technique is interesting, it would require the incorporation of Raman tag for the readout, which requires an additional preparation step.

Based on all these observations, we decided to focus our work on SC-PCFs. Indeed, they benefit from large and fix transmission bandwidths, which facilitates the selection of the fiber to fit the excitation and Raman signal. However, despite all the studies conducted so far, some interrogations remain. The first one concerns the ideal core size that would give the most sensitive and reliable sensor. Indeed, high sensitivity was obtained with fiber that featured both extremely small and extremely large core diameters. In addition, several studies tried to determine the fiber length that resulted in the strongest SERS intensity possible. It was demonstrated that this length depends on the NPs coverage density inside the fiber and thus, it should be adapted in every case. When it comes to NPs, no clear direction is mentioned regarding the choice of the configuration (anchored or injected) to achieve the most sensitive and reliable probe. Finally, the last interrogation concerns the reliability of SERS-based fiber sensors. Indeed, almost no study focused on their reliability, although this property is of utmost importance to fabricate clinically viable sensors. Furthermore, it is worth mentioning that most of the work reported so far was conducted with commercial or standard PCFs that are not specifically designed for SERS sensing (except for the SiC-PCF). During my PhD, I had the opportunity to conceive and fabricate fibers that are specifically designed for SERS biosensing. For that, we needed to clearly understand the effect of each fiber parameter on the final SERS response of the probe. The SERS intensity depends on the interplay between the area of light/analyte interaction, the size of the surface that collects the Raman

photons, the transmission losses and the coupling efficiency. Finding the best compromise between all these parameters would result in improving the detection abilities as well as the reliability of SERS-based fiber sensors. With this in mind, we first decided to optimize the parameters of SuC-PCFs. Indeed, they benefit from the large transmission bandwidth of SC-PCF, while facilitating the incorporation of the analyte thanks to the large holes in the cladding. In addition, the fraction of evanescent field overlapping in the cladding can be precisely tailored by changing the core size. In the following chapter, we present our work done on SuC-PCF to find the best compromise between all the parameters inherent to the fiber and to SERS sensing. The aim was to improve the sensitivity, and the reliability of SERS-based SuC-PCF probes with respect to the requirements created by the necessity to conceive a clinically viable sensor. In a second time, we created a totally novel PCF topology to further improve the sensitivity of fiber-based SERS sensors and to tailor even more precisely their response.

Chapter III. From basic simulation to detection of ovarian cancer biomarker with a SuC-PCF probe

Chapter III. From basic simulation to detection of ovarian cancer biomarker with a SuC-PCF probe

We discussed in Chapter I and Chapter II the general principles used for fiber-based SERS sensing. In the following chapter, we focus our work on SuC-PCFs, from simulations to SERS measurements while always keeping in mind our final goal to create a clinically relevant biosensor. The goal of this chapter is to obtain a SuC-PCF sensor that exhibits the best compromise between sensitivity and reliability. Unfortunately, the studies conducted so far do not allow determining precisely which core size and which fiber length is the best suited to achieve the best SERS response. For example, Oo *et al.* achieved the best sensitivity using a SuC-PCF with the smallest core diameter [201]. On the contrary, Chen *et al.* showed that SC-PCFs with very large core can support a higher coverage density of NPs, which results in a relatively good sensitivity [220]. In the same vein, Afshar *et al.* showed that the strongest fluorescence signal was not obtained with the fiber that possesses the smallest core size [221]. Although this result was obtained in fluorescence sensing and it did not take into account the effect of the NPs, it remains inspiring. Based on these observations, we first present more precisely through simulations the effect of the fiber parameters on the SERS sensitivity and reliability. Then, we describe the existing protocol developed at SBIC to anchor the NP inside the PCF in order to make the fibers SERS-active and we present its limitations. We also present the solutions implemented to overcome these limitations and improve the anchoring protocol. In addition, we also compare the two most used techniques to prepare SERS-based PCFs in order to have a clear idea of which technique should be used preferably. We also compare SuC-PCFs with different core size to experimentally ascertain the results presented in the simulation section. Finally, we demonstrate the relevance of our sensors during a clinical study. We prepared the best SuC-PCF using the best functionalization technique and we tried to detect a biomarker in clinical cyst fluid withdrawn from patients during surgery. Based on that, we succeeded in differentiating the stage of ovarian cancer in several patients. This last step represents an extremely promising proof that eventually SERS-based fiber probes could be used routinely to facilitate the early detection of severe diseases or help clinicians to monitor the response to a treatment as well as the success of surgery.

III.1. Determination of the optimum suspended core PCF parameters for SERS

III.1.1. Simulation

We first simulated the most basic situation: a silica rod surrounded by water. A simple model developed by Chen *et al.* allowed us to understand better the effect of the fiber parameters and the coverage density on the SERS signal. Then, we simulated the coupling efficiency of the laser into the core of a SuC-PCF. This is useful to understand how the excitation light can be coupled to the fiber core but also how the Raman signal emitted at the end of a SuC-PCF can be collected by the spectrometer. Indeed, for all the measurements presented below, we used backscattering configuration, i.e. the excitation laser was coupled to the fiber from a microscope objective and the Raman signal was collected from the same fiber end with the same objective. This geometry is presented in the following of this chapter, and an illustration is available in Figure 52. Thus, the coupling efficiency from the laser to the fiber core can also be assimilated to the coupling efficiency of the fiber to the Raman spectrometer. This simulation allowed determining the core size that results in the best reliability for SuC-PCF sensors.

III.1.1.1. Basic model used to approximate the final Raman intensity given by a suspended core PCF

Chen *et al.* [220] developed a simplified model to provide an insight on the interplay between the Raman gain and the loss inherent to the NPs discussed in chapter 2. This model takes into account the fiber features, i.e. its core size and its length, the coverage density of NPs and it is designed for setups that use forward propagation. The model proposed here aims to evaluate relatively the performances of SC-PCFs for SERS sensing by allowing to study the effect of a fiber parameter on the SERS response. For that, they considered the case of a rod suspended in water. To calculate the attenuation loss occurring when the evanescent field interacts with NPs, they introduced an effective layer between the core of the fiber and the surrounding media, i.e. the silica rod and water respectively. This effective layer is made of a composite material that represents the real layer where the NPs are anchored onto the fiber core. It consists of spherical inclusions of metal (NPs) inside a volume of water with a filling factor $f = V_{met}/V_{total}$, which is the volume of metallic inclusions per unit volume of the composite material. To express V_{met}, we first need to know the number of NPs present in the effective layer. To do so, we express S, the surface of the effective layer over the fiber length (L_{fiber}).

$$S = 2\pi R_{fiber} \times L_{fiber} \tag{20}$$

with R_{fiber} the radius of the fiber core. Then, the number of NPs (N) is the product of the coverage density (CD) with the surface:

$$N = S \times CD \tag{21}$$

Finally, the volume occupied by the NPs is the volume of one NP multiplied by the number of NPs:

$$V_{met} = \frac{4}{3}\,\pi \times \mathrm{R}_{\mathrm{NP}}^{3} \times N = \frac{8}{3}\pi^{2} \times R_{fiber} \times CD \times R_{NP}^{3} \times L_{fiber} \tag{22}$$

with R_{NP} the radius of one NP.

The total volume of the effective layer over the fiber length is defined by:

$$V_{total} = \pi \times \left[\left(R_{fiber} + 2R_{NP}\right)^{2} - R_{fiber}^{2}\right] \times L_{fiber} \tag{23}$$

Finally:

$$f = \frac{V_{met}}{V_{total}} = \frac{8\pi \times R_{fiber} \times CD \times R_{NP}^{3}}{3 \times \left[\left(R_{fiber} + 2R_{NP}\right)^{2} - R_{fiber}^{2}\right]} \tag{24}$$

This filling factor allows calculating the effective dielectric constant of the composite material given by [222]:

$$\epsilon_{\mathrm{eff}}(\lambda) = \epsilon_{h}(\lambda)\frac{\epsilon_{i}(\lambda) + 2\epsilon_{h}(\lambda) + 2f[\epsilon_{i}(\lambda) - \epsilon_{h}(\lambda)]}{\epsilon_{i}(\lambda) + 2\epsilon_{h}(\lambda) - f[\epsilon_{i}(\lambda) - \epsilon_{h}(\lambda)]} \tag{25}$$

with $\epsilon_{i}(\lambda)$ and $\epsilon_{h}(\lambda)$ the complex electric permittivities of the metal and the dielectric host (water) respectively.

The design with the effective layer used for the simulation is presented in Figure 40. Using the different parameters presented previously and finite element method (FEM), the imaginary effective indexes and

the portion of the evanescent field per mode are calculated. This allows calculating the modal attenuation coefficients at the excitation and detection wavelengths α_{exc} and α_{det}. Here, the subscript "exc" refers to the wavelength of the laser used to excite the analyte, while "det" refers to the wavelength of the Stoke scattered photons.

$$\alpha = \frac{4\pi}{\lambda\, Im[n_{eff}]} \tag{26}$$

From there, they approximated the factor proportional to the Raman intensity (f_{RI}) with the following formula:

$$f_{RI} \approx 2\pi R_{fiber} L_{fiber} CD \times \left[\eta_{exc} \frac{1 - e^{-\alpha_{exc} L_{fiber}}}{\alpha_{exc} L_{fiber}}\right] \times \left[\eta_{det} \frac{1 - e^{-\alpha_{det} L_{fiber}}}{\alpha_{det} L_{fiber}}\right] \tag{27}$$

The left term represents the total NPs coverage density over the entire surface of the fiber. By integrating the fiber particle coverage length, they averaged the power decay of the propagating fiber mode caused by the absorption in particles. This is possible only by assuming that CD is constant over the entire length of the fiber. The two right terms express the average excitation intensity and the average SERS signal decay respectively. η_{exc} and η_{det} represent the modal fractional power overlapping in the effective layer. These two terms introduce the evanescent coupling of the excitation signal inside the fiber holes, and the recoupling efficiency of the SERS signal inside the core. As highlighted previously, this model aims to simply provide an insight of the SERS sensing abilities of an SC-PCF. Thus, since the properties of the fiber are slowly evolving between the detection and Stoke signals, we make the following approximation: $\lambda \approx \lambda_{exc} \approx \lambda_{det}$. Hence, equation 27 becomes:

$$f_{RI} \approx 2\pi R_{fiber} L_{fiber} CD \times \left[\eta \frac{1 - e^{-\alpha L_{fiber}}}{\alpha L_{fiber}}\right]^2 \tag{28}$$

It is worth mentioning here that, although the properties of the fiber are close at λ_{exc} and λ_{det}, this is not necessarily true for the plasmonic response of the sensor, as shown in Figure 50.

If we wanted to simulate the most realistic case possible, we should have simulated the design represented in Figure 40(a), which corresponds to the real design of a SuC-PCF with an effective layer. Instead, we simulated the design represented in Figure 40(b), which corresponds to a silica rod surrounded by the effective layer and suspended in water. Although this design is not exactly the same as SuC-PCFs, it represents an ideal case, where no light is guided inside the silica struts that holds the fiber core. Except for that, the behavior of the light in silica rods is very much similar to the behavior of the light in the core of SuC-PCFs. Therefore, since our goal is to understand the relative effects of the core size, the fiber length and the NPs coverage density on the SERS intensity, the case of a simple rod in water is very well adapted. It is much simpler to simulate while giving the same insight as the full design. In the following, when we talk about fiber length and core size, it is in reality the length and the diameter of the rod but since the results are similar between the two designs, we use the fiber terminology.

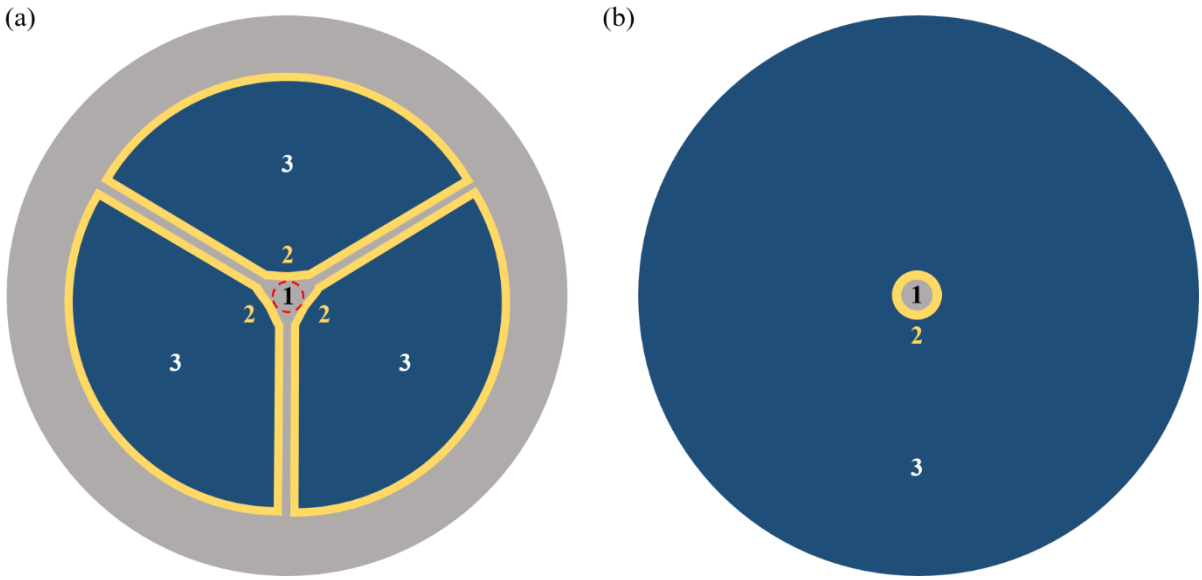

Figure 40 (a) Design of the SuC-PCF that should have been used in the simulation to fit more closely to real fibers. (b) Schematic of the ideal case of a silica rod surrounded by the effective layer and immersed in water. This design was used in the simulation to approximate the design of the SuC-PCFs. 1 represents the silica core (gray), 2 represents the effective layer (yellow) and 3 represents water (blue). The dashed circle in (a) represents the core simulated in (b).

As mentioned in the introduction to this chapter, the studies reported so far do not allow finding the fiber features to achieve the best compromise between sensitivity and reliability. Therefore, we simulated rods with different diameters and compared the percentage of light leaking in the effective and water layers. This allowed us to illustrate the effect of the core size on the amount of evanescent field that could overlap in the cladding. This is important because the evanescent field is the amount of light that can interact with the analyte. If we do not take into account the NPs, the more light interact with the analyte, the strongest the Raman intensity is. However, if too much light overlaps in the cladding, the transmission loss will become too great resulting in a smaller interaction length and thus a poorer sensitivity. Therefore, a compromise on the core size must be found to create a fiber that possesses a relatively strong evanescent field to interact with the analyte but not too strong, so the light can be guided for relatively long length. Now, if we consider the same case with NPs, the basic reasoning is similar: a compromise has to be found in the core size. The difference is that NPs simultaneously enhance the signal and increase the transmission loss due to their absorption and scattering loss, which tend to complicate the reasoning. This is further complicated by the addition of the coupling efficiency that determines the amount of light coupled to the fiber core. Logically, the core size also has a direct impact on the coupling efficiency. To facilitate the understanding, this matter will be discussed further in this manuscript, and here, we focus on the impact of the core size on the evanescent field. For this study, we used the following parameters:

Excitation wavelength and detection wavelength: $\lambda = 633\ nm$

We used gold NPs with a coverage density: $CD = 0.05\ particle/\mu m^2$

Fiber length: $L_{fiber} = 10\ cm$

Radius of Au NPs: $R_{NP} = 30\ nm$

Thickness of the water layer: 10 µm

Relative permittivity of water from Hale and Querry at 633 nm [223]: $\epsilon_h = 1.7734 + 3.9151 \times 10^{-8} i$

Relative permittivity of gold from Rakić *et al.* at 633 nm [224]: $\epsilon_i = -10.577 + 1.2741i$

Refractive index of silica calculated using Sellmeier equation: $n_{silica} = 1.457$ at 633 nm

The results are available in Table 1, and a representation of the simulated fundamental mode is available in Figure 41.

Table 1 Percentage of light in each layer of four SuC-PCFs with different core sizes.

Diameter of the fiber core	Percentage of HE_{11} mode intensity in the core	Percentage of HE_{11} mode intensity in the effective layer	Percentage of HE_{11} mode intensity in the water layer
1 µm	89.05%	4.63%	6.32%
1.5 µm	96.13%	1.80%	2.07%
3.5 µm	99.96%	0.02%	0.02%
10 µm	99.98%	0.01%	0.01%

Here, we clearly see the impact of the core size. For a core diameter of 1 µm, about 11% of the intensity propagated in the fundamental mode (HE_{11}) overlaps in the cladding and 5% of this light will be in the effective layer and will be responsible for most of the SERS intensity. Increasing the rod diameter to only 1.5 µm leads to a consequent drop in the evanescent field amount, since only 4% of the HE_{11} mode overlaps in the cladding and only 1.80% are situated in the active area. For a core diameter of 3.5 µm, less than 1% of the intensity propagated in HE_{11} mode overlaps in the cladding and further increasing the core size tends to increase further the amount of light confined inside the core.

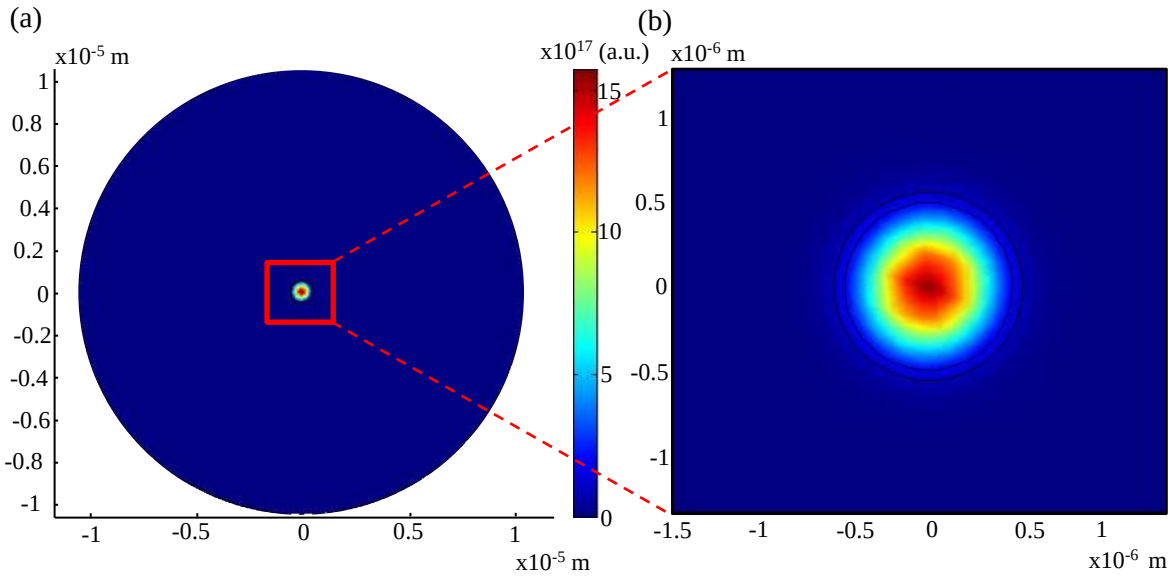

Figure 41 (a) Fundamental mode simulated for a 1 µm rod surrounded by the effective layer and water. (b) Zoom in the core area: the core, the effective layer and the beginning of the water layer are visible. The color scale is applicable for (a) and (b).

Now that we saw the impact of the core size on the amount of evanescent field, we could study its impact on the SERS response. For that, we calculated the factor proportional to the SERS intensity (f_{RI}) for core radii ranging from 0.2 to 8 µm using equation 28. It was necessary to fix the coverage density and the fiber length so we fixed: $CD = 0.05\ particle/\mu m^2$ and $L_{fiber} = 10\ cm$. The results of the simulation are plotted in Figure 42. For these specific values of coverage density and fiber length, the highest f_{RI} occurs for ~1 µm core SuC-PCFs and decreases rapidly as the core radius increases. This means that in this specific case, the factor proportional to the SERS intensity is increased with the

evanescent field, i.e. the losses due to the NPs are smaller than the EF (for core radius superior to 0.5 µm).

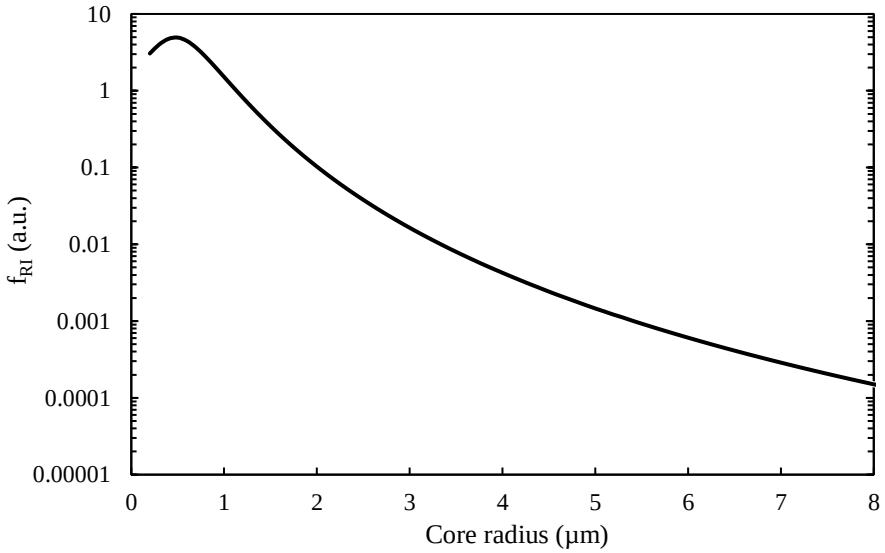

Figure 42 Variations of the calculated f_{RI} with the core radius for 10 cm long SuC-PCFs covered with 0.05 $NPs/\mu m^2$

Subsequently, we realized the same simulation with varying NPs coverage densities. The results are plotted in Figure 43. If we focus on the red curve ($CD = 0.01\, particle/\mu m^2$), we can see that the strongest f_{RI} is achieved with fiber with even smaller cores, compared to the previous case, i.e. $CD = 0.05\, particle/\mu m^2$. However, increasing CD leads to the opposite effect.

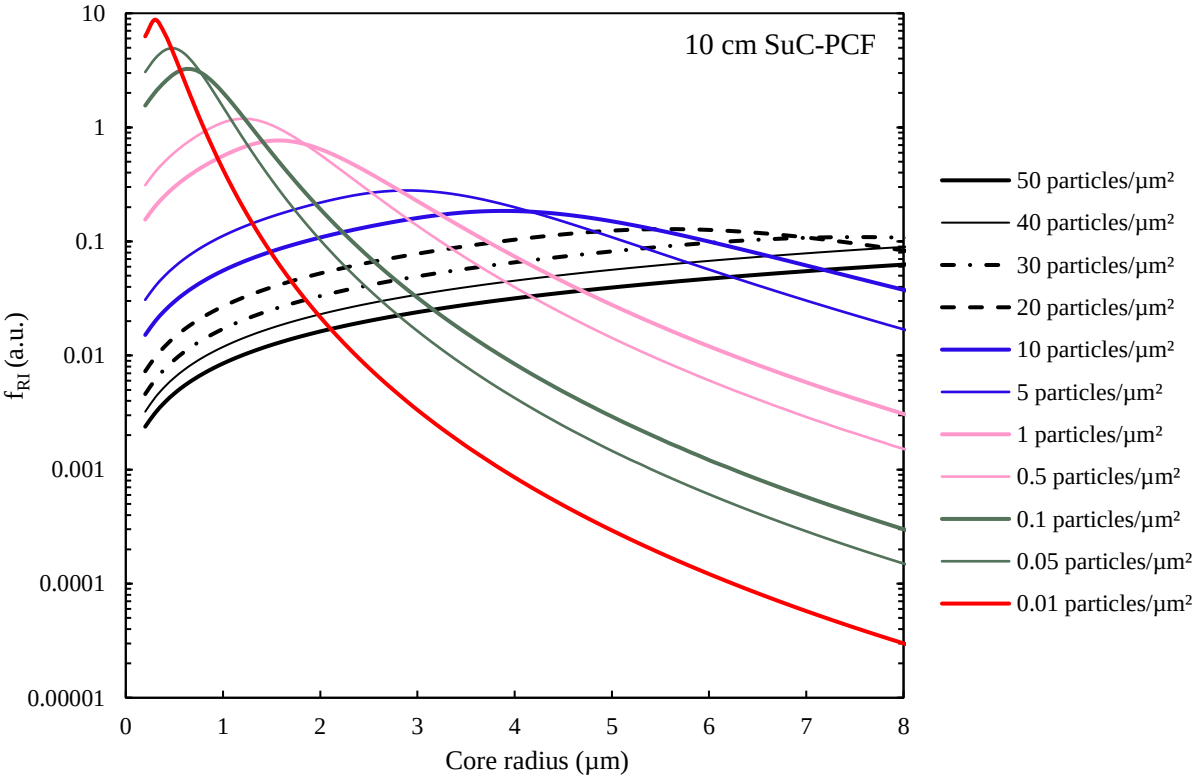

Figure 43 Variations of the calculated f_{RI} with the core radius for 10 cm long SuC-PCFs and different NPs coverage densities.

For $CD = 50\ particles/\ \mu m^2$, the maximum f_{RI} is not yet reached for SuC-PCFs with a core radius of 8 µm. In this case, the losses due to the NPs are greater than their EF and in order to reach the maximum f_{RI}, the amount of evanescent field needs to decrease sufficiently so that less light would be absorbed by the NPs along the fiber length. It is also worth noting that the absolute maximum f_{RI} between all coverage densities occurs for rather small values of CD. This is quite logic since for small values of CD, a larger portion of light can interact with the NPs and the analyte along the fiber length without suffering from extinction losses. This illustrates perfectly the inevitable compromise between the amount of evanescent field (and thus the core size) and the coverage density in order to achieve the highest SERS intensity possible.

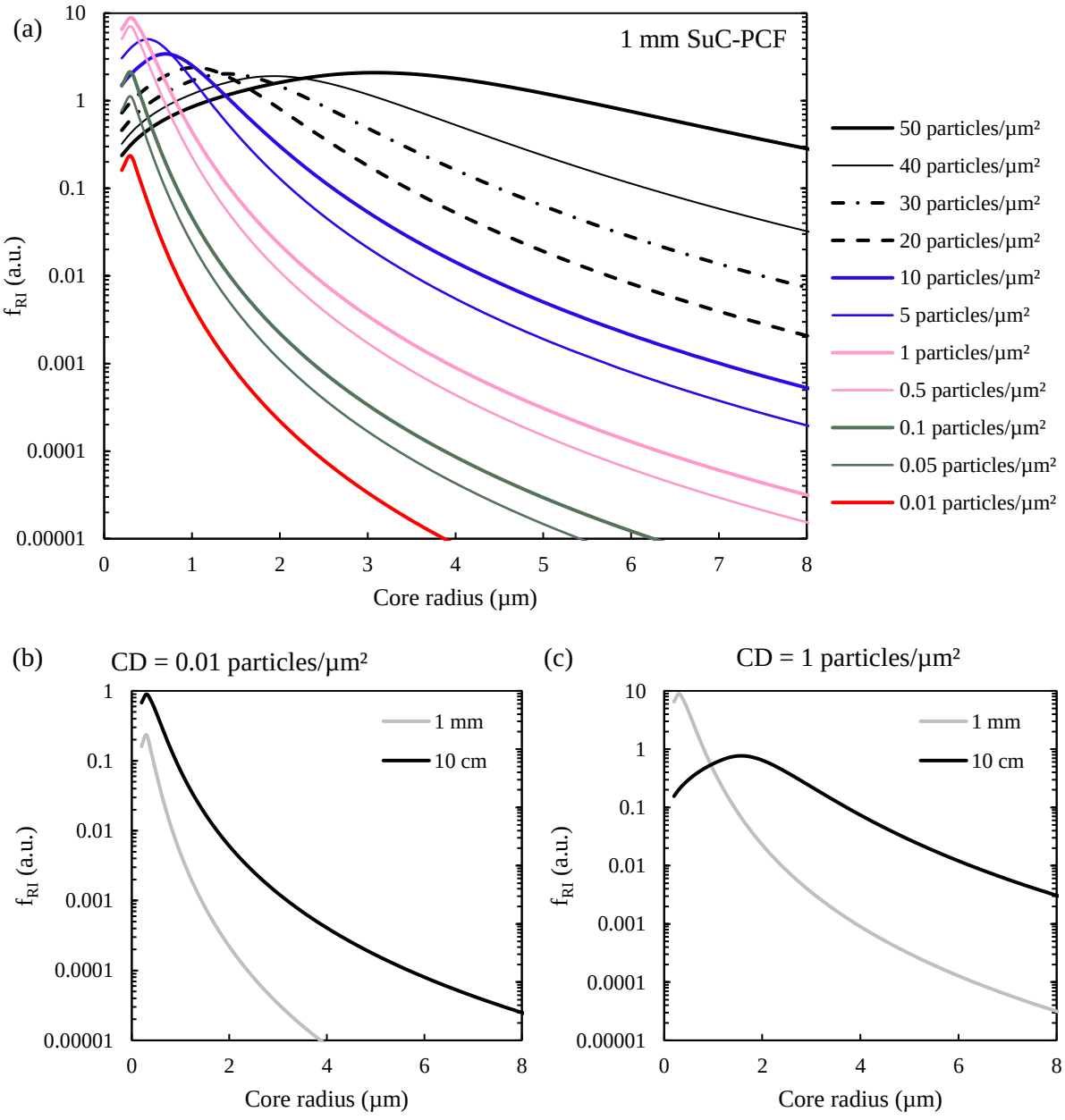

Figure 44 (a) Variation of the calculated f_{RI} with the core radius for 1 mm long SuC-PCFs and different NPs coverage densities. Comparison of the calculated f_{RI} for 1 mm and 10 cm SuC-PCFs for (b) $CD = 0.01\ particle/\mu m^2$ and (c) $CD = 1\ particle/\mu m^2$.

Until now, L_{fiber} remained constant (10 cm). If we decrease the fiber length to 1 mm, a new trend appears as shown in Figure 44(a). The lowest values of CD no longer exhibit the absolute maximum f_{RI}. It now occurs at $CD = 1\ particle/\mu m^2$ compared to $CD = 0.01\ particle/\mu m^2$ previously. Once again, this behavior is perfectly logic. If we consider the curve for $CD = 0.01\ particle/\mu m^2$, the maximum is lower than the maximum obtained for 10 cm fibers (Figure 44(b)). Indeed, we showed that for this coverage density, the EF was greater than the losses. Because the fiber is much shorter, the light can interact with fewer NPs and thus the resulting SERS signal is less intense. Now if we consider the curve for $CD = 1\ particle/\mu m^2$, we note that the maximum is more important and occurs for smaller cores than for 10 cm fibers (Figure 44(c)). Indeed, because the fiber is shorter, it can handle a higher coverage density before the losses become greater than the EF. We could say that the portion of the NPs that should have been encountered during the propagation of the light if the fiber had been longer can be anchored on the 1 mm fiber to increase thef_{RI}. Here, we consider only the number of NPs that increases the SERS signal and not supplementary NPs that increase mostly the losses.

To summarize, thanks to this simulation model we are able to say that three parameters influence greatly the final Raman intensity: the fiber length, the core size and the NPs coverage density. In order to obtain the best SERS intensity possible using PCFs, we should fix one of the parameters and find a compromise between the remaining two. In our case, we fixed the fiber length to ~10 cm. Indeed, keeping in mind that we want to realize biosensors that can be used in a clinical environment, fibers too long would not be practical. However, we can very well imagine that 10 cm long PCF immobilized inside biopsy needles could serve as a two-in-one sensor for both the sample collection and sensing. These simulations aim to show the complex interplay that exists between the fiber parameters and the coverage density. However, as we highlighted previously, the core size also has an impact on the coupling efficiency that in turn determine the amount of light in the fiber core. In the following section, we simulate the coupling efficiency of different core size SuC-PCFs in order to find out the best core size to exhibit good sensitivity and good reliability.

III.1.1.2. Simulation of the coupling efficiency between the laser and the fiber core

In this section, we want to highlight the importance of the core size in the coupling efficiency of the excitation light to the fiber core. We used finite element method (Comsol Multiphysics) to simulate the electromagnetic field distribution of the fundamental mode. The topologies of the SuC-PCFs simulated here are available in Figure 45(a) [225]. We used an excitation laser at 633 nm, which corresponds to one of the lasers available on our SERS measurement setup. The refractive indices used were 1.457 for the silica and 1.33 for the water in the holes. Once the distribution of the electromagnetic field was simulated, we computed the coupling efficiency of the light between the fiber and the Raman spectrometer by calculating the overlap integral of the electromagnetic field distributions of the fundamental mode with that of a Gaussian beam as described in [226,227]. The Gaussian beam represents the laser source. In order to model it, we simulated a silica rod surrounded by air, since the fundamental mode guided by such structure is a Gaussian beam. We define the radius of the silica rod so that the dimensions of the simulated beam are similar to the dimensions of the laser beam of the SERS setup used to do all our experiments in the following. In our Raman setup, the laser beam was measured to be 1.05 µm when using a 50x objective lens. The refractive index was also 1.457 for the silica rod and 1 for the air surrounding it. Here, it is worth mentioning that Fresnel's reflections are not included in the simulation.

Now that we have the electromagnetic field distribution of the source and the distribution of the fundamental mode, we can calculate the normalized amplitude coupling coefficient C_m. The definition

of C_m is based on the continuity of the transverse field components across the cross-section of the fibers between the incident beam and the excited fiber modes [227]:

$$C_m = \frac{1}{4} \times \frac{A}{\sqrt{B} \times \sqrt{C}} \tag{29}$$

With:

$$A = \int \left(E^*_{x\,In}(x,y) \times H_y(x,y) - E^*_{y\,In}(x,y) \times H_x(x,y) + E_x(x,y) \times H^*_{y\,In}(x,y) - E_y(x,y) \times H^*_{x\,In}(x,y) \right) dxdy \tag{30}$$

$$B = \frac{1}{2} \int Re \left(E_{x\,In}(x,y) \times H^*_{y\,In}(x,y) - E_{y\,In}(x,y) \times H^*_{x\,In}(x,y) \right) dxdy \tag{31}$$

$$C = \frac{1}{2} \int Re \left(E_x(x,y) \times H^*_y(x,y) - E_y(x,y) \times H^*_x(x,y) \right) dxdy \tag{32}$$

With $E_{x/y}$ and $H_{x/y}$ the x and y components of the electric and magnetic fields of the fundamental mode guided inside the fiber. $E_{x/y\,In}$ and $H_{x/y\,In}$ represent the x and y components of the electric and magnetic fields of the laser Gaussian beam.

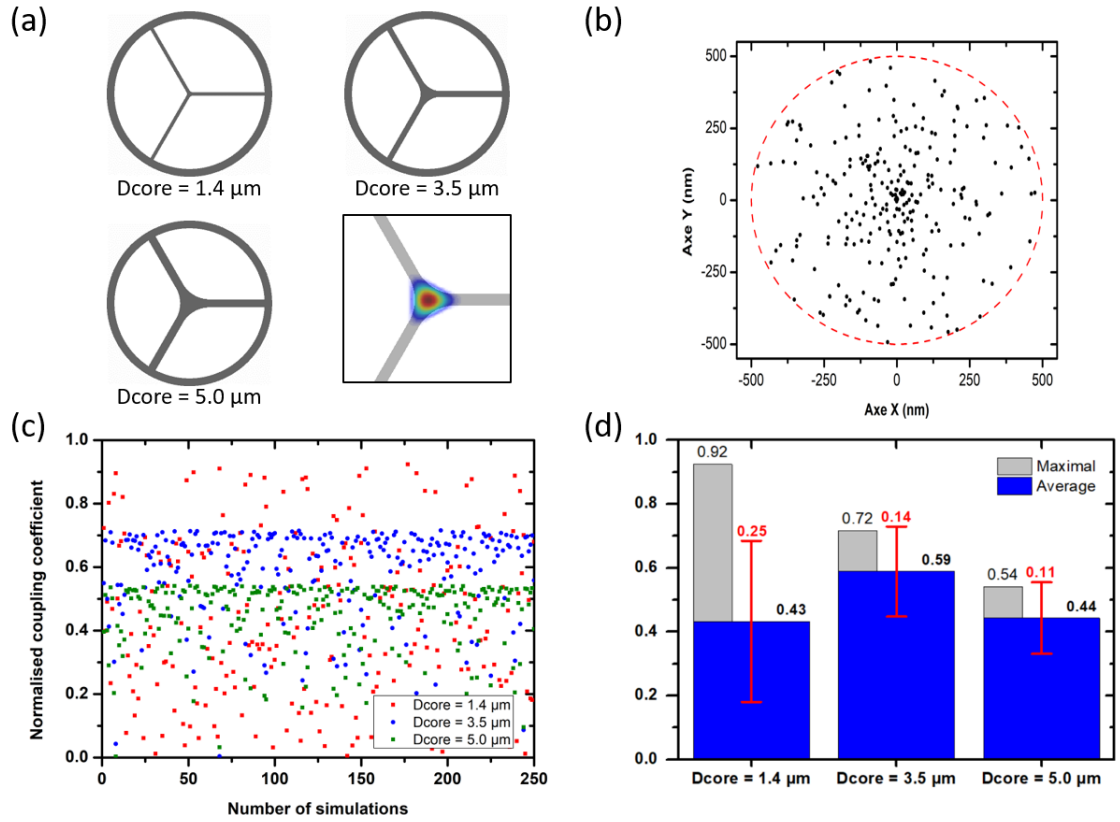

Figure 45 (a) Design of the simulated SuC-PCFs with different core sizes, and zoom-in on the 2D distribution of the Poynting vector of the fundamental mode propagated in a core diameter of 3.5 µm (superimposed in light gray). (b) Distribution of the center of a Gaussian beam (corresponding to the laser beam from the Raman spectrometer) randomly positioned (250 times) within an area limited by a circle of 0.5 µm radius around the center of the fiber. (c) Normalized coupling coefficients between the Gaussian beam (following the positions in, (b)) and the fundamental mode of SuC-PCFs with different core sizes. (d) Calculated maximum and average coupling coefficient values from the values plotted in, (c). SD in average coupling coefficient is denoted with red lines (reproduced from [225].

Finally, the center of the Gaussian beam was randomly positioned 250 times within a disk of 0.5 µm radius centered on the fiber core. This was used to simulate the possible misalignments occurring during measurements. Indeed, even by being extremely careful, the laser beam almost never enters the SuC-PCF exactly in the middle of the core, resulting in increased coupling losses. This calculation was made to take into account the operability of the fibers. For that, we simulated three SuC-PCFs with different core sizes: 1.4 µm, 3.5 µm and 5 µm in order to study the impact of the core size on the coupling efficiency. The Gaussian beam used as excitation remained constant for the three cases. On Figure 45(d), we can see that the 1.4 µm core fiber exhibits the highest coupling coefficient when the light enters the core close to the center. However, by coupling the light slightly off-center, the coupling efficiency drastically decreases. The 3.5 µm core SuC-PCF exhibits a lower maximal coupling coefficient (0.72 instead of 0.92 for the first fiber) but a much higher average coupling coefficient (0.59 instead of 0.43). This demonstrates that misalignments have less effect on the 3.5 µm core fiber. Further increasing the core size does not improve the coupling efficiency. Indeed, for 5 µm core SuC-PCF, thought the deviations due to misalignments are smaller, the maximum coupling efficiency is further decreased (0.54), which results in a decrease in the average coupling efficiency.

In conclusion, we can say that to couple the light as efficiently as possible inside a SuC-PCF, an optimum core size exists. On the one hand, if the core is too big, the variations due to misalignments are rather small but the maximum coupling efficiency is very low and that decreases the average coupling efficiency. On the other hand, if the core is too small, the maximum coupling efficiency is excellent but the misalignments largely decrease the average coupling efficiency. Therefore, selecting a SuC-PCF with an intermediary core size helps to benefit from a relatively good maximum coupling efficiency while limiting the impact of the misalignments, which improves the reliability of the measures. Now that the simulations allowed us to understand better the behavior of SERS-based PCFs, we could fabricate the fibers.

III.1.2. Fabrication of the different fibers

Several SuC-PCF with different core sizes had already been fabricated before my arrival. However, we needed SuC-PCFs with smaller cores to increase the evanescent field overlapping in the holes. In addition, the cladding of the existing SuC-PCFs was already extremely thin, making them quite difficult to handle. They broke easily during cleaving or during SERS measurements. Therefore, to obtain SuC-PCFs with smaller cores and a cladding large enough to facilitate the handling, we needed to increase the size of the jacket tube at the preform step. By doing so, we were able to fabricate three fibers with core size ranging from 0.9 µm to 1.4µm with claddings large enough to facilitate the cleaving and the handling. For information, the previous SuC-PCFs had core sizes ranging from 2 µm to 3.5 µm.

In order to fabricate the SuC-PCFs, we used the stack-and-draw process, which is a widely used technique [228]. A schematic presenting the different steps is available in Figure 46. The first step consists of drawing capillaries from commercial silica tubes. Once drawn, three capillaries are stacked in a jacket tube in order to form the stack preform. It is then drawn to obtain the cane. Finally, the cane is put in another jacket tube and drawn into the fiber. It is worth noting that the fiber can be drawn directly from the stack preform. In our case, the cane step increases the reducing factor, which allows us to obtain SuC-PCFs with smaller cores. In addition, because we put the cane in a relatively thick jacket tube, the final thickness of the fiber cladding is also increased. This is relatively important since in order to increase the size of the holes and to decrease the core size, pressure is usually applied inside the three holes. As expected, the more pressure applied inside the holes, the bigger the holes are and the smaller the core becomes. Thus, to have small core SuC-PCFs (~1 µm), we need to apply a sufficient amount of pressure inside the holes, resulting in bigger holes and thinner cladding.

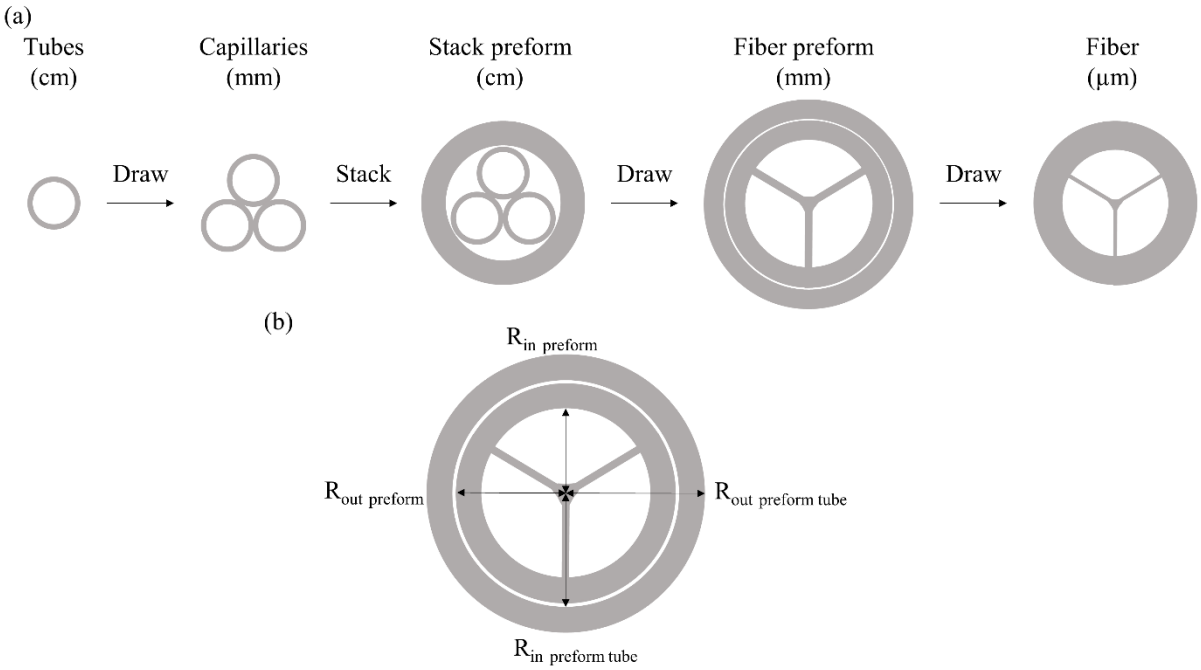

Figure 46 (a) Schematics of the different steps realized during the stack-and-draw process, in brackets is given the order of magnitude of the diameter. (b) Zoom-in on the preform step to define the parameters used in the calculation made to select the different tubes.

To select the jacket tubes for the cane and the preform, we needed to do some basic calculations. It is important to note that during the drawing, the ratio R_{in}/R_{out} remains constant for a given tube. Based on previous experiences, we wanted a final ratio $R_{in\ fiber}/R_{out\ fiber} = 1/4$ when we were not applying any pressure inside the holes, so that when we applied pressure, there would still be enough silica in the cladding. Based on that, we can say:

$$\frac{R_{in\ preform}}{R_{out\ preform\ tube}} = \frac{R_{in\ fiber}}{R_{out\ fiber}} = \frac{1}{4} \tag{33}$$

According to the tubes available, we fixed $R_{out\ preform\ tube} = 6\ mm$, which is the external radius of the jacket tube. Hence:

$$R_{in\ preform} = 1.5\ mm \tag{34}$$

The inner radius of the jacket tube is fixed and is $R_{in\ preform\ tube} = 2\ mm$, so we know the dimensions of the preform to use. Indeed, we found $R_{in\ preform} = 1.5\ mm$ and the preform has to fit in the jacket tube so $R_{out\ preform} = R_{in\ preform\ tube} = 2\ mm$ and we can determine the ratio of the preform:

$$\frac{R_{in\ preform}}{R_{out\ preform}} = \frac{1.5}{2} = 0.75 \tag{35}$$

This gives us the ratio of the jacket tube we need to use for the cane. The closest match at our disposal was a 7/10 mm tube, which possesses a ratio of 0.7.

Now that we know the size of the jacket tubes for the cane and the preform, we can select the tube for the capillaries. We used relatively thin tubes with an inner diameter of 19 mm and an outer diameter of 21 mm. The point of selecting thin tubes was to limit the quantity of silica at the intersection of the three capillaries during the following steps of the process in order to obtain the smallest core possible.

According to the stack layout and the 7/10 mm jacket tube selected for the cane, we drew the capillaries to 2.9 mm. Then, we closed the extremity of the three capillaries and prepared the stack. During the drawing, we applied vacuum between the capillaries and the jacket tube in order to facilitate the contact between them, as shown in Figure 47(a). Closing the capillaries helped in getting the structure. Indeed, the warm air coming out of the furnace ascended inside the tubes and was trapped at the end of the closed capillaries. This created a small overpressure that inflated slightly the holes. Once we drew the fiber preform, we put it inside the 2/6 mm jacket tube. Similarly to the cane step, we applied vacuum between the preform and the jacket tube but this time, instead of closing the top of the preform, we applied overpressure inside it, as schematized in Figure 47(b). This helped us in controlling more precisely the size of the holes and more importantly the size of the core of the final fiber. As mentioned previously, the more pressure we applied, the smaller the core was.

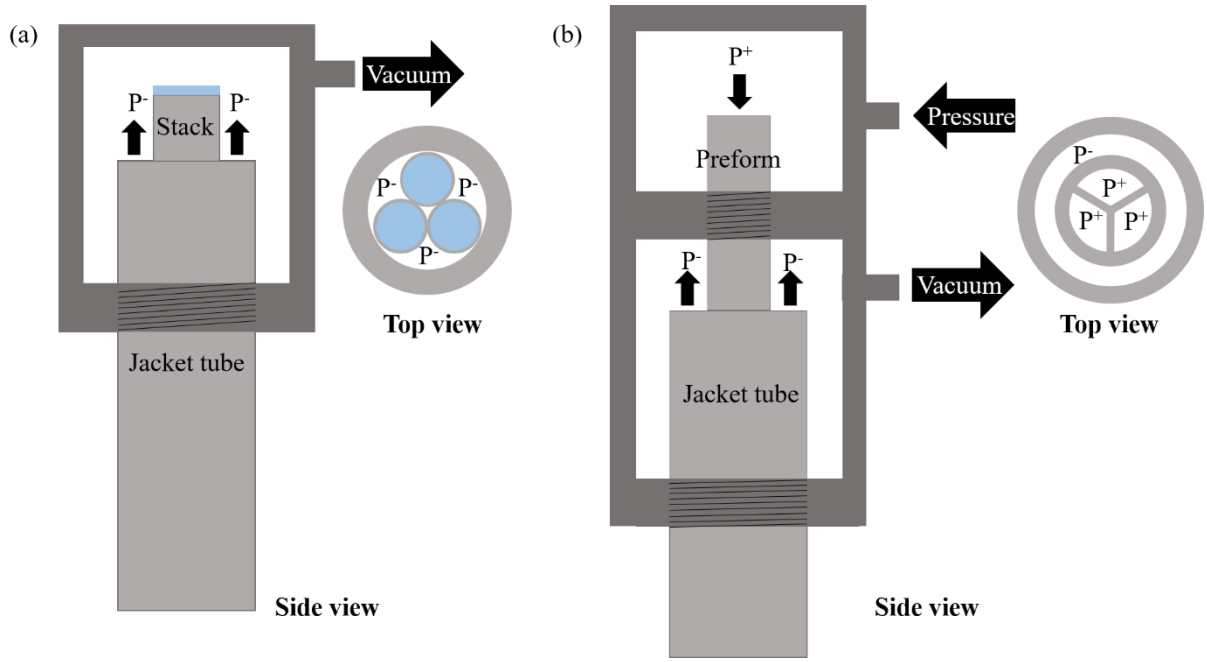

Figure 47 Schematics illustrating the pressurizing system used during the drawing of (a) the cane and (b) the preform. The blue sections represent the closed capillaries. Practically, we collapsed the end of the capillaries by torching them. P^- and P^+ represent respectively the vacuum and the overpressure applied in the different sections of the cane and preform.

The parameters of the different fibers drawn are available in Table 2 and SEM pictures are available in Figure 48. The first three fibers were drawn using the presented two intermediate steps to increase the thickness of the cladding. The 3.5 µm core SuC-PCF in Figure 48(d) was drawn before the beginning of my thesis using only one intermediate step, i.e. the fiber was drawn directly from the stack put in a jacket tube. It is worth noting that we succeeded in increasing the thickness of the cladding in order to facilitate the handling of the fibers. Indeed, the cladding of the first three SuC-PCFs (Figure 48(a), (b) and (c)), is approximately 2 to 3 times thicker than that of the fiber represented in figure (d).

Another aspect to note is the relation between the core size and the hole size described earlier. Indeed, we drew the first three fibers during a single session. The only difference was the pressure applied inside the holes and the drawing speed of the capstan. The difference in speed between the speed at which the preform descended into the furnace and the speed of the capstan allowed us to maintain the diameter of the fiber constant (+/- 1 µm). The outer diameter was not a requirement so it is not important if it is not exactly the same between each fiber. The only constraints were the size of the holes and the size of the core, which were controlled by the pressure inside the holes. The limitation for the size of the holes was

that they needed to be as big as possible, so an average-sized cell could pass inside them. This facilitates the incorporation of liquid inside them.

Table 2 Parameters of the fabricated SuC-PCFs measured with a SEM

Fiber	Core size (µm)	Struts thickness (µm)	Hole diameter (µm)	Cladding thickness (µm)	Outer diameter (µm)
Figure 48(a)	0.9	0.2	55.0	38.1	185
Figure 48(b)	1.1	0.3	45.6	40.2	175
Figure 48(c)	1.4	0.5	38.7	58.7	195
Figure 48(d)	3.5	1	84	20	204

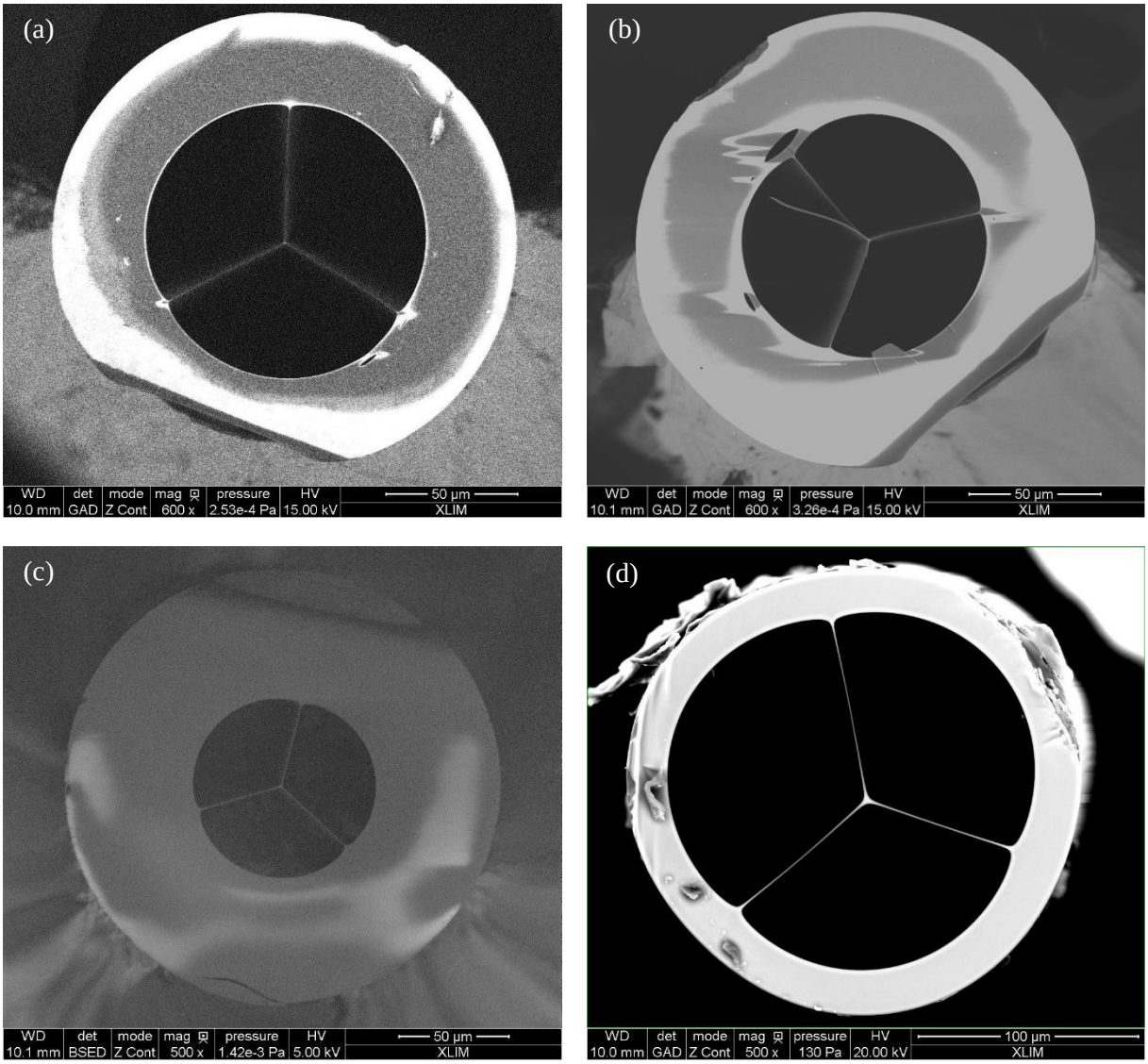

Figure 48 SEM pictures of fabricated SuC-PCFs with different core sizes. (a) 0.9 µm. (b) 1.1 µm. (c) 1.4 µm and (d) 3.5 µm.

In order to estimate the coupling and transmission losses of one of the SuC-PCF, we measured the power at the output of a 40x microscope objective lens (location 1 in Figure 49). Subsequently, we placed the fiber so that its core was situated in the focal point of the objective lens and we measured the power at the output of the fiber (location 2 in Figure 49). With this technique, the coupling and transmission losses were found to be ~0.9 dB for a 3.5 µm core SuC-PCF. This value was very low and illustrated perfectly the notions seen in chapter II and the interest of fibers for SERS sensing.

Figure 49 Schematic illustrating the locations where the power was measured to determine the coupling loss of a SuC-PCF.

III.2. Optimization of the anchoring protocol

Once the fibers were fabricated, we needed to make them SERS-active. To do so, we decided to anchor the Au NPs, as this configuration is more adapted for a use in a clinical environment. Indeed, it limits the steps were the fibers need to be handled by the user, which is preferable since clinicians are not necessarily familiar with optical fibers. Here, we used a specially designed protocol to anchor Au NPs inside the SuC-PCFs holes.

III.2.1. Presentation of the first developed protocol

III.2.1.1. Anchoring protocol

We saw in chapter II that the NPs responsible for the SERS enhancement can either be injected or anchored onto the wall of the fibers. Here, we present the first protocol developed by the team in SBIC to anchor the NPs inside the fibers. We decided to use 60 nm gold nanospheres from BBI Solutions (2.6×10^{10} particles/mL). Even though nanospheres do not exhibit the strongest SERS enhancement, due to their lack of sharp edges (hotspots), their fabrication is more easily controlled making them much more reliable than nanorods or nanostars. In addition, as previously mentioned, the biocompatibility of gold is better than that of silver. By simulating Mie theory with 60 nm gold nanosphere, it can be shown that the maximum of the absorbance occurs around 550 nm for a single Au NP surrounded on one side by glass and on the other sides by water. In the following, all the SERS measurements were realized using excitation lasers at 633 nm and 785 nm, which are quite far from the LSPR maximum. However, when NPs are close to one another, the interaction occurring between them shifts the LSPR maximum towards longer wavelengths. This results in the shift of the maximum EF also towards longer wavelengths as shown in Figure 50 for a gold nanospheres dimer [19]. Experimentally, when we compared the Raman signal obtained with and without NPs inside the fiber, the signal was increased by many folds when the NPs were present illustrating further the relevance of selecting gold nanospheres. To benefit from the best enhancement possible, the selection of NP is currently under investigations. Different shapes, materials and sizes of the NPs are being tested with SuC-PCFs to find the combination that gives the strongest and more reproducible SERS-based fiber probe.

That being said, we explained previously that we anchored chemically the NPs inside the SuC-PCFs. To do so we used (3-Aminopropyl)triethoxysilane (APTES) as the silane agent that allows for the Au NPs to be chemically attached to the silica surface of the fiber. A representation of the molecule is available in Figure 51(a). The silane group serves as an anchor for the APTES onto silica while the amine group binds to the NPs, as illustrated in Figure 51(b). Here, we only show one configuration in which APTES and Au NPs can bind to the silica. The other possibilities are presented in [109]. To inject the different solutions required for the anchoring of the NPs, we glued the fibers inside a needle, so we

just needed to connect the fiber/needle to a syringe containing the solution and to place the whole assembly on a syringe pump to dispense the liquids inside the fiber holes. A schematic is given in Figure 51(c).

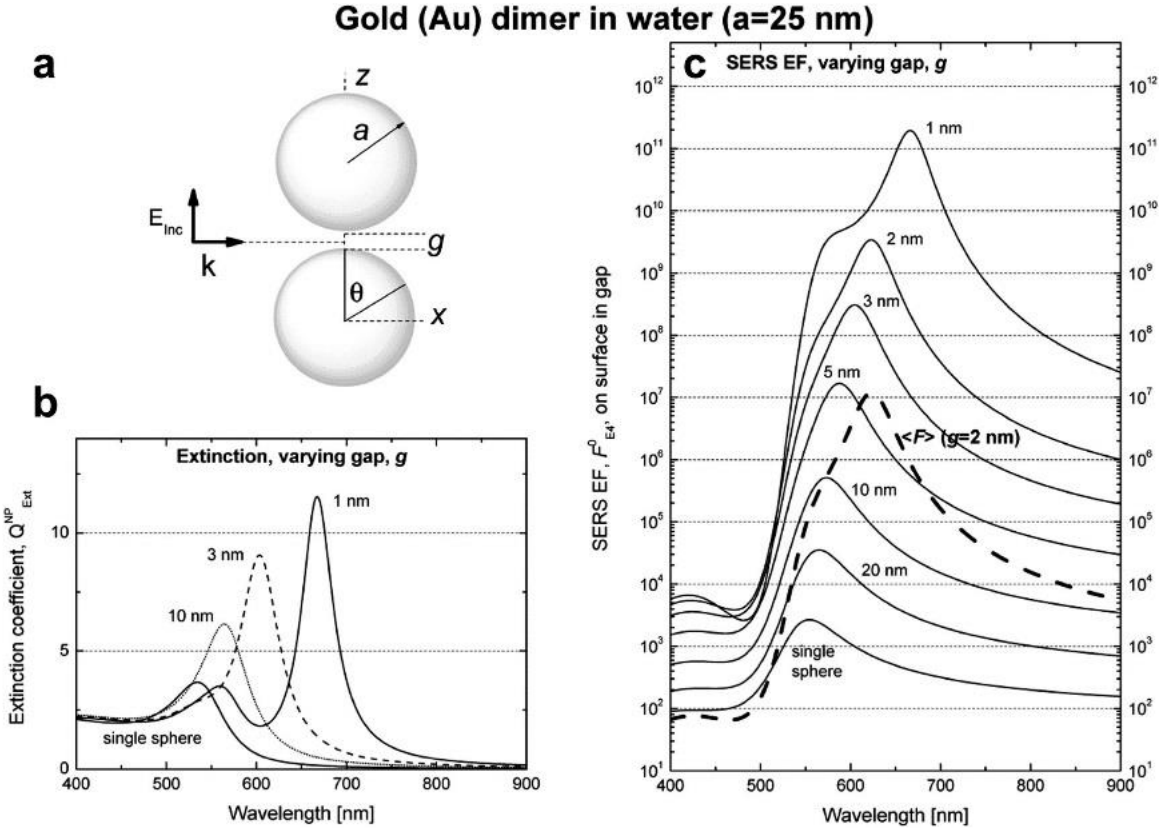

Figure 50 (a) Presentation of the dimer: a represent the radius of the two NPs and g the gap between them. The excitation light is polarized along the main axis. (b) Extinction coefficient as a function of the wavelength for a single NP and for the dimer (with different gaps). SERS enhancement factors for different gaps between the two NPs and for a single NP. Dashed line represents the SERS enhancement averaged over the entire metallic surface for a dimer with g=2 nm. Reproduced from [19].

The first step consisted of cleaning the fibers with acetone. To do so, we pumped acetone for 3 min at 50 µL/min and we dried the fibers by repeatedly pushing air inside the holes to help remove any trace of liquid. To avoid many repetitions in the description of the protocol, it is worth mentioning that we dried the fiber after pumping every solution. After drying the fibers, we prepared a solution of 2% APTES (Sigma-Aldrich) in acetone and dispensed it for 5 min and we left the solution inside the fibers for an additional 2 min in order to ensure that the silica walls of the fibers would be well functionalized. We rinsed thoroughly each fiber by pumping again acetone for 5 min. This was used to remove any unbound molecules of APTES. Once the SuC-PCFs were functionalized, we pumped for 10 min the colloidal solution of Au NPs and left it five more minutes inside to bind to APTES. Finally, we rinsed the SuC-PCFs with deionized water for 5 min to remove the unbound NPs and we dried the fibers one last time.

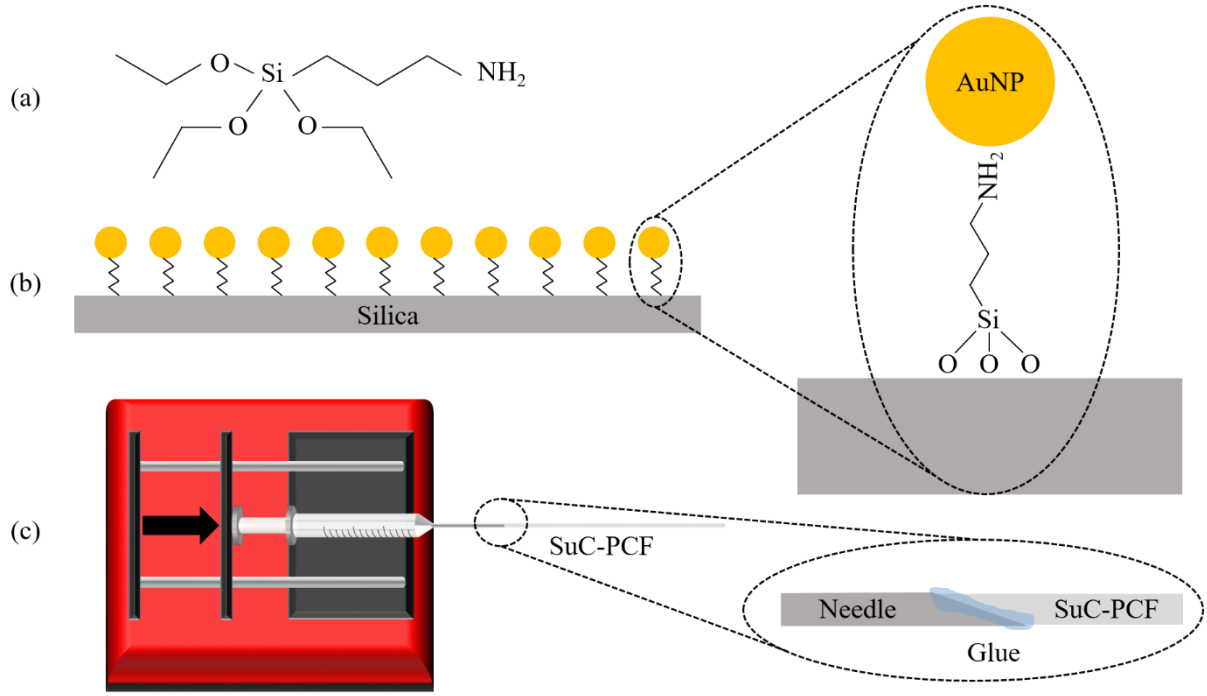

Figure 51 (a) Representation of an APTES molecule. (b) Schematics illustrating Au NPs anchored on the walls of a SuC-PCF. Zoom: illustration of one of the configurations in which APTES and Au NPs bind to silica. (c) Schematic showing the setup used to pump liquids inside the fiber holes Zoom: illustration of the needle/SuC-PCF assembly.

In order to test the SERS response of the prepared fibers, we prepared an aqueous solution of 10 mM of 4-aminothiophenol (ATP), which is a well-known Raman tag that has the ability to bind to the immobilized Au NPs through its thiol group as illustrated in the insert of Figure 53(a). We left the solution of ATP 10 min inside the SuC-PCFs, and we pushed the excess of solution with air. At this point, the SERS response of the fibers was ready to be measured.

III.2.1.2. First Raman measurements

The Raman setup used for all the measurements done in SBIC is a Renishaw InVia. This commercial spectrometer is set in backscattering configuration, which means that the collected Raman signal is coupled back to the spectrometer using the same objective used for the excitation of the sample. A schematic illustrating this configuration and the main components of the spectrometer is available in Figure 52. The device features two lasers, one emitting at 633 nm and the second emitting at 785 nm. The power of each laser can be controlled precisely. Two gratings are available depending on which laser is used. The first grating possesses 1200 l/mm, and the second one has 1800 l/mm. The excitation light and the Raman signal are coupled to and from the samples using a microscope (Leica), which possess several objectives, namely 5x, 20x, and 50x. The signal readout is improved by a CCD detector cooled at -70°C.

Once the fibers were ready for measurements, we cut the needle from the fiber and cleaved both ends. Then we placed one end into a fiber holder under the Raman microscope to measure the SERS spectrum. We focused the light on the core of the fiber using the XYZ stage of the microscope and a camera that displayed the fiber end face. We illuminated the fiber 10 s using the 633 nm laser and no average of the signal was done. A signature spectrum of ATP measured with our SuC-PCF is available in Figure 53(a). The two characteristic peaks at 1080 cm^{-1} and 1590 cm^{-1} are clearly visible, which means that we are

able to obtain a clear SERS signal with our SuC-PCF probes. These two peaks corresponds to stretching modes νCS, 7a and νCC, 8a respectively [229–231].

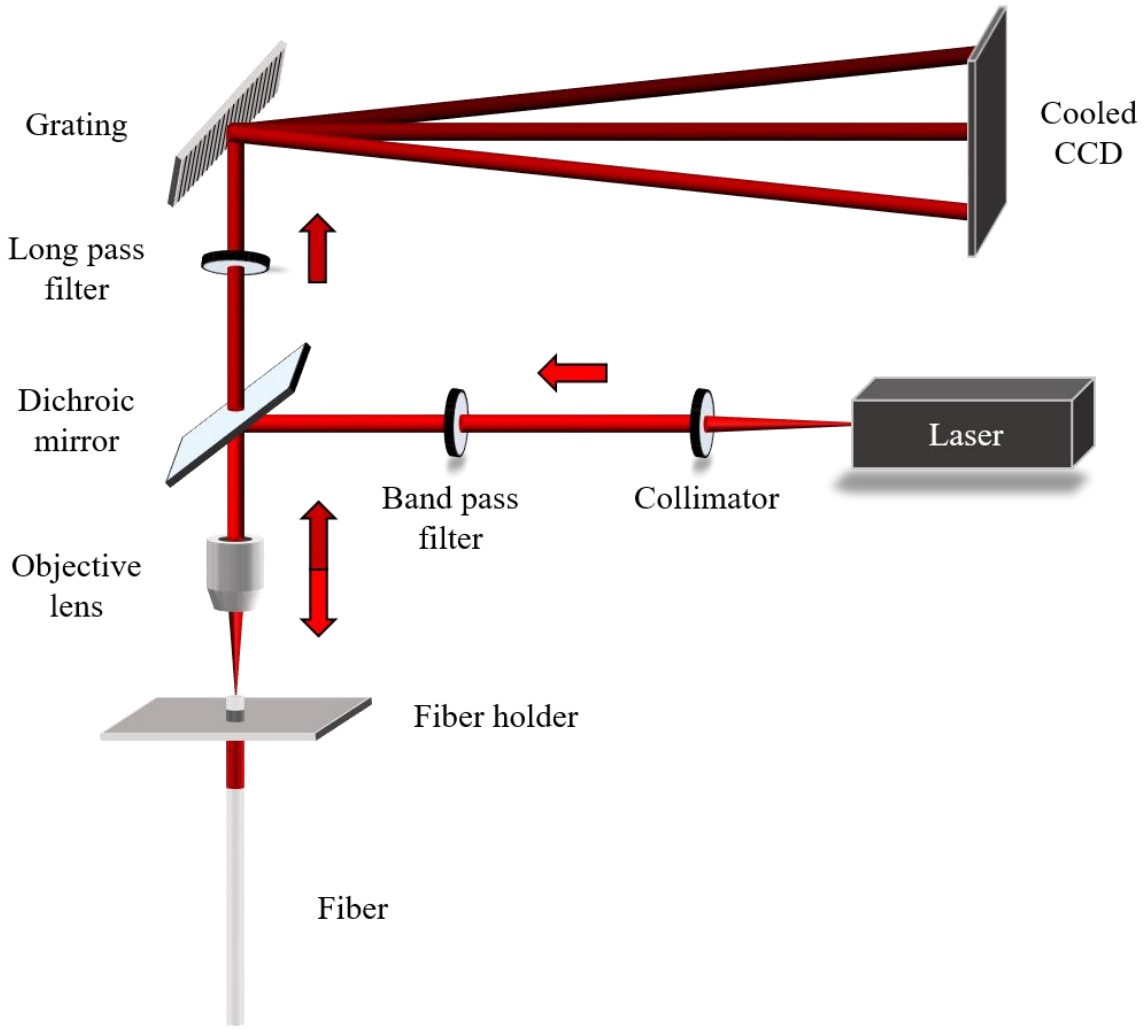

Figure 52 Schematic illustrating the main components of the Raman spectrometer used for the measurements.

The next step consisted of verifying that the Au NPs were anchored uniformly over the entire length of the fiber by monitoring the intensity of the 1080 cm^{-1} peak of ATP. To do so, we used 3.5 µm core SuC-PCFs and for each fiber, we measured the SERS signal coming from what we called the needle end and the free end of the fibers. As their names suggest, the needle end corresponds to the end that was glued to the needle during the anchoring protocol and the free end was the other one. This means that the different solutions entered inside the holes of the SuC-PCFs by the needle end. For each fiber, we cleaved and measured first the free end and then the needle end. For each end, we acquired seven spectra in order to average the SERS signal and avoid any outlier measurements and we subtracted the fluorescence background using a specialized software. We present in Figure 53(b) the normalized SERS intensity of the 1080 cm^{-1} peak of ATP obtained at both end of two SuC-PCFs. Here, we present only two fibers using the 633 nm laser for the sake of clarity but we did the same experiment for six SuC-PCFs and at 785 nm. Each time, the results were similar to the ones presented here. As we can see, the SERS intensity measured at the needle end is approximately twice stronger than the one obtained at the free end. These results demonstrate that during the anchoring protocol Au NPs are not anchored

uniformly inside the fibers and that more Au NPs are anchored close to the needle end. To rectify this, we decided to modify the anchoring protocol.

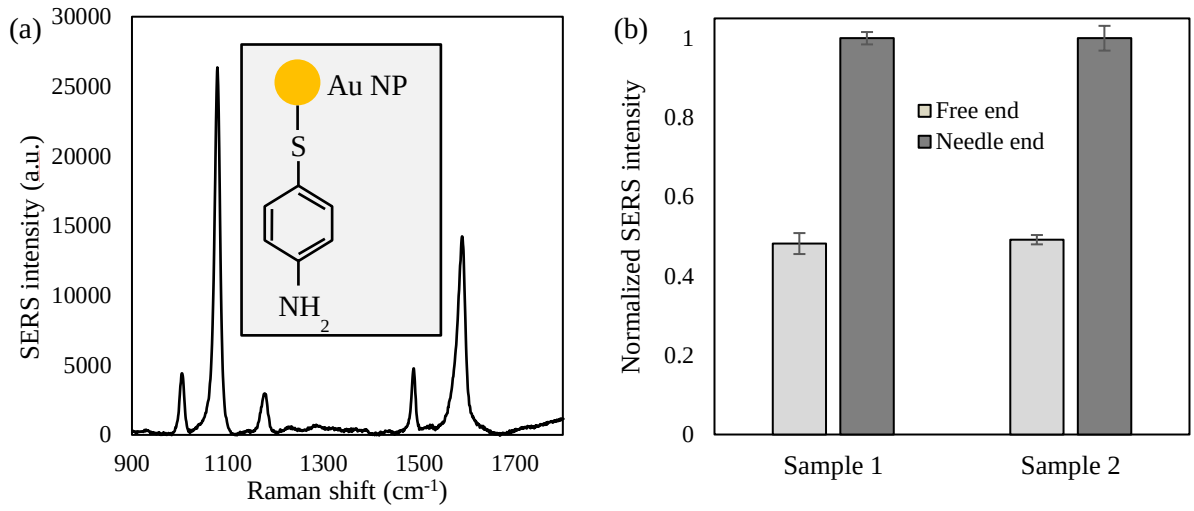

Figure 53 (a) Signature spectrum of ATP. The two main peaks are located at 1080cm^{-1} and 1590 cm^{-1}. Inset: Structure of ATP bound to an Au NP through its thiol group. (b) Normalized SERS intensity of the 1080 cm^{-1} peak of ATP for the two ends of two 3.5 µm core SuC-PCFs. The error bars represent the SD measured between the seven spectra per end.

III.2.2. New protocol used to improve the sensitivity and reliability of the sensors

III.2.2.1. Presentation of the new protocol

In many publications, APTES is left to react with silica for several hours [232–234]. In our previous protocol, we left the solution of APTES only seven minutes inside the fiber, which is quite short. Thus, we decided to increase the contact time between APTES and silica. In the new protocol, after washing the fibers with acetone, we pumped APTES for 1h and we left the 2% solution of APTES in acetone inside the SuC-PCFs over night to ensure that the molecules have more than enough time to interact with the silica over the entire length of the fiber. Then we rinsed the SuC-PCFs with acetone. We also increase the contact time with the colloidal solution of Au NPs. We pumped it for 1h inside the fiber and we left it 2h more inside the holes, so the Au NPs have enough time to bind to the anchored molecules of APTES. All the other steps described earlier remain unchanged. In order to have an idea of how the Au NPs are distributed inside the holes, we broke one SuC-PCF along the fiber length in order to have access to the inner walls of the fiber (Figure 54(a)) and we took SEM pictures using a field emission scanning electron microscope (FE-SEM) from JEOL. The pictures are available in Figure 54. In Figure 54(b), the cladding of the fiber is quite noticeable on the sides of the picture meanwhile the Au NPs on the inner wall of the fiber are not yet visible. When we zoomed, we started to see the Au NPs, as shown in Figure 54(c). By zooming further, the Au NPs are clearly visible. In Figure 54(c) and (d), it is worth noting that some Au NPs formed aggregates of various sizes while others are anchored by themselves. These two situations have an impact on the LSPR maximum and thus on the SERS enhancement factor.

After anchoring the Au NPs, we injected 1 mM ATP and we measured the intensity of the 1080 cm^{-1} peak of ATP at the two ends of each fiber in the same way that we did previously. The results are available in Figure 55. Here, it is obvious that the two ends of a single SuC-PCF exhibit approximately the same SERS intensity. This means that by increasing the incubation time of APTES and Au NPs inside the fiber holes, we managed to anchor more uniformly the Au NPs inside the SuC-PCFs. This finding is also verified using the 785 nm laser.

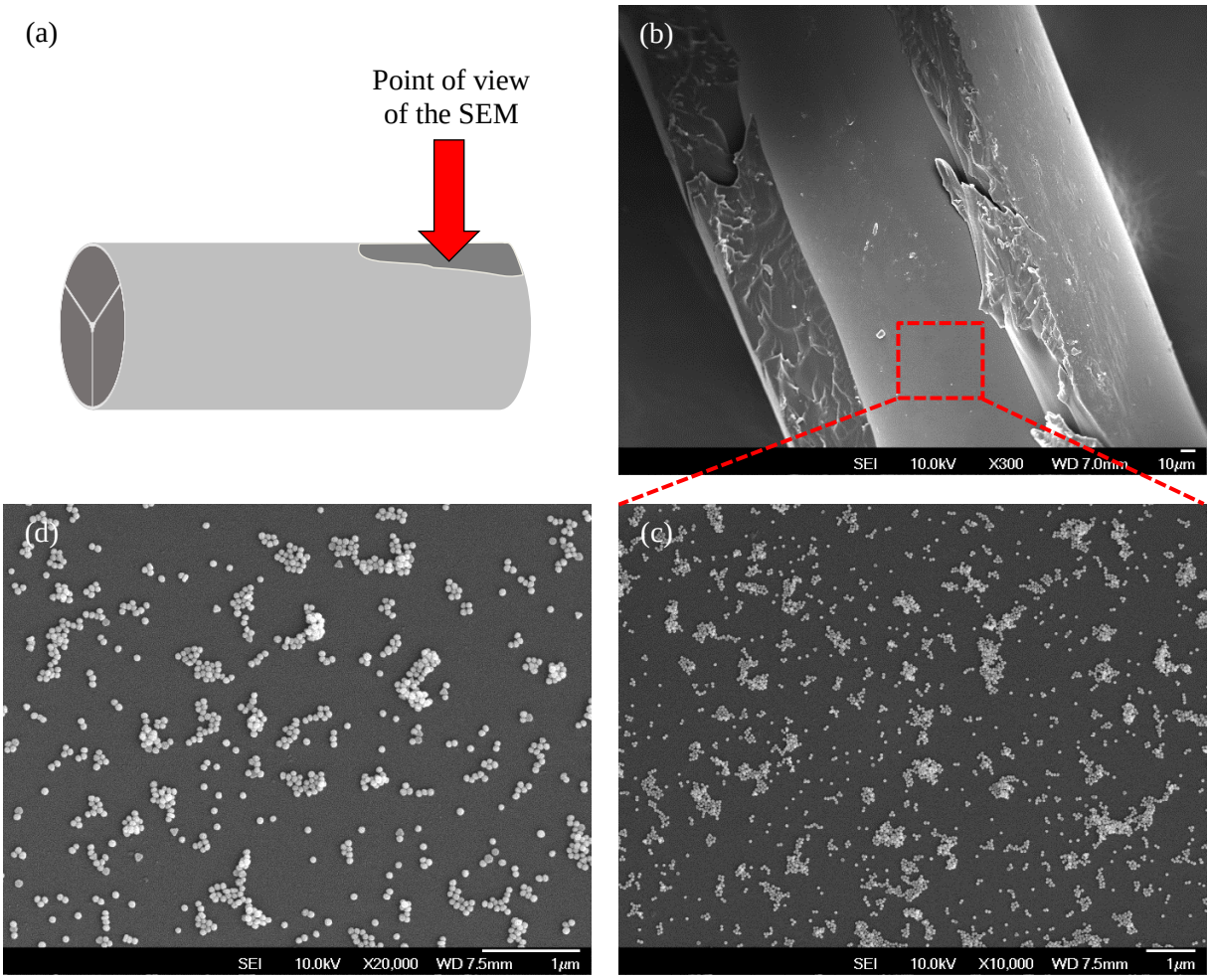

Figure 54 (a) Schematic illustrating the broken SuC-PCF that allowed us to take the pictures of the inner wall of the fiber. (b), (c), (d) SEM pictures of the inner wall of a SuC-PCF with Au NPs anchored using the new protocol at different magnifications.

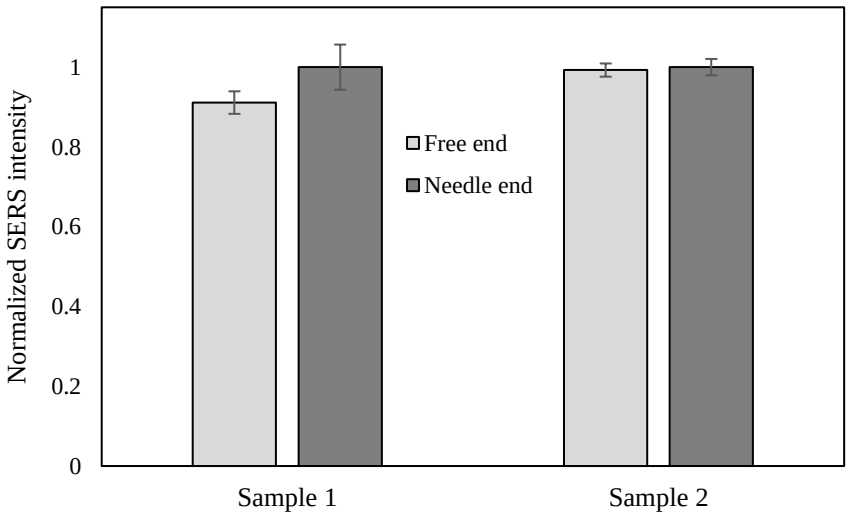

Figure 55 Normalized SERS intensity of the 1080 cm^{-1} peak of ATP for the two ends of two 3.5 µm core SuC-PCFs using the long anchoring protocol.

III.2.2.2. Comparison between the two protocols

We just saw that the long protocol improves the uniformity of the NPs anchoring inside the entire fibers. In addition, it also improves the sensitivity of the sensor. In the same excitation conditions, i.e., same laser power, same excitation time and same objective lens, the fibers prepared with the long protocol exhibit a much stronger signal (intensity of the 1080 cm^{-1} peak of ATP). According to Figure 56, it is clear that the long protocol helps in increasing the sensitivity of the sensors. This amelioration occurs when measuring the SERS signal from the free end as well as for the needle end, though the increase in intensity is more important on the free end side. This is correlated to the observations we made previously. Indeed, because the signals from the two ends are similar with the long protocol and much lower from the free end with the short protocol, the difference of signals observed between the two protocols is logically larger on this side of the fibers.

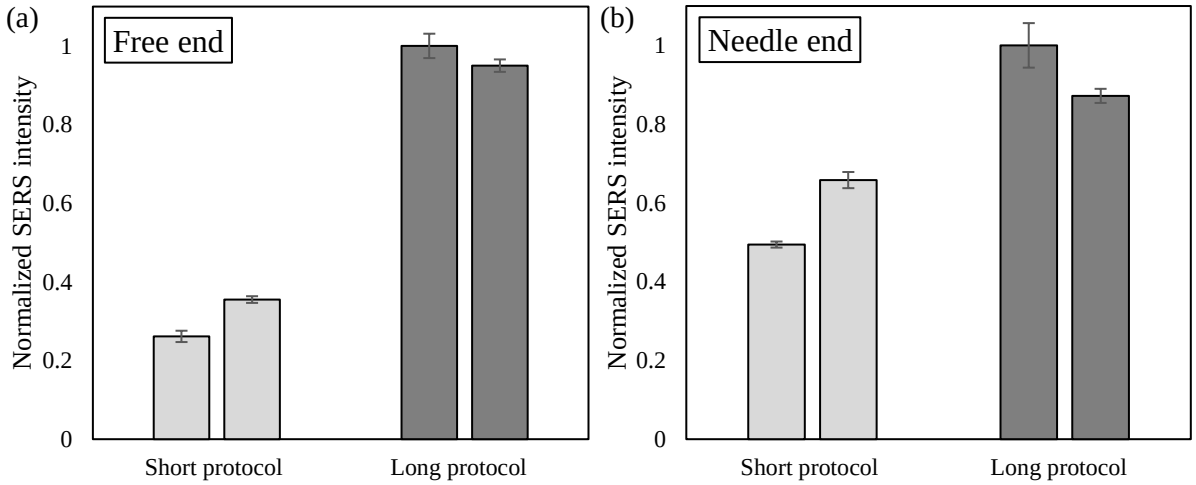

Figure 56 (a) Comparison of the effect of the short and long anchoring protocols on the normalized SERS intensities of the 1080 cm^{-1} peak of ATP at the free end of two 3.5 µm core SuC-PCFs. (b) Same comparison made at the needle end of the same fibers.

Here we showed that the long protocol improved the uniformity of the NPs anchoring and the sensitivity of 3.5 µm core SuC-PCFs. However, this might not be true for fibers with smaller cores. Indeed, increasing the incubation time of the solutions inside the fiber results in increasing the number of NPs anchored. Thus, since smaller core SuC-PCFs exhibit larger evanescent field, this might result in increasing further absorption and scattering losses inherent to the Au NPs. To ensure that the long protocol was also profitable for small core SuC-PCFs, we realized the same tests (short and long protocols) with 1.1 µm core SuC-PCFs. According to simulations, this fiber exhibited approximately 10% of evanescent field, which is much larger than the 0.04% exhibited by the 3.5 µm core. Despite the large difference in the amount of evanescent field, the trend of the study was notably the same as for 3.5 µm core SuC-PCFs:

- With the short protocol, the SERS intensities are stronger at the needle end than at the free end.
- With the long protocol, the intensities are approximately the same at both ends.
- The long protocol improves the sensitivity of the sensor at both ends.

In conclusion, we can say that the long protocol improves the quality of the Au NPs anchoring along the fibers and their general sensitivity both for small and large core SuC-PCFs. We are fully aware that even if this protocol improves significantly SuC-PCFs probes, other improvements may result in even more sensitive sensors, such as changing the NPs shape, size and material. However, this matter is still under

investigation, so we used the long protocol as our standard protocol for the fiber functionalization in the following of this manuscript.

III.3. Comparison between injected and anchored gold nanoparticles

As explained in chapter II, two main techniques are used in SERS sensing with optical fibers to allow the excitation of the analyte/NPs inside the fibers. The presented anchoring protocol corresponds to the first technique. The second one is the pre-mixing of the analyte/NPs solution outside the fiber followed by the injection. Among the literature, no clear direction is given with regard to which technique should be used preferably. No study has been conducted to directly compare these two techniques, authors only use one or the other without trying to understand which one is the best suited for fabricating SERS sensors. This is why in the following section we try to answer this question.

III.3.1. Description of injected gold nanoparticles

The first element to consider with the injected configuration is the optimum concentration of Au NPs resulting from the interplay between the Raman gain and the losses inherent to the Au NPs. To determine it, we prepared several colloidal solutions by diluting the stock solution of Au NPs (1X) in deionized water to result in 0.25X, 0.5X and 0.75X concentrations [235]. We also prepared 1.5X solution by centrifuging and re-suspending the colloids after removing one-third of the total volume. In order to be in the conditions used in the anchored configuration, we adjusted the concentration of ATP so that the final concentration inside the ATP/NPs mixture is equal to the one used in the anchored configuration. After preparing the different mixtures, we glued SuC-PCFs to 27G needles and we pumped the mixtures in separate fibers. The free end of each fiber was cleaved for enabling SERS measurements with the Raman spectrometer without parasitic effects from an overflowing analyte droplet. Once the mixtures were pumped inside the SuC-PCFs, they could flow freely inside the holes. For this study, we used SuC-PCFs with three different core sizes:

- D_{core} = 0.9 µm
- D_{core} = 1.4 µm
- D_{core} = 3.5 µm

Once again, we monitored the intensity of the 1080 cm^{-1} peak of ATP. For each fiber, we made eight measurements and removed any outliers. Then, we averaged the remaining intensities and we plotted in Figure 57 the variations of the average intensities with the concentration of Au NPs for the different core sizes.

We did several sets of measurements to confirm this trend and the optimum concentrations for 0.9 µm and 1.4 µm core SuC-PCFs oscillated between 0.5X and 0.75X. Concerning the 3.5 µm core SuC-PCFs, the optimum concentration was 1.5X. This demonstrates that the fibers with smaller cores possess a smaller optimum concentration of Au NPs. Given the simulations in section III.1.1.1, this makes perfect sense. Indeed, the amount of evanescent field that can interact with the Au NPs is much more important for the 0.9 µm and 1.4 µm fibers than for the 3.5 µm fiber (at least 100 times higher). Thus, the losses due to the NPs are much more important for these two fibers and the SERS enhancement is not sufficient to overweight them. As we saw in chapter II, simulations made by Zhang *et al.* showed that in the same conditions, the SERS intensity is supposed to reach a plateau after a certain concentration of Au NPs (for a fixed fiber length), as shown in Figure 29 [11]. Here, for higher concentrations of Au NPs the SERS intensity decreases. We hypothesize that this drop in intensity results from different interaction lengths between the high and low concentration of NPs. Indeed, as discussed in the simulation section, for high concentration of NPs, the losses are too important and the light may not be able to travel on

lengths, as long as it is possible with low concentrations of NPs. This results inevitably in a decrease in intensity. Another hypothesis lies in the degradation of the SERS enhancement. This degradation might be due to the uncontrolled aggregation of Au NPs near the core, which in some cases can influence the SERS enhancement [236]. For the 3.5 µm core SuC-PCF, the optimum concentration seemed to not yet be reached. However, further increasing the NPs concentration result in the creation of NPs aggregates, which, in turn, leads to a decrease in sensitivity and reliability.

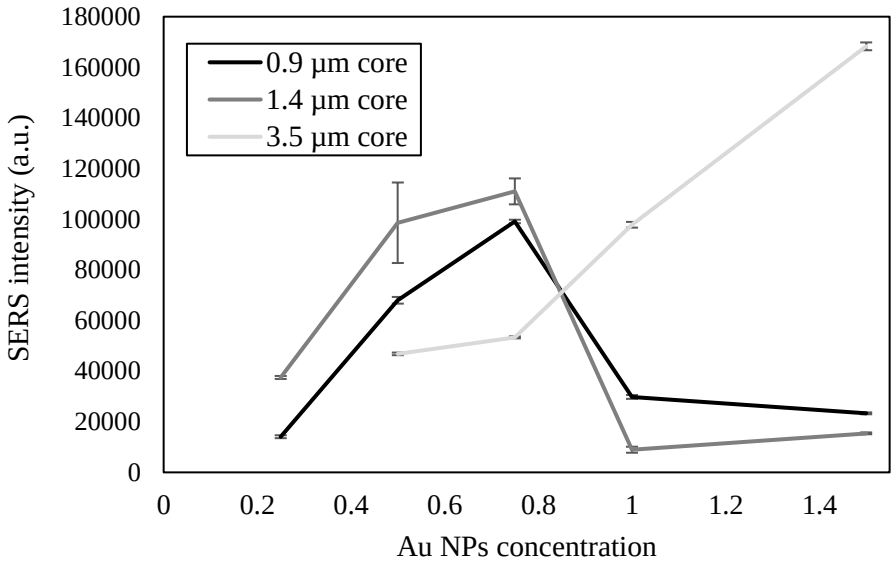

Figure 57 Variations in SERS intensity of ATP peak at 1080 cm^{-1} with the concentration of injected Au NPs for fibers with 0.9 µm, 1.4 µm and 3.5 µm core; error bars represent the standard deviation across 8 measurements obtained with the same fiber.

Now that we possess the optimum concentration for each set of fibers, we can compare it to our new anchoring protocol in order to determine which configuration is the best suited for the creation of a highly sensitive and reliable SERS biosensor.

III.3.2. Comparison between both configurations

Here, we want to compare both the sensitivity and the reliability of the sensors prepared with both configurations. We determined the fiber sensitivity by measuring the intensity of the 1080 cm^{-1} peak of ATP in fixed experimental conditions, the most sensitive sensors were the one exhibiting the highest intensity. The reliability was measured through reproducibility and repeatability. We expressed reproducibility as the relative standard deviation (RSD) calculated across eight measurements done on a single fiber sample. We measured a unique fiber sample eight times and between each measurement, we moved the focus point of the light onto slightly different locations on the core. Then we calculated the average and the standard deviation between these eight measurements and we calculated the ratio of the standard deviation on the average to obtain the RSD. Concerning the repeatability, we prepared fibers from the same batch under exactly the same conditions. For each fiber, we averaged the signal over eight measurements. Then, we calculated the RSD from these averaged intensities to deduce the repeatability. We plotted in Figure 58 the average SERS intensities and the RSDs of reproducibility and repeatability obtained from two to three SuC-PCFs prepared with the two techniques. The exact values are available in Table 3.

Table 3 Measured average SERS intensity, calculated average reproducibility and calculated average repeatability in anchored and injected configurations for 3 core size SuC-PCFs

	Average SERS intensity (a.u.)	Average RSD in reproducibility	Average RSD in repeatability
0.9 µm anchored	11113	1.04%	14.02%
0.9 µm injected	9869	7.06%	17.62%
1.4 µm anchored	22037	1.10%	13.87%
1.4 µm injected	12985	2.08%	23.54%
3.5 µm anchored	23524	0.93%	8.79%
3.5 µm injected	15203	1.02%	15.12%

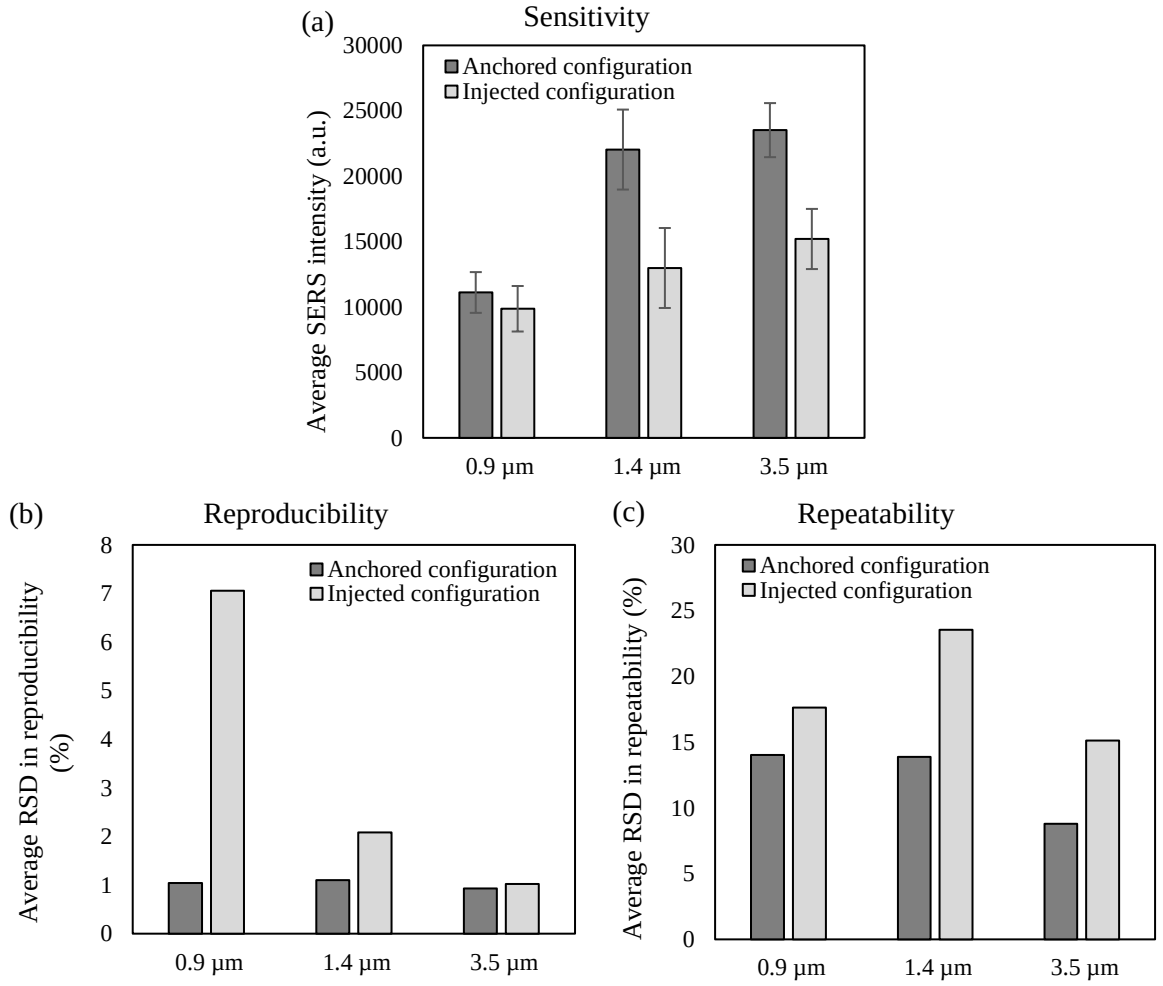

Figure 58 For each core size, comparison between the injected and anchored configurations of (a) the average SERS intensity at 1080 cm^{-1}; error bars represent the standard deviations across two or three samples, (b) the calculated average RSD in reproducibility, (c) the calculated average RSD in repeatability.

We noted that for each core size, the intensity was higher in the anchored configuration. In fact, the signal was 11%, 41% and 35% more intense in the anchored configuration for the 0.9 µm, 1.4 µm and 3.5 µm core SuC-PCF respectively. This increase in intensity can be seen as a major improvement for the sensitivity of the sensors, i.e. the new anchoring protocol helps in producing SERS probes more sensitive than the ones produced with the injected configuration.

We explained in chapter I the importance of the reliability for a SERS sensor in order to be clinically viable. When we compared the RSD obtained with both configurations, we observed that the signals were much more reproducible than those obtained even with the best planar substrates (around 5%) [83–

86], except for injected configuration with 0.9 µm core SuC-PCF. This great improvement is one of the benefits of SERS sensing with fibers. As mentioned previously, for planar substrates the excitation of the sample occurs only on the focused spot of the laser, which is only a few micrometers wide. However, in SERS fibers, the signal can interact with the NPs and the analyte for several centimeters. This greater interaction surface reduces the importance of irregularities in the deposition of the NPs, which results in higher reproducibility. To further illustrate this matter, it is worth mentioning that SuC-PCFs with freely flowing NPs inside their holes exhibit a better reproducibility than the best planar substrates. Another way to see the improvement due to the fiber is to refer to the SEM pictures of the anchoring protocol (Figure 54). We can clearly see that the NPs are not perfectly and regularly arranged inside the holes. However, the resulting reproducibility of the sensors is still excellent. Another aspect to note is that the anchoring protocol improves the general reliability of the sensors. Indeed the reproducibility and repeatability obtained in the anchored configuration are much better than the ones obtained with the injected configuration. The fact that the NPs are freely flowing inside the holes of the SuC-PCFs may explain the poorer reliability of the injected configuration.

Finally, the fact that the SuC-PCFs are intended to be used as biosensors inevitably guides the choice of the configuration as discussed in chapter II. The anchored configuration is more relevant from a clinical standpoint than the injected configuration.

III.3.3. Core size study

In this section, we want to demonstrate the role of the core size on the final Raman intensity detected by the spectrometer. Here, we only focus this study on the anchored configuration, since we showed that for every SuC-PCFs it gives the best sensitivity and reliability. We plotted in Figure 59 the average SERS intensity obtained with three fibers for each core size. The signal coming from each SuC-PCFs was measured eight times and averaged to remove any outlier. As we can see, the maximum intensity is obtained with the 3.5 µm core.

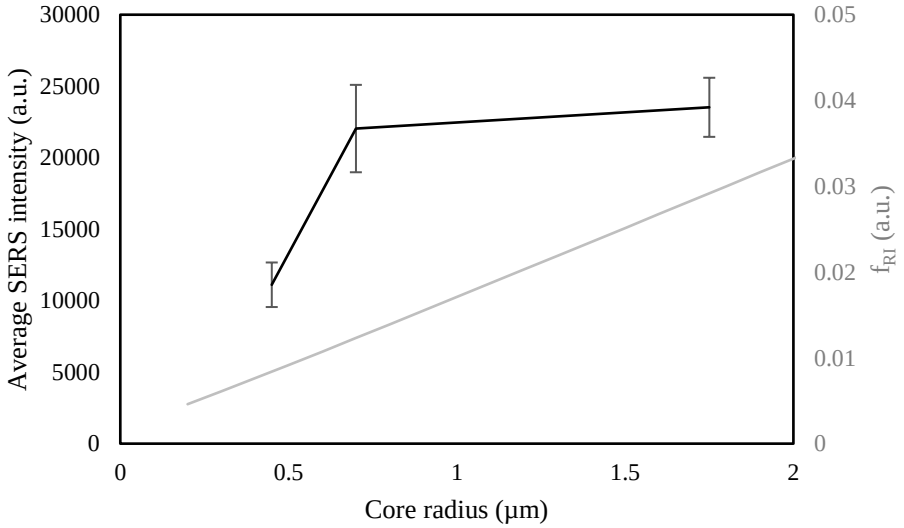

Figure 59 Black curve: variation of average SERS intensity of the 1080 cm^{-1} peak of ATP, in the anchored configuration, for 0.9 µm, 1.4 µm and 3.5 µm core SuC-PCFs. The error bars represent the standard deviation calculated for three fibers per core size. Gray curve: variation of the simulated f_{RI} with the core radius of 10 cm long rods with 30 particles/µm².

As explained before, the core size has an impact on the amount of excitation light that overlaps in the fiber holes. Increasing the incubation time would result in increased Au NPs deposited onto the fiber

walls. Using numerical simulations, we showed that too much increase of NPs coverage density for small core SuC-PCFs could result in a significant drop in the SERS intensity. Using the SEM pictures taken to illustrate the repartition of the anchored NPs after the long protocol (Figure 54(d)), we estimated a coverage density of ~34 particles/µm². Therefore, we plotted in light gray on the right axis of Figure 59 the f_{RI} calculated for 10 cm rod with 30 particles/µm² using the simulated model. Here, despite some discrepancies, the general trend of the two curves is similar: the larger the core, the stronger the SERS intensity and f_{RI}. This demonstrates that the simulation model used at the beginning of this chapter works in predicting the general behavior of SuC-PCFs for SERS sensing. The discrepancies can be explained by the difference between the simulated and real cases. For example, although the guiding properties are similar between a rod and a SuC-PCF, they are not exactly the same. Therefore, simulating a rod only allowed us to have an insight on the guiding properties of SuC-PCFs and not the exact ones. In addition, simulations were realized for equally distributed NPs on the core size and, according to the SEM pictures, this is not truly the case. Moreover, the NPs coverage density might vary between all the tested samples. Another plausible explanation is that in the simulation, no Raman active molecules are present, whereas in our experiment, ATP molecules were bound to the anchored NPs, which might create some variation in the plasmonic response. Finally, in the simulation, the coupling efficiency is not taken into account and, as we observed for small core SuC-PCFs, it can vary significantly between two measurements. In any case, despite these discrepancies, the simulation model predicted a SERS response that is close to the real one. According to the simulations, decreasing the coverage density for small core SuC-PCFs should theoretically result in a stronger SERS intensity. However, we demonstrated that relatively uniform anchoring of NPs inside PCFs requires some specific conditions, i.e. long interaction time of the solutions inside the fiber. Since the solutions must stay for a long time inside the fiber, the minimal number of NPs anchored cannot be extremely low. With these specific conditions, the 3.5 µm core SuC-PCF is the most sensitive of the three fibers.

Moreover, though all three fibers exhibit extremely good reproducibility of approximately 1%, the 3.5 µm core fiber also exhibits the best reproducibility (RSD = 0.93%) and repeatability (RSD = 8.79%). This could be explained by the first numerical simulation regarding the coupling efficiency. Indeed, we showed that for fibers with smaller core size, the misalignments between the excitation light and the center of the fiber core were responsible for a significant decrease in the coupling efficiency. This could result in a decrease in SERS intensity, as less light will interact with the NPs and the analyte. For instance, we consider a 0.9 µm core SuC-PCF with the excitation laser coupled right in the center of the core resulting in maximum SERS intensity. Then, if we imagine that there is a misalignment in the position of the fiber, it will result that the laser now enters the fiber with a small offset, which leads to poor coupling efficiency. In turn, this results in a drastic decrease in the final SERS intensity and thus in deteriorated reproducibility. Now, we consider a 3.5 µm core SuC-PCF. For a small misalignment, the drop in intensity is much smaller than that with the 0.9 µm core fiber and results in a final measured SERS intensity closer to the one obtained with the perfect excitation.

Similarly, the same reasoning can be applied to repeatability. A difference in excitation between two similar small core fibers results inevitably in a greater difference in SERS intensity than for big core SuC-PCFs. Therefore, in contrast to what was shown before [201], we think that the best fiber-based SERS sensor is not necessarily the one with the smaller core. In any case, we have to bear in mind that the best SuC-PCF for a given configuration remains necessarily a trade-off between every parameter (core size, fiber length, NPs coverage density). In addition, the specifications of the Raman spectrometer (size of the laser beam, objective lens used) play an important role in the choice of the fiber used. Consequently, in order to fabricate the best fiber-based SERS sensor, one should fix at least one parameter and optimize the others accordingly to benefit from the most advantages possible.

Now that we illustrated the sensitivity and reliability of our SuC-PCFs sensors, we wanted to demonstrate their relevance as biosensors in practical cases. For that, we detected haptoglobin, which is a biomarker that can be used to trace the stage of ovarian cancer, in clinical cyst fluids.

III.4. Detection of relevant biomarker in clinical body fluids

Many studies are conducted to discover new biomarkers that can help in detecting diseases at their earliest stages. Monitoring of these new biomarkers needs to simplify and/or replace the existing techniques in order to facilitate the earlier detection of the disease and improve the survival rate of the patients. Regarding ovarian cancer detection, several techniques are currently used as gold standard such as enzyme-linked immunosorbent assay (ELISA), electrochemical impedance spectroscopy, and chromogen staining. However, they are time consuming and quite tedious to perform [237–239]. To reduce the delay in surgery, surgeons can use intraoperative frozen section [240–242] but it suffers from variation in accuracy as a result of large cyst size, non-uniformity of the tissue malignancy leading to sampling error and limited availability of staining methods [242,243]. Thus, a fast and sensitive method that could be adopted in an intraoperative setting represents a very credible alternative method.

Haptoglobin (Hp), a glycoprotein secreted by hepatocytes is usually present in very small quantity in human serum. During an infection, an inflammation or after a trauma its concentration can rise significantly. A few years ago, several studies found that the amount of Hp in ovarian cyst fluids (OCF) and serum was strongly correlated to the stages of ovarian cancer [244–247]. Therefore, detecting Hp in cyst fluids withdrawn from patients with our SERS-based SuC-PCFs would represent an excellent first step towards the ultimate goal of detecting ovarian cancer as early as possible.

III.4.1. Sensitivity and reliability of 3.5 µm core suspended core PCF from a different batch

For this study, we used 3.5 µm core SuC-PCFs. However, this fiber did not come from the same batch used in section III.3, i.e. they were not drawn at the same time, so we wanted to ensure that the fiber was sensitive and reliable enough. To do so, we realized the same tests presented before. We anchored the 60 nm Au NPs using the long protocol and we monitored the intensity of the 1080 cm^{-1} peak of ATP using the same set up. This time, we measured fourteen times a single fiber sample in order to obtain the RSD relative to reproducibility. The fourteen spectra from one fiber sample are available in Figure 60(a) along with the intensity of the 1080 cm^{-1} peak of ATP. It is clear that all the measured spectra were similar and corresponds well to the signature spectrum of ATP (Figure 53). In addition, the variation of intensity for the 1080 cm^{-1} peak between each spectrum is comparable to the reproducibility obtained from the previous 3.5 µm core SuC-PCF (0.93%).

We also measured six separate SuC-PCFs prepared in the same condition to estimate the repeatability RSDThe variation of intensity for the 1080 cm^{-1} peak and a representative spectrum for each of the six fibers are available in Figure 60(b). Here we could see minor variations between the spectra but the two signature peaks of ATP are still clearly visible. The variations in intensity between the six fibers are ~4.6%. This is much lower than the RSD measured for three fibers in III.3.3. To this day, we are not completely sure of what could explain the difference between the two 3.5 µm core SuC-PCFs. Several causes might explain this difference. It might be due to the orientation of the fibers during the measurement. Because the fibers are not symmetrical, we noted that the SERS intensity varied according to the orientation of the fiber under the microscope objective. The final possibility is that the spectrometer and the conditions in which the measurements were made were not the same. Indeed, we noted that the humidity and the room temperature had a small impact on the SERS intensity measured by the spectrometer. Once again, this could not explain entirely the difference. That is why we think this

difference might be due to a combination of several factors. In any case, the reliability exhibited by the SuC-PCFs here is quite remarkable compared to planar substrates.

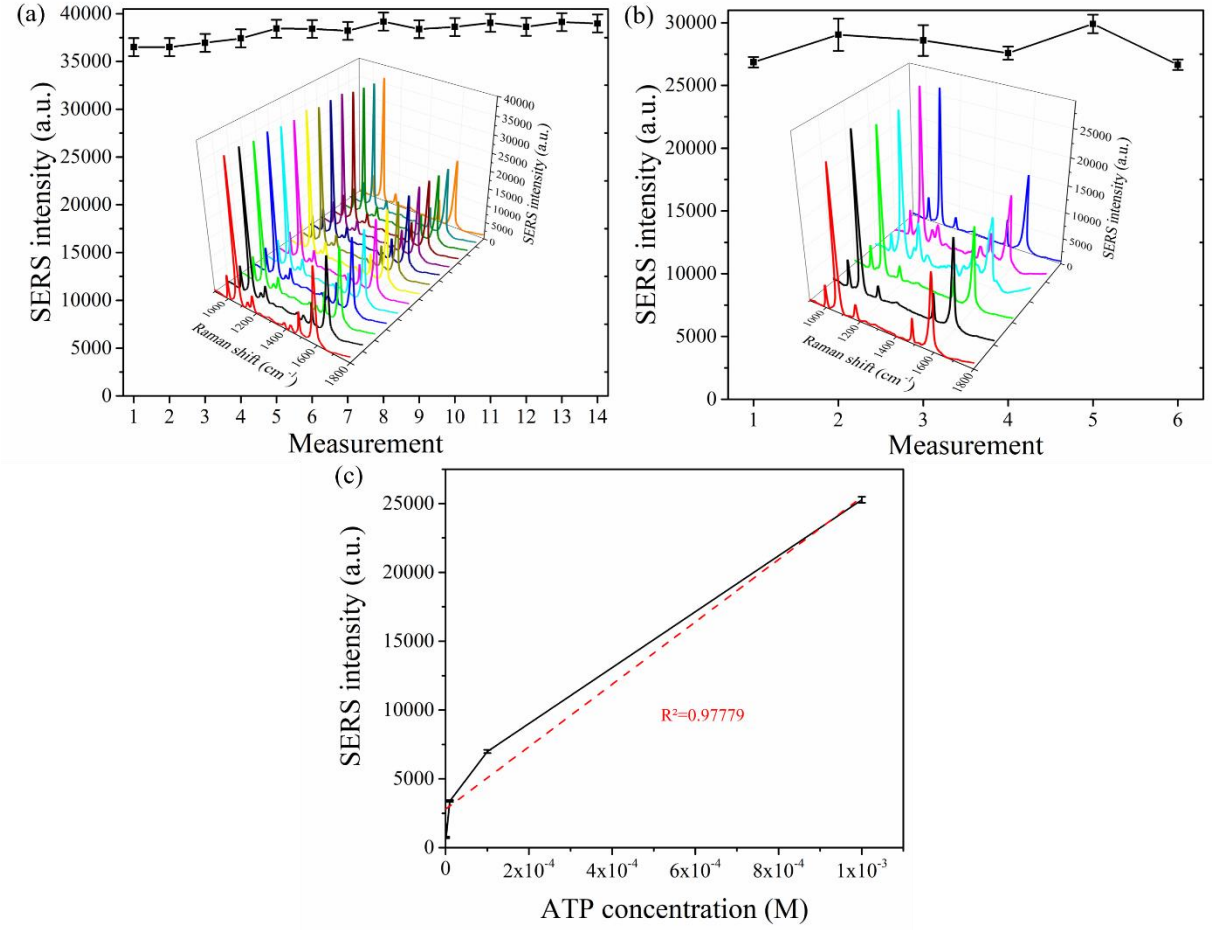

Figure 60 (a) Variations in the Raman intensity of 1080 cm^{-1} peak (14 measurements) from the SuC-PCF showing the excellent reproducibility of the sensor, error bars represent the SD of the 14 measurements. Inset: Acquired 14 spectra from one of the representative fibers. (b) Variations in the Raman intensity of 1080 cm^{-1} peak from six different fibers showing the good repeatability, error bars represent the SD of 14 measurements acquired for each fiber; Inset: individual spectrum from six different fibers. (c) Calibration curve of Raman intensity with ATP concentration showing the good linearity of the sensor, error bars represent the SD obtained from 14 measurements. Reproduced from [225].

The last aspect we wanted to study prior to the detection of Hp is the linearity of the sensor. This parameter is of prime importance for biosensors as it allows obtaining the concentration of an unknown sample. We functionalized four SuC-PCFs and we pumped 1, 10, 100 µM, and 1 mM solutions of ATP inside the fiber holes. After drying the fibers, we measured the SERS intensity of the same peak. The results are available in Figure 60(c). As we can see, the sensors exhibited an excellent linearity ($R^2 = 0.97779$). Now that we demonstrated the good sensitivity, reliability and linearity of this fiber batch, we can focus our study on the detection of Hp.

III.4.2. Detection of haptoglobin in clinical cyst fluids

III.4.2.1. Protocol

We detected Hp in OCF collected during surgery on several patients diagnosed with ovarian cancer. Each subject gave a written consent and the samples were used according to local ethics committee approved protocol number 2000/00856 (National Healthcare Group, Singapore). After being transported

on ice to the laboratory, the samples were centrifuged at 2,000g for 10 minutes at 4°C and the supernatant was stored at -80°C until analysis. We chemically added a sulfhydryl group (-SH) to the Hp molecules contained in the collected OCF so that they were able to bind to the anchored Au NPs inside the fiber [248–251]. For that, we incubated the clinical samples with EDTA (BIO-RAD) and Traut's reagent (Sigma Aldrich) for 30 minutes. Then, to remove the excess of reagents, we centrifuged the mixture and we re-suspended it in phosphate buffer saline (PBS) (1st BASE).

Once the Hp molecules were functionalized, we anchored 60 nm Au NPs onto the inner walls of the SuC-PCF using the long anchoring protocol describe in section III.2.2.1. Subsequently, we incubated for 30 minutes the prepared solution of SH-modified clinical sample inside the fiber. This allowed the modified Hp molecules to bind to the Au NPs. We rinsed the fiber with PBS and BSA (PAA Laboratories) and dried it. At this stage, the targeted molecule, i.e. Hp were immobilized on the Au NPs inside the fiber holes. However, Hp molecules do not possess a clear and strong Raman spectrum. Therefore, we needed to develop a readout probe.

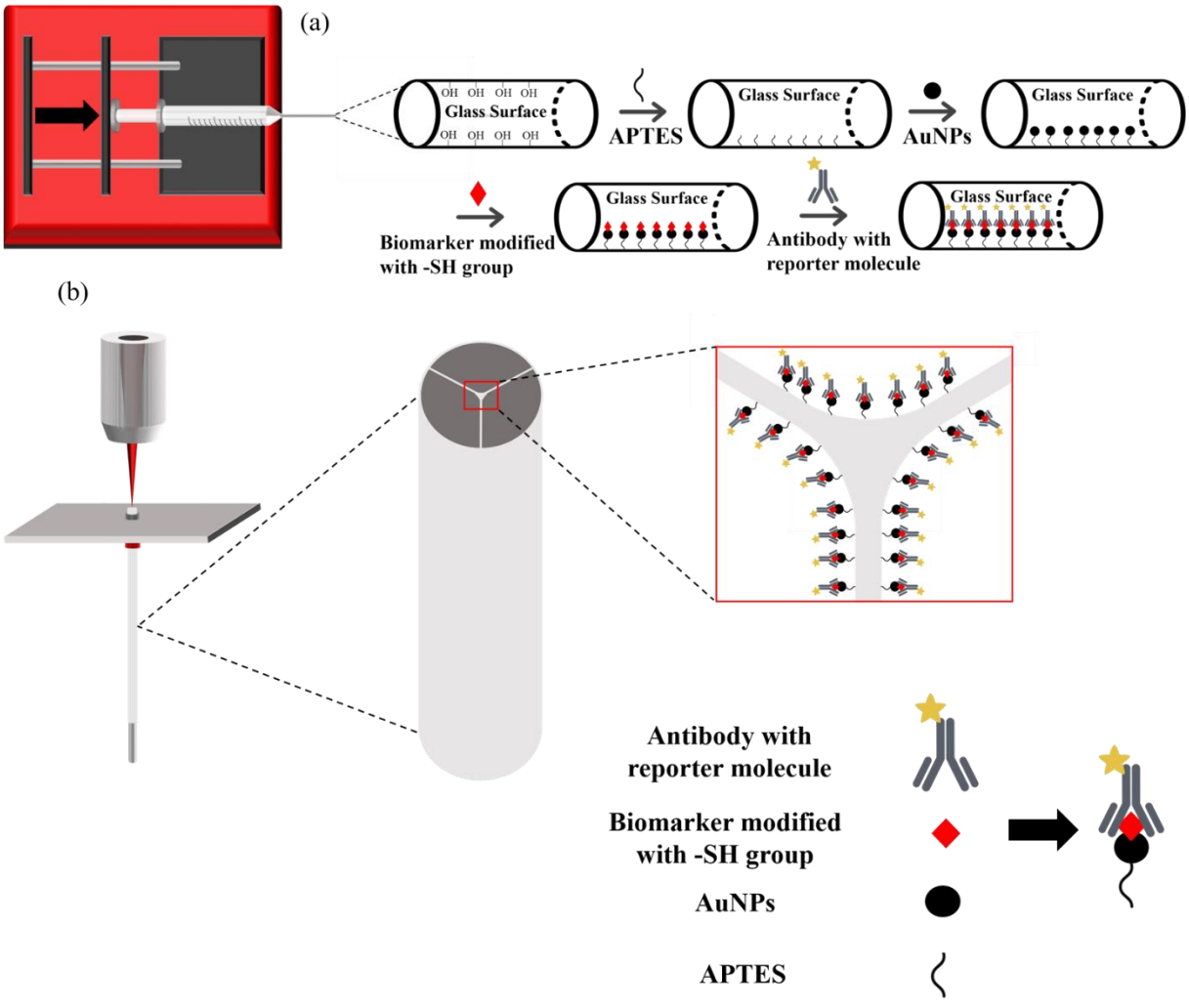

Figure 61 (a) Schematic of the functionalization process inside the holes of the PCF for biomarker sensing. (b) Coupling of the light from the objective lens of the Raman spectrometer and backscattering collection of the signal from the fiber end. Zoom-in on the fiber end face and holes with the attached protein and read out Raman tag. Reproduced from [225].

This was realized by attaching ATP molecules to Hp antibodies (Hp-AB). First, to activate the carboxylic group in the antibody, we mixed equal volumes of N-hydroxysuccinimide (NHS) (Thermo Fisher) and 1-éthyl-3-(3-diméthylaminopropyl)carbodiimide (EDC) (Thermo Fisher) with 100 µL of

Hp-AB stock solution and we left the mixture to react for 5 minutes. Then we added 10 mM ATP solution and left to incubate for 2 hours. This mixture was centrifuged with a membrane filter to remove the excess of unreacted ATP and antibody.

Once the readout probes were ready, we injected the solution inside the fiber so the Hp-AB/ATP complex can bind to the anchored Hp molecules. We rinsed the fiber one last time with PBS and water successively and dried them. Schematics of the main steps and of the structure of the anchored assembly are available in Figure 61. It is worth noting that this geometry is not well suited for the creation of a rapid biosensor that could be used in clinical environment. Indeed, here the clinician would have to inject the readout probe solution inside the fiber after having withdrawn the body fluid. The best option would consist of anchoring all the necessary elements for the SERS sensing inside the fiber so that the clinician only needs to withdraw the body fluid on the patient and put the fiber under the microscope for readout. We are currently working on improving our protocol to meet these requirements. The methodology used here simply allowed us to illustrate the sensing capabilities of our probes on clinically relevant biomarkers in patients' fluids.

III.4.2.2. Results

Using the same Raman setup described previously (section III.2.1.2), we measured the SERS response of the SuC-PCF after each step in order to ascertain that the signal we obtained after the final step resulted from the presence of the Hp-AB/ATP after the bonding of the Hp-AB with the Hp molecules. We plotted spectra after different steps in Figure 62(a) to illustrate this matter. For the sake of clarity, we added an offset to the spectra after APTES and after AB-4-ATP. We can clearly see that the two signature peaks of ATP are present after incorporating the AB-ATP probe inside the fiber while no characteristic peaks are present after the other steps. The ATP peaks denotes the presence of the AB-ATP probe, which can bind to the Hp molecules, i.e. Hp molecules are well anchored inside the fiber.

As mentioned previously, we tested OCF collected on patients with different stages of ovarian cancer. In Figure 62(b), we plotted the normalized intensity of the 1080 cm^{-1} peak of ATP obtained for three patients A (benign), B (early cancer) and C (advanced cancer). We noted that the lowest intensity was given by the benign OCF (~0.2). The patient with advanced cancer exhibited the highest normalized intensity (1), while patient B exhibited an intermediate value (~0.55). We performed T tests between the three samples to ensure that the three intensities were significantly different ($P<.0001$ compared to patient A). We achieved similar results for other sets of patients. Another one is presented in Figure 62(c). Each time, the patients with the more advanced cancer exhibited the stronger SERS intensity.

In addition to our tests, the patients' OCFs were also tested using the current gold standard used for ovarian cancers to determine the tumor malignancy. It consists of monitoring the concentration of CA125 (cancer antigen) in the patients' serum. If the concentration of CA125 is less than 35 U/mL (enzyme unit/mL), the tumor can be considered benign. Additionally, the histology of the tumors was also tested. Table 4 summarizes the different results obtained with the complementary tests for the five patients. It is worth noting that the results obtained with the other techniques supported our own results. In other words, we were able to differentiate the stage of ovarian cancer using our SERS-based PCF sensor.

In conclusion, we can say that we managed to create a highly sensitive and reliable SERS sensor based on PCF. With this sensor, we were able to accurately differentiate the stage of ovarian cancer by monitoring the amount of Hp in OCF collected on several patients during their surgery. The more Hp present in the OCF, the highest the SERS intensity was. This study should only be seen as a proof of concept, since a large-scale study is required in order to determine the exact correlation between the measured SERS intensity and the stage of ovarian cancer. This would allow determining a cut-off

normalized intensity below which a tumor could be considered benign, for example. These results remain extremely promising and illustrate perfectly the use that SERS-based PCF can play as biosensors. We can imagine that they could be translated as a highly sensitive opto-fluidic biopsy needle for the detection of biomarkers in body fluids and used in critical care units or operating theaters to continuously monitor the concentration of desired biomarkers. This would eventually reduce the time and cost involved in the current assessment of a disease severity.

Table 4 Histology and CA 125 results from OCF samples collected in five patients

Patient	Tumor condition	CA125 (U/mL)	Histology
A	Benign	11	Mucinous cystadenoma
B	Malignant (early)	45.9	Serous adenocarcinoma
C	Malignant (advanced)	133.3	Clear cell carcinoma
D	Benign	9.1	Serous cystadenoma
E	Malignant (advanced)	3283	Serous carcinoma

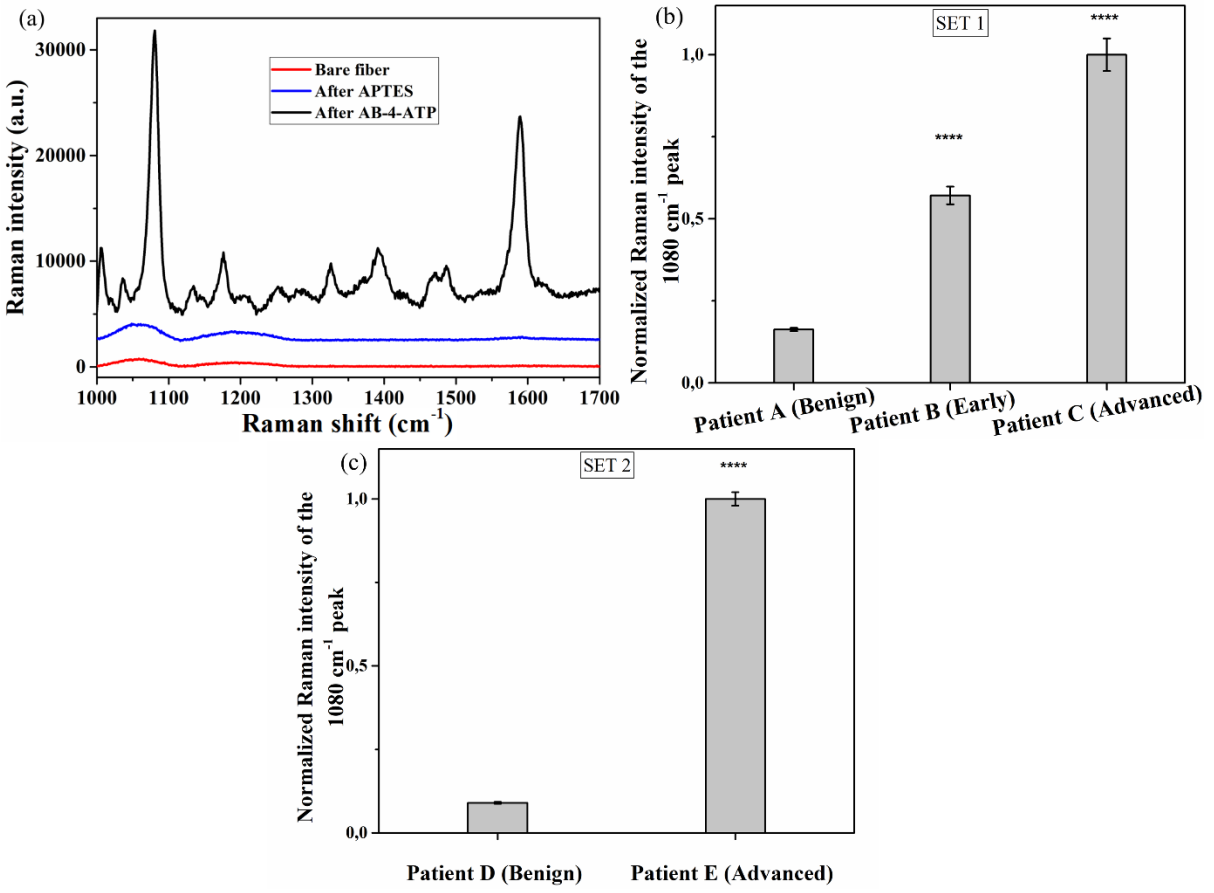

Figure 62 (a) SERS spectra of the bare fiber, the fiber after anchoring with APTES and after adding AB-ATP that binds to Hp biomarkers demonstrating the specificity. All prominent peaks of ATP are observed. (b) Normalized Raman intensity of 1080 cm^{-1} peak from clinical OCF having different stages of cancer. ****P<.0001 denotes significance when compared to patient A. (c) Normalized Raman intensity of 1080 cm^{-1} peak from the second set of clinical OCF depicting different stages of cancer. ****P<.0001 denotes significance when compared to patient D. Reproduced from [225].

III.5. Conclusion

SuC-PCFs have been used in many studies since the discovery of SERS-based PCF sensors. Several of them tried to explain their behavior, and the role played by the fiber parameters on the measured SERS intensity without succeeding in observing the full picture. In this chapter, we tried to include as many parameters as possible to procure the best overview possible. More importantly, through simulations, we showed the effect of the core size on the coupling of the light to the PCFs core and the mandatory trade-off between the core size, the fiber length and the NPs coverage density that results from the interplay between the SERS gain and the extinction losses inherent to metallic NPs. We also presented an optimized protocol to anchor NPs inside the PCF to make it SERS-active. With the new optimized protocol, we managed to improve the previously available high sensitivity and reliability of SERS-based PCFs. Compared to the best planar substrates, we obtained record-breaking reproducibility and repeatability using common Raman tags. The best SuC-PCF exhibited 1.5% variation in RSD over a unique sample, and 4.6% over six samples prepared using the same protocol. This is very promising since one of the major limitations of SERS for biosensing is the reliability of the measurements. Building on these excellent results, we used our SuC-PCFs sensors in a clinical study to detect a relevant biomarker in OCF. Though our study is only a proof-of-concept, it illustrates perfectly the great possibilities that SERS-based PCF probes have to offer. We were able to differentiate precisely the stage of ovarian cancer for several patients. We envision that this study could pave the way for future SERS biosensors based on optical fibers. Though these results are very promising, there is still room for improvement. In the following chapter, we present a totally novel fiber topology that could very well be one of the most sensitive SERS-based PCF sensors. So far, we had described that increasing the core size could lead to a decrease in the amount of evanescent field. Our new design could overcome this limitation and able to achieve a good portion of the evanescent field in the cladding for interacting with the analyte even with extremely large core of the fiber. Numerical simulations, design, fabrication and performance analysis of this new PCF are described in detail in the next chapter.

Chapter IV. Ring core fibers, a novel fiber design for improving the sensitivity of SERS based fiber sensors

Chapter IV. Ring core fibers, a novel fiber design for improving the sensitivity of SERS-based fiber sensors

IV.1. Observation on the limitation of sensitivity in SERS-based fiber sensors

This chapter is dedicated to a novel type of PCF specifically designed for improving the sensitivity of SERS-based fiber sensors. Almost all the studies of PCF-based SERS sensors are realized with standard or commercial fibers. Their primary purpose is not SERS sensing and thus their parameters are not optimized for this application. The first solution to improve the sensitivity of fiber sensors is to increase the amount of evanescent field that can interact with the analyte and NPs, while controlling the NPs coverage density. The second possibility is to increase significantly the interaction area. For that, the length of the fiber can be increased. However, in our case, for practical reasons, we fixed the fiber length to 10 cm. The other solution to increase the interaction area is to increase the core size of the fiber. Unfortunately, increasing the core size inevitably reduces the amount of evanescent field, as demonstrated in chapter III. For example, for a 10 µm rod surrounded by water, only 0.02% of the excitation light propagates in the cladding. Unfortunately, to this day, no SC-PCF design allows having a large core for increased interaction surface and a good portion of the evanescent field. This indicates that one should choose a fiber between having a good portion of evanescent field but a smaller surface of interaction or the opposite. An ideal solution would be a fiber that possesses a large core for improving the interaction surface while maintaining a high portion of evanescent field in order to have enough light interacting with the analyte. This would overcome the inevitable trade-off between interaction surface area and amount of evanescent field.

With this in mind, we developed what we called a ring core fiber (RCF). This innovative design features a silica ring that guides the light thanks to TIR. Thus, the fiber benefits from a fix and large transmission window and the interaction occurs through the evanescent field. The ring is held inside the fiber by thin silica struts. The diameter of the ring should be the largest possible (ideally around 100 µm or above) to increase as much as possible the interaction area. The great advantage of this design lies in the possibility to tune the thickness of the ring. This allows to precisely control the amount of evanescent field that overlaps in the cladding. Hence, with this topology, the fiber benefits from a giant surface of interaction while still having a good portion of evanescent field. A study by Chen *et al.* confirmed our hypothesis to increase significantly the diameter of the core in order to achieve a higher sensitivity [220]. Indeed, they were able to achieve a good sensitivity with a 100 µm large sapphire multimode fiber. In this study, higher sensitivity was no longer achieved due to the lower amount of evanescent field. The authors showed that because there is less evanescent field, the NPs coverage density could be increased by two orders of magnitude compared to SuC-PCFs while still maintaining the dominance of the SERS enhancement over the extinction losses along the fiber length. In addition, since the surface of interaction was much larger than that of a small core SC-PCF, the light could encounter more NPs and analyte molecules. Thus, the combination of the increased interaction area and the much larger coverage density can explain the relatively good sensitivity obtained with their 100 µm sapphire MMF. To demonstrate the interest of our design, we adapted the simulation model developed by Chen *et al.* described in chapter III.

IV.2. Simulation

IV.2.1. Adaptation of Chen's model to the new design

The silica rod simulated previously is replaced by a silica ring floating in water and surrounded on the inside and on the outside by the effective layer of Au NPs (see section III.1.1.1). We present in Figure 63 the design we used for the simulation of a 100 µm diameter ring. The simulated case is an ideal case

and does not correspond exactly to the real case since, in the simulation, the ring is not held by thin silica struts. In chapter III, we simulated rods of different diameters surrounded by the effective layer and water to estimate the SERS response of SuC-PCFs. As a comparison with our new design, we present the 3.5 µm rod (ideal case) simulated previously to have a true-to-scale representation of the increase in surface area that the ring core allows.

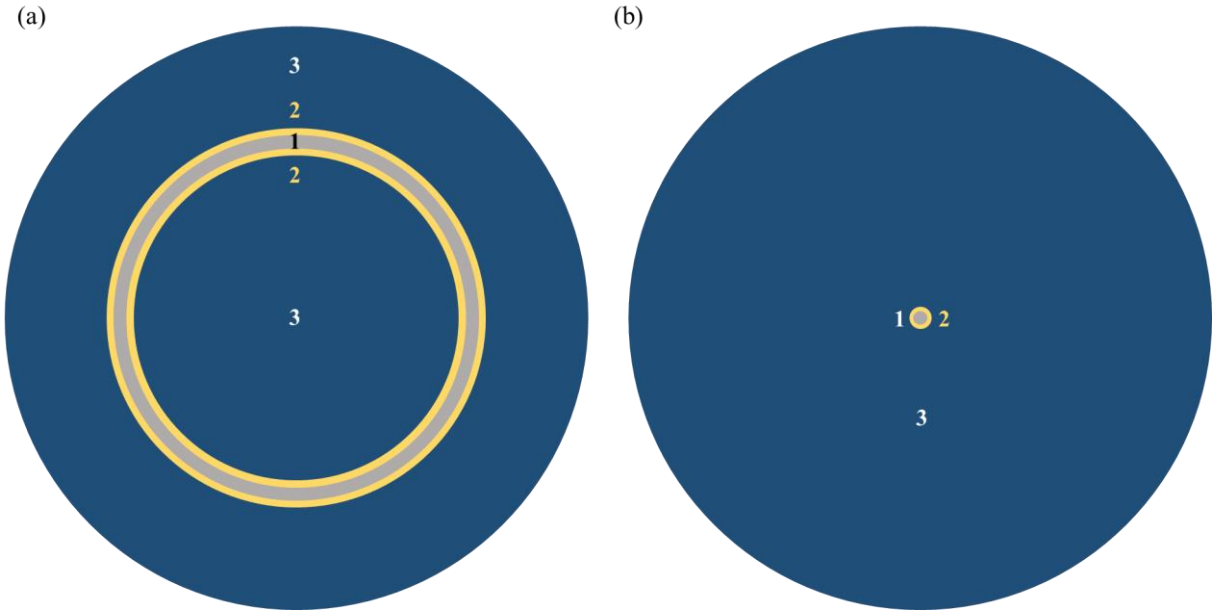

Figure 63(a) Schematic of the RCF design used for the simulation. (b) Design simulated in chapter III for a 3.5 µm rod. The core size in (a) and (b) are true-to-scale to have a better visualization of the surface increase. 1 represents the silica core (gray), 2 represents the effective layer (yellow, thickness not true-to-scale) and 3 represents water (blue).

The principle of effective layers described in chapter III is still valid for the ring core surrounded by water and we can calculate the effective dielectric constant of the composite material similarly to equation 25 in chapter III. After defining the design with two effective layers, one on the inside of the ring and one on the outside, we used FEM to compute the imaginary effective indices and the portion of the evanescent field per mode. This allowed us to calculate the modal attenuation coefficients (α_{exc} and α_{det}) at the wavelength of the laser used to excite the analyte and at the wavelength of the Stoke scattered photons respectively. Here, we also consider the excitation and detection wavelength close to one another. As a reminder, in chapter III, the factor proportional to the SERS intensity was estimated by:

$$f_{RI} \approx 2\pi R_{fiber} L_{fiber} CD \times \left[\eta \frac{1 - e^{-\alpha L_{fiber}}}{\alpha L_{fiber}}\right]^2 \quad (28)$$

In the case of the RCF, the equation becomes:

$$f_{RI} \approx 2\pi L_{fiber} CD \times \left[R_{Ifiber} \left(\eta_I \frac{1 - e^{-\alpha L_{fiber}}}{\alpha L_{fiber}}\right)^2 + R_{Efiber} \left(\eta_E \frac{1 - e^{-\alpha L_{fiber}}}{\alpha L_{fiber}}\right)^2\right] \quad (36)$$

The second term in bracket results from the second effective layer on the inner side of the ring. R_{Ifiber} and R_{Efiber} represent the internal and external radii of the ring and η_I and η_E represent the fractions of the evanescent field that overlap in the inner and outer effective layers.

For the first simulation, we used the following parameters:

Laser: λ_{ex}= 633 nm

Radius of the H_2O center: 12.5 µm

Thickness of the two Au NPs layers: 60 nm

Thickness of the silica ring: t_{ring} = 500 nm

L_{fiber}= 10 cm

Thickness of the surrounding layer filled with water: 10 µm

Coverage density of Au NPs: $CD = 0.05\ particles/\mu m^2$

Relative permittivity of water from Hale and Querry at 633 nm [223]: $\epsilon_h = 1.7734 + 3.9151 \times 10^{-8} i$

Relative permittivity of gold from Rakić *et al.* at 633 nm [224]: $\epsilon_i = -10.577 + 1.2741 i$

Refractive index of silica calculated using Sellmeier equation: $n_{silica} = 1.457$ at 633 nm.

There was a big difference in the size of the elements of the structure, from hundreds of nanometers for the ring thickness to tens of micrometers for the ring diameter. Even by using an adaptive mesh, i.e. larger mesh in the water region and smaller mesh in the silica ring and effective layers to improve the precision of the simulation, the calculation time remained quite long. Thus, to reduce it, we simulated only a quarter of the fiber and we used specific boundary conditions so that the results could be extended to the entire structure of the fiber.

We present in Figure 64 the 2D distribution of the Poynting vector of the first five modes guided inside the silica ring. HE_{11} mode possesses the highest effective index while HE_{91} mode exhibited the lowest. It is worth noting that none of them corresponds to the ring entirely excited. The different modes present several hotspots in the Poynting vector distribution, increasing with the mode number. However, the amount of light overlapping on the inside and outside of the ring are very similar between the five modes as shown in Table 5. Therefore, for the calculations of f_{RI}, we used only the mode with the highest effective index, namely HE_{11} mode in the table. The second noticeable element in the table is that logically the amount of evanescent field is quite similar on each side of the ring. This is easily understandable since the two effective layers have the same thickness and the two layers filled with water are far larger than the reach of the evanescent field.

Table 5 Percentage of evanescent field in every section of the simulated ring suspended in water

Mode	Hollow center filled with H_2O	Inner Au NPs layer	Silica ring	Outer Au NPs layer	Surrounding layer filled with water
HE_{11}	5.084%	3.764%	82.305%	3.764%	5.084%
HE_{31}	5.084%	3.764%	82.304%	3.763%	5.084%
HE_{51}	5.085%	3.766%	82.302%	3.763%	5.085%
HE_{71}	5.087%	3.768%	82.299%	3.762%	5.085%
HE_{91}	5.089%	3.770%	82.294%	3.760%	5.086%

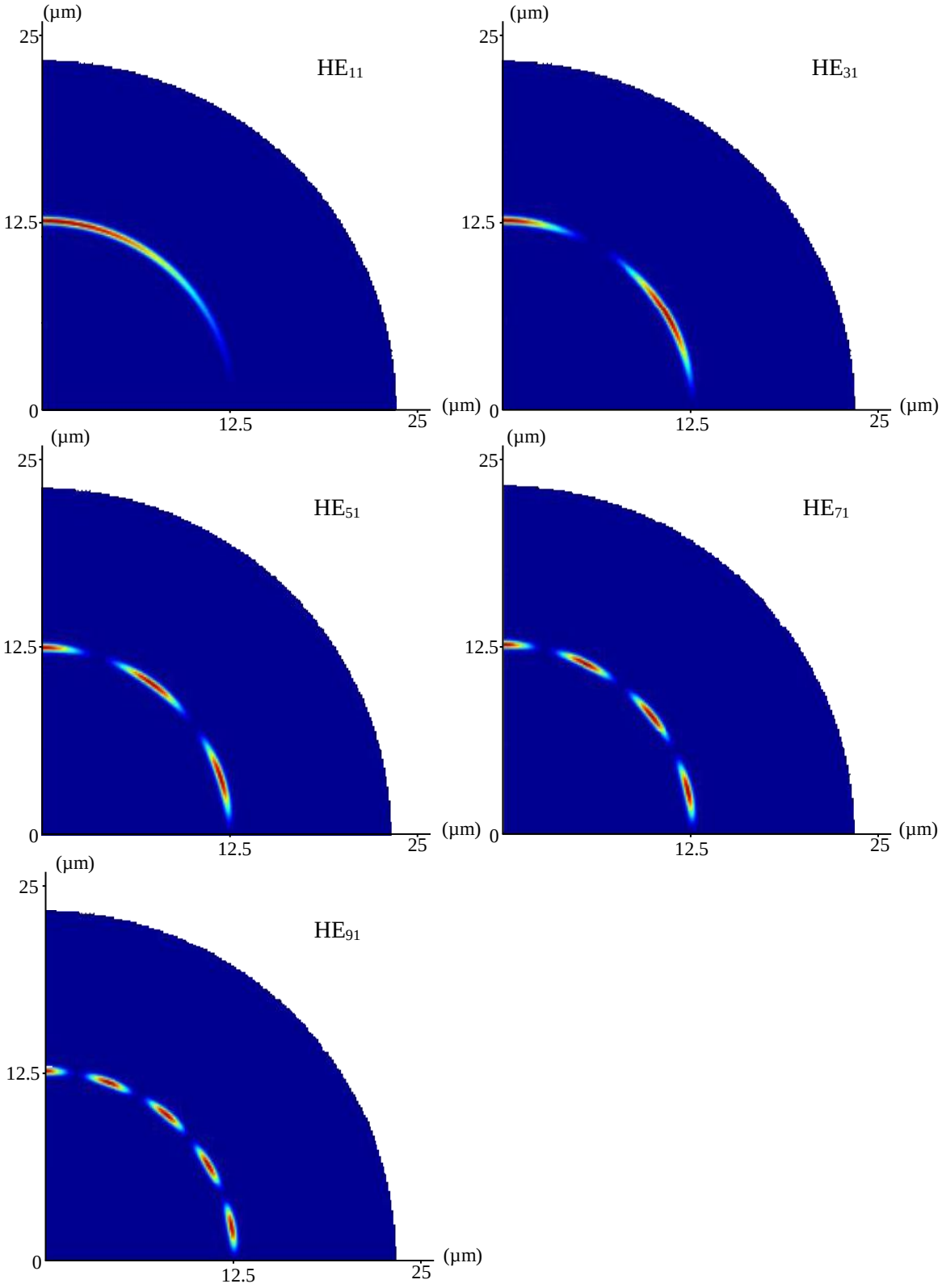

Figure 64 Simulated Poynting vectors of the first five simulated modes with decreasing values of n_{eff} obtained with D_{core}= 25 µm, t_{core} = 0.5 µm and CD = 0.05 particles/µm²

IV.2.2. Comparison between the new design and the standard suspended core fiber

Using the previous parameters and equation 36, we calculated that the factor proportional to the SERS intensity for HE_{11} mode was: $f_{RI} = 85.27\ a.u.$ in this case. To demonstrate the interest of the new

design, this value needed to be compared to the one calculated with a rod in the same conditions. In chapter III, we calculated that for a fiber length of 10 cm and a coverage density of 0.05 particles/µm², the maximum f_{RI} occurs for SuC-PCFs with a core radius of 0.5 µm. It was calculated to be $f_{RI} = 4.93\ a.u.$. This meant that, the RCF exhibits a signal 17.3 times higher than the SuC-PCF (for the used parameters), as shown in Figure 65(a). This is due to the increase in the interaction surface mentioned above and it demonstrates the interest of the RCF. Here, it is worth mentioning that the RCF is also subject to the interplay between the SERS enhancement and the extinction losses. For instance, increasing significantly the coverage density ($CD = 10\ particles/\mu m^2$) resulted in a proportional factor much lower: $f_{RI} = 0.4\ a.u.$ (Figure 65(b)).

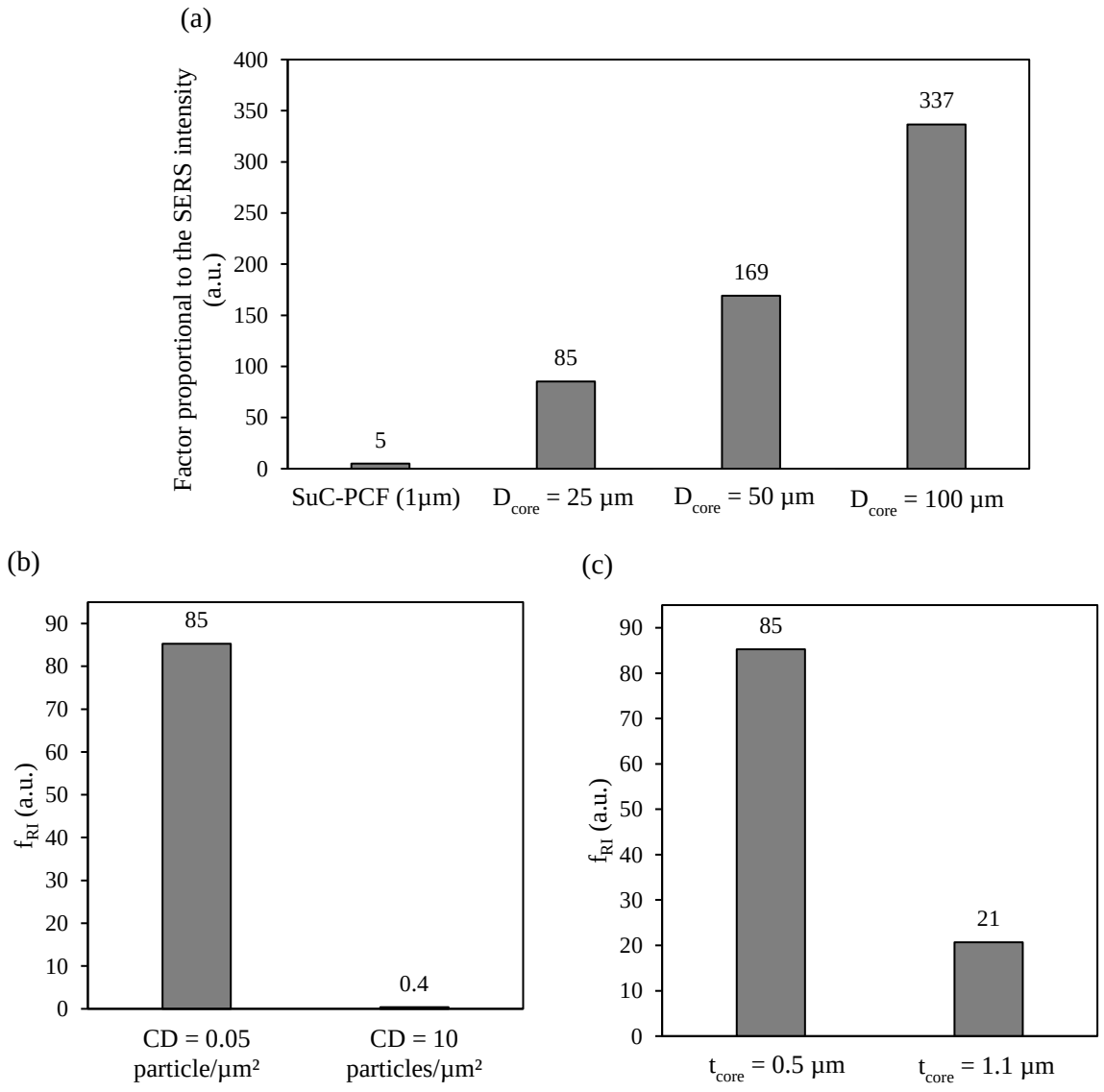

Figure 65 (a) Calculated factor proportional to the SERS intensity for increasing diameters of the ring and the best SuC-PCF with CD = 0.05 particles/µm² and t_{core} = 0.5 µm. (b) Comparison between calculated proportional factors for two CDs and for D_{core} = 25 µm and t_{core} = 0.5 µm. (c) Comparison between calculated proportional factors for two ring thicknesses and for D_{core} = 25 µm and CD = 0.05 particles/µm².

The second aspect that needed to be addressed is the thickness of the core (t_{core}). Indeed, similarly to SuC-PCFs, it has an influence on the amount of evanescent field. We present in Table 6 the portion of light guided in HE_{11} mode in every section of an RCF for the same Au NPs coverage density

($CD = 0.05\ particle/\mu m^2$) and the same diameter (D_{core} = 25 µm) as previously, but for t_{core} = 1.1 µm. It was clear that less light overlapped in the two effective layers. Here, only 1.6% of the light could interact with the analyte and the NPs. In this particular case, it led to a decrease in the factor proportional to the SERS intensity, from 85.27 a.u. to 20.65 (Figure 65(c)). Similar to the behavior studied with the SuC-PCFs, CD and the fiber length also had an impact on the final Raman intensity but we do not present it here, since the general trends are similar to the results presented in Chapter III.

Table 6 Percentage of evanescent field in every section of the simulated ring suspended in water when t_{core} = 1.1µm

Mode	Hollow center filled with H_2O	Inner Au NPs layer	Silica ring	Outer Au NPs layer	Surrounding layer filled with water
HE_{11}	0.848%	0.778%	96.7%	0.782%	0.852%

Finally, we fixed $CD = 0.05\ particle/\mu m^2$ and t_{core} = 0.5 µm and we increased the diameter of the ring. This resulted in increasing the surface of interaction, which, in turn, resulted in increasing the factor proportional to the SERS intensity. For a 50 µm ring, f_{RI} became 169.2 a.u. We kept increasing it until 100 µm, the f_{RI} became 336.6 a.u. (Figure 65(a)). As expected, increasing the diameter of the ring results in increasing the enhancement factor and thus the SERS intensity. However, keeping in mind the ultimate goal of creating a clinically viable SERS sensor, we cannot increase indefinitely the diameter of the ring. As mentioned previously, we envision to incorporate the PCFs inside biopsy needle. Thus, the size of usual needles limits the size of the RCF, which in turn limits the diameter of the ring. If we consider an RCF with 100 µm ring, the size of the external holes would be approximately the same as the center hole, resulting in a 300 µm fiber. We also have to add the thickness of the cladding (twice ~100 µm), which leads to a fiber with an outer diameter of ~500 µm. Although we could slightly decrease the thickness of the cladding and the diameter of the external holes to obtain a larger core, we think that RCFs with the previously mentioned parameters represent a good compromise. They allow for two orders of magnitude enhancements in sensitivity compared to SuC-PCFs while still fitting inside common needles.

To summarize, in this section, we presented a novel fiber topology specially developed for increasing the surface of SERS interactions. This fiber design allows overcoming the antagonism that forced to choose between a good amount of evanescent field and a large surface of interaction with SC-PCFs. In this way, a sensitivity improvement by more than two orders of magnitude can theoretically be reached. We demonstrated that our sensor exhibits the same behavior as SuC-PCF: the NPs coverage density and the length of the fiber played the same role. However, in the case of RCF, the parameters of the core have two separate effects:

- Increasing D_{core} increases the surface of interaction and thus the factor proportional to the SERS intensity
- Decreasing t_{core} increases the amount of evanescent field

This gave us the advantage of increasing significantly the surface of interaction while still being able to control precisely the amount of evanescent field that overlaps in the holes. Once again, this should result in unprecedented sensitivity. In order to verify this experimentally, we fabricated RCF prototypes.

IV.3. Fabrication process

As highlighted previously, in the simulation, the ring was floating in water. In reality, the ring is maintained inside the fiber by thin silica struts. These struts delimit holes. In our case, we decided to

fabricate RCF with six external holes and an additional hole in the center of the ring. This allowed us to have relatively large holes in the cladding to facilitate the incorporation of the analyte and to maintain a symmetrical shape for the ring, i.e. a hexagon shape as we presented here. The design of the RCF is somewhat similar to the design of a HC-PCF. However, in the RCF, the light is not guided inside the central hole but in the silica ring. The diameter of the ring core needs to be as big as possible so that its relatively vast perimeter creates a large surface of interaction whereas its controlled thickness ensure that a good amount of light interacts with the analyte.

The fibers were fabricated using the stack-and-draw process, similarly to SuC-PCFs. The main difference lies in the structure of the stack: here, seven capillaries were stacked. It is worth mentioning that preliminary fabrication tests of RCFs had already been fabricated by the team before the beginning of my PhD.

We aimed to get as close as possible to the ideal case of a silica ring suspended in water. For that, some requirements were necessary. The first one was that the ring needed to be thicker than the struts. In this way, the light would be preferably guided inside the ring. The second requirement was that the ring needed to be optically isolated from the struts holding it in place inside the fiber. If not, the RCF could have been seen as a six-core SuC-PCF, since the light would be confined at the apices formed by the struts and the ring instead of being guided in the entire ring. Therefore, to isolate the ring, we needed to maintain the apices open to avoid any confinement of the light inside them.

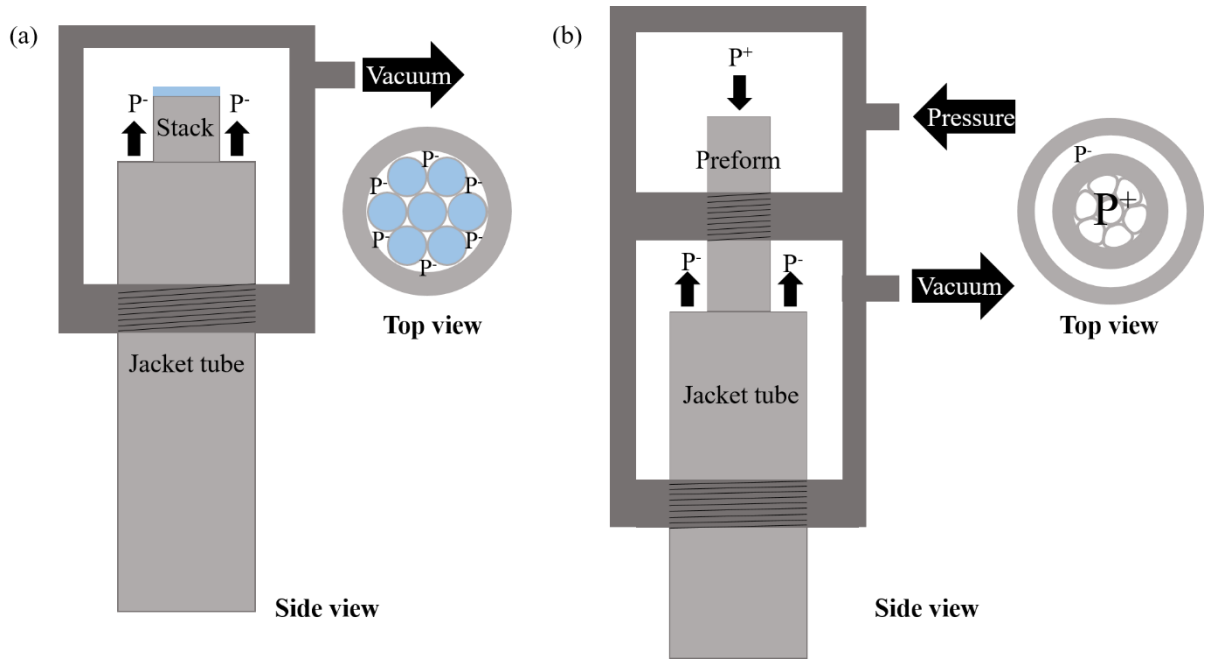

Figure 66 Schematics illustrating the pressurizing system used during the first attempts of (a) the cane and (b) the fiber drawings. The blue sections represent the closed capillaries. P^- and P^+ represent respectively the vacuum and the overpressure applied in the different sections of the stack and preform.

Several attempts were required to obtain the final RCFs. Similar to SuC-PCFs, the first step consisted of drawing the capillaries. We drew them from two tubes with different thicknesses. The thicker one was put in the middle of the stack and surrounded by six thinner capillaries. We did this to respect the first requirement, i.e. for the light to be guided preferably in the silica ring. The seven capillaries were fused with a burner to close the top end. Once the stack was assembled and put in a jacket tube, we used the same process as in Chapter III to apply vacuum between them as shown in Figure 66(a). Depending on the value of the vacuum applied, the structure of the cane was different. We first applied -2 kPa. The resulting cane is shown in Figure 67(a). Here, we can clearly see the structure of the stack and that the

apices were open around the center capillary. However, based on previous experiences, there were too open, which might have resulted in destabilizing the structure during the drawing of the fiber. We applied more vacuum (-5 kPa) to close further the apices (Figure 67(b)). This time, the apices were almost closed. Finally, we decreased the value of vacuum applied to -3 kPa (Figure 67(c)) and we obtained the cane we wanted, i.e. a regular structure with apices neither too open nor too closed.

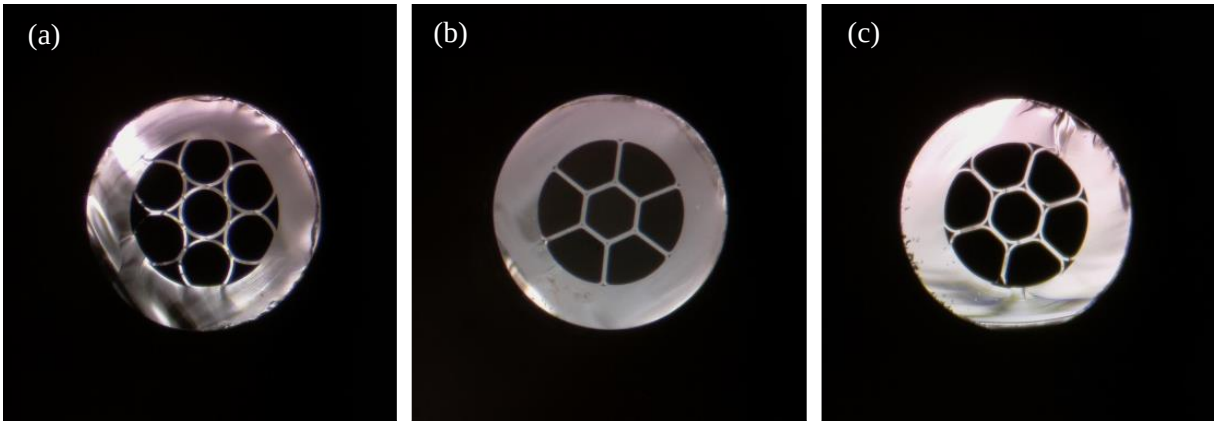

Figure 67 Pictures of the cane obtained for different values of vacuum applied between the jacket tube and the stack with closed capillaries: (a) vacuum = -2 kPa, (b) vacuum = -5 kPa, (a) vacuum = -3 kPa.

We put one of these canes in a jacket tube. We applied pressure inside the holes of the cane and vacuum between the cane and the jacket tube as illustrated in Figure 66(b). The main dimensions of the final fiber are available in Table 7 and SEM pictures are available in Figure 68(a) and (b). During the drawing, we wanted to see if increasing the outer diameter of the fiber also increased the diameter of the ring. For that, we fixed the temperature of the furnace, the tension on the fiber, the vacuum applied between the cane and the jacket tube, and the pressure applied in the cane holes. We changed only the descent speed of the preform in the furnace and the speed at which the fiber was rolled on the capstan at the bottom of the drawing tower. Figure 68(c) and (d) show the face of the RCF with an outer diameter of ~400 µm. Its parameters are also available in Table 7. We can see that increasing the core size of ~100 µm only increases the diameter of the ring by ~10 µm. Though we increased the RCF outer diameter, the thickness of the core and the struts remained relatively unchanged since we did not modify the others drawing parameters. It is worth noticing that for the two RCFs, the apices are well open for each fiber. In addition, the ring is significantly thicker than the struts. As already explained, these two conditions will facilitate the confinement of the light inside the ring. Finally, the thicknesses of the struts and the ring are quite remarkable. They are only few hundreds of nanometers, which is two orders of magnitude lower than the ring diameter. Fabricating a structure with these dimensions without any collapse is already a great achievement.

Table 7 Parameters of the first RCFs drawn during my PhD

RCF	Outer diameter (µm)	Hollow region diameter (µm)	Ring diameter (µm)	Ring thickness (nm)	Struts thickness (nm)
1	295	182	40	415	110
2	390	260	49	500	115

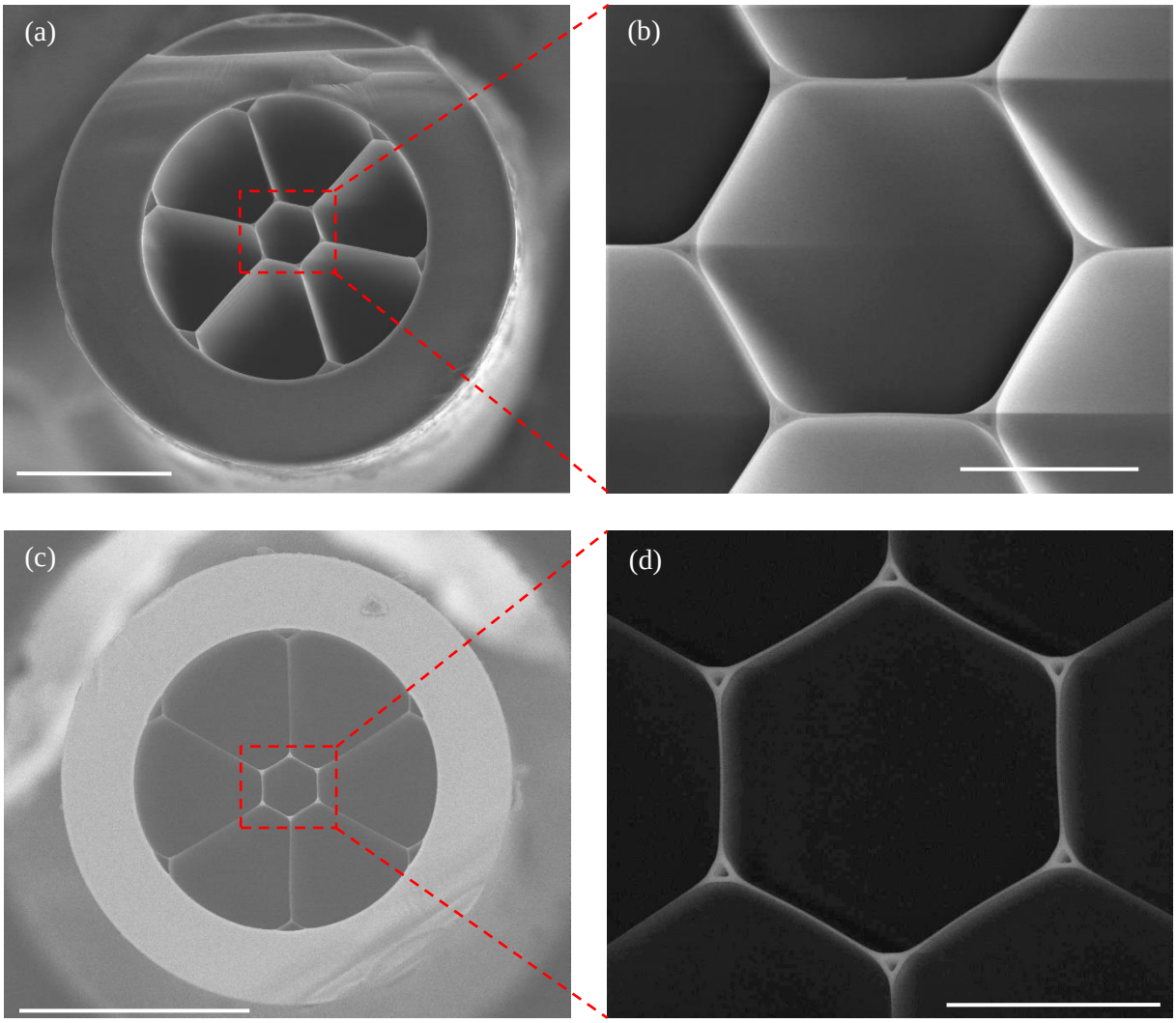

Figure 68 SEM pictures of (a) RCF 1, (b) zoom-in on the ring core, (c) RCF 2 and (d) zoom-in on the ring core. The open apices are visible on (b) and (d). The scale bars represent respectively (a) 100 µm, (b) 20 µm, (c) 200 µm and (d) 30 µm.

Based on the simulation and the parameters of the two fabricated RCFs, these two fibers should be more sensitive than SuC-PCFs. However, we wanted to draw RCFs with even larger diameter to benefit from the largest possible surface of interaction. With that in mind, we made several attempts using the same technique but the core size was still limited compared to the size of the other holes. Thus, we decided to try a new approach. Instead of closing the capillaries, we decided to apply pressure inside them. To do so, we need to close the interstitial holes between the capillaries at the top of the stack. If not, the two chambers would not have been sealed and the pressure and vacuum could not have been applied. We glued the center capillary to the other ones to isolate the two chambers, as shown in Figure 69.

It is worth mentioning at this point that the drawing tower has two sides, one assigned to the drawing of capillaries and canes and the other one assigned to the drawing of fibers. On the capillary side of the tower, the capillaries are drawn using tractors and they are regularly cut (usually every meter). On the fiber side of the tower, the fiber is drawn by a capstan and rolled onto a spool. Several hundreds of meters of fiber can be rolled on the spool during a single drawing. The final step of the previous fiber drawings (SuC-PCFs and RCFs) were systematically done on the fiber side. However, this time, we decided to draw the fiber on the cane side of the drawing tower. This allowed us to draw fibers with outer diameter superior to 500 µm more easily. To draw the last step of the RCF, we used the same

system of pressure as for the other fibers (Figure 66(b)). During our first try, we targeted an outer diameter of 500 µm without applying any pressure or vacuum. When the targeted outer diameter was obtained, we turned on the vacuum and the pressure successively. This resulted in inflating the holes and thus the outer diameter. We managed to have a ring with 110 µm diameter and 0.5 µm thick, which was what we were targeting. However, the pressure and vacuum applied also resulted in collapsing the interstitial holes, which led to closing the apices of the RCF. We tried to change the pressure and vacuum parameters during the drawing but the holes remained closed. A picture showing a zoom in the ring region of this fiber with closed apices is available in Figure 70.

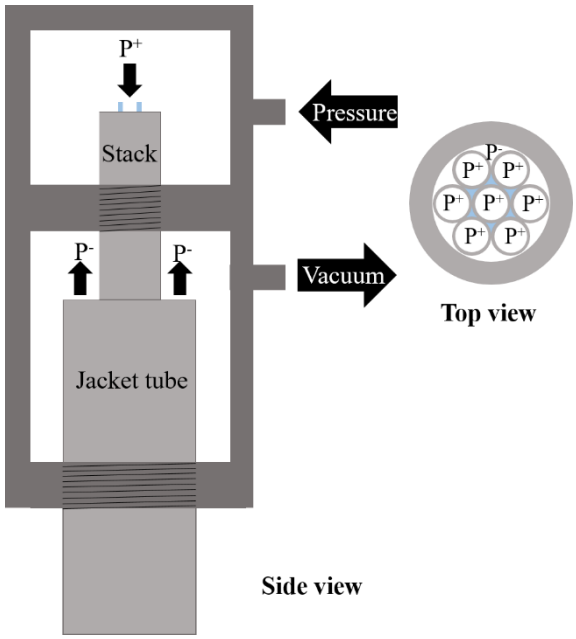

Figure 69 New pressurizing system used to fabricate the cane. The blue sections represent epoxy glue.

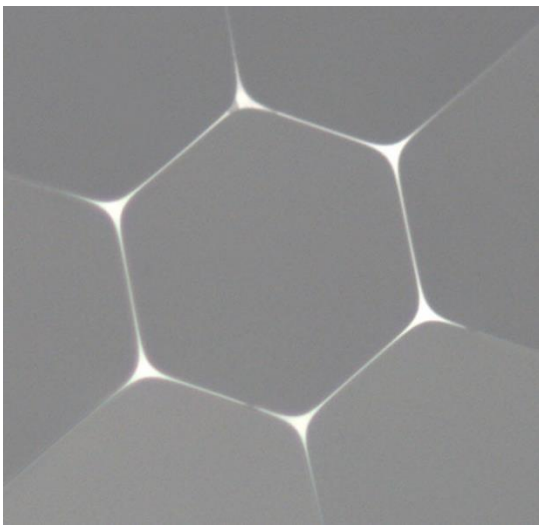

Figure 70 Zoom-in on the ring of the RCF with closed apices.

During a subsequent try, we decreased the temperature of the furnace from 2015°C to 1945°C. This tended to decrease the viscosity of the silica, which resulted in maintaining open the apices. The only counterpart was that we needed to apply more vacuum and pressure to inflate the holes. This gave us more accuracy for tuning the applied pressure. We managed to draw RCF 3 with a ring diameter of ~100 µm and a thickness of 0.5 µm. However, the struts were too thin and broke at some point during

the drawing. We decreased slightly the pressure and we obtained RCF 4 with a ring diameter of ~90 µm and a thickness of 0.7 µm with open apices. The dimensions of the two RCFs are summarized in Table 8, and SEM pictures are available in Figure 71. A zoom on one apex is available in Figure 72. For this fiber also, the ring core is thicker than the struts. In addition, the diameter of the ring is similar to the cladding diameter of a single mode fiber while its thickness is smaller than 1 µm. Therefore, the fabrication of such fiber is remarkable and to the best of our knowledge, this is the first time such fiber is reported.

Table 8 Parameters of the second set of RCFs drawn during my PhD. The strut thickness was too thin to be measured precisely so we do not present their dimensions here

RCF	Outer diameter (µm)	Hollow region diameter (µm)	Ring diameter (µm)	Ring thickness (nm)	Struts thickness (nm)
3	600	382	101	520	NA
4	580	330	89	740	NA

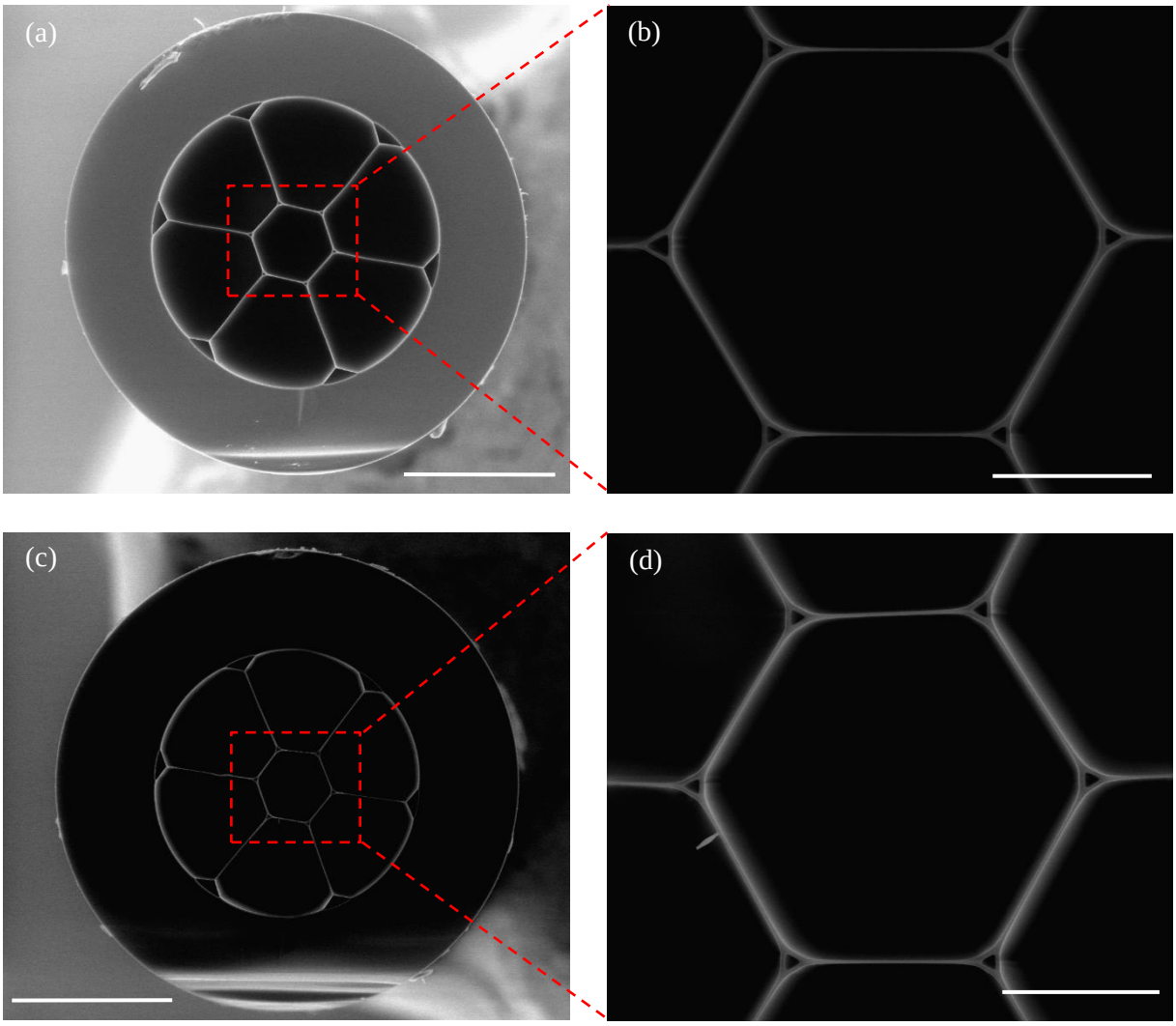

Figure 71 SEM pictures of (a) RCF 3 (outer diameter of 600 µm), (b) zoom-in on the ring core, (c) RCF 4 (outer diameter of 580 µm) and (d) zoom-in on the ring core. The open apices are visible on (b) and (d). The scale bars represent respectively (a) 200 µm, (b) 40 µm, (c) 200 µm and (d) 40 µm.

This fiber represents a great innovation since it demonstrates that we are able to fabricate fibers with large cores, i.e. large surface of interaction, while maintaining a core extremely thin that allows for

relatively large portion of evanescent field. In addition, the open apices and the difference of thickness between the core and the struts help in guiding the light preferably inside the silica ring. We envision that this fiber may be very well used with other optical sensing techniques, such as fluorescence, and exhibit remarkable properties. Now that we have fabricated the RCF with giant cores, we can focus on the application of these fibers for sensing.

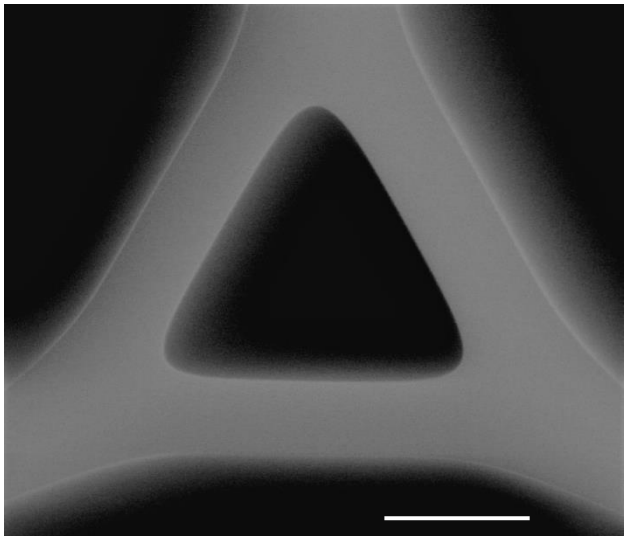

Figure 72 SEM picture presenting an open apex between the ring core and the struts holding it in place. The scale bar represents 2 µm.

IV.4. Configurations used to excite the core and SERS sensing

IV.4.1. Envisioned solutions to properly excite the ring core

Because of its dimensions and topology, it was clear that exciting properly the ring core would be a challenge. Indeed, for SuC-PCFs, the sizes of the laser beam and the core were similar resulting in a good coupling of the light. Here, the sizes of the laser beam under the Raman microscope and the core were extremely different, about two orders of magnitude. Hence, the coupling of the light to the fiber core was far from ideal. To illustrate this matter properly, we realized a series of tests. The first one consists of directly focusing the laser on the ring using a small magnification objective lens (5x). Indeed, small magnification objectives produce wider laser beams, which can facilitate the excitation of the entire ring. However, as shown in Figure 73, the majority of the light was guided inside the holes and not in the ring.

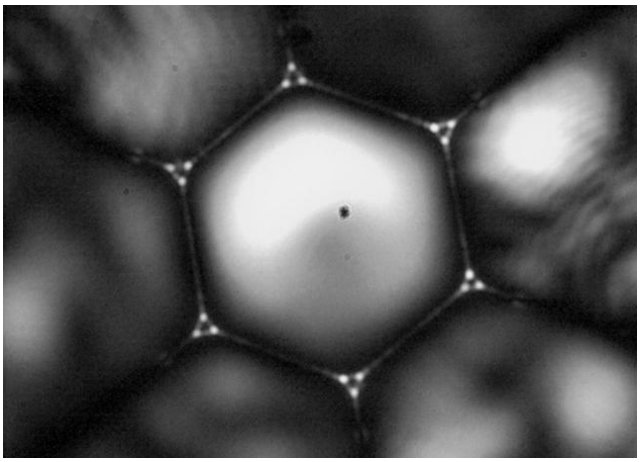

Figure 73 Picture of the output of an RCF excited by focusing the laser directly using 5x objective lens.

The second test consists of increasing the magnification of the objective lens. This would allow us to focus the laser on a small portion of the ring and illustrate that this configuration does not result in exciting the entire ring. In Figure 74(a), we present a picture of the entry face of the RCF taken with a 40x objective. The red circle represents the area excited with the laser. Figure 74(b) depicts the resulting output distribution of the light when excited by a 785 nm laser. It is clear that focusing the light only on a small portion of the core results in exciting non-uniformly the entire ring. Since the core is not entirely excited, it means that the benefit of a large surface of interaction is lost. In these conditions, the RCF would not possess any advantages over SuC-PCFs.

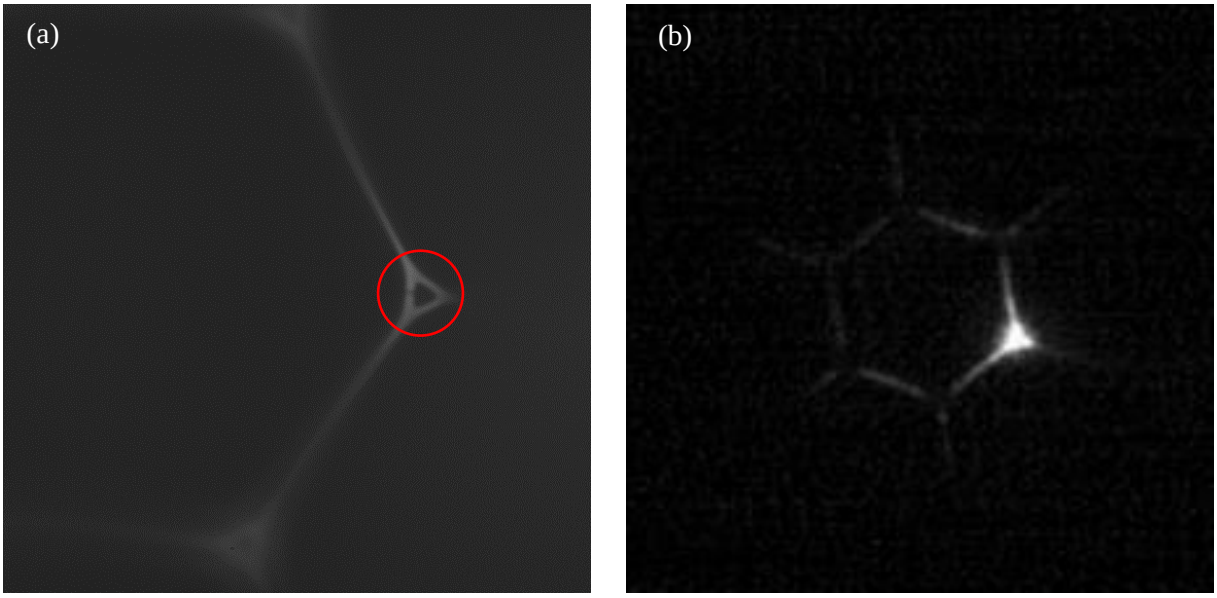

Figure 74 (a) Picture of the entry face of the RCF. (b) Output distribution of the light when the laser is focused on the circle of (a).

To further illustrate that; we realized SERS measurements in this configuration. For that, we prepared the RCF using the protocol describe in chapter III and instead of ATP, we used 2-naphthalenethiol (2-NT), which is another Raman tag that has the ability to bind to Au NPs through its thiol group [252]. The signature spectrum of 2-NT is available in Figure 75. This time, we used the main peak at 1380 cm^{-1} for the study. We focused the light directly on one apex of the ring of the RCF with a 40 µm core (RCF 1) and successively measured the signal coming from each apex. We acquired four spectra for each apex to remove any outliers, and we averaged the SERS signal. The measured SERS intensities were varying significantly depending on the apices as shown in Figure 76. We observed that 37% variation between the six apices with the 50x objective lens. We estimated that most of the variations may be explained by the position of the excitation laser, which was varying slightly despite our efforts to focus the laser on similar locations for each apex. The other source of variations might be due to the deposition of the NPs. Indeed, between two apices, the density of NPs may vary along the length of the fiber. We also measured the signal coming from the six sides of the ring and we obtained similar results. This further stresses the need to excite the ring entirely. Indeed, if the ring were fully excited, the SERS intensity would be averaged across all the apices and all the sides of the ring instead of coming from only one of them.

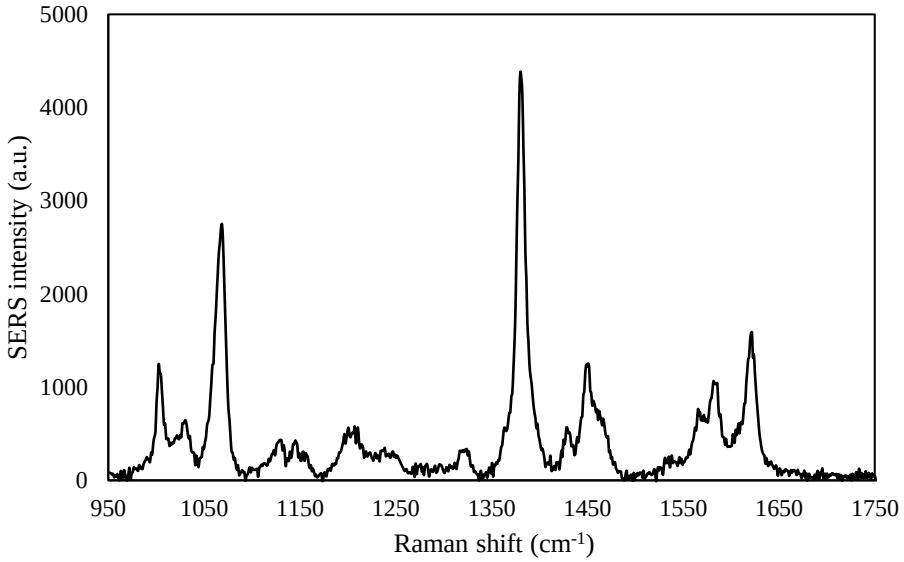

Figure 75 Signature SERS spectrum of 2-NT.

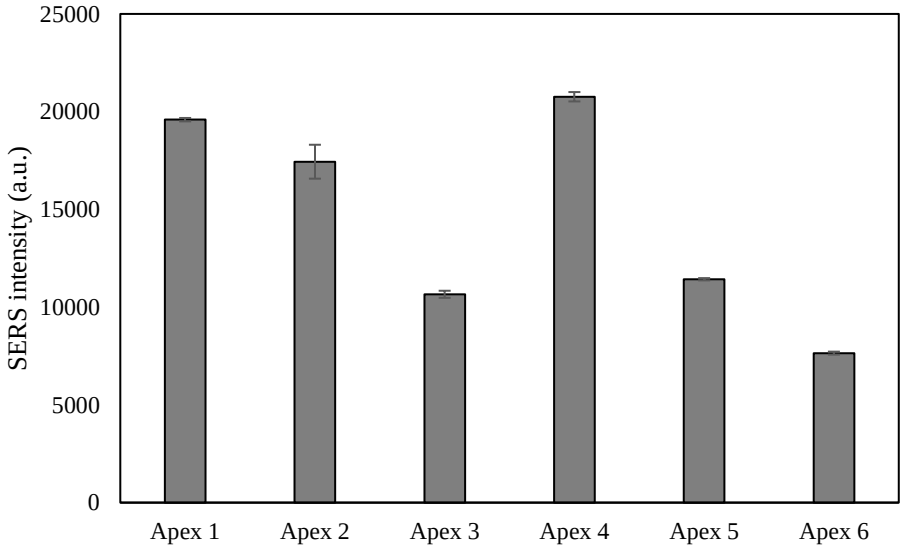

Figure 76 SERS intensity measured on the six apices of a single RCF. The error bars represent the variations measured across the four spectra for a single apex.

These results illustrate perfectly that exciting the core of the RCF is not trivial. To overcome these foreseen limitations, we envisioned two possible solutions:

1) Butt-coupling the RCF to a MMF

This solution is fast, very simple to realize and allows a plug-and-play setup. We can imagine that in the future, after developing as a biopsy needle, the clinician would only have to plug the fiber into a connector and measure for readout. Unfortunately, although this approach allows for exciting entirely the ring core, the coupling loss could remain relatively high.

2) Tapering the RCF on one end

In this configuration, the taper is fabricated so that the size of the ring is drastically decreased at the input end. This would allow coupling the light using large magnification objective lens (x40 or higher) like in SuC-PCF. Subsequently, the light would propagate in the ring until reaching the un-tapered side of the RCF, where it would be uniformly distributed over the entire ring. We estimate that this solution

is the best way to excite entirely the core with limited coupling loss. Unfortunately, tapering is more time-consuming than the butt-coupling to MMF and an additional care needs to be taken to ensure that the fabrication of the tapers is reproducible.

In the following sections, we describe in more detail each solution.

IV.4.2. Butt-coupling to multimode fiber

IV.4.2.1. Demonstration of light injection

The first solution imagined to fully excite the core was based on the butt-coupling technique. It consisted of exciting a MMF with a core large enough and then in butt-coupling the RCF at the output of the MMF. In this way, the light was shone onto the entire ring, yielding an overall excitation. This technique is fast and very simple to realize. A schematic illustration of the excitation principle is available in Figure 77. We did not represent the major part of the SERS setup since it remains unchanged compared to the one used in chapter III with SuC-PCFs. The only difference lied in the fiber region. Here, instead of focusing the laser directly into the core of the fiber probe as we did in chapter III, we focused the light on the large core of the MMF. Subsequently, we used XYZ precision translation platforms to align the other end of the MMF with the RCF so that the ring was set right next to the core of the MMF.

Figure 77 Schematic illustrating the principle of RCF excitation using a MMF.

Pictures of the used RCF and measured distribution (with a camera) of the field at the output of the RCF using the MMF excitation are available in Figure 78(a) and (b). Compared to the previous excitation technique, we can see that this time, the entire ring is excited. It means that butt-coupling the RCF to a MMF allows exciting properly the RCF. It is also worth mentioning that a small portion of the light is still guided inside the center hole. To illustrate the importance of leaving the apices open during the fabrication process, we did the same experiment with a similar fiber with closed apices. As we can see in Figure 78(d), the light stayed confined inside the apices and it did not propagate inside the sides of the ring. Therefore, this demonstrated that our requirement to leave the apices open during the drawing of the fiber was extremely important so that the ring can be more uniformly excited.

We just showed that exciting properly the RCF with a MMF was possible. Subsequently, we needed to measure two distinct coupling losses:

- The first one concerned the coupling from the MMF into the ring core to estimate the amount of light that will be guided in the RCF.
- The second one concerned the coupling from the ring core back to the MMF to estimate the amount of light that can enter the spectrometer.

To measure the first coupling loss, we measured the power at the MMF output (location 1 in Figure 79) and after the RCF (location 2 in Figure 79). We estimated that the loss was about 15 dB. It is worth mentioning that this value also includes the attenuation loss of the RCF. The measured loss was very large and it meant that for a given power of light exiting the MMF, the portion of light that would be guiding inside the ring core was much weaker. This limitation could be overcome by simply increasing

the power of the laser. Logically, the more power enters the MMF, the more power exits it and enters the ring, resulting in more light available to interact with the NPs/analyte.

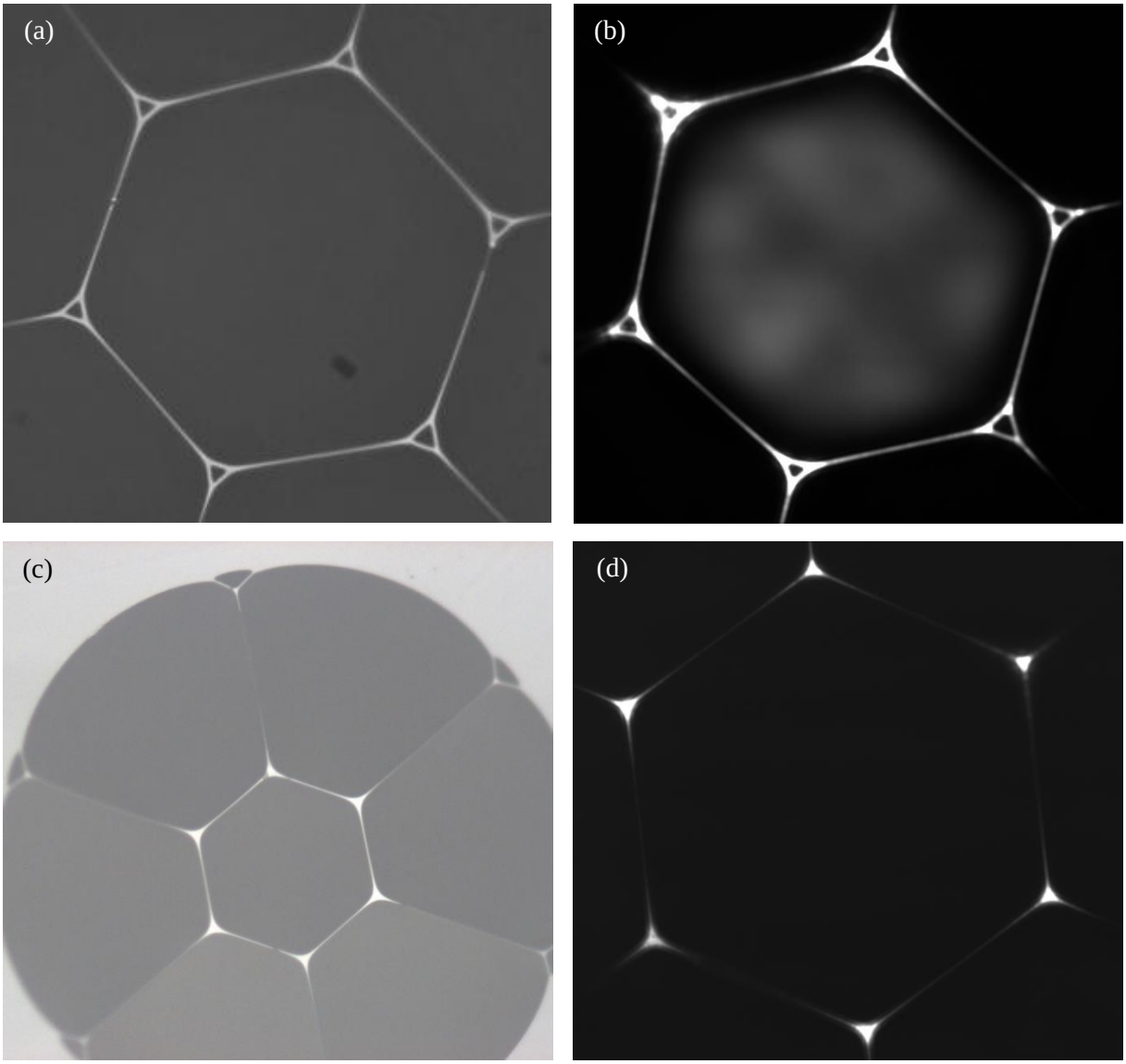

Figure 78 Pictures of (a) the RCF with open apices excited by a MMF, (b) the output distribution of the light at the end of the RCF, (c) the fiber with closed apices and (d) the distribution of the light at the end of this fiber.

The second coupling loss was a very important aspect since it would determine the amount of SERS signal that was coupled back from the RCF into the MMF and finally to the spectrometer. To estimate it, we excited a first section of MMF. Subsequently, we butt-coupled the RCF to excite the ring core and we measured the power at the output of the RCF (location 2 in Figure 79). Finally, we butt-coupled a new section of the same MMF after the ring core and measured the power at the output of this new MMF section (location 3 in Figure 79). In this way, the difference of power between the one measured after the RCF and after the second MMF allowed estimating the coupling loss of the light traveling from the RCF towards the MMF. With this technique, we estimated it to be between 3 and 4 dB. It is much lower than for the coupling from the MMF to the RCF. It is worth noting that in this configuration the attenuation loss of the RCF is not included in the measure. Nevertheless, the measured value appears logic because the MMF possesses a wide core that can collect a large portion of the light that propagated in the RCF. In summary, thanks to the butt-coupling between the MMF and the RCF, the ring core could

be entirely excited and the second coupling loss (from the RCF to the MMF) was not too important. Thus, we could start studying the effect of the new design on the final SERS intensity.

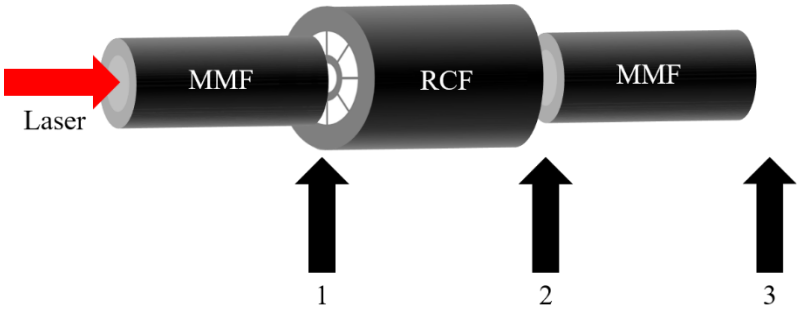

Figure 79 Schematic illustrating the locations where the power was measured to estimate the coupling loss from MMF towards RCF and from RCF towards MMF.

IV.4.2.2. SERS sensing with the multimode fiber and ring core fiber configuration

The ultimate goal of this section was to compare the sensitivity of the new design to the best SuC-PCF sensor realized in chapter III. Here, we wanted to validate the simulation results and demonstrated practically the interest of the new fiber design. Before being able to compare the two fiber designs, we needed to make sure that SERS sensing was possible using MMF-RCF configuration. In other words, we needed to check that this configuration allowed collecting a SERS signal strong enough to be detected and processed. Subsequently, we needed to find the best MMF/RCF combination. Indeed, it exists a wide variety of MMFs with different core sizes and numerical apertures. Finding the one that fitted the best the RCF features would ensure that the strongest SERS signal could be detected. This would allow us to compare the two fiber designs in the best conditions possible.

To make sure that SERS sensing could be achieved with the MMF-RCF configuration, we prepared RCF samples using the protocol presented in chapter III and we used ATP as Raman tag. We present in Figure 80(a) the SERS signal measured using the MMF excitation setup. We also measured the SERS signal using direct focus on one of the ring apices as a means of comparison. The signal measured by focusing the light directly onto an apex was similar to the ATP signature spectrum. However, the signal obtained using the MMF was much weaker and did not exhibit the two characteristic peaks of ATP. This difference in sensitivity may be explained by the two combined coupling losses (from the MMF towards the RCF and from the RCF back to the MMF and the spectrometer). As mentioned previously, increasing the power of the incident laser resulted in increasing the number of photons guided inside the ring, which in turn increased the number of Raman scattered photons. More practically, when we increased the power of the incident laser, we could see that the Raman signal of ATP was still present (Figure 80(b)). The two ATP peaks at 1490 and 1590 cm^{-1} were visible though they were less sharp than on the reference spectrum. This meant that we were able to achieve SERS sensing using MMF configuration. Unfortunately, we were forced to use large laser power to ensure that the SERS signal can be detected. Another important remark to note on Figure 80(b) is the presence of a strong signal in the 950-1300 cm^{-1} range. This signal came from the silica of the two fibers and mainly from the MMF. Here, it became problematic since it overshadowed a large portion of the ATP signal.

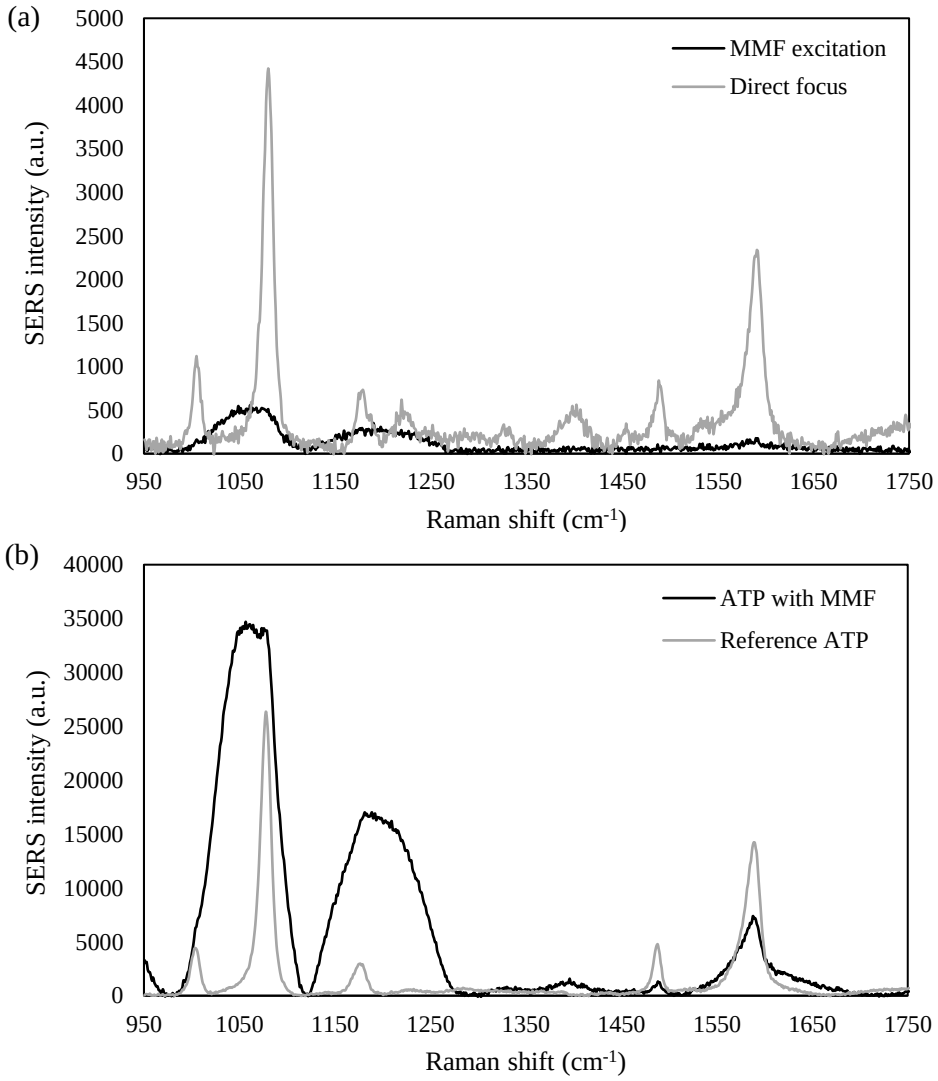

Figure 80 (a) SERS spectra obtained by exciting the RCF with a MMF (dark) and by directly focusing the laser on one apex (gray). (b) SERS spectra obtained by exciting the RCF with a MMF for larger laser power than in (a) (dark) and ATP signature spectrum (gray).

To limit the influence of the silica signal, two approaches could be used:

- Decreasing the length of the MMF
- Replace the analyte with one that possesses signature peaks outside the silica background.

In the following, we present the results obtained with the two approaches.

Decreasing the length of the MMF

We plotted in Figure 81(a) the spectrum measured with a 70 cm long MMF. For this fiber length, the silica was extremely intense. Subsequently, we cut the MMF repeatedly and measured the Raman intensity of the strongest peak of silica (~480 cm^{-1}) for each fiber length (Figure 81(b)). It can be noted that the intensity varies quite linearly with the fiber length. Thus, taking the shortest length of MMF possible would result in decreasing significantly the silica background. Unfortunately, due to the structure of the Renishaw spectrometer, a minimal length of 30 cm was required. As we can see in Figure 81(b), the silica signal remains quite intense for this MMF length. This yielded that we could not use this approach to reduce significantly the influence of the silica background.

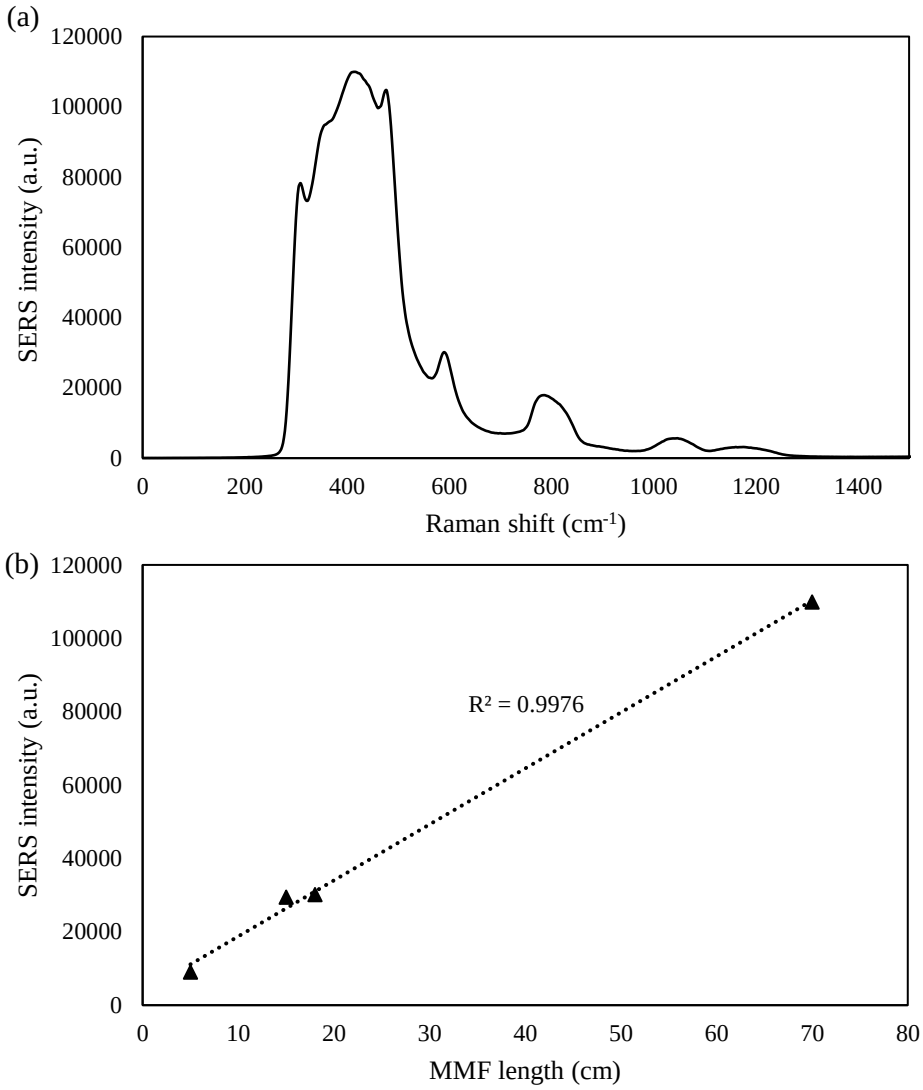

Figure 81 (a) Silica Raman signal measured using 70 cm long MMF. (b) Variation of the Raman intensity of the 480 cm^{-1} peak of silica for different lengths of MMF.

Changing the Raman reporter

The second approach envisioned was to replace the Raman reporter with one that possesses its signature peaks outside the silica background. In this way, they would still be detectable even with the strong silica signal. We selected 2-NT as it exhibited the same properties as ATP (ability to bind to Au NPs) and it possesses a strong peak at 1380 cm^{-1}. We present in Figure 82 the theoretical spectrum of 2-NT, the spectrum measured using the MMF without subtracting the background and the same spectrum after removing the background using a dedicated software. For more readability, we offset the three curves. As we can see, once the silica background was removed, the signal of 2-NT was well detected. Hence, we used this approach to limit the influence of the silica signal for the subsequent studies.

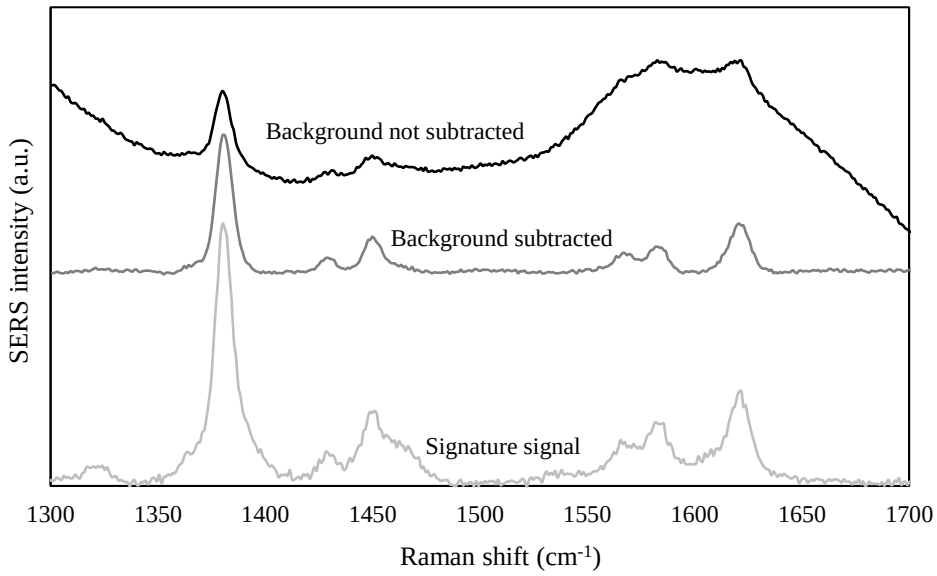

Figure 82 SERS spectrum of 2-NT collected with an RCF using the MMF configuration (black), same spectrum after removing the silica background (dark gray) and signature spectrum of 2-NT (light gray).

Subsequently, we could select the MMF that fitted the closest the RCF features to ensure that the RCF was in the best conditions possible in order to maximize the SERS signal detected. At the time, we did not have fabricated the RCFs with 101 µm and 89 µm core diameters (RCFs 3 and 4) so we studied the excitation of the ring core using the RCF with the 40 µm core (RCF 1). The test consisted of butt-coupling successively the same RCF sample to MMFs that possessed different features to determine which MMF/RCF combination exhibited the strongest SERS signal. For that, we used five MMFs with different core diameters and numerical apertures (NA):

- MMF 1: D_{core}= 200 µm, NA = 0.22
- MMF 2: D_{core}= 200 µm, NA = 0.39
- MMF 3: D_{core}= 200 µm, NA = 0.5
- MMF 4: D_{core}= 400 µm, NA = 0.39
- MMF 5: D_{core}= 400 µm, NA = 0.5

The experimental protocol was the following. First, we prepared a 10 cm long sample of RCF 1 using the short protocol described in chapter III. Then, we placed the RCF on the first XYZ platform. Later, we fixed one end of MMF 1 under the Raman microscope and the other end on the second XYZ platform. We aligned the two fibers so that the core of the MMF and the ring core were the closest possible to one another. Then, we acquired the SERS signal repeatedly. We first moved the end of the MMF under the microscope until we acquired the strongest SERS signal possible and we fixed the position of the microscope platform. Subsequently, we proceeded similarly with the XYZ platforms until we obtained the highest SERS intensity possible. Once the position of each platform was fixed, we acquired ten spectra and averaged the signal in order to remove any outliers. Finally, we proceeded likewise with the four other MMFs. We plotted in Figure 83 the average SERS intensities measured with each MMF. As we can see the MMF with 200 µm core and 0.39 NA was the one that gave the strongest SERS signal. Thus, we used this fiber as the excitation source for the comparison between the RCF and best SuC-PCF.

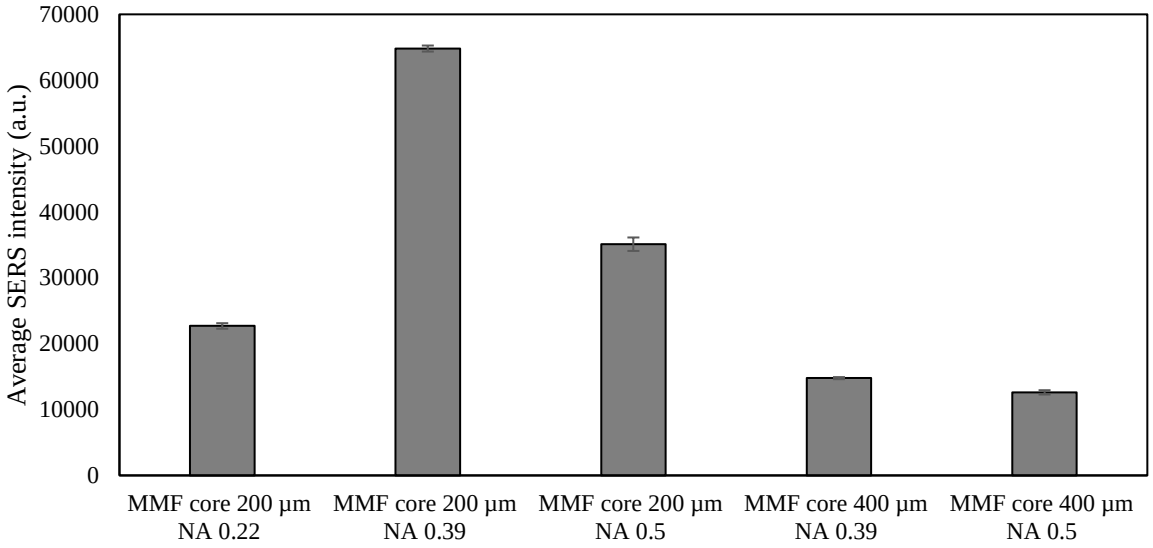

Figure 83 Average SERS intensities of the 2-NT 1380 cm^{-1} peak measured using different MMFs to excite RCF 1. The error bars represent the standard deviation between the 10 measurements acquired to calculate the average intensity.

Now that we were sure to be in the best conditions possible, we could compare the RCF and the 3.5 µm core SuC-PCF. To compare both fibers, they needed to be in the same configuration. Since the advantage of the RCF over the SuC-PCF lies in a greater surface of interaction due to the large ring, we were forced to compare them in the configuration where the ring was entirely excited, i.e. with MMF excitation. For that, we prepared the two fibers simultaneously using the short protocol. Then we used the setup with MMF 2 (Dcore= 200 µm, NA = 0.39) previously described and we placed the SuC-PCF on the XYZ platform. We moved the different platforms until obtaining the strongest SERS intensity and we acquired ten spectra to average the SERS intensity of the 1380 cm^{-1} peak of 2-NT. Then, we replaced the SuC-PCF by the RCF with the 40 µm ring (RCF 1) and we proceeded similarly. To ensure that the trend of the results was correct, we did the same experiment four times and for each case, we normalized the intensity based on the highest intensity between the two fibers. The results are shown in Figure 84.

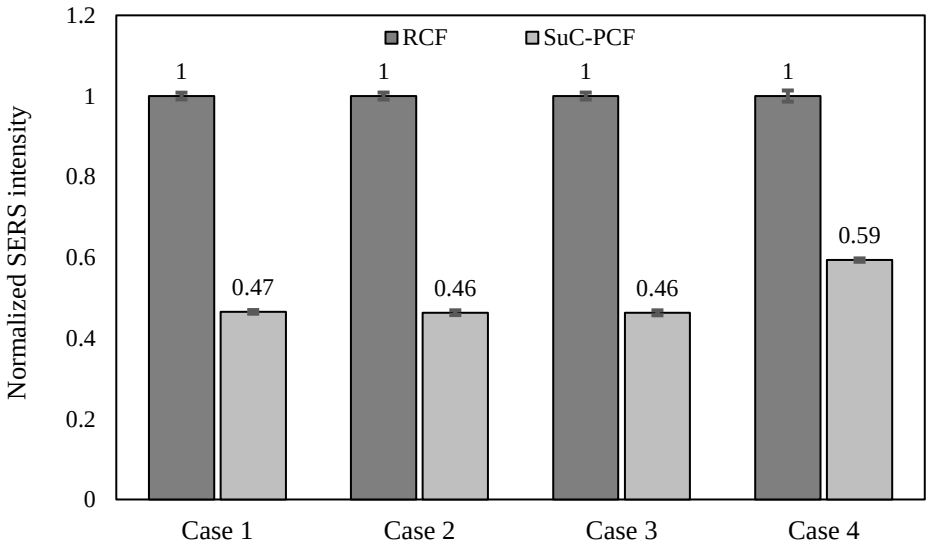

Figure 84 Comparison of the SERS intensities measured with RCF 1 and 3.5 µm core SuC-PCF. The experiment was repeated four times to ensure the authenticity of the results. The error bars represent the standard deviations measured over the ten spectra acquired per fiber.

We can see that, in each case, the RCF was more sensitive than the best SuC-PCF, with a signal approximately twice stronger. To see if these results were coherent, we calculated the factors proportional to the SERS intensity for each fiber design using equations 28 and 36. For this simulation, we used the approximated designs of a rod for SuC-PCF and a circular ring for RCF but we applied the parameters of the real fibers to be as close as possible to the real case. The parameters used for the simulation are summarized in Table 9. In addition, we simulated the two fiber designs surrounded by air this time since we dried them prior to the measurement. With these parameters, we calculated: $f_{RI\ SuC-PCF} = 0.68$ and $f_{RI\ RCF} = 5.43$ yielding an estimated enhancement factor due to the RCF design of approximately 8. This factor is quite far from the two orders of magnitude discussed at the beginning of this chapter. This can be explained by the value of the coverage density. Indeed, here we simulated a coverage density similar to the one measured on the SEM pictures of SuC-PCF in chapter III. Although this coverage density was optimized for 3.5 µm core SuC-PCF, it was not the case for the RCF. In any case, our experimental results fit relatively well with the simulated enhancement factor due to the RCF design (8). The discrepancies can be explained by the approximations made during the simulation:

- not the real fiber designs (rod and circular ring)
- equal distribution of the NPs in the simulation
- not the exact density of NPs simulated
- no Raman-active molecule simulated
- no coupling efficiency taken into account in the simulation.

Table 9 Parameters of the real SuC-PCF and RCF used to simulate their estimated f_{RI}

Fiber	L_{fiber} (cm)	D_{core} (µm)	t_{core} (µm)	CD (particles/µm²)
SuC-PCF	10	3.5	NA	30
RCF 1	10	40	0.415	30

To summarize, in this section we were able to compare the sensitivity of our new design with that of our best SuC-PCF. This was possible by exciting entirely the ring core using a fast and simple excitation technique. Unfortunately, the coupling losses from the MMF to the RCF (light injection) and inversely, from the RCF to the MMF (signal collection), were very large compared to the coupling loss obtained with a SuC-PCF by directly focusing the laser. These large losses decreased the sensitivity of the general setup (RCF butt-coupled to a MMF) compared to the sensitivity exhibited by focusing the laser directly onto a SuC-PCF. Hence, this setup suffers from relatively weak sensitivity. In addition, the strong silica background of the MMF may overshadow the signal of the target analyte. Solutions could be to decrease the length of the MMF (if the Raman microscope allows it) or to change the analyte. Nevertheless, exciting an RCF with a MMF remains a fast and simple technique that allows creating plug-and-play setups. With this approach, we demonstrated that in the same conditions of preparation and excitation, non-optimized RCFs already exhibited a better sensitivity than the best SuC-PCF prepared in chapter III.

IV.4.3. RCF taper

IV.4.3.1. Goal of the tapering

The second solution envisioned to efficiently inject the light into the core consisted of tapering the RCF. Tapered fibers have been used in a wide range of applications such as supercontinuum generation, sensing or light coupling [253–258]. Depending on their use, their geometry and fabrication process vary. The first fabrication process consists of etching the optical cladding of a fiber in order to expose

its core. In this way, the diameter of the etched section is much smaller than the original fiber. Here, it is worth mentioning that the core is not etched. Only the cladding is partially or entirely removed. The other fabrication process consists of heating and stretching precisely a fiber in order to scale down its topology. Once tapered, the fibers exhibit properties that the original fiber did not possess. For instance, tapering an SC-PCF decreases its core size, which in turn may result in an increased evanescent field. This is particularly attractive for sensing.

In our case, the idea was to decrease sufficiently the diameter of the ring core down to a very small circle or even a solid core on one end so that we were able to excite the entire core by focusing the light directly as we did in chapter III with SuC-PCFs. The other end of the fiber remained unchanged in order to benefit from the large surface of interaction. A schematic illustrating the excitation of the core of tapered and un-tapered RCFs is available in Figure 85. Previously, for a regular RCF, when we excited directly one of the RCF apices, the light stayed confined in the vicinity of this apex as represented in Figure 85(a). For tapered RCF, if the core were small enough in the tapered end, we could excite it entirely by focusing the laser on the core using high magnification objective lenses. Then, since the entire core is excited, the light can be guided by the entire ring at the un-tapered section of the RCF (Figure 85(b)). To be able to excite the entire ring by directly focusing the laser, the size of the collapsed core should be smaller than 5 µm. Here, it is worth reminding the original ring diameter is ~100 µm. This means that we had to taper the RCF so that the diameter of the ring could decrease from ~100 µm large to less than 5 µm while still preserving the structure of the RCF, i.e. not breaking the struts, not closing the external holes and not collapsing the core asymmetrically.

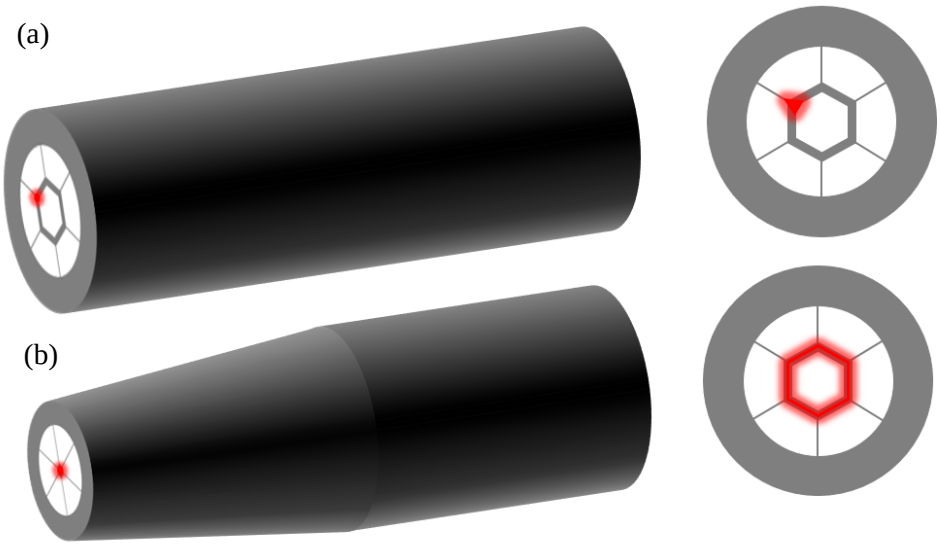

Figure 85 Schematic illustrating the principle of the direct excitation of the RCF with (a) an un-tapered end and (b) a tapered end. The figures on the right represent the un-tapered face of the RCF with the expected field distributions.

IV.4.3.2. Fabrication of tapered RCF

To fabricate the tapers, we used a Fujikura LZM 100 fusion splicer, which is a dedicated splicing system. It features a CO_2 laser instead of electrodes or filaments, which helps in controlling more precisely the size of the heating area. It comes with an on-board tapering program that allows configuring the length of the two slopes (L_{slope}), the length of the taper waist (L_{waist}), the targeted diameter of the taper (D_{waist}) and the speed of the translation stage on each side of the taper. All the geometrical parameters are presented in Figure 86. The software also allows precisely tuning the power of the CO_2 laser in the entire

zone and in the waist zone. This has a direct impact on the heating temperature of the material in the region. In the following, when we refer to heating temperatures, it implies the power of the CO_2 laser.

To fabricate the RCF tapers while preserving the inner structure, we needed to find the right combination between all the parameters. Although preset programs to taper standard fibers exist, we could not directly use them because of the unique topology of our RCF. Since all the parameters are connected, we needed to proceed methodically. In an ideal case, the first step would consist in finding the heating temperature (i.e. the CO_2 laser power) and the pulling speeds that would allow reducing the external diameter of the fiber to reach a target value of D_{waist}. Once, the right temperature and speeds would have been found, we would have cut the taper and put one end under a microscope to observe the cross-section of the tapered region. Based on our observations, we would have tuned the parameters one after the other. For example, if the inner structure were too distorted, we could decrease either the heating temperature or the heating time. Once, we would have succeeded in reaching the target outer diameter while maintaining the inner structure, we would decrease further the new targeted D_{waist}. We would proceed similarly until reaching the desired parameters, i.e. a core size lower than 5 µm so we could excite the entire ring by focusing the laser directly onto it.

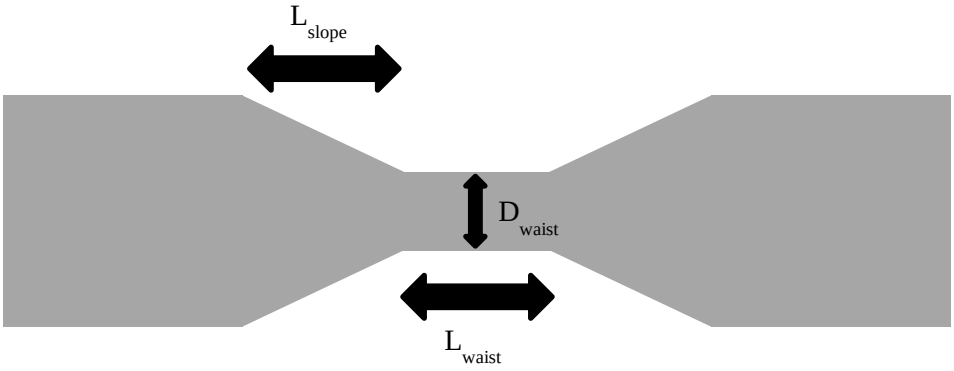

Figure 86 Schematic presenting the preset parameters used to fabricate the RCF tapers.

The procedure described in the previous paragraph would work for a homothetic reduction of the core size. In this case, decreasing the core size from 100 µm to 5 µm would result in decreasing the outer diameter from 600 µm to 30 µm. In our case, this would not have been possible since an outer diameter of 30 µm would result in holes smaller than 10 µm. Such holes would not have been compatible with the microfluidic application of the fiber. Therefore, we fixed the lower limit of the outer diameter to be 100 µm, leading to a diameter of a single hole superior to 30 µm. This meant that we needed to find a way to decrease the size of the core faster than the outer diameter. In the following of this section, we present the main steps of the employed procedure.

Demonstration of the homothetic reduction

To preserve the RCFs with 89 and 101 µm cores (RCFs 3 and 4) until having found the best parameters, we tried to taper the fibers with the closed apices, since they presented approximately the same parameters as the RCFs. We used a fiber that features an outer diameter of 560 µm, a ring diameter of 110 µm and a ring thickness of 2 µm. Based on preliminary tests, we needed to fabricate short tapers to limit the heating time. This prevented from obtaining a structure like the one in Figure 87. We set L_{waist} = 2 mm and L_{slope} = 5 mm. The first step was to find the parameters that allowed to homothetically reduce the outer diameter and the core size. We tuned the temperature of the entire area and the temperature of the waist until we obtained a taper with the inner structure perfectly maintained and a core diameter of ~38 µm as shown in Figure 88. If we consider the outer diameters of the original fiber

and that of the taper, the core size should have been 40 µm. This demonstrates well that the reduction occurring during the tapering is homothetic.

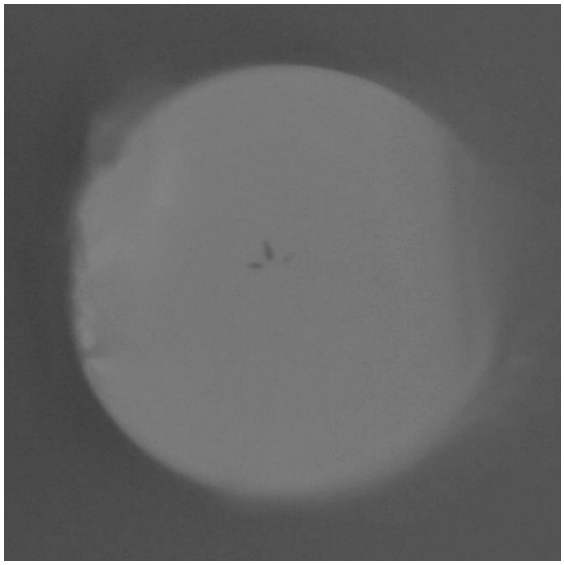

Figure 87 Fabricated tapers with long heating time. The structure is almost entirely collapsed.

The next step was to achieve similar results with an even smaller D_{waist}. We targeted a waist diameter of 100 µm, which was the limit we had fixed. This would allow us to know what core diameter could be reached by using a normal process. To reach this small outer diameter, we were forced to increase slightly the length of the waist. After having increased L_{waist} to 5 mm, we fabricated a taper with D_{waist} = 115 µm and a ring diameter of 17 µm. As hypothesized, when reaching the limit outer diameter of the taper, the core was still too big to be excited by directly focusing the laser.

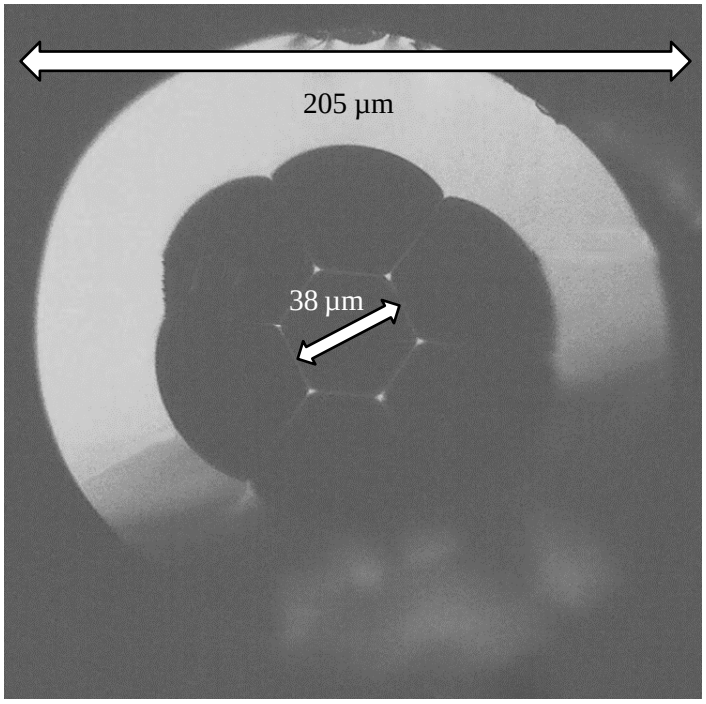

Figure 88 Fabricated taper of the fiber with closed apices with D_{waist} = ~200 µm.

Envisioned approaches for non-homothetic reduction

The first approach consisted of applying an overpressure inside the holes surrounding the ring. In this way, when we heated the fiber to fabricate the taper, the core would be collapsed more easily. To apply the overpressure, the holes of the RCF needed to be closed as shown in Figure 89(a). The second possibility was to apply vacuum inside the central hole. The goal was the same as the previous solution, i.e. make the core collapse more rapidly. For this solution, the holes needed to be closed as shown in Figure 89(b). For more practicability, we selected the second option. Indeed, gluing only the central hole turned out to be very arduous. To apply the vacuum, we simply sucked the air from the center hole using a syringe. The value of vacuum applied could be controlled relatively precisely by tuning the volume of air sucked from the center hole.

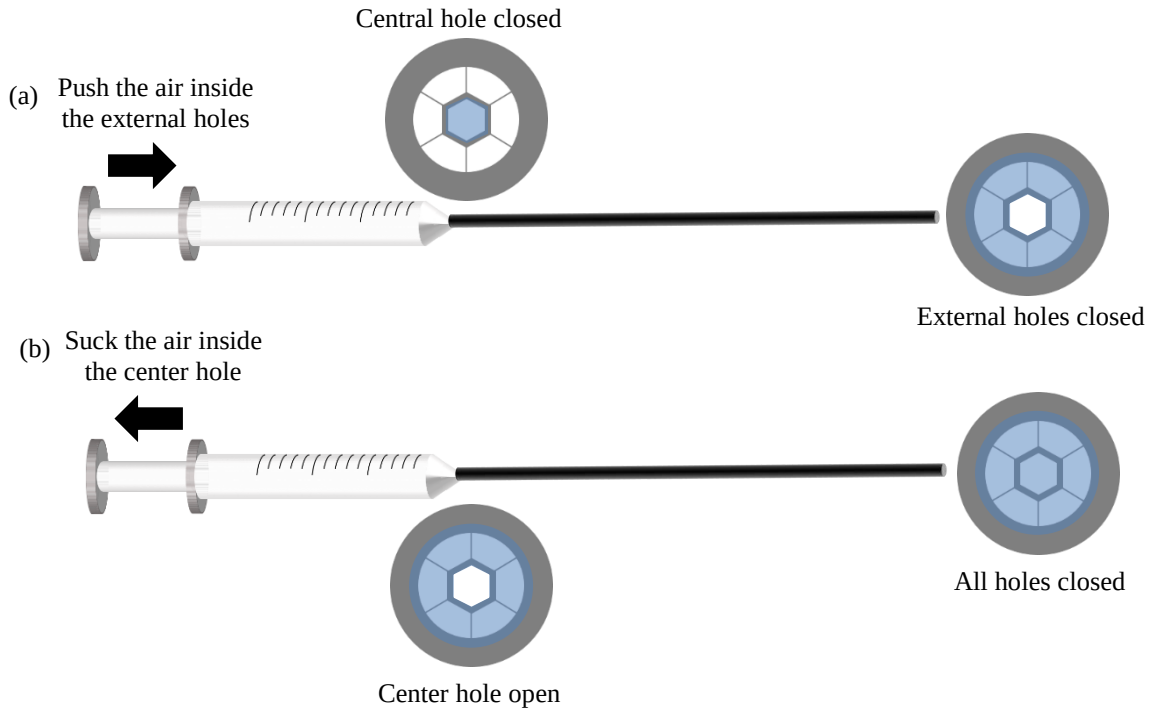

Figure 89 Schematics illustrating the setup used to apply (a) overpressure in the external holes of an RCF during tapering and (b) vacuum only inside the center hole. The blue sections represent epoxy glue.

Using the same tapering parameters as previously, we only played on the amount of vacuum to find the one that allowed collapsing almost entirely the core without breaking the structure. With this configuration, we managed to fabricate a taper that exhibited a core diameter of approximately 3 µm and an outer diameter of approximately 100 µm, as shown in Figure 90. This demonstrated that we were able to reduce drastically the core diameter of a fiber with a topology close to the RCF (open apices) until reaching a core size that allowed exciting the core by focusing the laser directly. In addition, the external holes were still large enough to facilitate fluid incorporation.

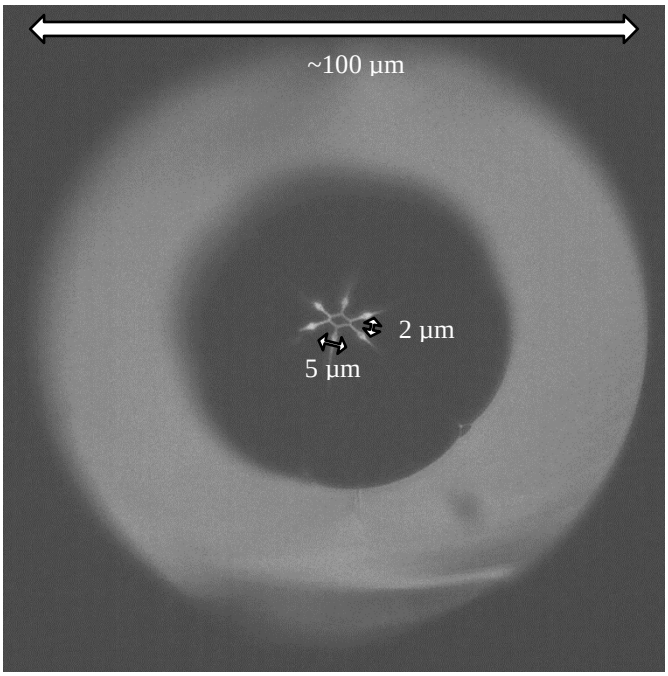

Figure 90 Fabricated taper of fiber with closed apices with D_{waist} = 100 µm and with vacuum applied in the center hole.

Sucking the air inside the center hole of the good RCF

Using the fiber with closed apices allowed us to determine the values of each tapering parameter. Now we could apply them to the real RCF. It is worth noting that the diameter and the thickness of the ring were not exactly the same as that of the RCF with closed apices. The RCF with open apices featured a core diameter of 89 µm (110 µm previously) and a core thickness of 0.7 µm (2 µm previously). Although these differences are not very large, the tapering parameters used with the closed apices RCF did not work with the good RCF. With them, the structure of the fiber broke every time. This demonstrates the precision required for the tuning of the parameters and the difficulty to fabricate the desired tapers.

After finely tuning the tapering parameters and the amount of vacuum applied in the center hole, we obtained viable tapers. Representative tapers are shown in Figure 91. It is worth noting that the structure is slightly different between the two tapers. The core of the second taper started to collapse on itself showing that we were near the optimum parameters concerning the vacuum. Another aspect to note is the bubble-shaped structure on each strut. We think that they might be the residue of the open apices of the original RCF. A solution to remove them could be to leave the apices open during the closing of the external holes before applying the vacuum inside the central hole. In this way, they would be collapsed similarly to the core. We present in Table 10 the dimensions of the two tapers. As we can see, we were able to obtain a core diameter around 3 µm in the waist of the taper while maintaining the external holes wide open (67 µm). Using the same parameters and the same fibers, we could fabricate reproducible tapers. This achievement is quite remarkable since we started from a fiber with a diameter ring of 89 µm. The next step of the process consisted of ensuring that the fabricated tapers allowed to properly excite the ring of the RCF.

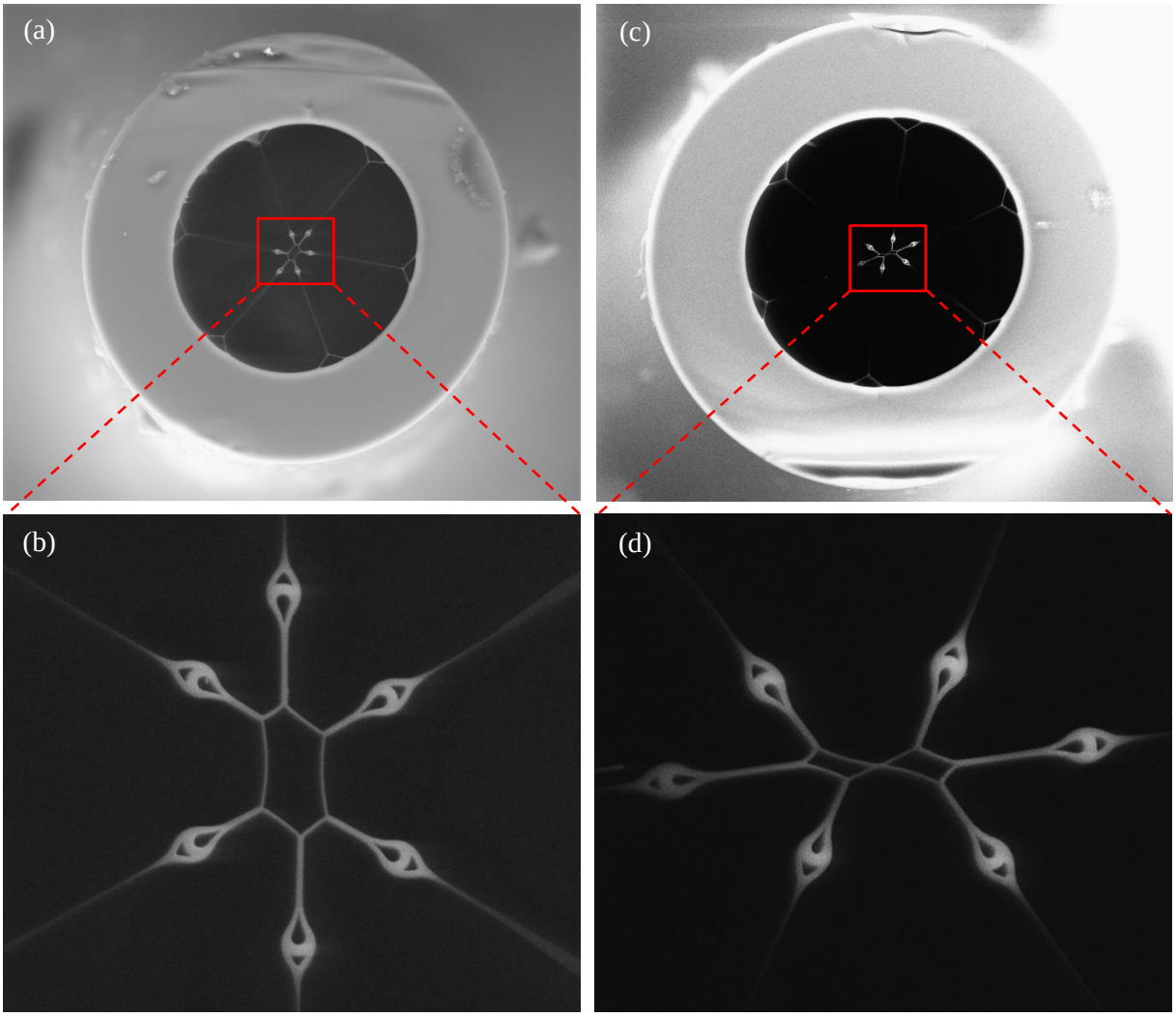

Figure 91 (a) and (c) SEM pictures representing two tapers fabricated using RCF 4 when withdrawing -0.7 mL of air inside the center hole (b) and (d) Zoom-in on the core region for each taper.

Table 10 Parameters of the tapers fabricated from RCF 4. The core of taper 2 was too thin to be measured precisely so we do not present its dimensions here

Taper	Outer diameter (µm)	Hollow region diameter (µm)	Long dimension of the ring (µm)	Short dimension of the ring (µm)	Ring thickness (nm)	L_{waist} (mm)
1	120	67	4.3	1.9	140	5
2	131	75	5.3	1.3	NA	5

IV.4.3.3. Optical characterization

To demonstrate qualitatively the improvement in the light confinement inside the ring core, we focused a laser on the tapered end of an RCF and we acquired the output field distribution at the other end. As shown in Figure 92(a), most of the excitation light is guided inside the ring. We compared this result with previously used excitation techniques for the same RCF. Figure 92(b) was obtained by focusing the light directly inside the RCF using 10x objective lens and trying to maximize the repartition of the field inside the entire ring. Most of the excitation light was guided inside the center hole and not inside the ring. Figure 92(c) was obtained using the MMF excitation technique. Here, a good portion of the light is guided inside the core. Nevertheless, there is still a relatively important amount of light guided

inside the holes of the RCF. As we can see, the light is almost exclusively confined inside the ring core with the tapered fiber whereas an important amount of light is guided inside the holes with the two other techniques. This was exactly what we expected when we decided to fabricate the RCF taper. Although this result is only qualitative, we could already say that the tapering helped in exciting the entire ring core more properly. To make sure of it, we measured the coupling loss of the tapered RCF.

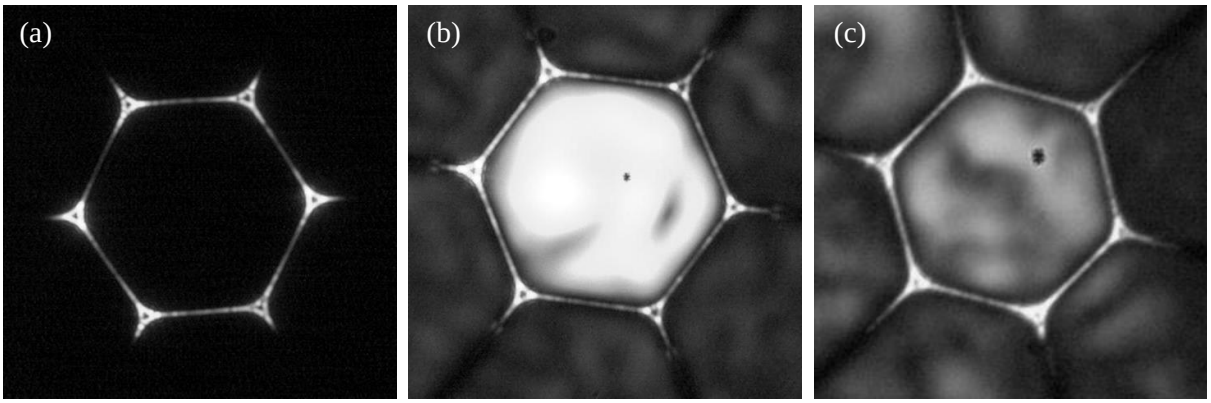

Figure 92 Distribution of the field at the output of an RCF with a core diameter of 89 µm (RCF 4) for several excitation techniques. (a) Tapered RCF, (b) direct focus with 10x objective lens and (c) MMF excitation.

For that, we used the same technique as in chapter III to estimate the coupling loss of the SuC-PCFs. First, we measured the power of the laser after the 40x coupling objective lens. Subsequently, we optimized the position of the tapered RCF using a XYZ platform and we measured the power at its output. The difference between the two powers allowed to estimate the coupling and transmission losses. Table 11 presents the values measured at each location for a 10 cm long tapered RCF, for an RCF excited with a MMF and for a 3.5 µm core SuC-PCF. Comparatively to the MMF excitation, the tapered RCF improved drastically the coupling loss, from 15.4 dB to 2.5 dB. Although it was not as low as the coupling loss of 3.5 µm core SuC-PCF (0.9 dB), the tapered RCF exhibited a coupling loss in the same range. This means that, at this point, we were able to compare the sensitivity of the two fiber designs while exciting them by focusing the laser directly onto their core.

Table 11 Powers measured to estimate the coupling loss of a tapered RCF and 3.5 µm core SuC-PCF

Fiber	Power measured after the objective or the MMF (dBm)	Power measured after the fiber (dBm)	Coupling and transmission loss (dB)
Tapered RCF	13	10.5	2.5
MMF + RCF	11.4	-4	15.4
3.5 µm core SuC-PCF	13	12.1	0.9

IV.4.3.4. SERS sensing with tapered ring core fiber

Similar to what we did in the SERS sensing section with the MMF, the goal of this section was to compare the sensitivity of the two fiber designs using ATP. Here, it is worth mentioning that this section was realized in XLIM research institute on an in-house setup and not on the Renishaw mentioned in chapter III. The general setup was substantially the same as the one presented in Figure 52. The laser wavelength was a 785 nm, and the Raman spectrometer was a QE PRO from Ocean Optics. Before being able to compare the two fiber topologies, we needed to ensure that the tapered configuration allowed for SERS sensing. For that, we fabricated tapered RCFs using the fiber with a core diameter of 89 µm (RCF 4) and we used the short protocol to anchor Au NPs. Compared to the protocol described in chapter III, here we used APTMS instead of APTES to anchor the NPs. Subsequently, we pumped a solution of 2 mM ATP inside the fibers so that the molecules of ATP could bind to the anchored Au

NPs. After drying the fibers, they were ready for measurement. A spectrum measured in these conditions is shown in Figure 93. This spectrum is similar to the signature spectrum of ATP, which meant that tapered RCFs could be used as SERS sensors and that the built-in setup was operational.

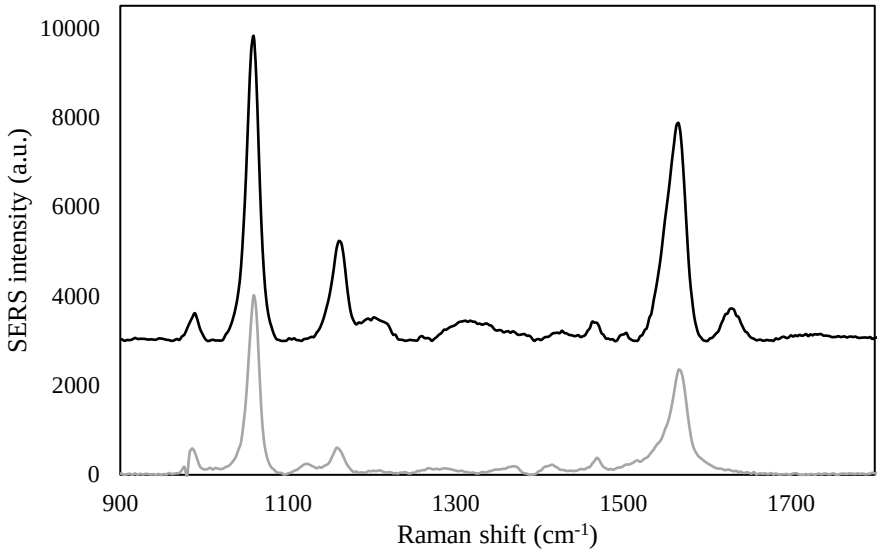

Figure 93 Measured SERS spectra of ATP under normalized conditions using a tapered RCF (black curve) and a 3.5 µm core SuC-PCF (gray curve). We offset the two spectra for more readability.

Once we were sure that tapered RCFs could be used for SERS sensing, we could compare the sensitivity of RCF and the 3.5 µm core SuC-PCF. Here, it is worth mentioning that these results are only preliminary results. We prepared the fibers using the short protocol and APTMS to anchor the NPs. Once again, we used 2 mM ATP as a Raman reporter. We first studied the sensitivity of the 3.5 µm core SuC-PCF. We acquired ten spectra to remove any outliers. Subsequently, we proceeded similarly with the tapered RCF. The measured spectra are shown in Figure 94. They were realized under fixed conditions for the two fibers. Then, we averaged the SERS intensity of 1080 cm^{-1} peak over the ten measurements and we measured the RSD for each fiber. The different values are summarized in Table 12. It is worth mentioning that the acquisition parameters were the same for the two fibers. With this first test, we could see that the averaged SERS intensity is approximately 1.8 times larger with the tapered RCF.

Table 12 Measured SERS intensities of the 1080 cm^{-1} peak of ATP for a 3.5 µm core SuC-PCF and tapered RCF

Measurement	Measured SERS intensity of the 1080 cm^{-1} peak (a.u.) with 3.5 µm core SuC-PCF	Measured SERS intensity of the 1080 cm^{-1} peak (a.u.) with tapered RCF
1	3984	7258
2	4040	7281
3	4020	7343
4	3988	7373
5	4037	7384
6	4059	7493
7	4085	7448
8	4061	7472
9	4083	7373
10	4118	7447
Calculated RSD	1%	1%

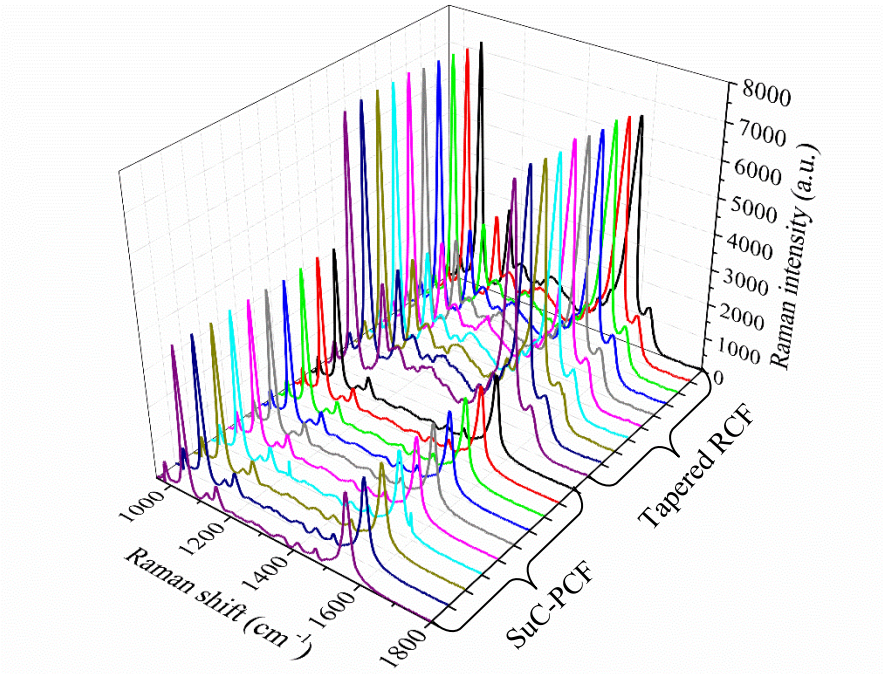

Figure 94 SERS spectra measured under fixed experimental conditions with the 3.5 µm core SuC-PCF and a tapered RCF

To estimate the validity of these results, we simulated an RCF featuring the same parameters as the real fiber with our simplified model. To understand more easily the comparison between the measured and simulated cases, we summarized in Table 13 the key values. First, we calculated the f_{RI} of the RCF to be 12.8 a.u. Once again, for this simulation, we hypothesized that the NPs coverage density was similar to the one measured on the SEM pictures of the SuC-PCF, i.e. 30 particles/µm². We made this assumption since we used the same anchoring protocol for the two fibers. We saw in chapter III that this NPs coverage density was optimized for the 3.5 µm core SuC-PCF. However, it is not optimized for the thickness of the ring core. This explains why we did not obtain the two orders of magnitude improvement simulated at the beginning of the chapter. To further illustrate this matter, we also simulated the same RCF with only 0.05 particles/µm². This time, the calculated f_{RI} was 549 a.u. Thus, an optimization of the coverage density for the RCF is mandatory to exhibit the best sensitivity possible.

Regarding the comparison between the two fiber topologies, we had already calculated the value of the f_{RI} for the 3.5 µm core SuC-PCF in the MMF excitation section. We found it to be 0.68 for a coverage density of 30 particles/µm². If we compare this value with the one simulated with the RCF in the same conditions (f_{RI} = 12.8), we can estimate that the RCF should improve the signal by ~19 times. However, we demonstrated experimentally that the RCF only improved the signal by 1.8 times. This means that relatively large discrepancies exist between the simulation and the experimental results. As mentioned previously, the coupling efficiency is not taken into account in the simulation. We saw that tapered RCFs exhibited stronger coupling losses (2.5 dB against 0.9 dB), which meant that for a given incident laser power, less light was guided inside the RCF core compared to that of the SuC-PCF. Other aspects can also explain the discrepancy between the simulated and experimental results. For instance, it is worth reminding that the two designs used for the simulation was not the exact ones. The tapered region was not simulated and we only considered a circular ring and a rod suspended in water. In addition, the simulations were made for NPs that are equally distributed at the core surface, which is not the case in reality. Furthermore, here we simulated the NPs coverage density measured on a 3.5 µm core SuC-PCF prepared with the long protocol. Therefore, it does not represent the exact coverage density anchored

inside the two fibers. Finally, the simulation does not consider any Raman-active molecules. All these aspects explain the relatively large discrepancy between simulated and experimental results.

Table 13 Measured average SERS intensities of the 1080 cm^{-1} peak of ATP and simulated f_{RI} for a 3.5 µm core SuC-PCF and tapered RCF

Fiber	Measured average SERS intensity of the 1080 cm^{-1} peak (a.u.)	Simulated f_{RI} for CD = 30 particles/µm² (a.u.)	Simulated f_{RI} for CD = 0.05 particles/µm² (a.u.)	Coupling and 10 cm propagation loss (dB)
3.5 µm core SuC-PCF	4048	0.68	0.07	0.9
Tapered RCF	7387	12.8	549	2.5
Resulting EF	1.8	19	7843	NA

Although this is only a preliminary study, the results are very encouraging, as we have already improved the SERS sensitivity. The next step of our experiment would be to measure precisely the average coverage density to simulate f_{RI} closer to the real ones. In addition, we need to measure the propagation losses of the RCF. Only then can we conclude more precisely on the results. In addition, in order to achieve the maximum enhancement possible with the RCF, several parameters need to be optimized. The first two are the coverage density and the thickness of the ring core. As shown in the simulation, decreasing the coverage density from 30 particles/µm² to 0.05 particles/µm² increases the f_{RI} of the RCF from 12.8 to 549 a.u. Compared to the best SuC-PCF (f_{RI} = 0.68), it would result in almost three orders of magnitude improve in sensitivity with the RCF. Increasing the thickness of the ring core could be required for decreasing the propagation losses, as this improves the field confinement in the silica. The other parameter that needs to be improved is the quality of the taper, i.e. removing the interstitial holes. This would reduce further the coupling loss of the RCF, which in turn would result in a better sensitivity.

IV.5. Conclusion

In this chapter, we presented a totally novel topology of PCF especially designed to improve the sensitivity of SERS-based fiber sensors. It is worth noting that this fiber design could also improve the response of fluorescence-based fiber probes since it allows maintaining a good portion of evanescent field while drastically increasing the diameter of the core and thus the interaction area. We showed through simulations that this design could theoretically lead to an increase in sensitivity of more than three orders of magnitude. Once the fibers were fabricated, we investigated two methods to launch the light properly in the ring since the topology of the fiber limits the usage of standard techniques. The first one consisted of a butt-coupling of a MMF with the RCF. The second approach consisted of tapering one end of the RCF. On the one hand, we demonstrated that with the coupling using MMF, a bigger portion of the light was guided inside the core, compared to the direct focusing of the laser using small magnification objectives. However, the coupling loss was quite large between the MMF and the RCF (~15 dB) and between the RCF and the MMF (up to 4 dB). Due to this great loss, the sensitivity exhibited in this configuration by both the RCF and SuC-PCF were limited. In addition, the large silica signal originating from the MMF could overshadow the signal of the analyte in the lower wavenumber region. On the other hand, tapering the RCF tremendously improved the coupling loss (2.5 dB) and avoided the strong background signal from silica. The RCF coupling loss was measured to be in the same range as the loss measured with a 3.5 µm core SuC-PCF (0.9 dB). Unfortunately, the tapering, and thus the relatively low loss coupling, requires an additional fabrication process. Using these two configurations, we were able to compare the sensitivity of two RCFs (D_{core} = 40 µm and 89 µm) with that of our best SuC-PCF. Each time the non-optimized RCF provided a stronger SERS intensity than the SuC-PCF.

This demonstrates that the novel fiber topology helped in increasing the sensitivity of fiber sensors. Finally, based on the latest simulation, it is clear that to benefit from a three orders of magnitude improvement thanks to the RCF design, some optimizations remain. We should either fabricate new fibers with a thicker core and thus a smaller evanescent field or we should largely decrease the NPs coverage density. In summary, in this chapter we showed that our new fiber topology improved the sensitivity of SERS-based fiber sensors when the entire ring could be excited. We also showed that in order to benefit from the larger EF, we needed to optimize the interplay between the ring parameters and the NPs coverage density.

Conclusion and perspectives

Conclusion and perspectives

Most of the reported SERS studies mainly focus on achieving the highest sensitivity possible without taking into consideration of the reproducibility, repeatability and practicability of the sensors. Here, we wanted to design a SERS-active PCF sensor with improved sensitivity and reliability that could be used rapidly and easily in a clinical environment. This resulted in additional constraints in the entire fabrication process. For example, the holes need to be as large as possible to facilitate the incorporation of liquid inside the fiber. It also has an impact on the length of the fiber, and on the technique used to functionalize it. In this manuscript, we used two approaches subsequently. (i) We started by tuning the features of an already reported fiber design (SuC-PCF) to improve its sensitivity and reliability. This allowed us to understand further the complex interplay between the fiber parameters and the density of NPs. (ii) Based on reported and experimental results, we fabricated a totally novel design of PCF. This allowed us to overcome the antagonism that forbid increasing simultaneously the surface of interaction and excitation light in SC-PCFs.

We saw in chapter II that the studies realized so far were conducted with commercial or standard PCFs. The primary goal of these fibers was not SERS sensing and thus, their parameters were not adapted for this application. In chapter III, we wanted to improve the sensitivity, reliability and practicability of the PCF-based probes. Some parameters of the SuC-PCF allowed to improve simultaneously the three aspects. For example, we showed that the core size could improve the sensitivity by tuning the amount of light that would interact with the NPs and analyte molecules. We also demonstrated that the core size had an impact on the sensor reliability, through the coupling efficiency. It was shown that an intermediate core size allowed to benefit from the best compromise between sensitivity and coupling reliability. In turn, this resulted in improving the practicability of the sensor since the impact of misalignments was reduced. In other words, it facilitates the handling of the probe by optical fibers non-specialists. We also improved the practicability of the sensor by increasing significantly the size of the cladding holes. This facilitates the incorporation of liquid and thereby reduces the time required to fill the fibers. The last parameter of the fiber that could have an impact on the SERS response is the length of the fiber. In our case, we fixed the length of the fiber to 10 cm so that the SuC-PCFs could fit inside a biopsy needle. Once the fiber length was fixed, it was possible to select the couple core size/NPs coverage density to achieve the best sensitivity possible.

The optimizations were not limited to the fiber parameters. We demonstrated experimentally that anchoring the NPs inside the fiber resulted in a better sensitivity for all SuC-PCFs at our disposal. In addition, anchoring the NPs also improved the reliability of the sensor. In this configuration, the analyte molecules and the NPs could no longer move freely inside the fiber, which improved the reproducibility and repeatability of the sensors. Finally, it also improved the practicability of the sensor since it reduces the number of actions that a clinician would have to do before readout. Compared to the injected configuration, the clinician does not have to mix the body fluid with an NPs colloidal solution with the anchored configuration. Here, it is worth reminding that the coverage density of anchored NPs has a giant impact on the SERS response of the sensor. Hence, it needs to be carefully adjusted together with the PCF core size to benefit from the best sensitivity.

These optimizations led to the fabrication of SuC-PCF sensors with ~41% improvement in sensitivity (compared to injected configuration) and a record-breaking reproducibility and repeatability of 0.9% and 4.6% respectively. Using our best SuC-PCF sensor, i.e. 3.5 µm core SuC-PCF, we were able to detect Hp, a biomarker for ovarian cancer in clinical cyst fluids from patients. The high reliability of the sensors allowed us to correlate the SERS intensity measured to various stages of cancer, yielding the repeatable differentiation between benign, borderline and malignant cancer. The results of this proof-

of-concept study were similar to clinical standards, which demonstrates the relevance of SERS-based fiber sensors for clinical sensing.

Although these results were very promising, we wanted to improve further the sensitivity of the sensors. This would allow detecting biomarkers at trace levels in body fluids in extremely small sample volumes. This is of paramount importance to create sensors the less possible invasive. For that, we fabricated a totally novel PCF design. The concept was quite simple: we wanted to increase the surface of interaction between the excitation light and the analyte while maintaining a good portion of the evanescent field in the cladding. In SuC-PCF, increasing the core size inevitably resulted in decreasing the amount of evanescent field. Our RCF design allowed to overcome this limitation. By increasing the ring diameter, we were able to significantly increase the interaction surface. In addition, tuning the thickness of the ring resulted in increasing the amount of evanescent field. This new fiber topology can theoretically improve the sensitivity by two to three orders of magnitude.

In addition to the previous requirements, such as large air channels in the cladding, the new RCF required additional features so that the light should be preferably guided by the entire ring. For that, the ring needs to be thicker than the struts holding it and its apices need to remain open in the final fiber. We fabricated several fibers with various ring core diameters and thicknesses. Due to the dimensions of the RCF, standard light coupling techniques could not be used to excite the ring properly. Thus, we envisioned two approaches to overcome this limitation. On the one hand, butt-coupling a MMF to the RCF was a fast and easy way to excite the entire core. This excitation technique is user-friendly since it allows plug-and-play: we could imagine a Raman setup where the user would only have to plug functionalized RCFs to the MMF using usual fiber connectors for the signal readout. However, this technique suffers from large coupling losses that result in a relatively poor sensitivity. Moreover, depending on the setup and the length of MMF needed, the strong silica signal could overshadow the signal from the analyte. On the other hand, tapering the RCF decreases drastically the coupling loss and allows for standard light coupling techniques. However, this technique is more tedious to realize compared to butt-coupling. With these two techniques, we demonstrated that RCFs were two times more sensitive than our best SuC-PCF sensor. This was true even if we had not yet optimized the parameters of the RCFs and the coverage density of the anchored NPs. Therefore, we are confident that once they are optimized, RCFs will exhibit the two to three orders of magnitude improve in sensitivity.

Before our fiber sensors can be used for disease detection, some work remains. Regarding SuC-PCF probes, we plan to realize a large-scale clinical study to validate the results obtained in the initial proof-of-concept study with Hp. In addition, this study would allow us to establish a cut-off SERS intensity value above which the ovarian cyst should be considered malignant. The second perspective is the improvement of the detection process. Indeed, the anchoring protocol of the target analyte needs to be reversed so that the clinician would only have to withdraw the sample and present the pre-functionalized and active fiber under the Raman microscope for readout. Subsequently, we could realize a prototype of functionalized PCF-based biopsy needle specifically designed to detect Hp biomarker in ovarian cyst fluid in an operating theater setting. Finally, the last perspective is to realize tapered SuC-PCFs. This is not mandatory for the SuC-PCF probes to be used in clinical settings but it would allow having a relatively large core (~3.5 µm) on the un-tapered side of the fiber to improve the coupling and a relatively large evanescent field in the tapered region where the core is smaller to improve the sensing. Of course, this would mean to adjust the NPs coverage density so that the SERS intensity is maximum in the tapered region. In such configuration, SuC-PCFs would benefit from good coupling efficiency on the un-tapered region and improved sensitivity in the tapered region.

Regarding the RCF probes, more work remains before they can be used routinely in a clinical setting. First, we would like to repeat the experiment to compare the performance of tapered RCFs and

SuC-PCFs to precisely quantify the improvement in SERS signal achieved using the un-optimized RCFs. As shown with simulations, decreasing the coverage density from 30 particles/µm² to 0.05 particles/µm² would result in an improvement of three orders of magnitude in sensitivity. Hence, we should modify the anchoring protocol to decrease the NPs coverage density anchored inside the RCFs. Another solution could be to fabricate a new version of the fiber with a thicker core in order to decrease the amount of evanescent field. The second aspect to improve is the tapering of the ring core. We must find a way to reduce the fabrication time of the tapers. In addition, it is mandatory to improve the shape of the core of the tapered region to facilitate the light coupling and decrease the injection loss.

Subsequently, we need to quantify the reliability of the tapered fiber. Indeed, we have to ascertain with optical characterization and SERS experiments that the fabrication process of the tapered RCF is repeatable. This would allow us to determine the reproducibility and repeatability of tapered RCFs. A good approach to show the relevance of the new fiber design for SERS biosensing would be to detect a biomarker, which is difficult to detect at small concentration in body fluids or due to other limitations in the current approaches. For instance, rapid detection of exosomes using SERS in RCFs could represent tremendous improvement in biosensing. As explained in the general introduction of this manuscript, exosomes are vesicles produced by eukaryotic cells that contained information on the cell type of origin. Exosomes from healthy cells are different from exosomes produced by cancerous cells, for example. However, to this day, the detection and isolation of exosomes remain tedious. Succeeding in detecting cancerous exosomes rapidly with our fiber probes could pave the way to novel fast and sensitive liquid biopsy sensors. Finally, once all this optimization work will be done, we will have to fabricate a fully functioning prototype of functionalized biopsy needle. It consists of immobilizing a functionalized fiber inside a biopsy needle and measure the SERS signal. This would require realizing a new fiber functionalization protocol to attach the fiber inside the needle and to modify the measurement protocol. Indeed, since the fiber would be entirely inside the needle, the actual technique of cleaving the fiber after having injected the analyte solution and prior to the measurement would not be possible. In addition, a solution facilitating the handling of fiber by a clinician who is not familiar with optical fiber is mandatory so that these probes could be used one day in a clinical setting. An ideal solution could be that the clinician only needs to plug the needle to a connector and directly measure the SERS response.

To conclude, this PhD allowed me to discover and to have a better understanding of SERS sensing with optical fibers. More importantly, we reported the best reproducibility and repeatability of SERS sensors after optimizing the parameters of a SuC-PCF and the NPs anchoring protocol. We also showed that the fiber with the strongest evanescent field was not mandatory to realize the best SERS sensor. Finally, we fabricated a totally new fiber design, specifically conceived for benefitting from the best features of optical fibers for sensing. The preliminary results showed that the new design provides about twice better sensitivity and this was achieved without optimizing the NPs anchoring protocol and the coverage density inside the fiber. We envision that with some refinements this novel design could exhibit record-breaking sensitivity. Finally, in a less scientific context, I consider myself very lucky to have had the opportunity to work for half of my PhD in France and the other half in Singapore. It was a very rewarding experience that allowed me to see different work conditions and different cultures, both inside and outside the laboratory.

Bibliography

1. A. B. E. Attia, S. Y. Chuah, D. Razansky, C. J. H. Ho, P. Malempati, U. S. Dinish, R. Bi, C. Y. Fu, S. J. Ford, J. S.-S. Lee, M. W. P. Tan, M. Olivo, and S. T. G. Thng, "Noninvasive real-time characterization of non-melanoma skin cancers with handheld optoacoustic probes," Photoacoustics **7**, 20–26 (2017).
2. C. J. H. Ho, Y. W. Yew, U. S. Dinish, A. H. Y. Kuan, M. K. W. Wong, R. Bi, K. Dev, X. Li, G. Singh, M. Moothanchery, J. Perumal, S. T. G. Thng, and M. Olivo, "Handheld confocal Raman spectroscopy (CRS) for objective assessment of skin barrier function and stratification of severity in atopic dermatitis (AD) patients," Journal of Dermatological Science **98**(1), 20–25 (2020).
3. J. Perumal, A. Mahyuddin, G. Balasundaram, D. Goh, C. Y. Fu, A. Kazakeviciute, U. Dinish, M. Choolani, and M. Olivo, "SERS-based detection of haptoglobin in ovarian cyst fluid as a point-of-care diagnostic assay for epithelial ovarian cancer," CMAR **Volume 11**, 1115–1124 (2019).
4. U. S. Dinish, C. Y. Fu, K. S. Soh, B. Ramaswamy, A. Kumar, and M. Olivo, "Highly sensitive SERS detection of cancer proteins in low sample volume using hollow core photonic crystal fiber," Biosensors and Bioelectronics **33**(1), 293–298 (2012).
5. U. S. Dinish, G. Balasundaram, Y. T. Chang, and M. Olivo, "Sensitive multiplex detection of serological liver cancer biomarkers using SERS-active photonic crystal fiber probe: SERS active photonic crystal fiber probe for multiplex biomarker detection," Journal of Biophotonics **7**(11–12), 956–965 (2014).
6. R. Dauliat, A. Benoît, D. Darwich, R. Jamier, J. Kobelke, S. Grimm, K. Schuster, and P. Roy, "Demonstration of a homogeneous Yb-doped core fully aperiodic large-pitch fiber laser," Applied Optics **55**(23), 6229–6235 (2016).
7. M.-A. Malleville, R. Dauliat, A. Benoît, B. Leconte, D. Darwich, R. du Jeu, R. Jamier, K. Schuster, and P. Roy, "Experimental study of the mode instability onset threshold in high-power FA-LPF lasers," Optics Letters **42**(24), 5230–5233 (2017).
8. H. Delahaye, G. Granger, J.-T. Gomes, L. Lavoute, D. Gaponov, N. Ducros, and S. Fevrier, "Generation of 35 kW peak power 80 fs pulses at 29 μm from a fully fusion-spliced fiber laser," Optics Letters **44**(9), 2318–2321 (2019).
9. H. Delahaye, G. Granger, D. Gaponov, L. Lavoute, S. Aleshkina, M. Salganskii, A. Hideur, M. Likhachev, and S. Février, "Megawatt solitons generated above 2000 nm in Bragg fibers," Optics Letters **44**(11), 2713–2715 (2019).
10. Stéphanie Leparmentier, Jean-Louis Auguste, Georges Humbert, Gaëlle Delaizir, Sylvie Delepine-Lesoille, Johan Bertrand, Stéphane Buschaert, Jocelyn Perisse, and Jean Reynald Macé, "Palladium particles embedded into silica optical fibers for hydrogen gas detection," in SPIE Photonics Europe, Brussels, Belgium, **9128** (2014).
11. N. Zhang, G. Humbert, T. Gong, P. P. Shum, K. Li, J.-L. Auguste, Z. Wu, D. J. J. Hu, F. Luan, Q. X. Dinh, M. Olivo, and L. Wei, "Side-channel photonic crystal fiber for surface enhanced Raman scattering sensing," Sensors and Actuators B: Chemical **223**, 195–201 (2016).
12. T. Gong, Y. Cui, D. Goh, K. K. Voon, P. P. Shum, G. Humbert, J.-L. Auguste, X.-Q. Dinh, K.-T. Yong, and M. Olivo, "Highly sensitive SERS detection and quantification of sialic acid on single cell using photonic-crystal fiber with gold nanoparticles," Biosensors and Bioelectronics **64**, 227–233 (2015).
13. Rayleigh, J. W. S., "Colours of the Sea and Sky," Nature 48 (1910).
14. A. Smekal, "Zur Quantentheorie der Dispersion," Naturwissenschaften **11**(43), 873–875 (1923).
15. C. V. Raman and K. S. Krishnan, "A New Type of Secondary Radiation," Nature **121**(3048), 501–502 (1928).

16. M. P. Buric, K. P. Chen, J. Falk, and S. D. Woodruff, "Enhanced spontaneous Raman scattering and gas composition analysis using a photonic crystal fiber," Applied Optics **47**(23), 4255–4261 (2008).

17. X. Yang, A. S. P. Chang, B. Chen, C. Gu, and T. C. Bond, "High sensitivity gas sensing by Raman spectroscopy in photonic crystal fiber," Sensors and Actuators B: Chemical **176**, 64–68 (2013).

18. R. Aroca, *Surface-Enhanced Vibrational Spectroscopy*, John Wiley & Sons, Ltd (2006).

19. E. C. Le Ru and P. G. Etchegoin, *Principles of Surface-Enhanced Raman Spectroscopy and Related Plasmonic Effects*, Elsevier (2009).

20. H. T. Ngo, H.-N. Wang, T. Burke, G. S. Ginsburg, and T. Vo-Dinh, "Multiplex detection of disease biomarkers using SERS molecular sentinel-on-chip," Analytical and Bioanalytical Chemistry **406**(14), 3335–3344 (2014).

21. P. Owens, N. Phillipson, J. Perumal, G. O'Connor, and M. Olivo, "Sensing of p53 and EGFR Biomarkers Using High Efficiency SERS Substrates," Biosensors **5**(4), 664–677 (2015).

22. L. Xu, W. Yan, W. Ma, H. Kuang, X. Wu, L. Liu, Y. Zhao, L. Wang, and C. Xu, "SERS Encoded Silver Pyramids for Attomolar Detection of Multiplexed Disease Biomarkers," Advanced Materials **27**(10), 1706–1711 (2015).

23. S. P. Ravindranath, Y. Wang, and J. Irudayaraj, "SERS driven cross-platform based multiplex pathogen detection," Sensors and Actuators B: Chemical **152**(2), 183–190 (2011).

24. K. K. Maiti, A. Samanta, M. Vendrell, K.-S. Soh, M. Olivo, and Y.-T. Chang, "Multiplex cancer cell detection by SERS nanotags with cyanine and triphenylmethine Raman reporters," Chemical Communications **47**(12), 3514–3516 (2011).

25. H. Kang, S. Jeong, Y. Park, J. Yim, B.-H. Jun, S. Kyeong, J.-K. Yang, G. Kim, S. Hong, L. P. Lee, J.-H. Kim, H.-Y. Lee, D. H. Jeong, and Y.-S. Lee, "Near-Infrared SERS Nanoprobes with Plasmonic Au/Ag Hollow-Shell Assemblies for In Vivo Multiplex Detection," Advanced Functional Materials **23**(30), 3719–3727 (2013).

26. M. Fleischmann, P. J. Hendra, and A. J. McQuillan, "Raman spectra of pyridine adsorbed at a silver electrode," Chemical Physics Letters **26**(2), 163–166 (1974).

27. M. G. Albrecht and J. A. Creighton, "Anomalously intense Raman spectra of pyridine at a silver electrode," Journal of the American Chemical Society **99**(15), 5215–5217 (1977).

28. D. L. Jeanmaire and R. P. V. Duyne, "Surface Raman Spectroelectrochemistry," Journal of Electroanalytical Chemistry **84**, 1–20 (1977).

29. M. Moskovits, "Surface roughness and the enhanced intensity of Raman scattering by molecules adsorbed on metals," The Journal of Chemical Physics **69**(9), 4159–4161 (1978).

30. J. Billmann, G. Kovacs, and A. Otto, "Enhanced Raman effect from cyanide adsorbed on a silver electrode," Surface Science **92**, 153–173 (1980).

31. D. Pines, "Collective energy losses in solids," Review of Modern Physics **28**(3), 184–199 (1956).

32. L. Tonks and I. Langmuir, "Oscillations in Ionized Gases," Physical Review **33**, 195–211 (1929).

33. U. Kreibig and M. Vollmer, *Optical Properties of Metal Clusters*, Springer-Verlag Berlin Heidelberg, Springer Series in Materials Science (1995), **25**.

34. R. L. McCreery, *Raman Spectroscopy for Chemical Analysis*, John Wiley and Sons (2000), **157**.

35. M. Kerker, D.-S. Wang, and H. Chew, "Surface enhanced Raman scattering (SERS) by molecules adsorbed at spherical particles: errata," Applied Optics **19**(24), 4159–4174 (1980).

36. D.-S. Wang and M. Kerker, "Enhanced Raman scattering by molecules adsorbed at the surface of colloidal spheroids," Physical Review B **24**(4), 1777–1790 (1981).

37. A. Otto, "The ‘chemical’ (electronic) contribution to surface-enhanced Raman scattering," Journal of Raman Spectroscopy **36**(6–7), 497–509 (2005).

38. C. McLaughlin, D. Graham, and W. E. Smith, "Comparison of Resonant and Non Resonant Conditions on the Concentration Dependence of Surface Enhanced Raman Scattering from a Dye Adsorbed on Silver Colloid," J. Phys. Chem. B **106**(21), 5408–5412 (2002).

39. H. Xu, J. Aizpurua, M. Käll, and P. Apell, "Electromagnetic contributions to single-molecule sensitivity in surface-enhanced Raman scattering," Phys. Rev. E **62**(3), 4318–4324 (2000).

40. C. L. Haynes and R. P. Van Duyne, "Plasmon-Sampled Surface-Enhanced Raman Excitation Spectroscopy," J. Phys. Chem. B **107**(30), 7426–7433 (2003).

41. A. D. McFarland, M. A. Young, J. A. Dieringer, and R. P. Van Duyne, "Wavelength-Scanned Surface-Enhanced Raman Excitation Spectroscopy," J. Phys. Chem. B **109**(22), 11279–11285 (2005).

42. X. Zhang, C. R. Yonzon, M. A. Young, D. A. Stuart, and R. P. Van Duyne, "Surface-enhanced Raman spectroscopy biosensors: excitation spectroscopy for optimisation of substrates fabricated by nanosphere lithography," IEE Proc., Nanobiotechnol. **152**(6), 195–206 (2005).

43. R. Pilot, A. Zoppi, S. Trigari, F. L. Deepak, E. Giorgetti, and R. Bozio, "Wavelength dispersion of the local field intensity in silver–gold nanocages," Phys. Chem. Chem. Phys. **17**(11), 7355–7365 (2015).

44. N. Michieli, R. Pilot, V. Russo, C. Scian, F. Todescato, R. Signorini, S. Agnoli, T. Cesca, R. Bozio, and G. Mattei, "Oxidation effects on the SERS response of silver nanoprism arrays," RSC Adv. **7**(1), 369–378 (2017).

45. D. Tuschel, "Selecting an Excitation Wavelength for Raman Spectroscopy," Spectroscopy **31**, 14–23 (2016).

46. E. Hemmer, A. Benayas, F. Légaré, and F. Vetrone, "Exploiting the biological windows: current perspectives on fluorescent bioprobes emitting above 1000 nm," Nanoscale Horiz. **1**(3), 168–184 (2016).

47. E. Hemmer, N. Venkatachalam, H. Hyodo, A. Hattori, Y. Ebina, H. Kishimoto, and K. Soga, "Upconverting and NIR emitting rare earth based nanostructures for NIR-bioimaging," Nanoscale **5**(23), 11339–11361 (2013).

48. A. M. Smith, M. C. Mancini, and S. Nie, "Bioimaging: second window for in vivo imaging," Nat Nanotechnol **4**(11), 710–711 (2009).

49. L. A. Dick, A. J. Haes, and R. P. Van Duyne, "Distance and Orientation Dependence of Heterogeneous Electron Transfer: A Surface-Enhanced Resonance Raman Scattering Study of Cytochrome c Bound to Carboxylic Acid Terminated Alkanethiols Adsorbed on Silver Electrodes," J. Phys. Chem. B **104**(49), 11752–11762 (2000).

50. G. Wang, R. J. Lipert, M. Jain, S. Kaur, S. Chakraboty, M. P. Torres, S. K. Batra, R. E. Brand, and M. D. Porter, "Detection of the Potential Pancreatic Cancer Marker MUC4 in Serum Using Surface-Enhanced Raman Scattering," Anal. Chem. **83**(7), 2554–2561 (2011).

51. A. V. Krasnoslobodtsev, M. P. Torres, S. Kaur, I. V. Vlassiouk, R. J. Lipert, M. Jain, S. K. Batra, and Y. L. Lyubchenko, "Nano-immunoassay with improved performance for detection of cancer biomarkers," Nanomedicine: Nanotechnology, Biology and Medicine **11**(1), 167–173 (2015).

52. C. Song, J. Chen, Y. Zhao, and L. Wang, "Gold-modified silver nanorod arrays for SERS-based immunoassays with improved sensitivity," J. Mater. Chem. B **2**(43), 7488–7494 (2014).

53. J. Ko, S. Lee, E. K. Lee, S.-I. Chang, L. Chen, S.-Y. Yoon, and J. Choo, "SERS-based immunoassay of tumor marker VEGF using DNA aptamers and silica-encapsulated hollow gold nanospheres," Phys. Chem. Chem. Phys. **15**(15), 5379–5385 (2013).

54. B. Kavosi, A. Salimi, R. Hallaj, and K. Amani, "A highly sensitive prostate-specific antigen immunosensor based on gold nanoparticles/PAMAM dendrimer loaded on MWCNTS/chitosan/ionic liquid nanocomposite," Biosensors and Bioelectronics **52**, 20–28 (2014).

55. M. B. Wabuyele and T. Vo-Dinh, "Detection of Human Immunodeficiency Virus Type 1 DNA Sequence Using Plasmonics Nanoprobes," Anal. Chem. **77**(23), 7810–7815 (2005).

56. H. T. Ngo, H.-N. Wang, A. M. Fales, and T. Vo-Dinh, "Label-Free DNA Biosensor Based on SERS Molecular Sentinel on Nanowave Chip," Anal. Chem. **85**(13), 6378–6383 (2013).

57. H. T. Ngo, H.-N. Wang, A. M. Fales, B. P. Nicholson, C. W. Woods, and T. Vo-Dinh, "DNA bioassay-on-chip using SERS detection for dengue diagnosis," Analyst **139**(22), 5655–5659 (2014).

58. B. J. Kennedy, S. Spaeth, M. Dickey, and K. T. Carron, "Determination of the Distance Dependence and Experimental Effects for Modified SERS Substrates Based on Self-Assembled Monolayers Formed Using Alkanethiols," J. Phys. Chem. B **103**(18), 3640–3646 (1999).

59. C. A. Murray and D. L. Allara, "Measurement of the molecule–silver separation dependence of surface enhanced Raman scattering in multilayered structures," The Journal of Chemical Physics **76**(3), 1290–1303 (1982).

60. J. A. Dieringer, A. D. McFarland, N. C. Shah, D. A. Stuart, A. V. Whitney, C. R. Yonzon, M. A. Young, X. Zhang, and R. P. Van Duyne, "Introductory Lecture Surface enhanced Raman spectroscopy: new materials, concepts, characterization tools, and applications," Faraday Discuss. **132**(0), 9–26 (2006).

61. S. S. Masango, R. A. Hackler, N. Large, A.-I. Henry, M. O. McAnally, G. C. Schatz, P. C. Stair, and R. P. Van Duyne, "High-Resolution Distance Dependence Study of Surface-Enhanced Raman Scattering Enabled by Atomic Layer Deposition," Nano Lett. **16**(7), 4251–4259 (2016).

62. G. J. Kovacs, R. O. Loutfy, P. S. Vincett, C. Jennings, and R. Aroca, "Distance dependence of SERS enhancement factor from Langmuir-Blodgett monolayers on metal island films: evidence for the electromagnetic mechanism," Langmuir **2**(6), 689–694 (1986).

63. T. M. Cotton, R. A. Uphaus, and D. Mobius, "Distance dependence of surface-enhanced resonance Raman enhancement in Langmuir-Blodgett dye multilayers," J. Phys. Chem. **90**(23), 6071–6073 (1986).

64. E. C. Le Ru, J. Grand, I. Sow, W. R. C. Somerville, P. G. Etchegoin, M. Treguer-Delapierre, G. Charron, N. Félidj, G. Lévi, and J. Aubard, "A Scheme for Detecting Every Single Target Molecule with Surface-Enhanced Raman Spectroscopy," Nano Lett. **11**(11), 5013–5019 (2011).

65. S. L. Kleinman, R. R. Frontiera, A.-I. Henry, J. A. Dieringer, and R. P. Van Duyne, "Creating, characterizing, and controlling chemistry with SERS hot spots," Phys. Chem. Chem. Phys. **15**(1), 21–36 (2013).

66. L. Tong, H. Xu, and M. Käll, "Nanogaps for SERS applications," MRS Bulletin **39**(2), 163–168 (2014).

67. S.-Y. Ding, J. Yi, J.-F. Li, B. Ren, D.-Y. Wu, R. Panneerselvam, and Z.-Q. Tian, "Nanostructure-based plasmon-enhanced Raman spectroscopy for surface analysis of materials," Nat Rev Mater **1**(6), 16021 (2016).

68. S.-Y. Ding, E.-M. You, Z.-Q. Tian, and M. Moskovits, "Electromagnetic theories of surface-enhanced Raman spectroscopy," Chem. Soc. Rev. **46**(13), 4042–4076 (2017).

69. M. Moskovits, "Surface-enhanced Raman spectroscopy: a brief retrospective," Journal of Raman Spectroscopy **36**(6–7), 485–496 (2005).

70. J. M. McMahon, S. Li, L. K. Ausman, and G. C. Schatz, "Modeling the Effect of Small Gaps in Surface-Enhanced Raman Spectroscopy," J. Phys. Chem. C **116**(2), 1627–1637 (2012).

71. E. C. Le Ru, E. Blackie, M. Meyer, and P. G. Etchegoin, "Surface Enhanced Raman Scattering Enhancement Factors: A Comprehensive Study," J. Phys. Chem. C **111**(37), 13794–13803 (2007).

72. B. Sharma, R. R. Frontiera, A.-I. Henry, E. Ringe, and R. P. Van Duyne, "SERS: Materials, applications, and the future," Materials Today **15**(1–2), 16–25 (2012).

73. R. Pilot, R. Signorini, C. Durante, L. Orian, M. Bhamidipati, and L. Fabris, "A Review on Surface-Enhanced Raman Scattering," Biosensors **9**(2), 57 (2019).

74. S. Nie, "Probing Single Molecules and Single Nanoparticles by Surface-Enhanced Raman Scattering," Science **275**(5303), 1102–1106 (1997).

75. K. Kneipp, Y. Wang, H. Kneipp, L. T. Perelman, I. Itzkan, R. R. Dasari, and M. S. Feld, "Single Molecule Detection Using Surface-Enhanced Raman Scattering (SERS)," Phys. Rev. Lett. **78**(9), 1667–1670 (1997).

76. E. C. Le Ru, P. G. Etchegoin, and M. Meyer, "Enhancement factor distribution around a single surface-enhanced Raman scattering hot spot and its relation to single molecule detection," J. Chem. Phys. **125**(20), 204701 (2006).

77. P. G. Etchegoin and E. C. Le Ru, "A perspective on single molecule SERS: current status and future challenges," Phys. Chem. Chem. Phys. **10**(40), 6079–6089 (2008).

78. N. P. W. Pieczonka and R. F. Aroca, "Single molecule analysis by surfaced-enhanced Raman scattering," Chem. Soc. Rev. **37**(5), 946–954 (2008).

79. S. L. Kleinman, E. Ringe, N. Valley, K. L. Wustholz, E. Phillips, K. A. Scheidt, G. C. Schatz, and R. P. Van Duyne, "Single-Molecule Surface-Enhanced Raman Spectroscopy of Crystal Violet Isotopologues: Theory and Experiment," J. Am. Chem. Soc. **133**(11), 4115–4122 (2011).

80. A. B. Zrimsek, N. L. Wong, and R. P. Van Duyne, "Single Molecule Surface-Enhanced Raman Spectroscopy: A Critical Analysis of the Bianalyte versus Isotopologue Proof," J. Phys. Chem. C **120**(9), 5133–5142 (2016).

81. X.-M. Qian and S. M. Nie, "Single-molecule and single-nanoparticle SERS: from fundamental mechanisms to biomedical applications," Chem. Soc. Rev. **37**(5), 912–920 (2008).

82. R. J. C. Brown and M. J. T. Milton, "Nanostructures and nanostructured substrates for surface-enhanced Raman scattering (SERS)," J. Raman Spectrosc. **39**(10), 1313–1326 (2008).

83. K. R. Strehle, D. Cialla, P. Rösch, T. Henkel, M. Köhler, and J. Popp, "A Reproducible Surface-Enhanced Raman Spectroscopy Approach. Online SERS Measurements in a Segmented Microfluidic System," Anal. Chem. **79**(4), 1542–1547 (2007).

84. Y. Jin, Y. Wang, M. Chen, X. Xiao, T. Zhang, J. Wang, K. Jiang, S. Fan, and Q. Li, "Highly Sensitive, Uniform, and Reproducible Surface-Enhanced Raman Spectroscopy Substrate with Nanometer-Scale Quasi-periodic Nanostructures," ACS Appl. Mater. Interfaces **9**(37), 32369–32376 (2017).

85. S. Jiang, J. Guo, C. Zhang, C. Li, M. Wang, Z. Li, S. Gao, P. Chen, H. Si, and S. Xu, "A sensitive, uniform, reproducible and stable SERS substrate has been presented based on MoS2@Ag nanoparticles@pyramidal silicon," RSC Adv. **7**(10), 5764–5773 (2017).

86. L. Wu, W. Wang, W. Zhang, H. Su, Q. Liu, J. Gu, T. Deng, and D. Zhang, "Highly sensitive, reproducible and uniform SERS substrates with a high density of three-dimensionally distributed hotspots: gyroid-structured Au periodic metallic materials," Npg Asia Materials **10**, e462 (2018).

87. M. J. Natan, "Concluding Remarks Surface enhanced Raman scattering," Faraday Discuss. **132**(0), 321–328 (2006).

88. T. C. Dakal, A. Kumar, R. S. Majumdar, and V. Yadav, "Mechanistic Basis of Antimicrobial Actions of Silver Nanoparticles," Front. Microbiol. **7**, (2016).

89. N. D. Israelsen, C. Hanson, and E. Vargis, "Nanoparticle Properties and Synthesis Effects on Surface-Enhanced Raman Scattering Enhancement Factor: An Introduction," The Scientific World Journal **2015**, 124582 (2015).

90. R. Stiufiuc, C. Iacovita, C. M. Lucaciu, G. Stiufiuc, A. G. Dutu, C. Braescu, and N. Leopold, "SERS-active silver colloids prepared by reduction of silver nitrate with short-chain polyethylene glycol," Nanoscale Research Letters **8**(1), 47 (2013).

91. B. Wiley, Y. Sun, B. Mayers, and Y. Xia, "Shape-Controlled Synthesis of Metal Nanostructures: The Case of Silver," Chemistry – A European Journal **11**(2), 454–463 (2005).

92. F. Tian, F. Bonnier, A. Casey, A. E. Shanahan, and H. J. Byrne, "Surface enhanced Raman scattering with gold nanoparticles: effect of particle shape," Anal. Methods **6**(22), 9116–9123 (2014).

93. F. Benz, R. Chikkaraddy, A. Salmon, H. Ohadi, B. de Nijs, J. Mertens, C. Carnegie, R. W. Bowman, and J. J. Baumberg, "SERS of Individual Nanoparticles on a Mirror: Size Does Matter, but so Does Shape," J. Phys. Chem. Lett. **7**(12), 2264–2269 (2016).

94. D. Jimenez de Aberasturi, A. B. Serrano-Montes, J. Langer, M. Henriksen-Lacey, W. J. Parak, and L. M. Liz-Marzán, "Surface Enhanced Raman Scattering Encoded Gold Nanostars for Multiplexed Cell Discrimination," Chem. Mater. **28**(18), 6779–6790 (2016).

95. J. Neddersen, G. Chumanov, and T. M. Cotton, "Laser Ablation of Metals: A New Method for Preparing SERS Active Colloids," Appl Spectrosc **47**(12), 1959–1964 (1993).

96. A. V. Kabashin and M. Meunier, "Synthesis of colloidal nanoparticles during femtosecond laser ablation of gold in water," Journal of Applied Physics **94**(12), 7941–7943 (2003).

97. M. Vinod and K. G. Gopchandran, "Au, Ag and Au:Ag colloidal nanoparticles synthesized by pulsed laser ablation as SERS substrates," Progress in Natural Science: Materials International **24**(6), 569–578 (2014).

98. V. Amendola and M. Meneghetti, "Laser ablation synthesis in solution and size manipulation of noble metal nanoparticles," Phys. Chem. Chem. Phys. **11**(20), 3805–3821 (2009).

99. S. Link and M. A. El-Sayed, "Size and Temperature Dependence of the Plasmon Absorption of Colloidal Gold Nanoparticles," J. Phys. Chem. B **103**(21), 4212–4217 (1999).

100. J. A. Creighton and D. G. Eadon, "Ultraviolet–visible absorption spectra of the colloidal metallic elements," J. Chem. Soc., Faraday Trans. **87**(24), 3881–3891 (1991).

101. M. Fan, F.-J. Lai, H.-L. Chou, W.-T. Lu, B.-J. Hwang, and A. G. Brolo, "Surface-enhanced Raman scattering (SERS) from Au:Ag bimetallic nanoparticles: the effect of the molecular probe," Chem. Sci. **4**(1), 509–515 (2013).

102. Y. Cui, B. Ren, J.-L. Yao, R.-A. Gu, and Z.-Q. Tian, "Synthesis of AgcoreAushell Bimetallic Nanoparticles for Immunoassay Based on Surface-Enhanced Raman Spectroscopy," J. Phys. Chem. B **110**(9), 4002–4006 (2006).

103. R. G. Freeman, M. B. Hommer, K. C. Grabar, M. A. Jackson, and M. J. Natan, "Ag-Clad Au Nanoparticles: Novel Aggregation, Optical, and Surface-Enhanced Raman Scattering Properties," J. Phys. Chem. **100**(2), 718–724 (1996).

104. Y.-C. Liu, K.-H. Yang, and S.-J. Yang, "Sonoelectrochemical synthesis of spike-like gold–silver alloy nanoparticles from bulk substrates and the application on surface-enhanced Raman scattering," Analytica Chimica Acta **572**(2), 290–294 (2006).

105. R. F. Aroca, R. A. Alvarez-Puebla, N. Pieczonka, S. Sanchez-Cortez, and J. V. Garcia-Ramos, "Surface-enhanced Raman scattering on colloidal nanostructures," Advances in Colloid and Interface Science **116**(1), 45–61 (2005).

106. J. F. Li, Y. F. Huang, Y. Ding, Z. L. Yang, S. B. Li, X. S. Zhou, F. R. Fan, W. Zhang, Z. Y. Zhou, D. Y. Wu, B. Ren, Z. L. Wang, and Z. Q. Tian, "Shell-isolated nanoparticle-enhanced Raman spectroscopy," Nature **464**(7287), 392–395 (2010).

107. R. G. Freeman, K. C. Grabar, K. J. Allison, R. M. Bright, J. A. Davis, A. P. Guthrie, M. B. Hommer, M. A. Jackson, P. C. Smith, D. G. Walter, and M. J. Natan, "Self-Assembled Metal Colloid Monolayers: An Approach to SERS Substrates," Science **267**(5204), 1629–1632 (1995).

108. R. G. Acres, A. V. Ellis, J. Alvino, C. E. Lenahan, D. A. Khodakov, G. F. Metha, and G. G. Andersson, "Molecular Structure of 3-Aminopropyltriethoxysilane Layers Formed on Silanol-Terminated Silicon Surfaces," J. Phys. Chem. C **116**(10), 6289–6297 (2012).

109. H. H. Kyaw, S. H. Al-Harthi, A. Sellai, and J. Dutta, "Self-organization of gold nanoparticles on silanated surfaces," Beilstein J. Nanotechnol. **6**, 2345–2353 (2015).

110. O. Péron, E. Rinnert, M. Lehaitre, P. Crassous, and C. Compère, "Detection of polycyclic aromatic hydrocarbon (PAH) compounds in artificial sea-water using surface-enhanced Raman scattering (SERS)," Talanta **79**(2), 199–204 (2009).

111. F. Toderas, M. Baia, L. Baia, and S. Astilean, "Controlling gold nanoparticle assemblies for efficient surface-enhanced Raman scattering and localized surface plasmon resonance sensors," Nanotechnology **18**(25), 255702 (2007).

112. K. C. Grabar, R. G. Freeman, M. B. Hommer, and M. J. Natan, "Preparation and Characterization of Au Colloid Monolayers," Anal. Chem. **67**(4), 735–743 (1995).

113. J. Prakash, R. A. Harris, and H. C. Swart, "Embedded plasmonic nanostructures: synthesis, fundamental aspects and their surface enhanced Raman scattering applications," International Reviews in Physical Chemistry **35**(3), 353–398 (2016).

114. S. J. Henley, M. J. Beliatis, V. Stolojan, and S. R. P. Silva, "Laser implantation of plasmonic nanostructures into glass," Nanoscale **5**(3), 1054–1059 (2013).

115. R. Carles, M. Bayle, and C. Bonafos, "Plasmon-enhanced scattering and charge transfer in few-layer graphene interacting with buried printed 2D-pattern of silver nanoparticles," Nanotechnology **29**(17), 175301 (2018).

116. M. T. Yaseen, M. Chen, and Y.-C. Chang, "Partially embedded gold nanoislands in a glass substrate for SERS applications," RSC Adv. **4**(98), 55247–55251 (2014).

117. J. Zhao, J. Lin, W. Zhang, H. Wei, and Y. Chen, "SERS-active Ag nanoparticles embedded in glass prepared by a two-step electric field-assisted diffusion," Optical Materials **39**, 97–102 (2015).

118. T. Hasell, L. Lagonigro, A. C. Peacock, S. Yoda, P. D. Brown, P. J. A. Sazio, and S. M. Howdle, "Silver Nanoparticle Impregnated Polycarbonate Substrates for Surface Enhanced Raman Spectroscopy: Silver Nanoparticle Impregnated Polycarbonate Substrates for SERS," Adv. Funct. Mater. **18**(8), 1265–1271 (2008).

119. C. D'Andrea, B. Fazio, P. G. Gucciardi, M. C. Giordano, C. Martella, D. Chiappe, A. Toma, F. Buatier de Mongeot, F. Tantussi, P. Vasanthakumar, F. Fuso, and M. Allegrini, "SERS Enhancement and Field Confinement in Nanosensors Based on Self-Organized Gold Nanowires Produced by Ion-Beam Sputtering," J. Phys. Chem. C **118**(16), 8571–8580 (2014).

120. R. Proietti Zaccaria, F. Bisio, G. Das, G. Maidecchi, M. Caminale, C. D. Vu, F. De Angelis, E. Di Fabrizio, A. Toma, and M. Canepa, "Plasmonic Color-Graded Nanosystems with Achromatic Subwavelength Architectures for Light Filtering and Advanced SERS Detection," ACS Appl. Mater. Interfaces **8**(12), 8024–8031 (2016).

121. D. Gkogkou, B. Schreiber, T. Shaykhutdinov, H. K. Ly, U. Kuhlmann, U. Gernert, S. Facsko, P. Hildebrandt, N. Esser, K. Hinrichs, I. M. Weidinger, and T. W. H. Oates, "Polarization- and Wavelength-Dependent Surface-Enhanced Raman Spectroscopy Using Optically Anisotropic Rippled Substrates for Sensing," ACS Sens. **1**(3), 318–323 (2016).

122. W. W. Yu and I. M. White, "Inkjet Printed Surface Enhanced Raman Spectroscopy Array on Cellulose Paper," Anal. Chem. **82**(23), 9626–9630 (2010).

123. L.-L. Qu, D.-W. Li, J.-Q. Xue, W.-L. Zhai, J. S. Fossey, and Y.-T. Long, "Batch fabrication of disposable screen printed SERS arrays," Lab Chip **12**(5), 876–881 (2012).

124. M. J. Oliveira, P. Quaresma, M. Peixoto de Almeida, A. Araújo, E. Pereira, E. Fortunato, R. Martins, R. Franco, and H. Águas, "Office paper decorated with silver nanostars - an alternative cost effective platform for trace analyte detection by SERS," Scientific Reports **7**(1), 2480 (2017).

125. Y. H. Ngo, D. Li, G. P. Simon, and G. Garnier, "Gold Nanoparticle–Paper as a Three-Dimensional Surface Enhanced Raman Scattering Substrate," Langmuir **28**(23), 8782–8790 (2012).

126. W. Wu, L. Liu, Z. Dai, J. Liu, S. Yang, L. Zhou, X. Xiao, C. Jiang, and V. A. L. Roy, "Low-Cost, Disposable, Flexible and Highly Reproducible Screen Printed SERS Substrates for the Detection of Various Chemicals," Scientific Reports **5**(1), 10208 (2015).

127. J. Yang, J. Li, Z. Du, Q. Gong, J. Teng, and M. Hong, "Laser Hybrid Micro/nano-structuring of Si Surfaces in Air and its Applications for SERS Detection," Scientific Reports **4**(1), 6657 (2014).

128. C.-H. Lin, L. Jiang, Y.-H. Chai, H. Xiao, S.-J. Chen, and H.-L. Tsai, "One-step fabrication of nanostructures by femtosecond laser for surface-enhanced Raman scattering," Opt. Express **17**(24), 21581–21589 (2009).

129. M. E. Stewart, C. R. Anderton, L. B. Thompson, J. Maria, S. K. Gray, J. A. Rogers, and R. G. Nuzzo, "Nanostructured Plasmonic Sensors," Chem. Rev. **108**(2), 494–521 (2008).

130. L. Billot, M. Lamy de la Chapelle, A.-S. Grimault, A. Vial, D. Barchiesi, J.-L. Bijeon, P.-M. Adam, and P. Royer, "Surface enhanced Raman scattering on gold nanowire arrays: Evidence of strong multipolar surface plasmon resonance enhancement," Chemical Physics Letters **422**(4–6), 303–307 (2006).

131. C. L. Haynes and R. P. Van Duyne, "Nanosphere Lithography: A Versatile Nanofabrication Tool for Studies of Size-Dependent Nanoparticle Optics," J. Phys. Chem. B **105**(24), 5599–5611 (2001).

132. D. Qin, Y. Xia, and G. M. Whitesides, "Soft lithography for micro- and nanoscale patterning," Nature Protocols **5**(3), 491–502 (2010).

133. F. S. Ou, M. Hu, I. Naumov, A. Kim, W. Wu, A. M. Bratkovsky, X. Li, R. S. Williams, and Z. Li, "Hot-Spot Engineering in Polygonal Nanofinger Assemblies for Surface Enhanced Raman Spectroscopy," Nano Lett. **11**(6), 2538–2542 (2011).

134. "Sigma-Aldrich, Nanomaterials," https://www.sigmaaldrich.com/materials-science/nanomaterials.html.

135. "Nanopartz," https://www.nanopartz.com/categories.asp?cat=23.

136. "Ocean Insight," https://www.oceaninsight.com/products/sampling-accessories/raman/sers/sers/.

137. "Hamamatsu," https://www.hamamatsu.com/eu/en/product/optical-components/sers-substrate/index.html

138. "Horiba," https://www.horiba.com/en_en/products/detail/action/show/Product/sers-substrates-1635/.

139. "SERSitive," https://www.sersitive.eu/.

140. Y. Liu, Y. Zhang, M. Tardivel, M. Lequeux, X. Chen, W. Liu, J. Huang, H. Tian, Q. Liu, G. Huang, R. Gillibert, M. L. de la Chapelle, and W. Fu, "Evaluation of the Reliability of Six Commercial SERS Substrates," Plasmonics **15**(3), 743–752 (2020).

141. J. Wang, K. M. Koo, E. J. H. Wee, Y. Wang, and M. Trau, "A nanoplasmonic label-free surface-enhanced Raman scattering strategy for non-invasive cancer genetic subtyping in patient samples," Nanoscale **9**(10), 3496–3503 (2017).

142. S. Feng, R. Chen, J. Lin, J. Pan, Y. Wu, Y. Li, J. Chen, and H. Zeng, "Gastric cancer detection based on blood plasma surface-enhanced Raman spectroscopy excited by polarized laser light," Biosensors and Bioelectronics **26**(7), 3167–3174 (2011).

143. J. Kneipp, H. Kneipp, M. McLaughlin, D. Brown, and K. Kneipp, "In Vivo Molecular Probing of Cellular Compartments with Gold Nanoparticles and Nanoaggregates," Nano Lett. **6**(10), 2225–2231 (2006).

144. K. Kneipp, A. S. Haka, H. Kneipp, K. Badizadegan, N. Yoshizawa, C. Boone, K. E. Shafer-Peltier, J. T. Motz, R. R. Dasari, and M. S. Feld, "Surface-Enhanced Raman Spectroscopy in Single Living Cells Using Gold Nanoparticles," Appl. Spectrosc. **56**(2), 150–154 (2002).

145. A. Walter, A. März, W. Schumacher, P. Rösch, and J. Popp, "Towards a fast, high specific and reliable discrimination of bacteria on strain level by means of SERS in a microfluidic device," Lab Chip **11**(6), 1013–1021 (2011).

146. H. Xu, E. J. Bjerneld, M. Käll, and L. Börjesson, "Spectroscopy of Single Hemoglobin Molecules by Surface Enhanced Raman Scattering," Phys. Rev. Lett. **83**(21), 4357–4360 (1999).

147. S. Shanmukh, L. Jones, J. Driskell, Y. Zhao, R. Dluhy, and R. A. Tripp, "Rapid and Sensitive Detection of Respiratory Virus Molecular Signatures Using a Silver Nanorod Array SERS Substrate," Nano Lett. **6**(11), 2630–2636 (2006).

148. X. X. Han, H. Y. Jia, Y. F. Wang, Z. C. Lu, C. X. Wang, W. Q. Xu, B. Zhao, and Y. Ozaki, "Analytical Technique for Label-Free Multi-Protein Detection Based on Western Blot and Surface-Enhanced Raman Scattering," Anal. Chem. **80**(8), 2799–2804 (2008).

149. Y. Wang, B. Yan, and L. Chen, "SERS Tags: Novel Optical Nanoprobes for Bioanalysis," Chem. Rev. **113**(3), 1391–1428 (2013).

150. R. Shukla, V. Bansal, M. Chaudhary, A. Basu, R. R. Bhonde, and M. Sastry, "Biocompatibility of Gold Nanoparticles and Their Endocytotic Fate Inside the Cellular Compartment: A Microscopic Overview," Langmuir **21**(23), 10644–10654 (2005).

151. M. Ahamed, M. Karns, M. Goodson, J. Rowe, S. M. Hussain, J. J. Schlager, and Y. Hong, "DNA damage response to different surface chemistry of silver nanoparticles in mammalian cells," Toxicology and Applied Pharmacology **233**(3), 404–410 (2008).

152. L. A. Lane, X. Qian, and S. Nie, "SERS Nanoparticles in Medicine: From Label-Free Detection to Spectroscopic Tagging," Chem. Rev. **115**(19), 10489–10529 (2015).

153. S. P. Mulvaney, M. D. Musick, C. D. Keating, and M. J. Natan, "Glass-Coated, Analyte-Tagged Nanoparticles: A New Tagging System Based on Detection with Surface-Enhanced Raman Scattering," Langmuir **19**(11), 4784–4790 (2003).

154. X. Qian, X.-H. Peng, D. O. Ansari, Q. Yin-Goen, G. Z. Chen, D. M. Shin, L. Yang, A. N. Young, M. D. Wang, and S. Nie, "In vivo tumor targeting and spectroscopic detection with surface-enhanced Raman nanoparticle tags," Nature Biotechnology **26**(1), 83–90 (2008).

155. F. Wang, R. G. Widejko, Z. Yang, K. T. Nguyen, H. Chen, L. P. Fernando, K. A. Christensen, and J. N. Anker, "Surface-Enhanced Raman Scattering Detection of pH with Silica-Encapsulated 4-Mercaptobenzoic Acid-Functionalized Silver Nanoparticles," Anal. Chem. **84**(18), 8013–8019 (2012).

156. C. Song, L. Min, N. Zhou, Y. Yang, B. Yang, L. Zhang, S. Su, and L. Wang, "Ultrasensitive detection of carcino-embryonic antigen by using novel flower-like gold nanoparticle SERS tags and SERS-active magnetic nanoparticles," RSC Adv. **4**(78), 41666–41669 (2014).

157. P. Zaca-Morán, J. P. Padilla-Martínez, J. M. Pérez-Corte, J. A. Dávila-Pintle, J. G. Ortega-Mendoza, and N. Morales, "Etched optical fiber for measuring concentration and refractive index of sucrose solutions by evanescent waves," Laser Phys. **28**(11), 116002 (2018).

158. D. L. Stokes and T. Vo-Dinh, "Development of an integrated single-fiber SERS sensor," Sensors and Actuators B: Chemical **69**(1), 28–36 (2000).

159. Y. J. He, "Novel D-shape LSPR fiber sensor based on nano-metal strips," Opt. Express **21**(20), 23498–23510 (2013).

160. Z. Tian, S. S.-H. Yam, and H.-P. Loock, "Refractive index sensor based on an abrupt taper Michelson interferometer in a single-mode fiber," Opt. Lett. **33**(10), 1105–1107 (2008).

161. G. F. S. Andrade, M. Fan, and A. G. Brolo, "Multilayer silver nanoparticles-modified optical fiber tip for high performance SERS remote sensing," Biosensors and Bioelectronics **25**(10), 2270–2275 (2010).

162. Z. Yin, Y. Geng, Q. Xie, X. Hong, X. Tan, Y. Chen, L. Wang, W. Wang, and X. Li, "Photoreduced silver nanoparticles grown on femtosecond laser ablated, D-shaped fiber probe for surface-enhanced Raman scattering," Appl. Opt. **55**(20), 5408–5412 (2016).

163. Z. Chen, Z. Dai, N. Chen, S. Liu, F. Pang, B. Lu, and T. Wang, "Gold Nanoparticles-Modified Tapered Fiber Nanoprobe for Remote SERS Detection," IEEE Photonics Technology Letters **26**(8), 777–780 (2014).

164. H. Yan, C. Gu, C. Yang, J. Liu, G. Jin, J. Zhang, L. Hou, and Y. Yao, "Hollow core photonic crystal fiber surface-enhanced Raman probe," Appl. Phys. Lett. 204101 (2006).

165. F. M. Cox, A. Argyros, M. C. J. Large, and S. Kalluri, "Surface enhanced Raman scattering in a hollow core microstructured optical fiber," Optics Express **15**(21), 13675–13681 (2007).

166. Y. Han, S. Tan, M. K. K. Oo, D. Pristinski, S. Sukhishvili, and H. Du, "Towards Full-Length Accumulative Surface-Enhanced Raman Scattering-Active Photonic Crystal Fibers," Advanced Materials **22**(24), 2647–2651 (2010).

167. U. S. Dinish, F. Beffara, G. Humbert, J.-L. Auguste, and M. Olivo, "Surface-enhanced Raman scattering-active photonic crystal fiber probe: Towards next generation liquid biopsy sensor with ultra high sensitivity," Journal of Biophotonics **12**(11), e201900027 (2019).

168. A. Khetani, A. Momenpour, E. I. Alarcon, and H. Anis, "Hollow core photonic crystal fiber for monitoring leukemia cells using surface enhanced Raman scattering (SERS)," Biomedical Optics Express **6**(11), 4599–4609 (2015).

169. V. S. Tiwari, A. Khetani, M. Naji, and H. Anis, "Study of surface enhanced Raman scattering (SERS) within hollow core photonic crystal fiber," in *2009 IEEE Sensors* (IEEE, 2009), Christchurch, New Zealand, 367–370.

170. A. Knebl, D. Yan, J. Popp, and T. Frosch, "Fiber enhanced Raman gas spectroscopy," TrAC Trends in Analytical Chemistry **103**, 230–238 (2018).

171. S. Unterkofler, R. J. McQuitty, T. G. Euser, N. J. Farrer, P. J. Sadler, and P. S. J. Russell, "Microfluidic integration of photonic crystal fibers for online photochemical reaction analysis," Optics Letters **37**(11), 1952–1954 (2012).

172. L. Xiao, N. V. Wheeler, N. Healy, and A. C. Peacock, "Integrated hollow-core fibers for nonlinear optofluidic applications," Optics Express **21**(23), 28751–28757 (2013).

173. N. Zhang, K. Li, Y. Cui, Z. Wu, P. P. Shum, J.-L. Auguste, X. Q. Dinh, G. Humbert, and L. Wei, "Ultra-sensitive chemical and biological analysis via specialty fibers with built-in microstructured optofluidic channels," Lab Chip **18**(4), 655–661 (2018).

174. G. K. L. Wong, A. Y. H. Chen, S. W. Ha, R. J. Kruhlak, S. G. Murdoch, R. Leonhardt, J. D. Harvey, and N. Y. Joly, "Characterization of chromatic dispersion in photonic crystal fibers using scalar modulation instability," Opt. Express **13**(21), 8662–8670 (2005).

175. T. A. Birks, J. C. Knight, and P. S. J. Russell, "Endlessly single-mode photonic crystal fiber," Optics Letters **22**(13), 961–963 (1997).

176. J. C. Knight, T. A. Birks, P. S. J. Russell, and D. M. Atkin, "All-silica single-mode optical fiber with photonic crystal cladding," Optics Letters **21**(19), 1547–1549 (1996).

177. T. M. Monro, P. J. Bennett, N. G. R. Broderick, and D. J. Richardson, "Holey fibers with random cladding distributions," Opt. Lett. **25**(4), 206–208 (2000).

178. J. C. Knight, J. Arriaga, T. A. Birks, A. Ortigosa-Blanch, W. J. Wadsworth, and P. S. J. Russell, "Anomalous dispersion in photonic crystal fiber," IEEE Photon. Technol. Lett. **12**(7), 807–809 (2000).

179. I. Shavrin, S. Novotny, and H. Ludvigsen, "Mode excitation and supercontinuum generation in a few-mode suspended-core fiber," Optics Express **21**(26), 32141–32150 (2013).

180. Y. Guo, M. K. Khaing Oo, K. Reddy, and X. Fan, "Ultrasensitive Optofluidic Surface-Enhanced Raman Scattering Detection with Flow-through Multihole Capillaries," ACS Nano **6**(1), 381–388 (2012).

181. A. M. Apetrei, M. C. Phan Huy, N. Belabas, J. A. Levenson, J.-M. Moison, J. M. Dudley, G. Mélin, A. Fleureau, L. Galkovsky, and S. Lempereur, "A dense array of small coupled waveguides in fiber technology: trefoil channels of microstructured optical fibers," Optics Express **16**(25), 20648–20655 (2008).

182. J. M. Moison, A. M. Apetrei, J. A. Levenson, G. Mélin, P. Pédeboscq, A. Fleureau, S. Lempereur, and L. Gasca, "Light transmission in multiple or single subwavelength trefoil channels of microstructured fibers," Optics Express **13**(4), 1193–1201 (2005).

183. Y. Zhang, D. Yong, X. Yu, L. Xia, D. Liu, and Y. Zhang, "Amplification of Surface-Enhanced Raman Scattering in Photonic Crystal Fiber Using Offset Launch Method," Plasmonics **8**(2), 209–215 (2013).

184. G. Bouwmans, F. Luan, J. Knight, P. St. J. Russell, L. Farr, B. Mangan, and H. Sabert, "Properties of a hollow-core photonic bandgap fiber at 850 nm wavelength," Optics Express **11**(14), 1613 (2003).

185. J. C. Knight, J. Broeng, T. A. Birks, and P. S. J. Russell, "Photonic Band Gap Guidance in Optical Fibers," Science **282**(5393), 1476–1478 (1998).

186. R. F. Cregan, B. J. Mangan, J. C. Knight, T. A. Birks, P. S. J. Russell, P. J. Roberts, and D. C. Allan, "Single-Mode Photonic Band Gap Guidance of Light in Air," Science **285**(5433), 1537–1539 (1999).

187. P. J. Roberts, F. Couny, H. Sabert, B. J. Mangan, D. P. Williams, L. Farr, M. W. Mason, A. Tomlinson, T. A. Birks, J. C. Knight, and P. St. J. Russell, "Ultimate low loss of hollow-core photonic crystal fibres," Optics Express **13**(1), 236–244 (2005).

188. T. A. Birks, D. M. Bird, T. D. Hedley, J. M. Pottage, and P. S. J. Russell, "Scaling laws and vector effects in bandgap-guiding fibres," Optics Express **12**(1), 69–74 (2004).

189. G. Antonopoulos, F. Benabid, T. A. Birks, D. M. Bird, J. C. Knight, and P. S. J. Russell, "Experimental demonstration of the frequency shift of bandgaps in photonic crystal fibers due to refractive index scaling," Optics Express **14**(7), 3000–3006 (2006).

190. G. Humbert, J. C. Knight, G. Bouwmans, P. S. J. Russell, D. P. Williams, P. J. Roberts, and B. J. Mangan, "Hollow core photonic crystal fibers for beam delivery," Optics Express **12**(8), 1477–1484 (2004).

191. E. Nguema, D. Férachou, G. Humbert, J.-L. Auguste, and J.-M. Blondy, "Broadband terahertz transmission within the air channel of thin-wall pipe," Opt. Lett. **36**(10), 1782–1784 (2011).

192. F. Benabid, "Stimulated Raman Scattering in Hydrogen-Filled Hollow-Core Photonic Crystal Fiber," Science **298**(5592), 399–402 (2002).

193. F. Couny, F. Benabid, P. J. Roberts, P. S. Light, and M. G. Raymer, "Generation and Photonic Guidance of Multi-Octave Optical-Frequency Combs," Science **318**(5853), 1118–1121 (2007).

194. B. M. Trabold, R. J. R. Hupfer, A. Abdolvand, and P. St.J. Russell, "Broadband high-resolution multi-species CARS in gas-filled hollow-core photonic crystal fiber," Optics Letters **42**(17), 3283–3286 (2017).

195. F. Couny, F. Benabid, and P. S. Light, "Large-pitch kagome-structured hollow-core photonic crystal fiber," Opt. Lett. **31**(24), 3574–3576 (2006).

196. T. D. Bradley, G. T. Jasion, J. R. Hayes, Yong Chen, L. Hooper, H. Sakr, M. Alonso, A. Taranta, A. Saljoghei, H. C. Mulvad, M. Fake, I. A. K. Davidson, N. V. Wheeler, E. N. Fokoua, Wei Wang, S. R. Sandoghchi, D. J. Richardson, and F. Poletti, "Antiresonant Hollow Core Fibre with 0.65 dB/km Attenuation across the C and L Telecommunication Bands," in *45th European Conference on Optical Communication (ECOC 2019)* (Institution of Engineering and Technology, 2019), 294.

197. V. T. Hoang, D. Dobrakowski, G. Stępniewski, R. Kasztelanic, D. Pysz, K. X. Dinh, M. Klimczak, M. Śmietana, and R. Buczyński, "Antiresonant fibers with single- and double-ring capillaries for optofluidic applications," Opt. Express **28**(22), 32483–32498 (2020).

198. S. Yiou, P. Delaye, A. Rouvie, J. Chinaud, R. Frey, G. Roosen, P. Viale, S. Février, P. Roy, J.-L. Auguste, and J.-M. Blondy, "Stimulated Raman scattering in an ethanol core microstructured optical fiber," Optics Express **13**(12), 4786–4791 (2005).

199. R. Altkorn, I. Koev, R. P. Van Duyne, and M. Litorja, "Low-loss liquid-core optical fiber for low-refractive-index liquids: fabrication, characterization, and application in Raman spectroscopy," Applied Optics **36**(34), 8992–8998 (1997).

200. A. Khetani, V. S. Tiwari, A. Harb, and H. Anis, "Monitoring of heparin concentration in serum by Raman spectroscopy within hollow core photonic crystal fiber," Optics Express **19**(16), 15244–15254 (2011).

201. M. K. Khaing Oo, Y. Han, J. Kanka, S. Sukhishvili, and H. Du, "Structure fits the purpose: photonic crystal fibers for evanescent-field surface-enhanced Raman spectroscopy," Optics Letters **35**(4), 466–468 (2010).

202. B. M. Philip, J. G. Brock-Utne, H. J. M. Lemmens, R. A. Jaffe, and P. E. Shuttleworth, "Does a Delay in Performing an Activated Clotting (ACT) Test Really Matter? A Study in Nonheparinized Blood and a Single ACT Machine," The Journal of ExtraCorporeal Technology **40**, 193–195 (2008).

203. X. Yang, A. Y. Zhang, D. A. Wheeler, T. C. Bond, C. Gu, and Y. Li, "Direct molecule-specific glucose detection by Raman spectroscopy based on photonic crystal fiber," Analytical and Bioanalytical Chemistry **402**(2), 687–691 (2012).

204. A. J. Berger, T.-W. Koo, I. Itzkan, G. Horowitz, and M. S. Feld, "Multicomponent blood analysis by near-infrared Raman spectroscopy," Applied Optics **38**(13), 2916–2926 (1999).

205. K. E. Shafer-Peltier, C. L. Haynes, M. R. Glucksberg, and R. P. Van Duyne, "Toward a Glucose Biosensor Based on Surface-Enhanced Raman Scattering," Journal of the American Chemical Society **125**(2), 588–593 (2003).

206. D. Yan, J. Popp, M. W. Pletz, and T. Frosch, "Highly Sensitive Broadband Raman Sensing of Antibiotics in Step-Index Hollow-Core Photonic Crystal Fibers," ACS Photonics **4**(1), 138–145 (2017).

207. K. K. Chow, M. Short, S. Lam, A. McWilliams, and H. Zeng, "A Raman cell based on hollow core photonic crystal fiber for human breath analysis," Medical Physics **41**(9), 092701 (2014).

208. S. Hanf, T. Bögözi, R. Keiner, T. Frosch, and J. Popp, "Fast and Highly Sensitive Fiber-Enhanced Raman Spectroscopic Monitoring of Molecular H_2 and CH_4 for Point-of-Care Diagnosis of Malabsorption Disorders in Exhaled Human Breath," Anal. Chem. **87**(2), 982–988 (2015).

209. S. Hanf, R. Keiner, D. Yan, J. Popp, and T. Frosch, "Fiber-Enhanced Raman Multigas Spectroscopy: A Versatile Tool for Environmental Gas Sensing and Breath Analysis," Anal. Chem. **86**(11), 5278–5285 (2014).

210. A. Khetani, V. S. Tiwari, A. Momenpour, and H. Anis, "Monitoring of adenosine within hollow core photonic crystal fiber by surface enhanced Raman scattering (SERS)," in *2011 11th IEEE International Conference on Nanotechnology* (2011), 973–977.

211. B. Knowles, C. Howe, and D. Aden, "Human hepatocellular carcinoma cell lines secrete the major plasma proteins and hepatitis B surface antigen," Science **209**(4455), 497–499 (1980).

212. G. J. Darlington, J. H. Kelly, and G. J. Buffone, "Growth and hepatospecific gene expression of human hepatoma cells in a defined medium," In Vitro Cellular & Developmental Biology **23**(5), 349–354 (1987).

213. A. Varki, "Sialic acids in human health and disease," Trends in Molecular Medicine **14**(8), 351–360 (2008).

214. M. Mareel, L. de Ridder, and J. Deman, "Histochemical study of the distribution of sialic acid on the surface of HeLa cells in culture," Histochemie **32**(4), 335–341 (1972).

215. C. Mylonas and D. Kouretas, "Lipid peroxidation and tissue damage," In Vivo **13**(3), 295–309 (1999).

216. T. Gong, N. Zhang, K. V. Kong, D. Goh, C. Ying, J.-L. Auguste, P. P. Shum, L. Wei, G. Humbert, K.-T. Yong, and M. Olivo, "Rapid SERS monitoring of lipid-peroxidation-derived protein modifications in cells using photonic crystal fiber sensor," Journal of Biophotonics **9**(1–2), 32–37 (2016).

217. F. Poletti, "Nested antiresonant nodeless hollow core fiber," Optics Express **22**(20), 23807–23828 (2014).

218. S. Gao, Y. Wang, X. Liu, C. Hong, S. Gu, and P. Wang, "Nodeless hollow-core fiber for the visible spectral range," Optics Letters **42**(1), 61–64 (2017).

219. Y. Zhang, C. Shi, C. Gu, L. Seballos, and J. Z. Zhang, "Liquid core photonic crystal fiber sensor based on surface enhanced Raman scattering," Applied Physics Letters **90**(19), 193504 (2007).

220. H. Chen, F. Tian, J. Chi, J. Kanka, and H. Du, "Advantage of multi-mode sapphire optical fiber for evanescent-field SERS sensing," Optics Letters **39**(20), 5822–5825 (2014).

221. S. Afshar V., S. C. Warren-Smith, and T. M. Monro, "Enhancement of fluorescence-based sensing using microstructured optical fibres," Optics Express **15**(26), 17891–17901 (2007).

222. A. Stalmashonak, G. Seifert, and A. Abdolvand, "Optical Properties of Nanocomposites Containing Metal Nanoparticles," in *Ultra-Short Pulsed Laser Engineered Metal-Glass Nanocomposites*, A. Stalmashonak, G. Seifert, and A. Abdolvand, eds. (Springer International Publishing, 2013), 5–15.

223. G. M. Hale and M. R. Querry, "Optical Constants of Water in the 200-nm to 200-Mm Wavelength Region," Applied Optics **12**, 555–563 (1973).

224. A. D. Rakić, A. B. Djurišić, J. M. Elazar, and M. L. Majewski, "Optical properties of metallic films for vertical-cavity optoelectronic devices," Appl. Opt. **37**(22), 5271–5283 (1998).

225. F. Beffara, J. Perumal, A. Puteri Mahyuddin, M. Choolani, S. A. Khan, J.-L. Auguste, S. Vedraine, G. Humbert, U. S. Dinish, and M. Olivo, "Development of highly reliable SERS-active photonic crystal fiber probe and its application in the detection of ovarian cancer biomarker in cyst fluid," Journal of Biophotonics **13**(3), e201960120 (2020).

226. N. S. Kapany and J. J. Burke, "Waveguide Mode Lauching," in *Optical Waveguides*, Quantum Electronics–Principles and Applications (Academic Press, 1972), 159–179.

227. T. Ma, A. Markov, L. Wang, and M. Skorobogatiy, "Graded index porous optical fibers – dispersion management in terahertz range," Opt. Express **23**(6), 7856–7869 (2015).

228. T. G. Euser, J. S. Y. Chen, M. Scharrer, P. S. J. Russell, N. J. Farrer, and P. J. Sadler, "Quantitative broadband chemical sensing in air-suspended solid-core fibers," Journal of Applied Physics **103**(10), 103108 (2008).

229. M. Osawa, N. Matsuda, K. Yoshii, and I. Uchida, "Charge transfer resonance Raman process in surface-enhanced Raman scattering from p-aminothiophenol adsorbed on silver: Herzberg-Teller contribution," J. Phys. Chem. **98**(48), 12702–12707 (1994).

230. J. Zheng, Y. Zhou, X. Li, Y. Ji, T. Lu, and R. Gu, "Surface-Enhanced Raman Scattering of 4-Aminothiophenol in Assemblies of Nanosized Particles and the Macroscopic Surface of Silver," Langmuir **19**(3), 632–636 (2003).

231. K. Uetsuki, P. Verma, T. Yano, Y. Saito, T. Ichimura, and S. Kawata, "Experimental Identification of Chemical Effects in Surface Enhanced Raman Scattering of 4-Aminothiophenol," J. Phys. Chem. C **114**(16), 7515–7520 (2010).

232. D. Enders, T. Nagao, A. Pucci, and T. Nakayama, "Reversible adsorption of Au nanoparticles on SiO2/Si: An in situ ATR-IR study," Surface Science **600**(6), L71–L75 (2006).

233. Y. Wang, W. Qian, Y. Tan, and S. Ding, "A label-free biosensor based on gold nanoshell monolayers for monitoring biomolecular interactions in diluted whole blood," Biosensors and Bioelectronics **23**(7), 1166–1170 (2008).

234. Q. Su, X. Ma, J. Dong, C. Jiang, and W. Qian, "A Reproducible SERS Substrate Based on Electrostatically Assisted APTES-Functionalized Surface-Assembly of Gold Nanostars," ACS Appl. Mater. Interfaces **3**(6), 1873–1879 (2011).

235. F. Beffara, G. Humbert, J.-L. Auguste, J. Perumal, U. S. Dinish, and M. Olivo, "Optimization and performance analysis of SERS-active suspended core photonic crystal fibers," Opt. Express **28**(16), 23609–23619 (2020).

236. A. Tycova, K. Kleparnik, and F. Foret, "Bi-Ligand Modification of Nanoparticles: An Effective Tool for Surface-Enhanced Raman Spectrometry in Salinated Environments," Nanomaterials **9**(9), 1259 (2019).

237. T. Porstmann and S. T. Kiessig, "Enzyme immunoassay techniques an overview," Journal of Immunological Methods **150**(1), 5–21 (1992).

238. Y.-C. C. Liu, N. Rieben, L. Iversen, B. S. Sørensen, J. Park, J. Nygård, and K. L. Martinez, "Specific and reversible immobilization of histidine-tagged proteins on functionalized silicon nanowires," Nanotechnology **21**(24), 245105 (2010).

239. T.-M. Cheng, J.-P. Pan, S.-T. Lai, L.-P. Kao, H.-H. Lin, and S. J. T. Mao, "Immunochemical property of human haptoglobin phenotypes: Determination of plasma haptoglobin using type-matched standards," Clinical Biochemistry **40**(13), 1045–1056 (2007).

240. P. Baker and E. Oliva, "A Practical Approach to Intraoperative Consultation in Gynecological Pathology," International Journal of Gynecological Pathology **27**(3), 353–365 (2008).

241. P. Cross, R. Naik, A. Patel, A. Nayar, J. Hemming, S. Williamson, J. Henry, R. Edmondson, K. Godfrey, K. Galaal, A. Kucukmetin, and A. Lopes, "Intra-operative frozen section analysis for suspected early-stage ovarian cancer: 11 years of Gateshead Cancer Centre experience," BJOG: An International Journal of Obstetrics & Gynaecology **119**(2), 194–201 (2012).

242. N. D. Ratnavelu, A. P. Brown, S. Mallett, R. J. Scholten, A. Patel, C. Founta, K. Galaal, P. Cross, and R. Naik, "Intraoperative frozen section analysis for the diagnosis of early stage ovarian cancer in suspicious pelvic masses," Cochrane Database of Systematic Reviews (2016).

243. P. M. A. J. Geomini, L. D. Zuurendonk, G. L. Bremer, J. de Graaff, R. F. P. M. Kruitwagen, and B. W. J. Mol, "The impact of size of the adnexal mass on the accuracy of frozen section diagnosis," Gynecologic Oncology **99**(2), 362–366 (2005).

244. C. Zhao, L. Annamalai, C. Guo, N. Kothandaraman, S. C. L. Koh, H. Zhang, A. Biswas, and M. Choolani, "Circulating haptoglobin is an independent prognostic factor in the sera of patients with epithelial ovarian cancer," Neoplasia (New York, N.Y.) **9**(1), 1–7 (2007).

245. J. Perumal, G. Balasundaram, A. P. Mahyuddin, M. Choolani, and M. Olivo, "SERS-based quantitative detection of ovarian cancer prognostic factor haptoglobin," International journal of nanomedicine **10**, 1831–1840 (2015).

246. A. Mahyuddin, L. Liu, C. Zhao, N. Kothandaraman, M. Salto-Tellez, B. Pang, D. Lim, L. Annalamai, J. Chan, T. Lim, A. Biswas, G. Rice, K. Razvi, and M. Choolani, "Diagnostic accuracy of haptoglobin within ovarian cyst fluid as a potential point-of-care test for epithelial ovarian cancer: an observational study," BJOG: An International Journal of Obstetrics & Gynaecology **125**(4), 421–431 (2018).

247. J. Perumal, A. Mahyuddin, G. Balasundaram, D. Goh, C. Y. Fu, A. Kazakeviciute, U. Dinish, M. Choolani, and M. Olivo, "SERS-based detection of haptoglobin in ovarian cyst fluid as a point-of-care diagnostic assay for epithelial ovarian cancer," Cancer Management and Research **Volume 11**, 1115–1124 (2019).

248. Cao, R. Jin, and C. A. Mirkin, "DNA-Modified Core−Shell Ag/Au Nanoparticles," J. Am. Chem. Soc. **123**(32), 7961–7962 (2001).

249. J. J. Storhoff, S. S. Marla, P. Bao, S. Hagenow, H. Mehta, A. Lucas, V. Garimella, T. Patno, W. Buckingham, W. Cork, and U. R. Müller, "Gold nanoparticle-based detection of genomic DNA targets on microarrays using a novel optical detection system," Biosensors and Bioelectronics **19**(8), 875–883 (2004).

250. L. Carlini, C. Fasolato, P. Postorino, I. Fratoddi, I. Venditti, G. Testa, and C. Battocchio, "Comparison between silver and gold nanoparticles stabilized with negatively charged hydrophilic thiols: SR-XPS and SERS as probes for structural differences and similarities," Colloids and Surfaces A: Physicochemical and Engineering Aspects **532**, 183–188 (2017).

251. Y. Xue, X. Li, H. Li, and W. Zhang, "Quantifying thiol–gold interactions towards the efficient strength control," Nature Communications **5**, 4348 (2014).

252. N. R. Agarwal, A. Lucotti, M. Tommasini, F. Neri, S. Trusso, and P. M. Ossi, "SERS detection and DFT calculation of 2-naphthalene thiol adsorbed on Ag and Au probes," Sensors and Actuators B: Chemical **237**, 545–555 (2016).

253. T. A. Birks, W. J. Wadsworth, and P. S. J. Russell, "Supercontinuum generation in tapered f ibers," Optics Letters **25**(19), 1415–1417 (2000).

254. G. Humbert, W. Wadsworth, S. Leon-Saval, J. Knight, T. Birks, P. St. J. Russell, M. Lederer, D. Kopf, K. Wiesauer, E. Breuer, and D. Stifter, "Supercontinuum generation system for optical coherence tomography based on tapered photonic crystal fibre," Optics Express **14**(4), 1596–1603 (2006).

255. H.-Y. Lin, C.-H. Huang, G.-L. Cheng, N.-K. Chen, and H.-C. Chui, "Tapered optical fiber sensor based on localized surface plasmon resonance," Opt. Express **20**(19), 21693–21701 (2012).

256. H. A. Rahman, S. W. Harun, M. Yasin, S. W. Phang, S. S. A. Damanhuri, H. Arof, and H. Ahmad, "Tapered plastic multimode fiber sensor for salinity detection," Sensors and Actuators A: Physical **171**(2), 219–222 (2011).

257. C. Bariáin, I. R. Matías, F. J. Arregui, and M. López-Amo, "Optical fiber humidity sensor based on a tapered fiber coated with agarose gel," Sensors and Actuators B: Chemical **69**(1), 127–131 (2000).

258. T. Alder, A. Stohr, R. Heinzelmann, and D. Jager, "High-efficiency fiber-to-chip coupling using low-loss tapered single-mode fiber," IEEE Photonics Technology Letters **12**(8), 1016–1018 (2000).

Published work and conferences

Patent:

- Provisional patent: U. S. Dinish, M. Olivo, G. Humbert, F. Beffara, J.-L. Auguste, “Novel design of optical fiber for sensing analytes”, PCT/SG2020/050197, 31 March 2020.

Papers:

- F. Beffara, J. Perumal, A. Puteri Mahyuddin, M. Choolani, S. A. Khan, J.-L. Auguste, S. Vedraine, G. Humbert, U. S. Dinish, and M. Olivo, "Development of highly reliable SERS-active photonic crystal fiber probe and its application in the detection of ovarian cancer biomarker in cyst fluid," Journal of Biophotonics 13(3), e201960120 (2020).
- F. Beffara, G. Humbert, J.-L. Auguste, J. Perumal, U. S. Dinish, and M. Olivo, "Optimization and performance analysis of SERS-active suspended core photonic crystal fibers," Opt. Express **28**(16), 23609-23619 (2020).
- U. S. Dinish, F. Beffara, G. Humbert, J.-L. Auguste, and M. Olivo, "Surface-enhanced Raman scattering-active photonic crystal fiber probe: Towards next generation liquid biopsy sensor with ultra high sensitivity," Journal of Biophotonics 12(11), e201900027 (2019).

Conferences:

- F. Beffara, G. Humbert, J-L. Auguste, S. Vedraine, Dinish U.S., M. Olivo, “SERS based specialty optical fiber probe for bio-sensing”, Journée thématique Plasmonique organique et moléculaire, 29 January 2018, Paris, France. (Poster)
- F. Beffara, J. Perumal, A. Puteri Mahyuddin, M. Choolani, S. A. Khan, J-L. Auguste, S. Vedraine, G. Humbert, Dinish U. S, M. Olivo, “Improved SERS-based photonic crystal fiber: a step further towards next generation liquid biopsy needle”, Photonics Global Student Conference 2020, 7-11 September 2020, Shenzhen, China. (Oral)
- F. Beffara, G. Humbert, J-L. Auguste, Dinish U. S, M. Olivo, “Ring core fiber: a novel design of PCF for SERS sensing”, Photonics West, BIOS, 2021 paper BO603-18, 6-11 March 2021, San Francisco, California United States. (Oral: accepted)
- Dinish U. S, G. Humbert, J. Perumal, F. Beffara, J-L. Auguste, S. Vedraine, S. A. Khan, A. Puteri Mahyuddin, M. Choolani, M. Olivo, “SERS-active Photonic Crystal Fiber Probe: Towards Next Generation Biopsy Needle” Photonics West, BIOS, 2019 paper 10885-28, 2-7 February 2019, San Francisco, California United States. (Oral)

SERS biosensors based on special optical fibers for clinical diagnosis

Despite important breakthroughs in biosensing, we are still in need of new sensors that would facilitate the early detection of severe diseases such as cancer. Classical tissue biopsy remains the gold standard in many cases. Although this approach has shown its potential, it remains invasive for the patients and the detection techniques are either tedious or lack the sensitivity to detect the disease at an early stage. Raman spectroscopy has demonstrated its interests for biosensing. Its ability to characterize the chemical nature, structure and the orientation of an analyte makes it an ideal candidate. The sharp Raman peaks of a molecule can be seen as a true fingerprint. Regrettably, Raman scattered signal is extremely weak. This limitation was overcome by surface enhanced Raman spectroscopy (SERS), since it drastically increases the Raman scattered signal while maintaining the sharp peak of the fingerprint spectrum of a molecule. Unfortunately, most of the current SERS substrates are 2D nano-roughened metal surfaces or colloidal nanoparticles, which lack the sensitivity and reliability in measurement with poor repeatability and reproducibility in the data.
In the recent years, special optical fibers have been used as SERS platforms. They feature holes that run along their entire length. These holes allow for the analyte to be incorporated inside the fiber. Thus, such platform represents a promising alternative to planar substrates since the analyte and the excitation light can interact for longer length inside the fibers. In addition, optical fibers are very flexible, compact and allow for low-loss light guiding. Therefore, such fiber sensors exhibit the outstanding detection abilities of SERS, the advantages of optical fibers and improved sensitivity and reliability. In this manuscript, we aim to create a biosensing platform that could be routinely used in a clinical setting. For that, we propose to optimize the features of an already reported fiber topology. This allows us to increase its sensitivity while simultaneously improving its reliability and practicability. With this improved sensor, for the first time, we could detect the biomarker for ovarian cancer in clinical cyst fluids, which allowed us to differentiate the stage of the cancer. Subsequently, we propose a novel fiber topology, specifically designed to further increase the sensitivity of SERS-based fiber probes. This is achieved by increasing the surface of interaction compared to standard fiber sensors. For that, the core diameter is significantly increased and the amount of light that interacts with the analyte is precisely controlled. We envision that such functionalized fiber sensors could be incorporated inside a biopsy needle to create a two-in-one sensor for body fluid collection and readout that can eventually overcome the limitations associated with existing biopsy needle platforms, which demands for two-step sample collection and readout.

Keywords: Sensing, surface enhanced Raman spectroscopy, SERS, optical fiber.

Biocapteur SERS actif basé sur les fibres optiques spéciales pour le diagnostic médical

Malgré d'importantes percées dans le domaine de la biodétection, nous avons toujours besoin de nouveaux capteurs qui faciliteraient la détection précoce de maladies graves comme le cancer. La biopsie tissulaire classique reste la référence dans de nombreux cas. Bien que cette approche ait montré son potentiel, elle reste invasive pour les patients et les techniques de détection sont fastidieuses ou manquent de sensibilité pour détecter la maladie à un stade précoce. La spectroscopie Raman a démontré son intérêt pour la biodétection. Sa capacité à caractériser la nature chimique, la structure et l'orientation d'un analyte, en fait un candidat idéal. Les pics Raman très nets d'une molécule peuvent être considérés comme une véritable empreinte digitale. Malheureusement, le signal Raman diffusé est extrêmement faible. Cette limitation a été surmontée par la spectroscopie Raman exaltée de surface (SERS), car elle augmente considérablement le signal Raman diffusé tout en maintenant la largeur des pics du spectre d'une molécule. Malheureusement, la plupart des substrats SERS actuels sont soit des surfaces métalliques nano-rugueuses en 2D soit des nanoparticules colloïdales, qui manquent de sensibilité et de fiabilité dans les mesures avec une faible répétabilité et reproductibilité des données.
Ces dernières années, des fibres optiques spéciales ont été utilisées comme plateformes SERS. Elles comportent des trous qui s'étendent sur toute leur longueur. Ces trous permettent d'incorporer l'analyte à l'intérieur de la fibre. Ainsi, une telle plate-forme représente une alternative prometteuse aux substrats plans puisque l'analyte et la lumière d'excitation peuvent interagir sur une plus grande longueur à l'intérieur des fibres. De plus, les fibres optiques sont très flexibles, compactes, et permettent un guidage de la lumière à faible perte. Par conséquent, ces capteurs à fibres présentent à la fois les capacités de détection exceptionnelles du SERS, les avantages des fibres optiques et une sensibilité et une fiabilité améliorées. Dans ce manuscrit, nous visons à créer une plateforme de biodétection qui pourrait être utilisée dans un cadre clinique. Pour cela, nous proposons d'optimiser les caractéristiques d'une topologie de fibre déjà existante. Cela nous permet d'augmenter sa sensibilité tout en améliorant sa fiabilité et sa facilité d’utilisation. Grâce à ce capteur amélioré, nous avons pu pour la première fois détecter le biomarqueur du cancer de l'ovaire dans les fluides de kystes cliniques, ce qui nous a permis de différencier le stade du cancer. Par la suite, nous proposons une nouvelle topologie de fibre, spécifiquement conçue pour augmenter encore la sensibilité des sondes à fibre basées sur le SERS. Cette amélioration est réalisée en augmentant la surface d'interaction par rapport aux sondes à fibre standard. Pour cela, le diamètre du noyau est considérablement augmenté et la quantité de lumière qui interagit avec l'analyte est contrôlée avec précision. Nous envisageons que de tels capteurs à fibres fonctionnalisés puissent être incorporés à l'intérieur d'une aiguille de biopsie afin de créer un capteur deux-en-un pour la collecte et l’analyse de fluides corporels. Les limitations associées aux aiguilles de biopsie actuelles, qui exigent une collecte et une analyse des échantillons en deux étapes, pourraient ainsi être surmontées.

Mots-clés: Détection, spectroscopie Raman exaltée de surface, SERS, fibre optique.